THE UNIVERSITY *of* EDINBURGH

Charge density waves and superconductivity in U_6Fe

William George Whitley

A thesis submitted in fulfilment of the requirements
for the degree of Doctor of Philosophy
to the
University of Edinburgh
May 2015

Abstract

U_6Fe has the highest superconducting transition temperature $T_{SC} \sim 4$ K out of all of the U-based compounds. Unusually, the Pauli limit ($1.84T_{SC} = 7.36$ T) is less than the observed critical field for both the a and c axes in this tetragonal material. Neither Pauli or usual BCS orbital limit is apparently respected [1]. In order to explain why superconductivity exceeds the Pauli limit, it must be considered that either the superconducting state is unaffected by paramagnetic effects, or there is a large amount of spin-orbit scattering. Superconductivity is in the dirty limit for typical samples of U_6Fe, which means that the latter cannot be precluded.

Another unusual property of the superconducting state of U_6Fe is that T_{SC} has a positive dependence on the applied pressure P, for $P < 4$ kbar [2]. This combined with other subtle signals in various measurements [3,4] have led to the suggestion that a Charge Density Wave (CDW) state may exist in U_6Fe below 110 K. The CDW state is typically favoured by materials with low-dimensional structural features such as chains of atoms. Such materials, if superconductors, are also candidates to exhibit the sought-after Fulde-Ferrell-Larkin-Ovchinnikov (FFLO) state, an unusual state in which the superconducting order parameter is modulated in real space [5].

The FFLO is expected to be suppressed except in clean, Pauli limited materials. Therefore if U_6Fe can be produced at high enough quality to bring the superconducting state into the clean limit, it would be a potential candidate for an FFLO state. Part of this project discusses apparatus and techniques applied with the goal of producing such quality samples of U_6Fe. We have succeeded in the application of the Solid State Electrotransport (SSE) method to purifying samples, and have been able to replicate the highest Residual Resistivity Ratios (RRRs) achieved ($\sim$9, compared to 4 for typical samples), but for single crystals

instead of the polycrystals produced in the past. In parallel with the progress made towards higher quality samples of U_6Fe, a new X-ray scanner has been developed for grain mapping of samples. This has found application in the course of our synthesis studies.

The best quality samples have been studied by X-ray diffraction on the XMaS beamline at the ESRF in Grenoble, France. Below $T_{\mathrm{CDW}} \sim 10$ K, satellites at $(\delta H, \delta K, 0) = (\pm 0.11, \pm 0.11, 0)$ were observed that confirm a CDW state, albeit at much lower temperatures than anticipated. By examination of systematic satellite absences we have determined that the displacement vector $\vec{u}$ is perpendicular to the modulation direction in k-space. Additionally it has been found that the symmetry of the lattice below T_{CDW} is reduced from that of the room temperature $I4/mcm$ structure.

The appearance of additional Bragg peaks below $\sim$110 K during these experiments were later cast into doubt by multiple scattering. We have, however, detected a signal in the form of a jump at $\sim$110 K in specific heat measurements of our samples. These measurements also show a kink near to T_{CDW}.

We have additionally extended the investigation of the effect of pressure on the superconducting state. The maximum of T_{SC} is confirmed in our samples, and the subsequent suppression of T_{SC} and H_{c2} is investigated up to 8 GPa. We have analysed our $H_{c2}(T)$ curves at different pressures under a simple two-band model that fits the observed trends well and suggest that at the highest pressures U_6Fe is approaching even more unusually enhanced H_{c2} values.

Declaration

This thesis has been composed by the author. Except where otherwise stated, the research undertaken in this thesis was the unaided work of the author. Where the work was done in collaboration with others, a significant contribution was made by the author. This work has not been submitted for any other degree or professional qualification except as specified. Any included publications are the author's own work, except where indicated throughout the thesis and summarised and clearly identified on the declarations page of the thesis.

W. Whitley
May 2015

Acknowledgements

This work is indebted to the contributions of many people who I will take the opportunity to mention here.

I would like to thank: my supervisor Professor Andrew Huxley for his continual direction, encouragment, and patience; Dmitry Sokolov, for useful guidance in crystal growth techniques; Chris Stock, for organising the initial setup of the Laue scanner; Davide Marenduzzo, for advice regarding the SSE simulations; Andrew Downie, for engineering and equipment design advice; Derek Low, for manufacture and repair of the drop casting furnace crucibles; and Hunter Scullion, for electronics work relating to the Laue scanner.

In addition, I would like to thank Didier Wermeille, who worked closely with us during our XMaS experiments. These would not have been possible without his expertise. The other members of the beamline staff were also very helpful, providing advice and support throughout our experimental time there. The in-house PPMS and MPMS measurements were performed thanks to the help of Xiao Wang, Angel Lopez, and Martin Misek.

I would like to thank my colleagues Julian Schmehr, Chris O'Neill, Rachel Husband, Michal Kepa, Fred Farrell, and Dr Gino Abdul-Jabbar, for advice, support and reassurance.

Finally, I would like to thank Imogen, my parents and my sister for their love and support, without which this work would not have been possible.

Contents

List of Figures

List of Tables

Chapter 1

Introduction

1.1 The context of U_6Fe

Superconductors are an unusual class of materials which are classified by absolute zero resistivity and perfect diamagnetism [19, 20]. Since their discovery in the early 20^{th} century [21] the field of their study has broadened considerably. The class of non-conventional superconductors now covers a wide range of materials, of which Heavy Fermion (HF) superconductors are a subset. These superconductors are characterised by a significant renormalisation of the electron mass (often the effective mass m^* is of the order of 100 times the bare electron mass m_e) [20]. Such materials typically contain heavy elements such as Ce or U, which are considered to be the cause of the effective mass enhancement [20].

There are now many known uranium-based, HF superconductors (for example, UPt_3, URhGe, UGe_2) which exhibit a range of unusual phenomena [22]. U_6Fe has the highest superconducting transition temperature (T_{SC}) of any U-based compound at approximately 4 K, but the documented mass enhancement is on the low side for a HF compound ($m^*/m_e \approx 23$ [14]). U_6Fe is part of an isostructural series of superconducting compounds of U with transition metal elements with the formula U_6X, where X = Mn, Fe, Co, Ni [23]. Some measured properties [24, 25] of U_6Fe suggest that its superconducting nature can be described by the Bardeen Cooper Schrieffer (BCS) model [26]. There are, however, some significant properties which cannot be satisfactorily explained by this model.

One such property is that the dependence of the upper critical field (H_{c2})

on temperature is very steep near to T_{SC}. In this introductory chapter, the physical phenomena that set the upper critical field in type II superconductors will be discussed, introducing the idea of orbital and Pauli limiting fields. For superconductors where the Pauli limiting field is less than the orbital limiting field (as in U_6Fe) the Fulde-Ferrell-Larkin-Ovchinnikov (FFLO) state becomes a viable prospect [7]. This state is known to be favoured by materials with anomalies in the Fermi surface that may also favour the presence of modulated states such as the Charge Density Wave (CDW) state. Both the FFLO and CDW states are discussed below. Following this, a brief literature review is presented, highlighting the properties of U_6Fe that suggest it as a good candidate for both of these states. The core goal of this project was to obtain further evidence to support this hypothesis, and this chapter concludes by detailing the steps that were taken to this end. The chapters subsequent to this introduction further elucidate these steps.

1.2 The Upper Critical Field H_{c2}

1.2.1 Type I superconductors

For a sufficiently small applied field H, superconductors are perfectly diamagnetic materials, entirely excluding the field from the bulk. This is arguably the property that sets superconductors apart as a class of materials [20]. This is because metals in the limit of no impurities may exhibit perfect conductivity at 0 K, but they are not perfect diamagnets. The perfect diamagnetism of superconductors comes at an energy cost of $H^2/8\pi$ [20]. This means that the energy of the superconducting state increases quadratically with H (see the red curve in Fig. 1.1). At a critical field H_c, the superconducting state free energy density f_{SC} exceeds that of the normal state f_N, so that the normal state is energetically favourable and a transition occurs from the superconducting to the normal state. At this field, $H^2/8\pi$ is equal to the zero-field energy difference between f_N and f_{SC}. Therefore:

$$\frac{H_c(T)^2}{8\pi} = f_N(T, H = 0) - f_{SC}(T, H = 0). \tag{1.1}$$

This equation defines the thermodynamic critical field H_c, a quantity which is defined the same way in all superconductors. However, the critical field at which superconductivity breaks down is only equal to the thermodynamic critical field for type I superconductors. The behaviour under field of a different class (type II) of superconductor is described in the next section.

1.2.2 Type II superconductors and the orbital limit

The defining feature of type II superconductors is that above a lower critical field (H_{c1}), they allow some permeation of the magnetic field in the form of a lattice of Abrikosov vortices [27]. Each of these vortices contains one quantum of magnetic flux equal to $\phi_0 = 2.068 \times 10^{-15}$ Wb. These vortices are essentially normal state regions inside the material, leading to this configuration being termed the "mixed state". The vortices are packed together in an increasingly dense fashion as the magnetic field is increased towards an upper critical field (H_{c2}^{orb}) [19]. Above H_{c2}^{orb}, the magnetic field permeates the sample entirely and the superconducting state breaks down. The field at which Abrikosov vortices overlap, causing superconductivity to break down is known as the "orbital limit". When this happens, the flux density is equal to one quantum of flux ϕ_0 divided by the area of the vortex core (which has dimensions $\sim\xi$, where ξ is the superconducting coherence length), multiplied by a geometrical factor. Therefore, the orbital limit (in units of Wb m^{-2}) is given by:

$$H_{c2}^{orb} = \frac{\phi_0}{2\pi\xi^2}, \tag{1.2}$$

The partial penetration of the magnetic field means that the energy cost of field exclusion is less. Therefore, the free energy density of the superconducting state is lowered from the quadratic type I dependence above H_{c1}, as shown in Fig. 1.1 [6]. The orbital limit can be calculated from the slope of the $H_{c2}(T)$ curve near to T_{SC} using the equation [28]:

$$H_{c2}^{orb} = -C \left.\frac{dH_{c2}}{dT}\right|_{T_{\mathrm{SC}}} T_{\mathrm{SC}}. \tag{1.3}$$

C varies with the scattering length. In the clean limit, where the electron mean free path ℓ is much greater than the BCS coherence length ξ_0, $C = 0.7273$.

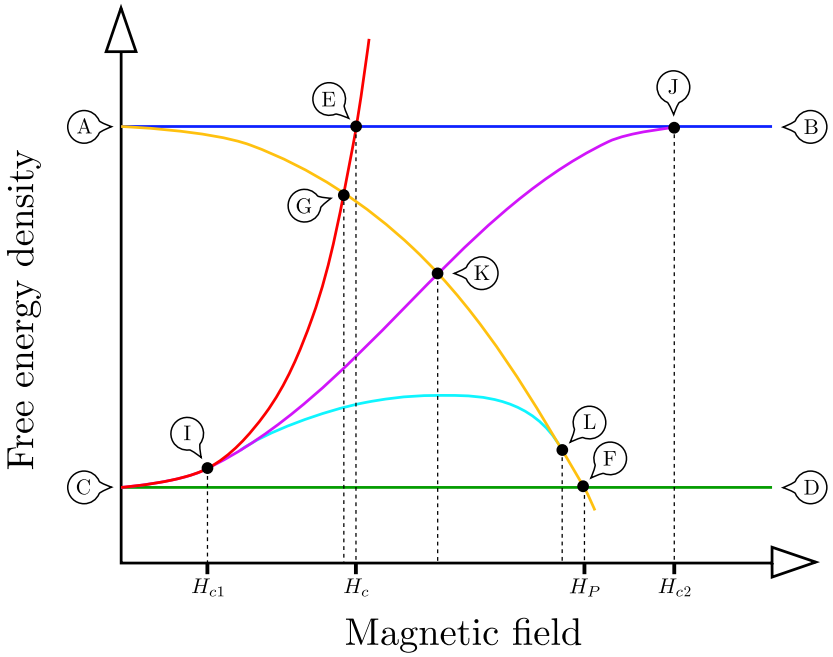

Figure 1.1: Plot of the change of the free energies of the normal and superconducting state under an applied field, adapted from [6]. The blue (A→B) and green (C→D) lines show the free energies of the normal and superconducting states neglecting any field effects. In type I materials, the superconducting energy is increased with applied field H by $H^2/8\pi$, until the normal state becomes energetically favourable at a field H_c (the red curve C→E illustrates this). Pauli paramagnetism reduces the energy of the normal state by $\chi_P H^2/2$, where χ_P is the Pauli susceptibility. This is shown by the yellow line A→F. Where the yellow and green lines intersect (F) defines the Pauli limiting field H_P. The field at which the red and yellow curves intersect (at G) is the critical field for a type I superconductor including Pauli effects. For type II superconductors in the absence of Pauli paramagnetism, the superconducting state follows the purple curve (I→J), becoming equal to the normal state energy at J. This defines the orbital limit, which sets H_{c2} for most superconductors. Where red and purple lines deviate (I) defines the lower critical field H_{c1}. Including paramagnetic effects in the normal state leads to the normal and superconducting state energies being equal at a lower field than H_{c2} or H_P (K). Including the paramagnetic effects in the mixed state leads to further reduction of the superconducting state energy, as shown by the cyan line (I→L).

In the dirty limit where $\ell \ll \xi_0$, $C = 0.69$ [28]. Eq. 1.3 follows from BCS theory, as described in well known papers by Werthamer, Helfand and Hohenberg (WHH) [6, 28].

1.2.3 Pauli paramagnetic effects

So far in this section, the field dependence of the normal state has been neglected. Including Pauli paramagnetic effects will lower the energy of the normal state quadratically with field by an energy $\chi_P H^2/2$, where χ_P is the Pauli susceptibility (this is shown by the yellow line in Fig. 1.1) [29]. The energy difference between the superconducting and normal states is therefore reduced, and the critical field decreases as a consequence. The limiting field of superconductivity due to these Pauli paramagnetic effects is called the Pauli limit H_P. The value of H_P (neglecting the field dependence of the superconducting state) can be calculated by considering simple energetics as follows. The energy gained from co-aligning spins due to Pauli paramagnetism is:

$$E_P = \frac{1}{2}\chi_P H^2, \tag{1.4}$$

where H is the applied field, and χ_P is the Pauli susceptibility:

$$\chi = g^2 \mu_B^2 N(E_F)/4. \tag{1.5}$$

In this equation, g is the Landé g-factor, μ_B is the Bohr magneton, and $N(E_F)$ is the electronic density of states at the Fermi level. The difference in energy between the superconducting and normal states is the condensation energy E_c:

$$E_c = \frac{1}{2}N(E_F)\Delta^2, \tag{1.6}$$

where Δ is the superconducting energy gap. Equating E_P and E_c gives the Pauli limit:

$$H_P = 2\Delta/g\mu_B. \tag{1.7}$$

In BCS theory, $\Delta = 1.76\ k_B T_{\mathrm{SC}}$ and so (using the free electron value for g of 2):

$$H_P^{BCS} = 1.84\ T_{\mathrm{SC}}. \tag{1.8}$$

The Pauli limit as derived here is known as the Clogston-Chandrasekhar limit [29].

For type I superconductors, including paramagnetic effects has little consequence, because the normal state energy is reduced relatively slowly with field, compared to the steep increase in the superconducting state energy. For type

II superconductors the critical field could potentially be much reduced from the orbital limit if H_P is comparable to H_{c2}^{orb} as is the case in Fig. 1.1. This neglects Pauli paramagnetism affecting the normal regions inside the vortices, when the material is in the mixed state. This lowers the energy of the mixed state further, leading to the cyan curve in Fig. 1.1. Lowering the mixed state energy results in the limiting field being increased, up to a value which is close to H_P.

For most superconductors, H_P is much larger than H_{c2}^{orb}. The Maki parameter $\alpha = \sqrt{2}H_{c2}^{orb}/H_{c2}^{P}$ is used to parameterise whether orbital or Pauli limiting is the dominant effect that sets the value of H_{c2} [30]. Clearly, a large α indicates Pauli limiting in a material. Equivalently, $\alpha \propto 3/2mv_F^2\tau$ where m is the electron mass, v_F is the Fermi velocity, and τ is the electron scattering time [6]. An enhanced electron mass reduces the Fermi velocity, which increases α, and the degree of Pauli limiting present. As previously mentioned, U_6Fe is a heavy fermion material in which the electron mass is indeed enhanced. The type of limit has consequences for the investigation of a novel state of matter known as a FFLO phase. This unusual state is the subject of the following section.

1.3 The Fulde-Ferrell-Larkin-Ovchinnikov Phase

In 1964, Fulde and Ferrell [31] discussed the nature of the superconducting state when in the presence of an exchange field. They suggested the scenario of paramagnetic atoms dissolved in a superconducting metal, but noted that the situation could be generalised from an exchange field to an applied field, provided that orbital effects could be neglected. In such an applied field, the Fermi surfaces of the up and down spins are split in momentum space by the Zeeman effect [32]. Under the usual mechanism [26], superconductors form by the pairing of opposite-spin, opposite-momentum electrons as seen in Fig. 1.2 a). Therefore, Zeeman-split electrons at the Fermi surface should not be able to form pairs, because on either spin surface their opposite spin counterparts have different momenta. Fulde and Ferrell, and also separately Larkin and Ovchinnikov [33], suggested that the pairing might be possible if the superconducting order parameter was modulated. The wavevector $\vec{q}$ of this modulation would be such that, for an electron on one Fermi surface with momentum $\vec{k}$, an electron exists on the opposite spin Fermi surface with momentum $-\vec{k} + \vec{q}$. This is illustrated in Fig. 1.2 b).

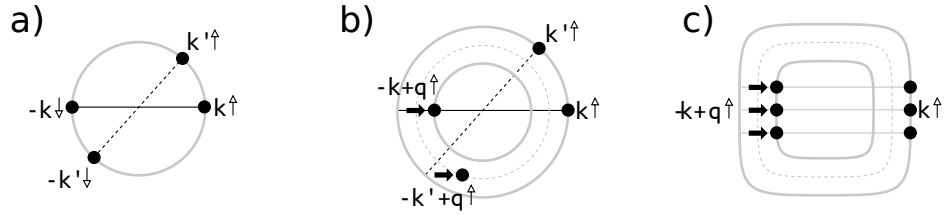

Figure 1.2: Schematic figure of pairing states, adapted from [7]. a) BCS pairing state between electrons of opposite momentum ($k\uparrow$,$k\downarrow$). b) FFLO pairing state ($k\uparrow$, $k+q\downarrow$). The Fermi surfaces of the spin up and down electrons are now split. Therefore, in order for opposite spins to be paired, the pairing must occur with an additional momentum q. Note that the q only works for pairing between k and $-k$: the electron with momentum $-k'+q$ does not lie on the Fermi surface. c) Split Fermi surface of a different shape. In this example, the same q works for a larger area of the Fermi surface.

In terms of the form of the modulation, Fulde and Ferrell proposed a modulated phase of the superconducting order parameter, whereas Larkin and Ovchinnikov proposed the form:

$$\Delta(\mathbf{r}) = 2\Delta_1 \cos(\mathbf{q}\cdot\mathbf{r})\,. \tag{1.9}$$

It has been shown that the form in Eq. 1.9 provides a lower free energy [33]. While other superconductors have been found to exhibit gap functions which are modulated in momentum space (*i.e.* the size of the gap is different at different points on the Fermi surface in k-space) [34], this form is clearly modulated in real space.

The presence of the FFLO will alter the appearance of the $H_{c2}(T)$ curve. Without considering the FFLO state, and in the case of no orbital limiting, the gradient of the H_{c2} *versus* T curve will be infinitely steep at T_{SC} [6] (see Fig. 1.3 a)). At lower temperatures, the second-order transition curve is expected to reach a maximum at a temperature T^{+}, with a first order curve appearing at higher fields. This situation has been shown to be energetically unstable to the formation of the FFLO [7]. With the FFLO, the phase diagram changes to as in Fig. 1.3 b). This figure shows how the FFLO state is expected to emerge through a first order transition below $T \approx T_{\mathrm{SC}}/2$ at fields above a critical field $H'(T)$. Further applied field will return the system *via* a second order transition to the normal state above H_{c2}.

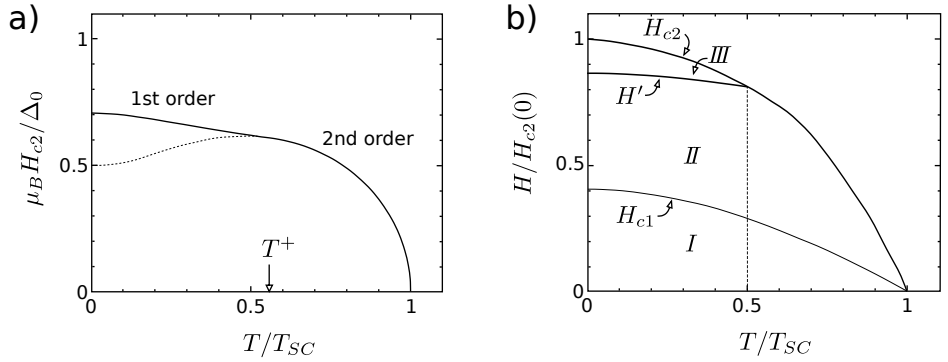

Figure 1.3: $H_{c2}(T)$ curves for Pauli limiting and FFLO cases. a) In Pauli limited superconductors without any orbital limiting, the slope of $H_{c2}(T)$ at $T_{\rm SC}$ should be infinite. The second order curve will reach a maximum at T^+, below which a first order transition appears at higher field. FFLO showed that this situation is less energetically favourable than a state with a spatially modulated order parameter. b) Phase diagram for the FFLO state, including orbital limiting effects. Transition to the FFLO state occurs for temperatures below $\approx T_{\rm SC}/2$, and fields above H'. The transition from the mixed state II to the FFLO state III is first order, and the transition from III to the normal state second order at H_{c2}. The lower critical field H_{c1} and the diamagnetic state I are also shown.

It has also been shown that the FFLO state is possible in the presence of orbital limiting, but including orbital effects has been calculated to be detrimental to its existence [35]. The FFLO state is theoretically possible if $\alpha > 1.8$ (for U_6Fe using the H_P and H_{c2} formulae calculated in the previous section in the dirty limit, $\alpha_{a\text{ axis}} \approx 1.8$, $\alpha_{c\text{ axis}} \approx 2.3$ [1]). In the absence of orbital limiting, the type of modulation is theorised to change from one-dimensional to modulation in several directions [7]. Impurities are also unfavourable to the state's formation [36].

Systems of lower dimensionality (*e.g.* those where atoms are localised into chains) typically have Fermi surfaces with large flat regions running parallel to each other [32]. The term for this is that the Fermi surfaces are "nested", and such a configuration increases the feasibility of the FFLO state [7]. Consider Fig. 1.2 b): the $\vec{q}$ vector of the modulated order parameter only satisfies pairing for the k, $-k+q$ pair of electrons. The electron at k' in this figure requires an electron at $-k'+q$ to pair, but such an electron would not be on the Fermi surface. In Fig. 1.2(c), parts of the Fermi surface are almost parallel. In this figure, electrons nearby to k can still pair using the same vector q as the electron at k. Nested Fermi surfaces are also favourable for the formation of certain other

states, notably CDWs and Spin Density Waves (SDWs), as will be discussed in the following section.

1.3.1 Potential candidates for the FFLO state

Despite its long history, the FFLO state has not yet been unambiguously observed in any material, although there have been many proposed candidates. Perhaps the best-known candidates include layered organic superconductors such as $\kappa - (\text{BEDT-TTF})_2\text{Cu(NCS)}_2$ [37], and the compound $CeCoIn_5$ [7].

For the organic superconductors, the orbital effect is restricted in the case of an applied field that is parallel to the layers. A recent low-temperature Nuclear Magnetic Resonance (NMR) study [38] of the material $\kappa - (\text{BEDT-TTF})_2\text{Cu(NCS)}_2$ showed relaxation rates in a narrow range near H_{c2} differ from both the normal and low-field superconducting behaviour, suggesting a phase diagram similar to that described above for the FFLO case. This builds on the past evidence for an unusual phase diagram from magnetic torque measurements [39]. The exact nature of the new phase has not yet been established.

$CeCoIn_5$ has a superconducting transition temperature of 2.3 K, but an upper critical field of almost 12 T, when the applied field is in the $a - b$ plane [7]. It is well-established that the normal-to-superconducting transition becomes first order at low temperatures [22], as would be expected in the case of a purely Pauli-limited superconductor. In addition, an additional phase has been detected within the superconducting region, referred to as the Q-phase [40]. The exact nature of the Q-phase has been debated, however. This is because $CeCoIn_5$ is close to an antiferromagnetic Quantum Critical Point (QCP), as shown by various measurements (for example, those showing a linear dependence of resistivity on temperature above T_{SC} [41]). The antiferromagnetic order was eventually discovered in the superconducting region, which has lead to the suggestion that the Q-phase may instead be a new state arising from interactions between antiferromagnetism and superconductivity [42].

1.4 Charge Density Waves

CDWs are a concept originally introduced in the 1930s by Rudolf Peierls. The fundamental idea came from considering a 1D periodic chain of atoms,

as described in [43]. The electrons of such a system would form a band with quadratic dispersion as shown in Fig. 1.4 a). The electrons fill the band up to the Fermi level, which in the case of this diagram means half-filling. The overall energy of the band can be reduced, however, if the periodicity of the lattice is changed due to a Periodic Lattice Distortion (PLD) as shown in Fig. 1.4 b) which opens up a gap in the band at the Fermi surface. The electrons just below the Fermi surface have their energy lowered, while the part of the band which has a raised energy is unoccupied, so the net energy is lower. The argument could be extended to further distortion of the lattice, but the PLD also increases the elastic energy of the system, and this counterbalances the lowering of the energy due to gaps to the extent that an equilibrium is reached.

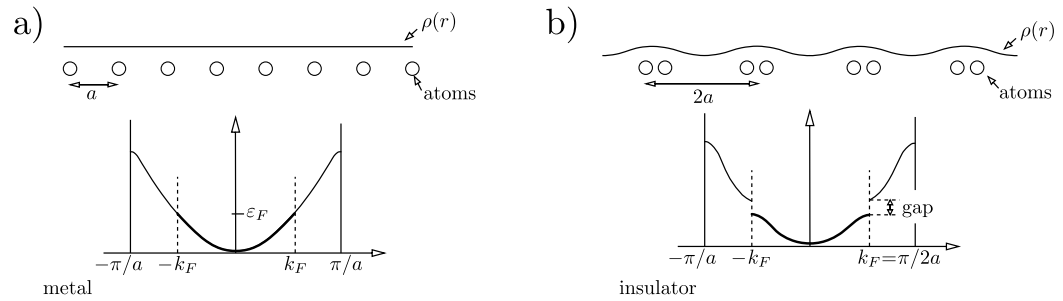

Figure 1.4: Splitting of a band due to a Peierls distortion, reproduced from [8].

The presence of the PLD will in turn cause a bunching of the electrons towards the areas of dense atomic charge. This spatial dependence of the electronic charge is the CDW. The CDW is then an interaction between the electrons and phonons and can be explained in a similar fashion to the modelling of superconductivity using BCS theory. The strength of the electron-phonon interaction has a significant impact on whether a CDW state forms [44]. The CDW state is also favoured if wavevectors exist that nest large areas of the Fermi surface, in the same way as described previously for the FFLO state. Therefore, as with the FFLO state, it is more likely that the CDW state will form in systems of lower dimensionality.

A notable and important (especially in the context of U_6Fe) example of a material that exhibits a CDW is α-U [45]. α-U forms a CDW at 43 K, but the unit cell does not obviously display low-dimensional elements in the way that many other CDW materials do. The $\vec{q}$ vector corresponding to the modulation that forms below 43 K has three components, and the direction changes with

temperature resulting in three CDW-related transitions. The clearest evidence for the α-U CDW is in X-ray scattering data where satellite peaks in intensity are observed around Bragg positions. Such satellites indicate a modulation of the underlying crystal lattice [46]. Signals of the change to the electronic and lattice configuration that the CDW transition causes are seen in resistivity [47] and specific heat [48], among other properties [45].

Superconductivity is also present in some samples of α-U, but the value of T_{SC} varies significantly in the literature [47]. T_{SC} increases as pressure is applied, while T_{CDW} falls [45]. The common interpretation of this is that applied pressure destroys the CDW state, which frees the Fermi surface that was previously gapped by the CDW. This extra Fermi surface is gapped instead by the superconducting state, and the larger amount of gapped Fermi surface is reflected in the increase in T_{SC}. Such "competition" between superconducting and CDW states is usually observed in CDW materials and reflects the intimate relationship between these two states [49].

In the next section of this chapter, we will discuss some of the properties of U_6Fe that are detailed in the literature. It will become clear that certain aspects of the material are quite suggestive that it may well show some of the behaviour that has been explained so far.

1.5 Literature review of and proposals for U_6Fe

U_6Fe has a body-centred tetragonal structure (space group *I4/mcm* [4]), as illustrated in Fig. 1.5. In the unit cell, the U atoms lie in sheets, and the Fe atoms effectively form chains because they are widely separated in the *a*-*b* plane. This structure is shared by the materials U_6X (X=Mn, Fe, Co, Ni). Across this series, the superconducting transition temperature T_{SC} mirrors the trend of the *a* lattice parameter [50] (*i.e.* U_6Fe has the smallest value of *a* and also the largest value of T_{SC}). Olsen *et al.* [51] studied the ambient temperature structure of powdered U_6Fe up to 50 GPa, observing a reduction of *a* by $\sim$0.6 Å, but no structural phase transition.

As with all U-based superconductors, the superconducting transition temperature is fairly modest. The gradient of H_{c2} of U_6Fe *versus* temperature is unusually steep, however. For example, a gradient of $|dH_{c2}/dT|_{T_{SC}}\sim$3.45 T/K is

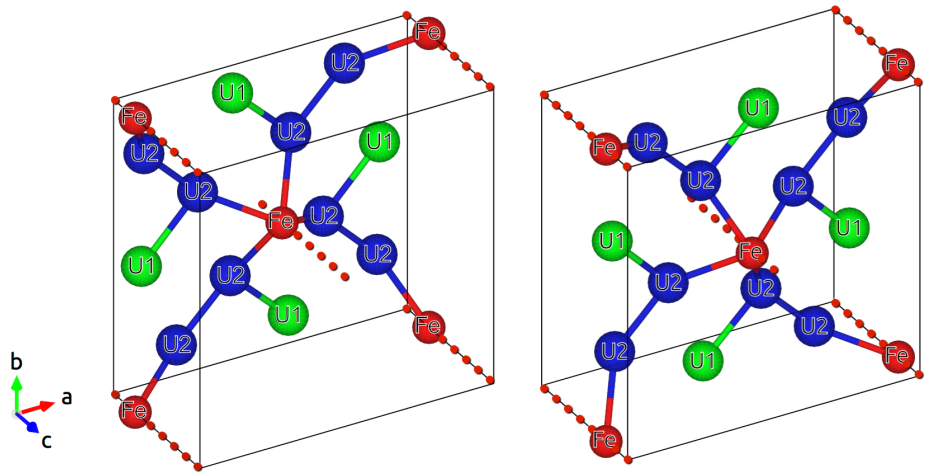

Figure 1.5: Structure of U_6Fe. The red coloured spheres are the Fe atoms, and the green and blue coloured spheres are the U_1 and U_2 atoms respectively, showing the two U sites in the cell. The first figure shows the view between $z = 0$ and $z = \frac{1}{4}$, and the second figure shows the view between $z = \frac{1}{2}$ and $z = \frac{3}{4}$. The U_1 atoms sit at $(x, x + \frac{1}{2}, 0)$ sites, while the U_2 sit at $(x, y, 0)$ sites. Red dotted lines illustrate the position of the chains of Fe atoms. The Fe atoms are significantly closer together along these chains than they are in the perpendicular direction.

found along the a-axis for a sample with T_{SC} of ~3.9 K, as shown in Fig. 1.6 [1]. Using these values in Eq. 1.3 for the clean limit predicts $H_{c2}^{orb} = 9.88$ T. By contrast, Eq. 1.8 predicts $H_P = 7.24$ T. This being the case means that the upper critical field for U_6Fe should be set by H_P. $H_{c2}(T = 0)$ of less than 10 T has never been observed, however. This is completely at odds with the expected critical field behaviour as $H_{c2}(T = 0)$ exceeds both the Pauli and orbital limits regardless of whether the clean or dirty limit is considered. In fact, even though the Chandrasekhar-Clogston limit is significantly lower than the orbital limit predicted by WHH theory, the $H_{c2}(T)$ curves are best fitted only by completely neglecting paramagnetic limitation effects, as shown in Fig. 1.6.

It is therefore necessary to look beyond the normal BCS theory of superconductivity in order to explain the high value of $H_{c2}(T = 0)$ in U_6Fe. Several theories exist for explaining the unusual $H_{c2}(T)$ curves. Two examples are strong coupling theory [16], where the electron-phonon interaction is enhanced, and multi-band models [15] where more than one electron band is gapped. Application of these models to the $H_{c2}(T)$ curves found in U_6Fe is detailed later in this thesis.

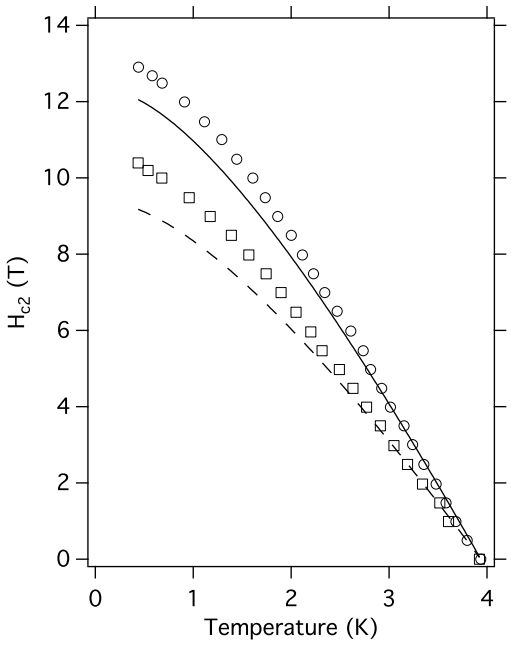

Figure 1.6: Data reproduced from [1] for the $H_{c2}(T)$ curves of single-crystalline U_6Fe. Circles show the data for applied field along the $(0, 0, 1)$ direction, squares show the data for applied field along the $(1, 1, 0)$ direction. The solid and dashed lines show curves obtained from the WHH theory [6] for the respective data, assuming $\alpha = 0$ (*i.e.* purely orbital limiting) in the clean limit.

Signals of a transition in U_6Fe have been observed in the ^{57}Fe Mössbauer spectra [4,52] at around 100 K. A very slight kink was also observed in resistivity measurements in high-quality polycrystalline samples at 100 K [3]. The quality factor usually used for U_6Fe samples is the Residual Resistivity Ratio (RRR), the ratio of the room temperature resistivity to that at low temperatures where impurity scattering is dominant. For the sample of U_6Fe showing a kink in resistivity at $\sim$ 100 K the RRR was $\approx$ 9. In addition to these findings, unpublished neutron scattering data taken by Huxley *et al.* shows a clear kink in the thermal expansion at around the same temperature (see Fig. 1.7).

The origin of these signals is not understood, and indeed they show no signs in various other measurements such as powder neutron diffraction [4] or measurements of the phonon density of states by inelastic scattering [53]. The aforementioned unpublished neutron scattering study showed no resolvable change in Laue photographs between 150 K and 50 K, as shown in Fig. 1.8. It has been suggested [3] that the origin of the signals at 110 K could be the

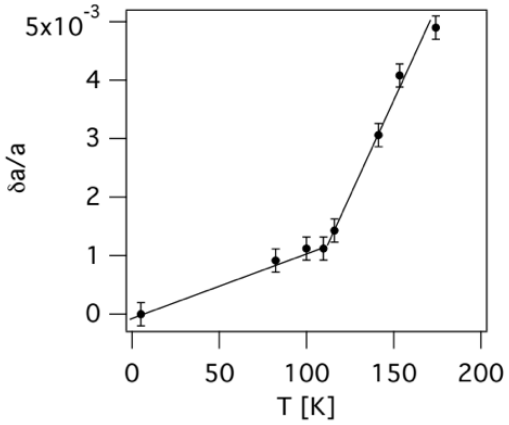

Figure 1.7: The thermal expansion of U_6Fe measured with D23 at the ILL for the (0,10,0) reflection (data taken by A D Huxley, unpublished). The thermal expansion is large with a very clear change of slope at around 110 K.

emergence of a CDW at low temperatures. Assuming that this is the case could help to explain the pressure dependence of T_{SC}, which is enhanced to a maximum at pressures of about 4 kbar [2]. This is very similar to the behaviour of α-U under applied pressure as discussed above.

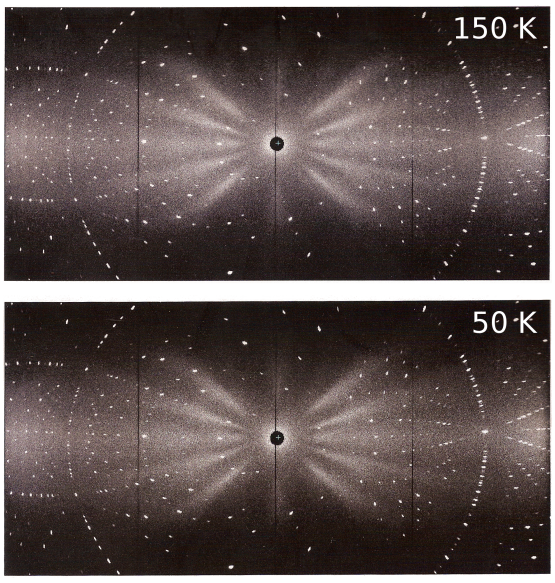

Figure 1.8: Laue neutron scattering photographs of U_6Fe captured at 150 K and 50 K (data taken by A D Huxley, unpublished). There is no resolvable change in the images with temperature in the form of obvious satellite peaks or significantly altered intensity from Bragg peaks.

U_6Fe is then a possible candidate for the FFLO state, as the Maki parameter is sufficiently high, and a possible candidate for a CDW. These states have been hinted at by different properties of the system which remain to be fully investigated, but they may be linked together as they are favoured by materials with some properties in common (primarily, they are both favoured by nesting of the Fermi surface).

There is significant motivation for improving the quality of grown samples of U_6Fe. Based on resistivity data in the literature it can be estimated that samples grown in the past have small values of ℓ that put the superconductivity in the dirty limit, but if a reduction in residual resistivity by a factor of 10 could be achieved then ℓ would become comparable to ξ. Such improvements should be possible, but may require a paradigm shift away from traditional sample preparation methods. Although the pure orbital limit presents the best WHH fit to experimentally observed $H_{c2}(T)$ curves, Pauli limited predictions are enhanced towards the orbital case when strong scattering from magnetic impurities is considered [6]. There is a case, therefore, to suggest that if the purity of U_6Fe can be significantly increased, interesting behaviour such as an FFLO state will become apparent in $H_{c2}(T)$ curves. Additionally, we hope that increasing the purity and quality of our samples will encourage the formation of a CDW at around 100 K. As mentioned above, resistivity measurements in the literature have only shown a signal of this transition in a high-quality polycrystal (RRR of 9 [3]). We hope that we can replicate this success in the form of a high-quality single crystal, by employing new crystal-purification techniques.

1.6 Thesis Structure

The underlying objective to this project was to be able to explain the unusual behaviour of U_6Fe that has been described above. One of the major limiting factors to start with was the difficulty in producing high quality samples, as they typically have an RRR of about 4 when produced by quench or Czochralski pulling, with a variation of approximately ± 0.5. In chapter 2 we detail the progress made in the area of sample preparation. We explain why U_6Fe is in particular a difficult material to produce at high purity. This chapter also documents the application of Solid State Electrotransport (SSE) to U_6Fe single

crystals, an approach which has been found to reliably produce single crystal samples of RRR $\sim 7-9$, comparable in quality to the highest-quality polycrystals documented.

Various sample preparation and characterisation facilities have been developed as part of this project. One of these is an X-ray scanner, which is able to map grains in large polycrystalline samples. This was in part used during this project to characterise the samples of U_6Fe that were grown and documented in chapter 2. This scanner is described in chapter 3.

The subsequent chapters focus on the results of experiments carried out on single-crystal samples of U_6Fe. Chapter 4 details the findings of X-ray scattering carried out at the XMaS beamline at the European Synchrotron Radiation Facility (ESRF) in Grenoble, France. During this experiment it was discovered that U_6Fe does indeed exhibit a CDW state, but that the transition temperature T_{CDW} is an order of magnitude lower than expected, at approximately 10 K. Chapter 5 documents measurements preformed of the specific heat of U_6Fe. A jump is obvious in the data at around 110 K that suggests a transition in line with that previously documented in the literature. Finally, chapter 6 focuses on in house measurements performed investigating the effects of pressure on single crystal samples of U_6Fe. In this chapter we focus on how to explain the very large $H_{c2}(T = 0)$ and document how applied pressure affects this.

Finally, chapter 7 addresses the conclusions which may be arrived at from the work presented in this thesis, and considers further work which may prove fruitful.

Chapter 2

Synthesis of U_6Fe

2.1 Introduction

In chapter 1, some of the unusual properties of the compound U_6Fe were discussed. These include the high values of T_{SC} and $H_{c2}(T = 0)$, and the maximum with applied pressure of T_{SC} [2]. This chapter will document work relating to the synthesis and purification of high-purity poly- and single-crystalline samples of U_6Fe, motivated by the possibility that some of these unusual properties may be significantly influenced by the presence of impurity phases in the compound. We will discuss the sample growth methods of quench and anneal, Czochralski pulling, and purification of samples by Solid State Electrotransport (SSE). The last of these was implemented using new equipment which will be described over the course of this chapter.

The U-Fe binary system forms two compounds, U_6Fe and UFe_2, as shown in the binary phase diagram of Chatain *et al.* [9] (see Fig. 2.1). U_6Fe forms peritectically from the melt. This means that if a melt of the correct stoichiometry is cooled slowly to room temperature, inclusions of γ-U will form before U_6Fe can solidify. This will move the melt off stoichiometry, and eventually result in inclusions of UFe_2 when the last of the melt finally solidifies (see Fig. 2.2).

It is quite possible that impurities of UFe_2 may have a significant role in changing the properties of a sample of U_6Fe when present as inclusions. UFe_2 is a cubic material that undergoes a ferromagnetic transition at 165 K [54]. Although there is little anisotropy in the magnetic behaviour, the transition to ferromagnet

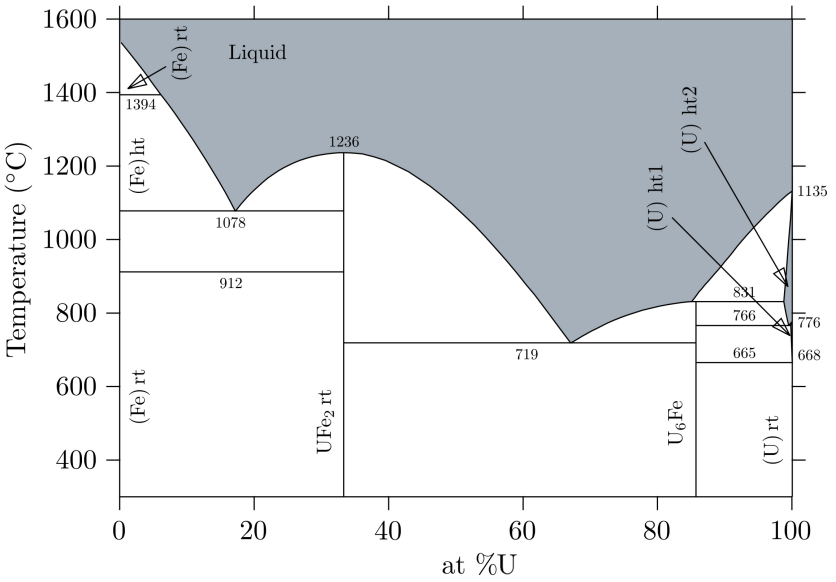

Figure 2.1: Phase diagram of the U-Fe system, reproduced from [9].

is accompanied by a large rhombohedral distortion to the lattice [54, 55]. This suggests that UFe_2 impurities could be a cause of significant magnetic and structural force applied to a U_6Fe host lattice. Studies of the effect of melt stoichiometry show that the T_{SC} of U_6Fe is reduced when the composition is U_xFe with $x < 6$, but the case of $x > 6$ does not show reduction in T_{SC}. The reduction of T_{SC} on the Fe rich side was attributed to the magnetism of UFe_2 [25]. From these studies of T_{SC} *versus* stoichiometry it is suggested that α-U inclusions have little impact on the equilibrium state of U_6Fe at low temperatures. α-U famously shows a Charge Density Wave (CDW) state below 43 K, however, and this could also conceivably be a source of strain to the U_6Fe lattice, as it is accompanied by abrupt changes in thermal expansion [45].

Single crystal samples are usually obtained by slow-cooling methods such as Czochralski pulling. These slow methods prevent the formation of many nucleation points that occur when a melt is rapidly cooled (quenched), but they also favour foreign-compound inclusions as is clear from the phase diagram and discussion above. This makes it intrinsically difficult to produce high-quality single crystals of U_6Fe by Czochralski pulling. It is unsurprising then that the purest samples recorded in the literature (1147B, Residual Resistivity Ratio (RRR) = 9) are polycrystals that were produced by quenching from the melt [2]. These were also annealed at 675°C for 1 week, followed by 760°C for 1 day.

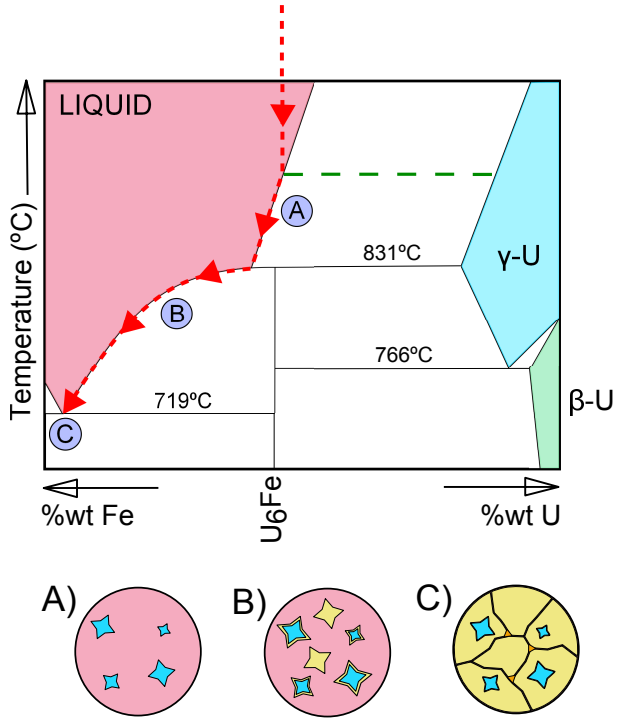

Figure 2.2: Expanded, distorted view of the binary phase diagram of [9]. Shown here is the high U concentration end of the diagram. The red dashed line marks an example cooling curve, which is slightly off stoichiometry for U_6Fe in the U-rich direction at high temperatures. When the melt cools slowly, the liquidus line is followed (as is traced out by the dashed red line). This is done by γ-U solidifying from the melt, starting at the temperature of the dashed green line. Subfigure A shows what the microscopic structure would look like, with the melt shown as pink, and the U inclusions shown as blue. The solidification of U from the melt increases the %wt of Fe in the melt, which is why the dashed red line moves to the left as the melt cools. When the temperature is sufficient for U_6Fe to solidify, the melt is off stoichiometry in the Fe direction, so that as U_6Fe starts to solidify the melt becomes increasingly Fe-rich. U_6Fe begins to form around the inclusions of γ-U, and given enough time the core of the U inclusions could combine with the Fe in the melt, but in practice the timescales are very large for such diffusion processes. Subfigure B shows the change in the microscopic structure from A, with yellow areas denoting the appearance of U_6Fe. At 719°C, the increasingly Fe-rich melt finally solidifies at the eutectic point. Some of the melt will solidify as U_6Fe, and some as UFe_2. At this stage most of the melt will have solidified as U_6Fe, so if there are inclusions of UFe_2 will appear at the interfaces between U_6Fe grains. Subfigure C illustrates this, showing small patches of UFe_2 as orange regions.

For quenched samples, annealing has also been shown to increase T_{SC} [25]. The effect of annealing could be to allow diffusion of U and UFe_2 inclusions to the surface, where they combine to make U_6Fe. We note that the explanation of the T_{SC} dependence on stoichiometry as due to UFe_2 inclusions only makes sense for quenched samples - for samples cooled slowly from a U-rich melt the melt stoichiometry will gradually change from $U_{6+x}Fe$ from $x > 0$ to $x < 0$ before the U_6Fe formation temperature is reached.

It is also important to consider for sample preparation that elemental Fe has a high vapour pressure, which starts to rise steeply near to the melting temperature of U_6Fe [10] (see Fig. 2.3). In order to make the purest samples, we concern ourselves with Ultra-High Vacuum (UHV) synthesis (pressures of $\sim 10^{-9}$ torr). Fig. 2.3 suggests that Fe would be evaporating from the melt at molten U_6Fe temperatures under UHV, which would gradually make the melt more U rich over time. When the Fe is present in a very U-rich mixture close to forming a compound, however, the vapour pressure could be altered significantly. The vapour pressure of U is significantly smaller over the same range and evaporation of U is unlikely.

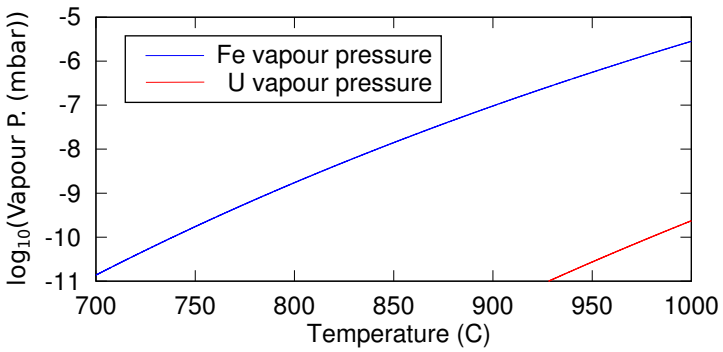

Figure 2.3: Plot of the vapour pressure of Fe and U as a function of temperature, over the range 700°C-1000°C plotted using the equation given in [10].

Based on the apparent difficulties inherent in Czochralski growth, our initial plan of action for producing high quality U_6Fe samples was therefore to try to reproduce the success of Delong *et al.* in producing high RRR polycrystals. To this end we performed several quenches under UHV conditions, and studied the effect of annealing on the measured sample RRR.

2.2 Quench-anneal studies

2.2.1 Preparation and growth

All of our sample growth was carried out under UHV conditions, achieved by the use of ion pumps and chambers assembled using standard metal seals. The sample heating was induced by an externally applied Radio Frequency (RF) magnetic field. Such a field causes eddy currents on the surface of materials inside the UHV region, and these currents resistively heat the sample to the melting point. The melting is carried out inside a water-cooled Hukin-style Oxygen-Free High Conductivity (OFHC) Cu crucible [56]. An advantage of this technique is that the applied field lifts the melt away from the crucible, reducing the chance of any impurity transferring from crucible to sample. This lifting is due to the interaction of eddy currents (which are induced in the material by the applied field) with the applied field, resulting in a levitation force.

For all of the samples synthesised as described in this chapter, the same source of depleted U was used. The U (after being cut to the desired mass) was electrochemically etched as a cathode at an applied voltage of 12 V in a solution of perchloric acid and glacial acetic acid. The ratio of 70% concentration perchloric acid to glacial acetic acid was 4:50. An iron cylinder was used as an anode. The U was then melted under UHV as described above in order to outgas impurities. The etch and melt was repeated, as the etch is expected to remove oxides that should come to the surface during the melt process. This is the same process as that applied when growing samples of other U-based compounds such as UGe_2 which have been produced to extremely high qualities [57].

For all of the quenches we describe here, we used cuts from a 99.995% pure Fe bar from Alfa Aesar. For the first quench, this was etched and melted under an Ar atmosphere twice. For the second and third quenches, it was only etched and melted under Ar atmosphere once. For the fourth quench, we annealed the Fe under UHV at 850 °C. Fe cannot be left to outgas impurities while molten under UHV as U can, due to the high vapour pressure of Fe.

The pre-treated samples were combined under UHV and kept molten for several hours to promote homogeneity. There was no noticeable deposition of Fe on the vacuum chamber walls indicating that if the Fe does escape the melt it is a very slow process. The value of x in the chemical formula U_xFe of the

quenches can be estimated from the starting compositions as 6.001, 6.000, 6.070, and 5.997 in order of synthesis. The first quench was not measured before being annealed, but the subsequent quenches showed standard RRR values for this material of 4.05, 4.00, and 3.58 respectively. These and subsequent RRRs were determined by a four-point resistivity measurement between 2 K and 300 K.

2.2.2 Study of annealing methods

For all of the sample anneals, the piece in question was wrapped in tantalum foil and heated in a tantalum crucible under UHV conditions. Initially, several samples were destroyed trying to anneal close to the recorded melting temperature of 830 °C. It was necessary to anneal at least 50 °C below this to avoid the sample melting during treatment. This suggests that the thermocouple calibration of the annealing furnace was miscalibrated by up to 50 °C. An alternative explanation would be that the stoichiometry of our samples were not close to U_6Fe. From Fig. 2.1 it can be seen, however, that the stoichiometry would need to be unrealistically far away from that of the compound to account for such a difference in melting point. Fig. 2.4 shows the effect on the RRR of several different annealing temperatures that were tried, plotted using the thermocouple readings for anneal temperature.

Our results suggest that annealing samples at temperatures much lower than the melting temperature is a method more favourable to producing the best quality samples. Notably, using the annealing method that Delong *et al.* previously used to produce their best quality samples, for us produced the worst results. There is also a reasonably clear correlation here between T_{SC} and the RRR value for all of the samples produced.

2.3 Solid State Electrotransport

Our quench-anneal studies show a slight improvement in the RRR of polycrystals as a result of annealing at temperatures below 600 °C. In order to try to substantially increase the RRR of our samples, we decided to try treating samples of U_6Fe by the SSE method to see if this approach was more successful for improving sample quality. The remainder of this chapter is concerned with the SSE method and its application to U_6Fe.

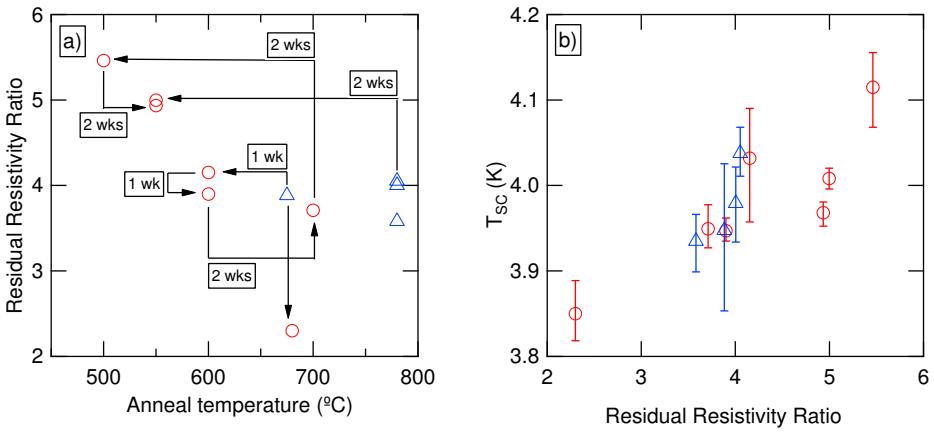

Figure 2.4: Results from several anneals carried out on polycrystalline samples of U_6Fe formed by quenching. a) The obtained Residual Resistivity Ratio (RRR) for samples plotted as a function of their annealing temperature. b) Variation of the superconducting critical temperature as a function of the measured RRR for these samples. Blue triangles show the data corresponding to the quenched samples, and red points show the data corresponding to annealed offcuts from these samples. The arrows show the order in which the anneals were tested, and the length of time for which the anneal was performed is marked next to the arrows. The first quenched sample was annealed before any samples were cut from it, and is therefore shown at the temperature of its anneal (675 °C) in Fig. a). In b), the error bars of the transition temperatures indicate the temperatures at which the signal voltage was 10% and 90% of the normal state voltage.

2.3.1 Basic experimental and theoretical concepts of SSE

The usual way in which SSE treatment occurs is that a large current is applied along the length of a rod-shaped sample. The principle is that the applied field will cause a separation of ions based on their charge. This is intended to cause the impurity ions to move to one end of the sample leaving the other end clean. At high sample temperatures, the mobility of the impurities is enhanced because it is easier for them to break free of their bonds. High temperatures are achieved by resistive heating generated by the sample's intrinsic resistance to the applied current.

This advection-diffusion problem can be simply formulated as follows. The flux of ions moving along the bar J is given by the formula:

$$J = -D\frac{\partial N}{\partial x} \pm \mu E N \tag{2.1}$$

where N is the concentration of ions, E is the applied electric field strength, and x is the position along the bar. The temperature effects enter into this equation through the temperature dependence of the diffusion coefficient D and the mobility μ. The $\pm$ sign reflects that the effect of the applied field depends on the sign of the ionic charge. We document the results of simulations of the predicted effects of SSE that were produced using this equation in the next section.

The problem is in principle more complicated than this. For example, a more complete theory would include the Seebeck effect, where a field arises due to the application of a thermal gradient. Depending on the material properties, however, the field which arises is likely to be small in comparison to that applied.

A feature of SSE particularly relevant to U_6Fe synthesis is that the movement of ions potentially allows for a stoichiometric gradient to be built up along the length of a sample. Off-stoichiometry of samples is a potential stumbling block on the path to high quality single crystals of U_6Fe that SSE could perhaps address.

Additionally, SSE has also been shown to encourage the growth of single crystalline regions by the transport of grain boundaries [58]. In the simulation of the effects of SSE that follows, this effect is not considered. This property of SSE could be investigated in the future with the use of the grain mapping equipment that is described in chapter 3.

2.3.2 Simulations of SSE

We have applied Eq. 2.1 to the scenario of simulating ionic flow is SSE-like conditions. We follow the strategy of Lee *et al.* [59], with some small modifications to their method. Perhaps most importantly, we have included the effects of a time varying temperature profile. This has enabled us to make predictions about the potential benefits to varying the time profile of an applied current. This has previously been investigated experimentally with some significant success [60], but has not seen any theoretical study to our knowledge.

The model for the time-varying temperature profile uses a modified version for the heat equation that accounts for two extra terms. The extra forcing term

is the Ohmic heating term which contributes I^2R Joules per second to a volume. A damping term that we have also included is the heat loss due to radiation. The radiated energy per unit area j_{rad} can be estimated from the Stefan-Boltzmann law:

$$j_{\text{rad}} = \varepsilon\sigma\left(T^4 - T_0^4\right), \tag{2.2}$$

where T_0 is the temperature of the medium into which the radiation occurs, σ is the Stefan-Boltzmann constant and ε is the emissivity of the radiating material. We have neglected any radial diffusion of heat to and from the surroundings, assuming that there is little exchange while under UHV conditions. Including these terms the heat equation takes the form:

$$\frac{\partial T}{\partial t} = \frac{1}{c_p\rho_d}\left(\frac{\partial}{\partial x}\kappa\frac{\partial T}{\partial x} + \frac{I^2\rho}{\pi^2 r^4} - \frac{2\epsilon\sigma\left(T - T_0\right)^4}{r}\right). \tag{2.3}$$

In this equation, t is time, c_p is the specific heat of the material, ρ_d the density, κ is the thermal conductivity, and I is the applied current. We have used a simple model for κ, assuming just the electronic contribution given by the Wiedemann-Franz law:

$$\kappa = 2.44 \times 10^{-8}\frac{T}{\rho}. \tag{2.4}$$

The above equation describes only the contribution of electrons to the thermal conductivity. A more complete simulation should include the effect of phonons, but this contribution should saturate at high temperatures as the lattice specific heat saturates.

We have applied the forward-Euler approach [61] to solve Eq. 2.3. Boundary conditions were applied to fix the temperatures at the first and last points of the simulated system at 300 K. The effect of using Cu clamps was included in the simulations by allowing the material properties to be different in regions near to the ends. In addition, we have also applied Eq. 2.1 at each point to simulate the motion of ions with changing temperature.

The forward-Euler approach is the most basic numerical approach to solving such equations, and requires that we simulate using small time steps. If the time steps used are too large, then small fluctuations will grow to the point that the

simulation will "blow up". Initially, we attempted to apply a more sophisticated Crank-Nicolson approach [61] to solving the time-dependent profiles. This has the advantage that the simulations are numerically stable to such fluctuations. We encountered problems with this approach, however, involving the total number of ions decreasing as a function of time. This was clearly unrealistic, as we had also fixed the boundary conditions in order to conserve the total number of particles. Use of the forward-Euler approach makes the task of proving that there is conservation of particles between time steps significantly simpler.

For the temperature dependence of the ionic mobility and diffusion coefficient, Lee *et al.* used the Einstein relation $\mu(T) = eDZ^*/k_BT$ where e is the electronic charge, k_B is the Boltzmann constant, and Z^* is the effective valence of the ion. $D(T) = D_0e^{-Q/k_BT}$ where Q is the activation energy of the diffusion process (the energy needed to break the bonds that hold the ions in place) and D_0 is a proportionality constant.

We note here that there is no clear consensus with regards to the effective valence of ions undergoing electrotransport. Some argue that the conduction electrons very efficiently screen the charge of the ions, in some cases making them effectively uncharged [62]. Another model suggests the movement of the conduction electrons can be thought of as a "wind" that carries the ions along, which some argue is a much more dominant effect than ionic flow due to the Lorentz force [63]. For now, we wish only to use these simulations to determine whether modulated currents are more effective than unmodulated currents. For these purposes, the value of μ is not so important as long as it is consistently used.

Constant current

Under a constant applied current, the impurity profiles that our simulations predict are qualitatively similar to those of [59] over long timescales. For short timespans, the distribution is approximately symmetric, as shown in Fig. 2.5.

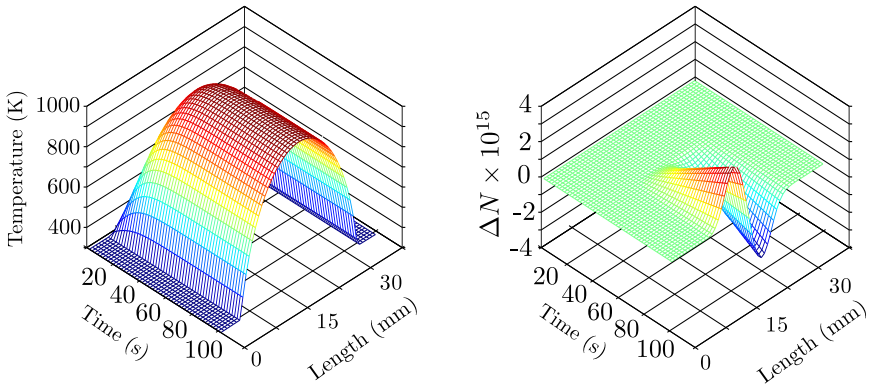

Figure 2.5: Example simulated temperature profiles and impurity change profiles for constant applied current. The initial conditions for this simulation were $N = 10^{19}$ and $T = 300$ K for all points in the system.

We have investigated the expected effect of treating samples of different lengths with equivalent central temperatures. We find that the movement of impurities is less in long samples. Even though the temperature uniformity is enhanced in longer samples, and therefore there is more thermal activation, a lower current is necessary and this is more important for transport of ions.

Time varying current

A time varying current can be easily integrated into the simulations, creating a temperature profile that is always time-dependent. The supposed advantage behind varying the current with time is that a higher average current can be applied at the same average temperature, due to the thermal lag that is a result of a sample's heat capacity. The current will need to be low following the pulse to prevent the sample from overheating.

Using the simulations as introduced above, we have examined the effects on varying the duty cycle of a square wave signal on the movement of ions. At different duty cycles, the maximum temperature reached will change, so we used an iterative procedure to find the applied current amplitude for a given duty cycle that would give a maximum temperature of 1000 K. Then we ran the simulations again, and logged the final ionic concentration profile change. We used a time step of 0.1 ms for these simulations.

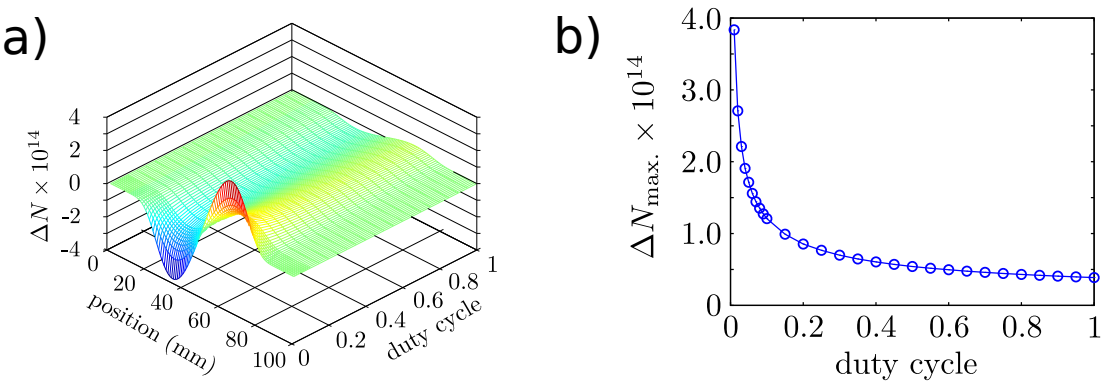

Figure 2.6: Difference in ionic concentration N along the rod from the starting concentration of 10^{19}, at 1000 K and after 100 s (10^6 time steps). a) Mesh showing the change in shape of the final impurity profile with duty cycle. b) Plot of just the maximum impurity concentration as a function of duty cycle. This uses a very large D_0 of about 300, which effectively speeds up the simulations. The oscillation frequency is 1 Hz here. The effect of changing duty cycle on the final impurity profile is most dramatic at the very lowest values.

As illustrated in Fig. 2.6, these simulations predict that at very low duty cycles, where the pulsed current amplitude is sharply enhanced (*e.g.* at a duty cycle of 0.05, $I_{max} = 80.79$ A, at a duty cycle of 0.1, $I_{max} = 57.33$ A, and at duty cycle of 1, $I_{max} = 19.047$ A), the movement of ions is significantly increased.

2.4 Sample growth apparatus

Two pieces of equipment were developed as part of this project for the purposes of SSE treatment. The first was a Drop Casting Furnace (DCF) that is intended to produce large polycrystalline samples which can be then treated by the SSE process to improve the purity of the rods produced. The second was a simplified SSE device for the purification of long single crystals of U_6Fe that were previously grown by A Huxley. We discuss the development and application of these instruments in this section.

2.4.1 Drop Casting Furnace

As described above, the most convenient form for SSE treatment is a long bar. The DCF described here is designed to be able to cast molten material into such a shape under ultra-high purity conditions. Although the bars are intended to

be purified by the SSE technique, it will be much harder to purify the produced samples if the starting bar is not the result of a pure environment, hence the motivation for a DCF that makes samples under UHV.

Design

The mechanism for melting samples in this furnace is the same induction approach as that which was applied to produce our quenched samples. The crucible is necessarily significantly larger as the samples that the DCF is intended to produce are reasonably large when in bar form. Once the samples are molten, the base of the crucible is removed to allow the molten material to flow into a cast, where the melt solidifies in the desired shape. The cast was designed to produce bars of diameter 8.5 mm and length 100 mm.

The drop of molten liquid requires the crucible to have a moveable base mechanism that works under the UHV conditions. We considered two possibilities for the drop mechanism, which are as follows: 1) the crucible base is plugged by a finger, that drops down through centre of the cast (the "vertical" mechanism); 2) the base is plugged by a finger that moves sideways (the "horizontal" mechanism). These two mechanisms are illustrated in Fig. 2.7. The vertical mechanism is beneficial in terms of simplicity and the amount of space required. In addition, this mechanism has already been successfully applied in a DCF based at the Technical University of Munich (TUM) (this DCF is only implemented under High Vacuum (HV) conditions, however). With the horizontal mechanism, it is potentially possible to cast two charges on top of each other, although the extent to which bonding is possible between charges is uncertain. Both types of crucibles have been assembled, although only the former has been tested to date.

The vertical mechanism was implemented using a large bellows which expanded to pull the central finger down. The large force required to enable this was supplied by a pneumatic cylinder, attached to the bellows by a steel frame: expansion of the cylinder forces the bellows to increase in length (see Fig. 2.8 for an illustration). The horizontal mechanism uses a short bellows which allowed a plate at the base of the system, onto which the central finger is attached, to tilt. This tilt pulls the finger out from the centre of the crucible, enough for it to spring sideways out of the way of the melt. The cast, crucible and finger for both designs were designed and constructed with significant help

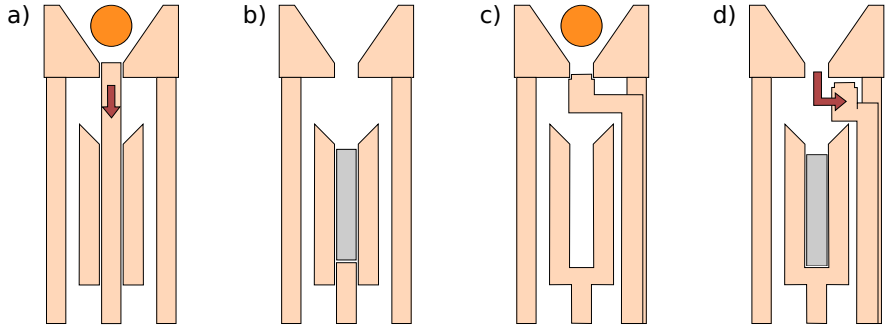

Figure 2.7: Possible drop mechanisms considered for the cast/crucible/finger. a) and b) show the first design considered, where the central finger is drawn down through the centre of the cast. c) and d) show the second design, in which the central finger moves down and sideways. The secondary method could be used to cast on top of an existing rod section, but is more complex than the first, requiring more space in the UHV enclosure.

from D Low of the mechanical workshop at Edinburgh university.

We used an inverted magnetron gauge to measure the pressure in the vacuum, which was maintained by a 150 l/s starcell ion pump. As with the other induction furnaces, the crucible is covered with a glass tube, although for this design the glass is connected to a CF63 flange by way of several different grades of glass. This makes a glass to metal seal which is robust for assembly and disassembly of the apparatus. Unlike the other RF melting furnaces that were used during this project, the glass of this system must be removed to retrieve the samples made.

Application

For the purposes of testing the DCF and the SSE apparatus, casts of elemental Ce and the compound $CeRu_2$ were attempted. $CeRu_2$ bars have previously been treated by the SSE technique resulting in a change of RRR from 30 to 300 [64], so it was desirable to produce similar bars for comparison of our SSE facilities. $CeRu_2$, like U_6Fe, also forms peritectically from the melt.

Ce has a relatively low melting temperature of 795°C, which makes it a good candidate for initial testing of the system operation. By contrast, Ru has a very high melting temperature of 2334°C, and is therefore a test of the heating power limits for metals inside this new crucible. The crucibles used for Czochralski growth are of similar design but are smaller in capacity, which undoubtedly reduces the required heating needed to melt samples, simply because

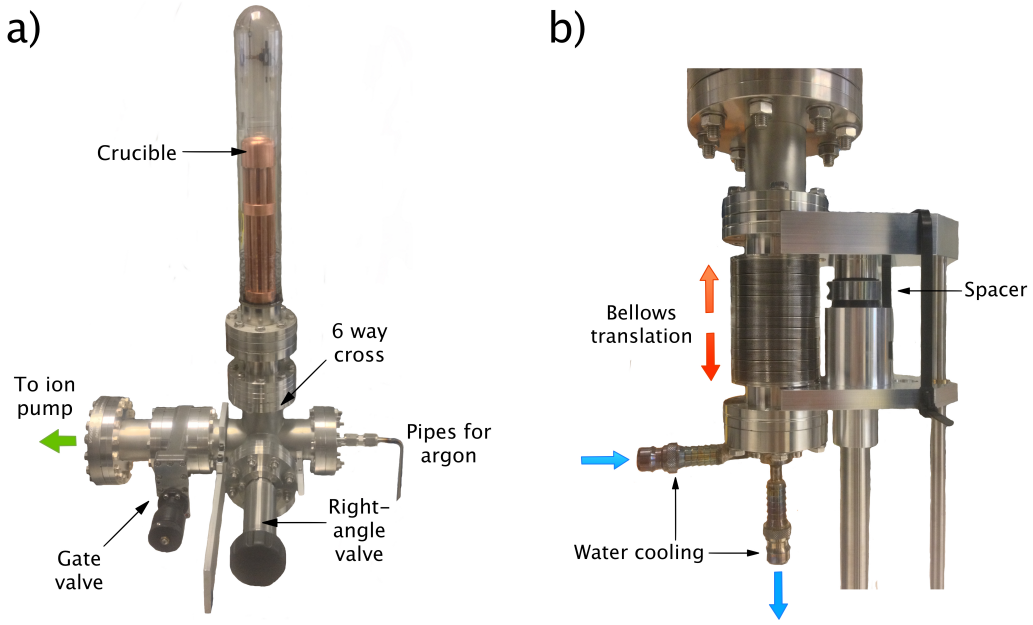

Figure 2.8: Photos of completed construction. These images show the system using the first drop mechanism. Fig. a) shows the top half of the system, and Fig. b) shows the bellows mechanism underneath. Not seen in Fig. a) is the inverted magnetron gauge, which is behind the 6-way cross.

the quantities are less.

Several tests on Ce were performed with mixed results. We used Ce supplied by Alfa Aesar (99.8% purity) for the tests. The last test carried out was reasonably successful, in that a long enough Ce rod was cast that we were able to use this subsequently in SSE treatment, as was intended (see Fig. 2.9). A common problem was that the molten material would initially flow into the cast, but would subsequently begin to gather at the top. This can be seen in Fig. 2.9b) where there is a clear "clean" part of the cast, and then a section corresponding to the melt that gathered at the top, that mirrors the shape of the cast's lip.

After Ce tests proved promising, we proceeded to casting rods of $CeRu_2$. As the Ru available was in the form of a powder, some oxidation was expected. Instead of attempting to purify the Ru by melting under UHV, the Ru powder was treated under a hydrogen atmosphere (which has previously been found as an effective way to reduce RuO_2 [65]) before being pressed into pellets. X-ray powder diffraction data was taken before the hydrogen treatment. Oxygen peaks were

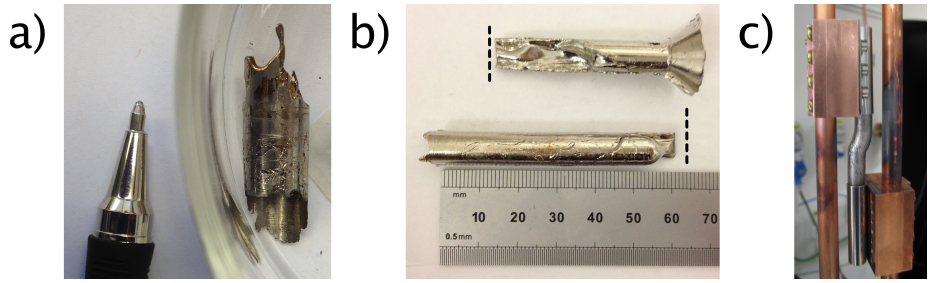

Figure 2.9: Photo of Ce test casts. a) shows a small quantity tested initially. b) shows a larger quantity cast from the second test. Although the quantity cast in this second test was enough that we were able to attempt solid-state electrotransport treatment of the sample (as shown in c), the rod was short of the length of the cast. This can be seen in b), where the dashed lines show where the rod was cut, and the conical section of the removed piece is where the top of the cast would have been.

not visible in the diffraction data, however. As a result it was not possible using this method to make a comparative analysis of the effectiveness of the hydrogen treatment. The cerium was supplied by Ames labs. It was melted on its own twice in the DCF before being combined with the Ru powder.

The compound $CeRu_2$ forms at 1566 °C, so the Ce must be made molten and the Ru powder should then fall into the melt for the compound to form at reasonable temperatures. The initial outgassing was slow, requiring a very gradual increase of power over approximately 2 weeks. Most likely this is because of the powdered ruthenium used, releasing trapped hydrogen gas deposited during the purification process. Initially it was not possible for the compounds to fuse together entirely: even at the highest applied powers, some Ru pellets did not fall into the melt, instead sitting on top. We subsequently changed the resonant frequency of the LC circuit to increase the heating power supplied, which enabled further but not complete melting. In order to ensure homogeneity, the charge was removed and turned over. On second melting, the melt was much more homogeneous and fluid.

The drop, however was unsuccessful, because upon dropping the finger the majority of the sample stayed in the crucible. Of the material that dropped, the majority remained at the top of the cast (see Fig. 2.10 c). A larger problem with the design became apparent, because the surface of the central finger evidently melted. This can be seen in Fig. 2.10 a). A significant amount of material was

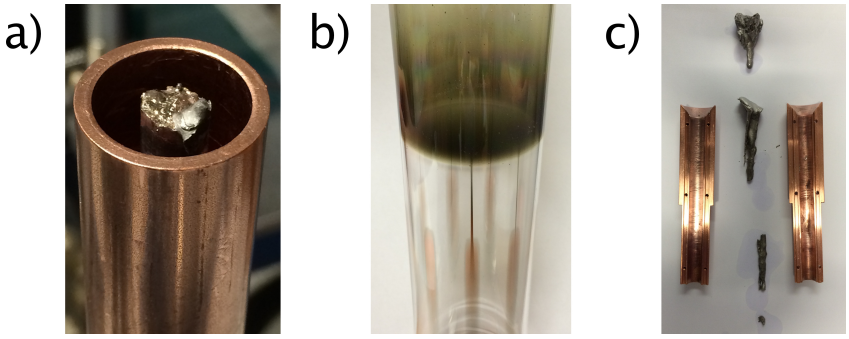

Figure 2.10: Photos taken after the attempted $CeRu_2$ cast. Fig. a) shows the effect of the melting on the surface of the central finger. Fig. b) shows the markings on the glass from the outgassing of $CeRu_2$. Towards the bottom of Fig. b), Cu-coloured streaks can be seen, probably due to the melting of the Cu finger. Fig. c) shows the resolidified melt. As can be seen, not as much of the melt flowed into the cast when the drop was activated as compared to the earlier tests of casting Ce.

deposited on the surface of the glass tube, and there was some spitting of the material out from the melt, in contrast to the melting of the test casts of cerium. This is probably because of the much higher temperatures involved: Ce has a vapour pressure of $\sim 10^{-5}$ mbar at temperatures of 1566 °C [10]. As a result of the finger being damaged, the design was altered to increase the range of the OFHC copper tip. Due to the skin effect, a good conductor like copper reduces the penetration of the magnetic field below the surface and as such does not heat as much as steel, the material used below the Cu tip. Increasing the size of the Cu tip therefore should reduce the heating to the central finger.

Conclusions and Suggested Improvements

In this section we have briefly described the design, construction and use of a UHV DCF. Although applied with some success to Ce, a material with a low melting point, we encountered significant difficulty with application to the compound $CeRu_2$, which has a comparatively high melting point. One of the most significant problems that we encountered was that it was difficult to ensure that the melt would make its way to the bottom of the cast reliably. Possibly the use of the second crucible would help to alleviate some of the issues regarding this as semi-successful casts could be re-attempted. The drop mechanism of the second crucible has not been tested, however. Part of the reason for this was

because we encountered significant issues with the water cooling pipes in both of the crucibles, which were sometimes very difficult to trace. It is not clear why this would be a much more significant risk for the large crucibles used in the DCF as opposed to those used for the smaller induction furnaces.

2.4.2 Small solid state electotransport furnace

The DCF described in the preceding section was designed to produce polycrystalline samples that could be treated by a large SSE machine that is described in [11]. Although the initial plan for synthesis and SSE treatment of U_6Fe was to cast large bars using this apparatus, it was later decided to attempt SSE treatment of Czochralski-pulled single crystals. Since the larger SSE machine is built to process polycrystalline rods it is not well equipped to handle single crystal samples of U_6Fe which usually pull into thin rods with a slightly irregular surface. Single crystals are usually quite delicate, although in the case of U_6Fe it has been found that they can be surprisingly difficult to cleave. In this section we describe a simple SSE machine that we designed and constructed to treat single crystal samples of U_6Fe.

Design

The small SSE system was housed in a UHV chamber, maintained at vacuum using an ion pump that was turned on at HV pressures. These HV pressures would be achieved using a turbo pump connected through a right-angle valve, which seals the UHV chamber from atmospheric conditions when the turbo pump is not connected. The sample could be observed under vacuum through a window attached to the chamber. The sample is clamped between two thick Cu rods inside the vacuum chamber, across which the current is applied as described in the previous sections of this chapter. The rods therefore needed to extend through one of the ConFlat (CF) plates in order to get the current into the UHV chamber from atmosphere. The Cu rods that were installed were rated to 150 A, a value that was estimated to be sufficient from the simulations described above to heat samples of U_6Fe to near melting temperature.

In larger systems, it is necessary to cool the clamps that hold the sample in the circuit. We anticipated that, for our small system, the Cu rods would be sufficiently conducting to carry away the heat efficiently (this is reflected in

the simulations above). In operation it was expected that the heating would, however, be sufficient to cause degassing from the chamber walls. Therefore a Cu water-cooled pipe was coiled around the outside of the chamber to extract the heat and prevent the walls outgassing contaminants into the sample environment.

Without any automated feedback of the temperature, we decided to heat samples until they began to glow visibly, as judged by eye. We used a readily-available webcam to observe the glowing in the IR range, by removing the IR filter that most webcams are fitted with. It provided a useful sanity check to see that the sample was actually glowing when it can be quite difficult to judge by eye. It was not intended to be used as an accurate gauge of temperature, as it is probable that there is on-board exposure compensation, and the pixel depth is limited. A sample image captured by this camera is shown in Fig. 2.11.

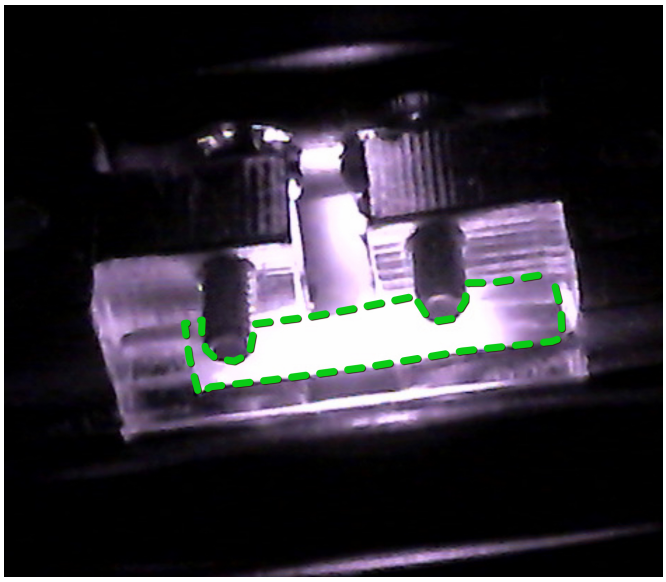

Figure 2.11: Image of the first sample with 75 A passing through it, taken using a webcam with infrared filter removed. By comparison, at this current the sample can only just be seen glowing by eye. The bar shape of the sample is outlined by the green dashed line.

The pressure was read out of the system by the gauge on the ion pump power supply. We used another webcam to convert the analog gauge to a digital signal. This fed into software that logged the pressure and power supply readings over time, to ensure that the sample was not outgassing too much. It also provided a safety cutoff, although the risk of the sample melting was relatively

low considering that the sample was never allowed to glow brightly.

The final version of the sample clamps used to hold the sample in place are shown in Fig. 2.12. These clamps were designed with a zig-zagged section to allow for thermal expansion, but in reality the Cu is probably too stiff to properly allow for this. The sample sits in a piece of Ta foil that is screwed into copper blocks at either end. By tightening a screw on the side of the clamps, the blocks are pushed together which tightens the Ta around the circumference of the sample, as illustrated in Fig. 2.12b). This ensures good contact across the sample surface. At the same time, this fastening mechanism is simple to do up and places relatively little stress on the sample. In Fig. 2.13, one of the samples treated is shown held in place by these clamps.

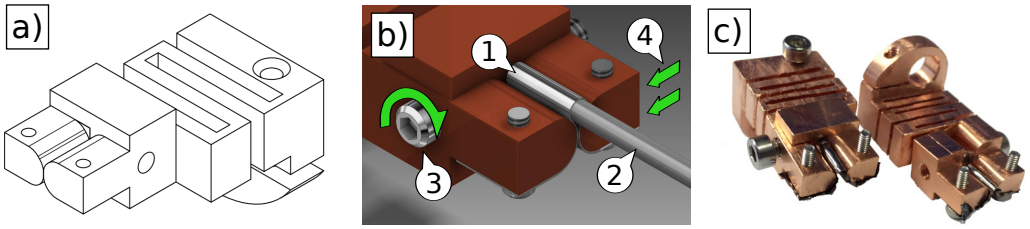

Figure 2.12: Final version of the SSE clamps. a) Schematic drawing b) Enlarged schematic showing how a strip of Ta foil (1) is used to hold the sample (2) in the clamp. The Ta foil is pressed against the Cu clamps by steel screws. A third screw (3) pushes together the two halves of the Cu clamp (4). c) Constructed clamps.

2.5 SSE treatment of U_6Fe

Finally in this chapter we discuss the results of the application of SSE to single crystal sample of U_6Fe. The first three of these samples were grown by the Czochralski method prior to the start of this project, and purified using the small SSE apparatus described in the preceding section. A final sample was also grown by the Czochralski method and purified using a larger SSE machine using pulsed currents. The samples treated using the small SSE machine were initially pulled from a melt that contained a slight excess of Fe.

2.5.1 First treatment

The first testing was carried out on a small, roughly symmetrical single crystal of approximate diameter 2 mm and length 15 mm. After being loaded, the current through the sample was increased gradually to 75 A, where it remained for 3 weeks. Comparison of the RRR showed no significant improvement of the sample quality after the sample treatment. Fig. 2.11 shows an image of this sample during treatment.

2.5.2 Second treatment

The second testing was carried out on another sample of U_6Fe, which was a much thinner and longer sample (shown in Fig. 2.13). This was treated at 17.6 A for 3 weeks. Prior to the treatment the RRRs measured at 3 points along the sample were 4.07, 3.81 and 3.73. After the treatment there was improvement of the RRR measurements to 7.18, 6.74 and 6.29, showing a clear gradient of RRR along the rod, with the highest RRR found at the end nearest the anode of the power supply. The treated sample is shown mounted in the Cu clamps in Fig. 2.13. The resistivity curves for a piece cut from this sample are shown in Fig. 2.14.

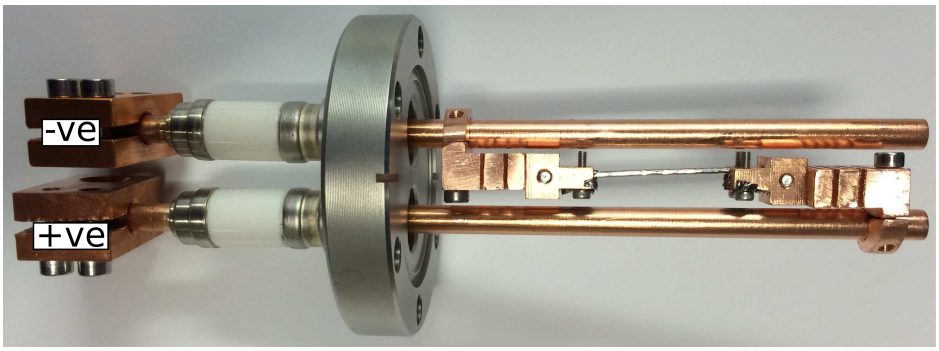

Figure 2.13: Second sample in mount, shown after treatment. The clamps on the ambient pressure side of the steel flange are labelled according to which side of the power supply they were connected to.

As this sample was the most significantly improved sample at the time, this sample was studied by several other experimental methods. The high-pressure resistivity, X-ray scattering, and specific heat experiments which used offcuts from this sample are discussed in later chapters of this thesis. In addition we

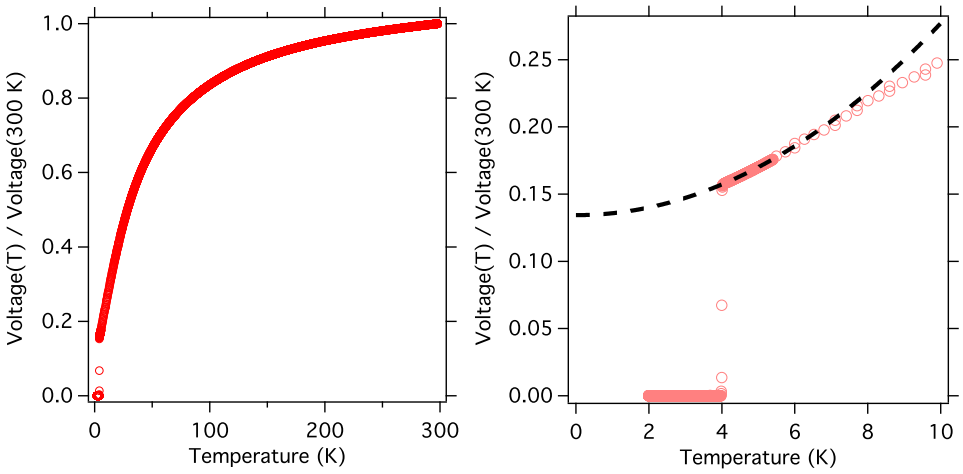

Figure 2.14: Voltage curves from a four-point resistivity measurement for the second sample treated by the SSE method, measured along the sample's c-axis.

briefly investigated the magnetic response of this sample using a Quantum Design SQUID magnetometer. We found a significant ferromagnetic signal present below ~165 K, the T_{Curie} of UFe_2. Based on the magnitude of this, and the documented moment per UFe_2 formula unit [55], we have estimated the percentage of UFe_2 in our samples as ~0.05%.

2.5.3 Third treatment

The last Czochralski grown sample treated using this small SSE system was of similar dimensions to the second. The average RRR value measured initially was 3.6. After a two month long treatment at 15.8 A, the highest measured RRR on the sample was 9.16, as shown in Fig. 2.15. As with the second test, the higher quality end was closer to the anode of the power supply. This RRR is comparable to the highest quality samples reported in the literature. Even in this high-quality single crystal sample, we have not observed any anomaly in the resistivity curves near 110 K.

2.5.4 Pulsed SSE of single crystal U_6Fe

The success of the small SSE setup in improving the quality of previously Czochralski-grown samples led us to attempt pulsed SSE treatment of a new growth. We first briefly discuss the Czochralski growth here. The setup used was

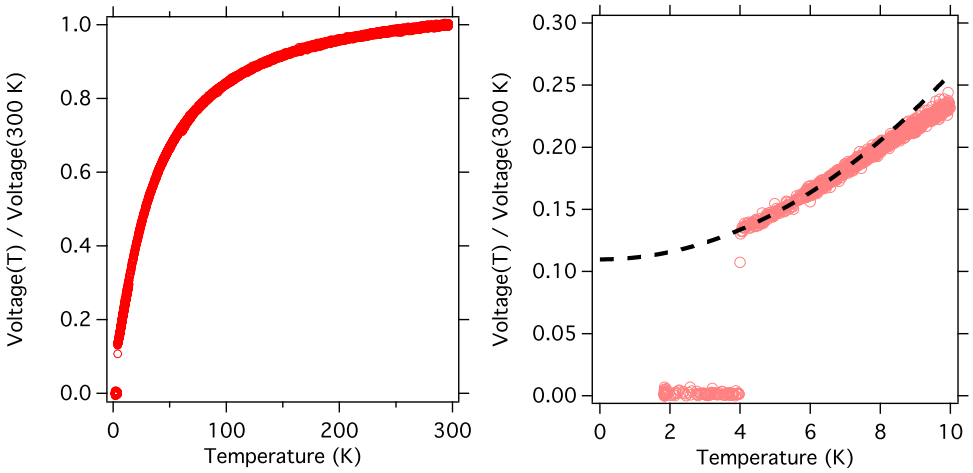

Figure 2.15: Voltage curves from a four-point resistivity measurement for the third sample treated by the SSE method, measured along the sample's *c*-axis.

as described in [66]. The U was twice melted in UHV conditions, as described previously for the quenched samples. Powdered Fe of 99.998% purity was used, heat treated in a 5% H in Ar mixture at 1200 °C for 24 hours to remove any oxides.

There were some difficulties involved in obtaining the optimal conditions for Czochralski pulling, because the melting temperature of U_6Fe is much lower than other samples usually pulled using this Czochralski setup. It was necessary to try to reduce the heating power of the induction coil by adding more coils in series. The first attempted pull was unsuccessful, as the W needle used fell into the melt and could not be extracted. Because of the low temperature of the melt, however, it was possible that the melt was not significantly contaminated. As such, the pull was continued using the part of the melt which could be separated by spark erosion from the remainder with the needle embedded.

The pull was carried out at a speed of ∼1 cm/hour. The pressure when the needle was initially submerged was fairly high ($\sim 1.7 \times 10^{-7}$ torr) but dropped to the low 10^{-9} torr over the course of the pulling process. The mass of the initial melt was 12.024 g, and the mass of the final pulled sample plus the W needle was 5.596 g. There was no reason to expect that this growth was significantly more pure than other Czochralski growths and so we predict a RRR of approximately 4 for this sample. X-ray grain mapping (using the equipment described in chapter 3) found 4 grains, although these regions show patterns which suggest that the

sample was almost entirely one grain, as can be seen from Fig. 2.16.

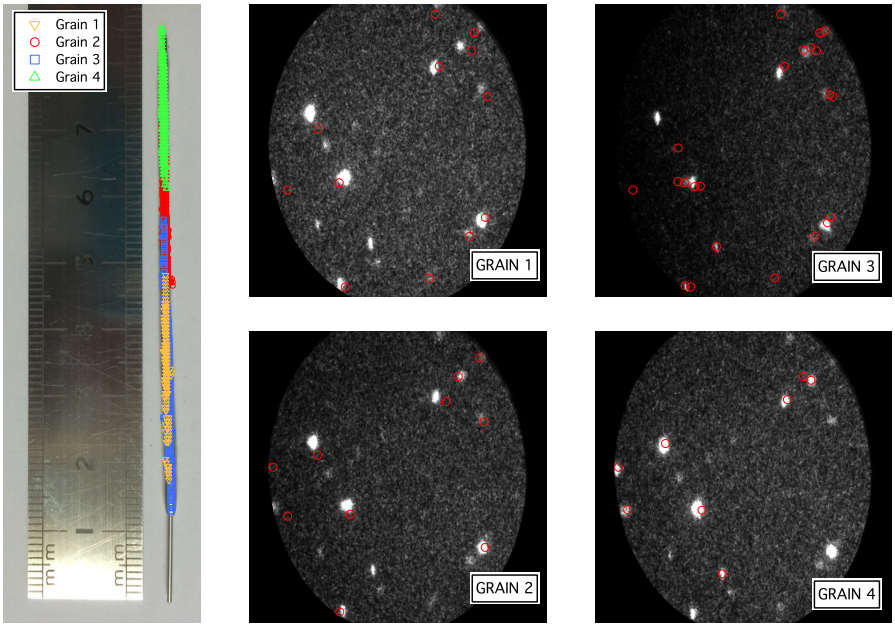

Figure 2.16: Photo of the pulled sample, with overlaid grain map. The map was produced using the X-ray grain mapping equipment described in Ch. 3. 4 grain regions were found, as shown. The patterns associated with these regions are shown right. The patterns share significant features which suggests the sample is monocrystalline.

This sample was loaded into a pulsed SSE machine detailed in [11]. The sample was clamped in place using Cu blocks covered in Ta foil. The sample was treated at peak current of ∼100 A with duty cycle of 10%. The sample length was approximately a cm longer than the previous samples treated. The measured RRR of this sample after treatment was measured to vary from $\sim 6-8$, with the highest RRR measured closest to the anode of the power supply.

For this SSE device, there is a pyrometer attached that can measure the sample temperature down to a minimum of 600 °C, but the sample was too cold to read by this gauge. Instead, current was applied until the sample was glowing by eye as with the other SSE treatments described here. This means that most likely for all of these treatments, the temperature of the sample was less than 600 °C. This is significant because of the results of the quench-anneal study which suggest that it is these low temperatures that produce the most significant

increase in sample quality.

2.5.5 Discussion of SSE treatment results

The SSE treatment has been shown by the above to be consistently effective at improving the quality of U_6Fe single crystal samples. It has been consistently found in the applied treatments that the samples are most improved towards the anode of the power supply. We have compared our results to those of Haga *et al.* [67] who applied SSE to the treatment of U rods. They found that Fe impurities were most removed from the cathode, implying that Fe impurities in U accumulates at the anode. If we assume that the Fe in U_6Fe rods behaves the same way, it would appear that the higher RRR end is where Fe accumulates. Our results would therefore imply that Fe defecit is the cause of low RRRs. This is not expected from the results of White *et al.* [25]. While this is an interesting conclusion, it must be considered that there are many factors to consider in this treatment process. For one, this assessment neglects to consider the effects of other impurities which may be more significant in affecting the RRR than the effects of an off-stoichiometry melt.

2.6 Conclusions

In this chapter we have investigated the quench-anneal and SSE approaches to producing improved-quality samples of U_6Fe. Our original attempts to replicate the formula described in the literature for producing high quality polycrystals found that high temperature anneals, such as those previously used to achieve samples of relatively high quality by Delong *et al.*, were actually less effective than anneals below 600 °C.

Subsequently we moved to attempts to purify single crystal samples by the SSE method. This involved the construction of new apparatus which we have briefly reported here. The apparatus in question was a UHV DCF, designed to produce large polycrystalline rods, and a small SSE furnace. We found moderate success with the former device, however we encountered significant difficulties in our attempts to produce the compound $CeRu_2$. In part this was due to the high melting temperature of Ru. Some work is possibly required, however, to address the issue of the melt gathering at the top of the Cu cast as was found to happen

during the test casts of Ce.

The small SSE furnace described in this chapter was shown to reliably and effectively improve the quality of long Czochralski-grown samples. Due to the low temperature of the treatments, it is difficult to know to what extent the improvement in quality stems from annealing the sample at low temperatures, instead of being due to transport of impurity ions. We can be fairly certain, however, that the latter effect at least plays some role in the purification, as indicated by the gradients in the RRR. If the improvement in quality was purely due to annealing, there should not be such a gradient because the thermal profile would be symmetric about the sample centre. It is also interesting to note that none of the purified samples show a significant increase in T_{SC}, and that the superconducting transition is extremely sharp at 4 K for all of the samples of increased purity.

We have also tested the effects of applying the SSE treatment using a pulsed current. We have predicted by means of simple numerical simulations that pulsed currents should produce better quality samples at the lowest duty cycles. A test of pulsed current treatment of U_6Fe at duty cycle of 10% shows only similar results to the steady current approach, however.

Chapter 3

Grain mapping with X-ray diffraction

3.1 Introduction

In chapter 2, the application of the Solid State Electrotransport (SSE) method as a way of producing high quality samples of U_6Fe was discussed. Part of the advantage of this technique is its potential for stimulating grain growth. The X-ray apparatus documented here serves multiple purposes, one of which is the characterisation of the grain structure in polycrystals. This could be used to determine the extent to which SSE causes grains to grow by assessment of the grain size of samples before and after SSE treatment. A more general application of the equipment is the determination of the position of large single crystals within a polycrystalline structure. This can be applied not only to the polycrystalline rods from the Drop Casting Furnace (DCF), but also to large structures produced by other crystal-growth methods such as Czochralski pulling (both of these growth methods are discussed in chapter 2). This is useful because many experiments require single crystal samples in order for them to produce meaningful results.

Laue X-ray diffraction [32] is a commonly used technique in the determination of the orientation of single crystals. In this method, a collimated white X-ray beam is shone at a sample, and the presence of a broad range of wavelengths at once allows for diffraction at many angles by Bragg's law. The beam is usually backscattered onto an area detector and the pattern produced can then

be analysed with sufficient knowledge of the system geometry to determine the sample orientation.

This approach is also useful for determining the size of grains in a polycrystalline sample. There is usually a noticeable difference between the Laue diffraction patterns either side of a grain boundary, due to the change in orientation between the grains that the boundary separates. Moving a sample across a beam and noting the points on the surface at which the pattern changes is one way to map out the grain structure of the sample. Unfortunately, when carried out by hand, this method is rather labourious and time-consuming. Part of the reason the system detailed here was developed was to automate this procedure.

This method is similar in approach to what is often referred to as micro X-ray diffraction (μXRD) [68], in that μXRD involves an X-ray beam being rastered over a surface, and the diffraction patterns that are obtained are used to determine the position of the grain boundaries. The name Micro X-ray Diffraction (μXRD) comes from the size of the beam used, which with modern optics can be reduced down to microns [69]. μXRD setups typically automatically index images before determination of the grain boundaries. With the indexation information it is much simpler to plot the grain boundaries, but in order to perform the indexation automatically a reasonably large detector area is needed to capture a sufficient number of spots. X-ray diffraction contrast tomography is another common method used for grain mapping [70], but this method requires much higher powered sources that would not normally be found outside a central facility, because the X-rays need to penetrate through the sample. Such scattering is even more unfeasible in Heavy Fermion (HF) materials such as U_6Fe which usually contain heavy elements that strongly scatter X-rays.

This chapter describes equipment that automates the production of surface grain maps. First, the experimental setup and geometry are discussed. This discussion includes description of how Bragg peaks from different orientations of a sample can be mapped onto each other. This is useful to do because it provides a way for many diffraction patterns to be combined to make a wider-angle diffraction pattern. The remapping of spots relies upon the precise alignment and calibration of the instrument, and procedures that were followed to ensure this are described. Finally, the methods for processing images to find Bragg spots,

and forming grain maps from the images, are discussed.

The work in this chapter has been distilled into a brief laboratory report article that has been accepted for publication in the Journal of Applied Crystallography [71].

3.2 Equipment and Setup

The X-ray source used was a 3 kW tungsten source. Tungsten is a good choice for a white-beam X-ray source (as used in Laue imaging) as it provides a smooth spectrum over a broad range of wavelengths. The normal operating current and voltage used were 30 mA and 35 kV respectively. Scattered X-rays were observed using a Gemstar X-ray detector, provided by Photonic Science Laboratories. The detector has a circular sensitive area of 66 mm diameter. Behind the 12 μm thick Al foil at the front of the detector is a thin layer of scintillating material, connected by fibre-optic cables to an image intensifier and subsequently to the charge-coupled device where the image is digitised. The sensitive surface area is documented as 66 mm diameter, and raw captured images have a pixel size of 58 μm$\times$58 μm, in images of size 1392$\times$1040. The detector is remote controlled by a PC through a firewire connection. The sample stage was a six-axis goniometer, provided by Huber. The goniometer has a large translational movement of 20 mm x 20 mm x 100 mm making this system ideal for scanning the large samples from the DCF described in chapter 2. The goniometer was also remote controlled by a PC. The PCs that controlled the capture from the detector and the goniometer control were controlled by ethernet from a third PC. This last computer was where images were processed and analysed, and where scans were managed. Fig. 3.1 shows a sketch of how the equipment was positioned.

Fig. 3.2 shows a typical image captured by the detector. The detector is a "square in a circle" setup, which means that the detector CCD has a rectangular cross-section, but the cross-section of X-rays allowed through to the detector is circular. Hence there is a dark border around the images where counts are blocked from being detected (a vignette).

For grain mapping, the resolution of the map is limited by the size of the beam. To reduce the size, the beam was fitted with a focussing optic, supplied by XOS (serial number 6190). X-ray focussing optics from XOS use many capillaries

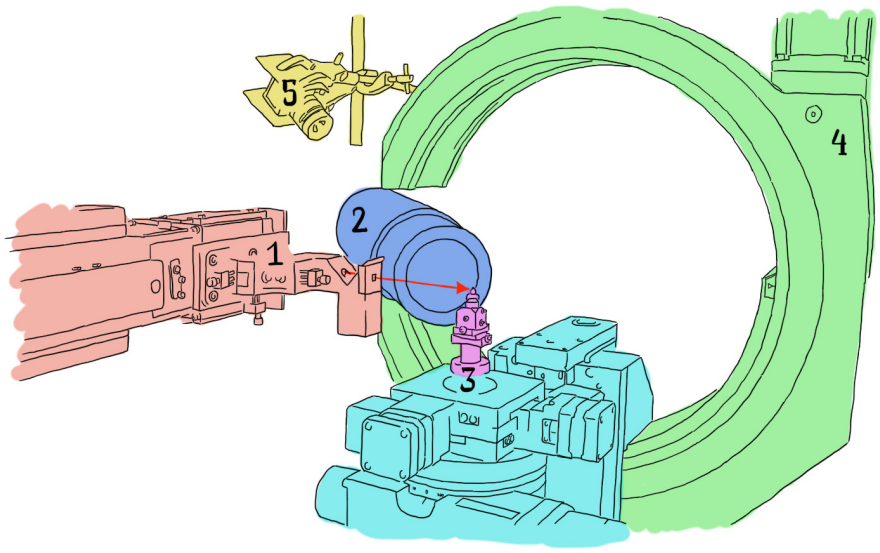

Figure 3.1: Labelled sketch of the setup. Shown items: 1) X-ray source and focussing optic; 2) detector; 3) sample mounting stage of six-axis goniometer (shown fitted with a smaller goniometer used for system alignment); 4) six-axis goniometer; 5) over-beam webcam. The red arrow shows the path of the incident beam, parallel to the x-axis.

to bend the X-rays into a focussed path. This has the additional benefit of effectively increasing the intensity of the beam. The quoted output focal distance is 140 mm, with a Full Width at Half Maximum height (FWHM) focal spot size of < 0.34 mm at an X-ray energy of 17.4 keV. The ability of the optic to focus the beam will depend on the energy of the incident beam, but this energy dependence is not documented. The optic specifications were tested as described in section 3.5.1.

3.3 Geometry

The Huber goniometer has six axes of motion: three translational and three rotational axes. The translational axes are configured such that the equipment uses a right-hand co-ordinate system, where the z-axis points downwards in the vertical direction, as shown in Fig. 3.3. This figure also shows that the ϕ and ω rotational directions are left-handed around the downward-pointing z-axis, and χ is left-handed around the y-axis. The three axes of rotation are nested such that ω is the outermost rotation axis and ϕ is the innermost rotation axis.

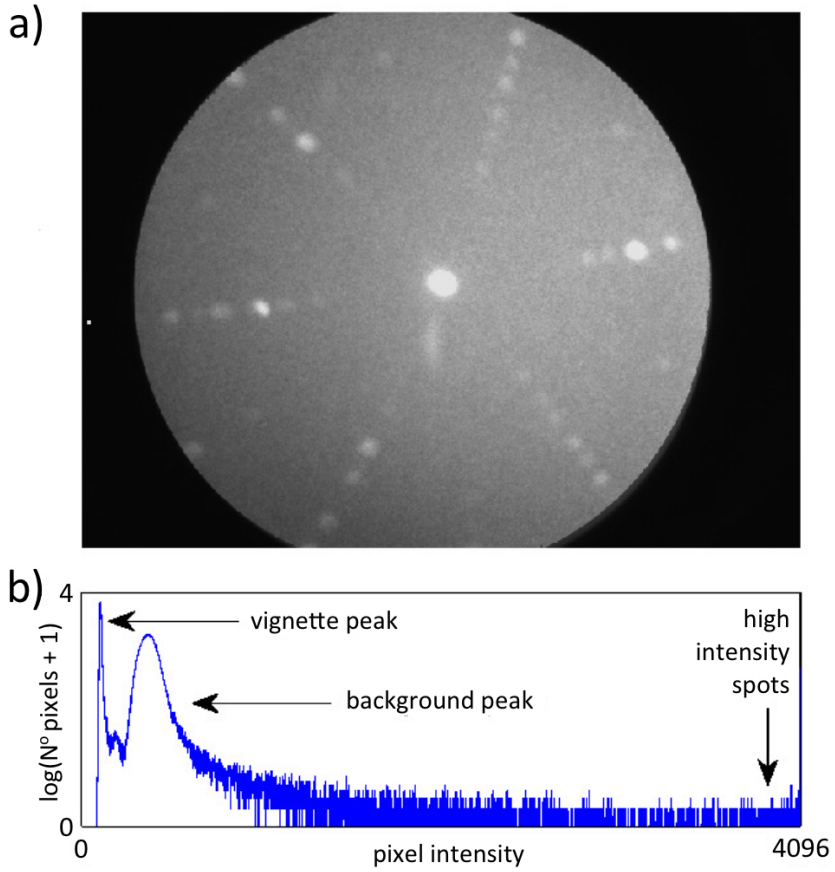

Figure 3.2: a) An example image produced by the Gemstar detector (this image is an averaged image composed from 3 second long exposures taken on a sample of MgV_2O_4); b) a histogram which shows the different features seen in a typical image. This image is 645×487, corresponding to a raw image (1392×1040) with 2×2 binning. The diameter of the illuminated circle corresponds to the 66 mm diameter of the scintillator.

It is useful to define a "lab" and a "sample" frame, where the "lab" frame is static, and the "sample" frame rotates with the sample stage when the Huber rotations are applied, as shown in Fig. 3.3 b). The sample frame (unit vectors $\hat{x}_s$, $\hat{y}_s$, and $\hat{z}_s$) is defined by the Huber axes of translation at any rotation, and the lab frame (unit vectors $\underline{\hat{x}}_l$, $\underline{\hat{y}}_l$, and $\underline{\hat{z}}_l$) is defined by the Huber translations when the stage is not rotated (it is also partly defined by the beam direction). The apparatus software for scanning the sample surface rasters samples in directions perpendicular to the beam. This requires movement of the sample in directions defined by vectors in the lab frame, but the Huber axes are defined in the sample frame. To convert lab frame vectors $\vec{v}_l$ to sample frame vectors $\vec{v}_s$, the rotations

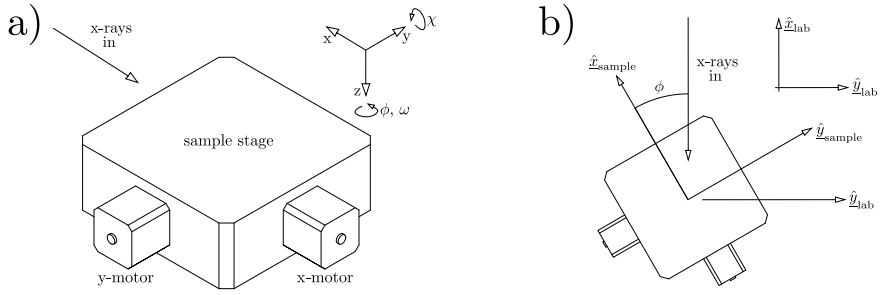

Figure 3.3: Geometry of the sample stage. a) View showing translation and rotation directions of the sample stage. b) View illustrating how the lab and sample frame co-ordinates are related to each other. In this example, the sample stage is rotated by an angle ϕ around the lab-frame z-axis. This changes the sample-frame x and y directions as shown by the unit vectors $\hat{x}_{\text{sample}}$ and $\hat{y}_{\text{sample}}$. In the rotated position, the $\hat{y}_{\text{sample}}$ vector is equivalent to the vector $-\hat{x}_{\text{sample}} \sin\phi + \hat{y}_{\text{sample}} \cos\phi$. Note that positive z translation moves the sample platform down, but moves the X-ray beam up the sample.

of the goniometer are applied, as shown in Eq. 3.1:

$$\vec{v}_s = R(\omega)R(\chi)R(\phi)\vec{v}_l = R(\omega, \chi, \phi)\vec{v}_l \tag{3.1}$$

The order of rotations (innermost first) is important, and reflects the nesting order of the rotation axes. These matrices are defined as:

$$R(\omega) = \begin{pmatrix} \cos\omega & \sin\omega & 0 \\ -\sin\omega & \cos\omega & 0 \\ 0 & 0 & 1 \end{pmatrix} \tag{3.2}$$

$$R(\chi) = \begin{pmatrix} \cos\chi & 0 & -\sin\chi \\ 0 & 1 & 0 \\ \sin\chi & 0 & \cos\chi \end{pmatrix} \tag{3.3}$$

$$R(\phi) = \begin{pmatrix} \cos\phi & \sin\phi & 0 \\ -\sin\phi & \cos\phi & 0 \\ 0 & 0 & 1 \end{pmatrix}. \tag{3.4}$$

Conversion from the sample frame to the lab frame works in the opposite order

and with the angles negated:

$$\vec{v}_l = R(-\phi)R(-\chi)R(-\omega)\vec{v}_s = R(-\phi, -\chi, -\omega)\vec{v}_s. \tag{3.5}$$

The Bragg condition defines the angle θ at which X-rays of wavelength λ incident on a set of atomic planes will coherently scatter:

$$n\lambda = 2d\sin\theta. \tag{3.6}$$

In this equation, d is the interatomic spacing, and n is an integer (which indicates that the same diffraction condition is also valid for wavelengths that are doubled, tripled, *etc.*). The Bragg condition is true for elastic scattering, where the X-ray wavelength is not changed by interaction with the material. When the Bragg condition is satisfied, the X-rays are effectively reflected by planes of atoms as shown in Fig. 3.4 a). These planes are described by their perpendicular vectors, henceforth referred to as τ-vectors.

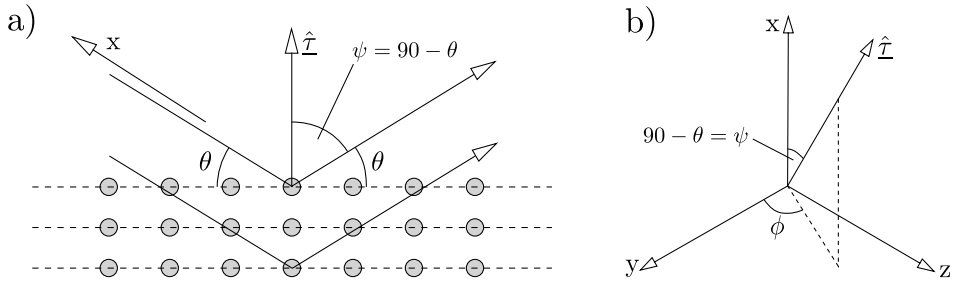

Figure 3.4: a) Elastic scattering of X-rays from a lattice of atoms. Scattering can be considered as reflection from planes of atoms, as shown in this figure, with a reflection angle θ made between the incident X-ray and the vector $\vec{\tau}$ perpendicular to the reflection surface. This assumes that the wavelength λ of the incident beam satisfies the Bragg condition $\lambda = 2d\sin\theta$, where d is the inter planar spacing. The lab-frame x-axis described in the text is antiparallel to the incoming beam path. b) Axes and angles which define the diffraction system of this X-ray apparatus, as described in the text. The axes here are fixed in the lab frame.

In the equipment described here, X-rays are incident along the lab-frame x-axis, therefore the angle $\psi = 90° - \theta$ is the angle between this axis and the τ-vector, and 2ψ is the angle between the lab-frame x-axis and the diffracted beam. ψ is zero when the beam is diffracted by 180°. In a way that is analogous

to the usual spherical polar co-ordinate system, we define ϕ as the angle between the lab-frame y-axis and the projection of the τ-vector in the lab-frame y-z plane. Fig. 3.4 b) illustrates this.

The language and methods used here for considering the geometry of the system are similar to those of Busing and Levy [72]. This was discovered after the completion of this work and is coincidental.

3.3.1 Remapping of pixels

For X-rays incident on a single crystal of a random orientation, the Bragg condition is satisfied for any given atomic plane only at specific wavelengths. In Laue or white-beam diffraction a range of wavelengths are used, so that the Bragg condition is satisfied for many planes at once. This results in high intensity diffracted beams leaving the sample surface at various angles. Intercepting these beams with an area detector, such as the Gemstar detector used here, results in a diffraction pattern such as the one shown in Fig. 3.2. In this figure, the bright spots correspond to the high intensity diffracted beams, while a broad background results from diffuse X-ray scattering.

It is possible to map from pixel positions to τ-vectors, so that a diffraction pattern captured by the Gemstar detector can be described by a set of τ-vectors and a set of diffracted intensities. This is useful because when a sample is rotated in the beam, the diffracted beams do not rotate in the same way as the sample, but the τ-vectors do (because they are defined by the atomic planes). If the diffraction pattern is mapped onto a set of τ-vectors, then the new position of the Bragg peaks on the detector when the sample rotates is fairly simple to predict. The remainder of this section describes this mapping process. The simplest case to consider is when diffraction occurs at the Centre of Rotation (COR) of the goniometer. In this case the diffraction geometry is as shown in Fig. 3.5.

In Fig. 3.5, (r_x, r_y) is the distance in mm between the detector centre and the point on the detector where the diffracted beam is incident (calculated from the pixel distance and the documented pixel pitch). The x-y plane component of twice the diffraction angle (2ψ) is denoted $2\psi_{xy}$, and the x-y plane projection of the vector between the point of diffraction and the spot position on the detector has a length denoted d. The angle formed between the incident beam and the detector axis is labelled $2\psi_D$. This can be read off from the goniometer. By

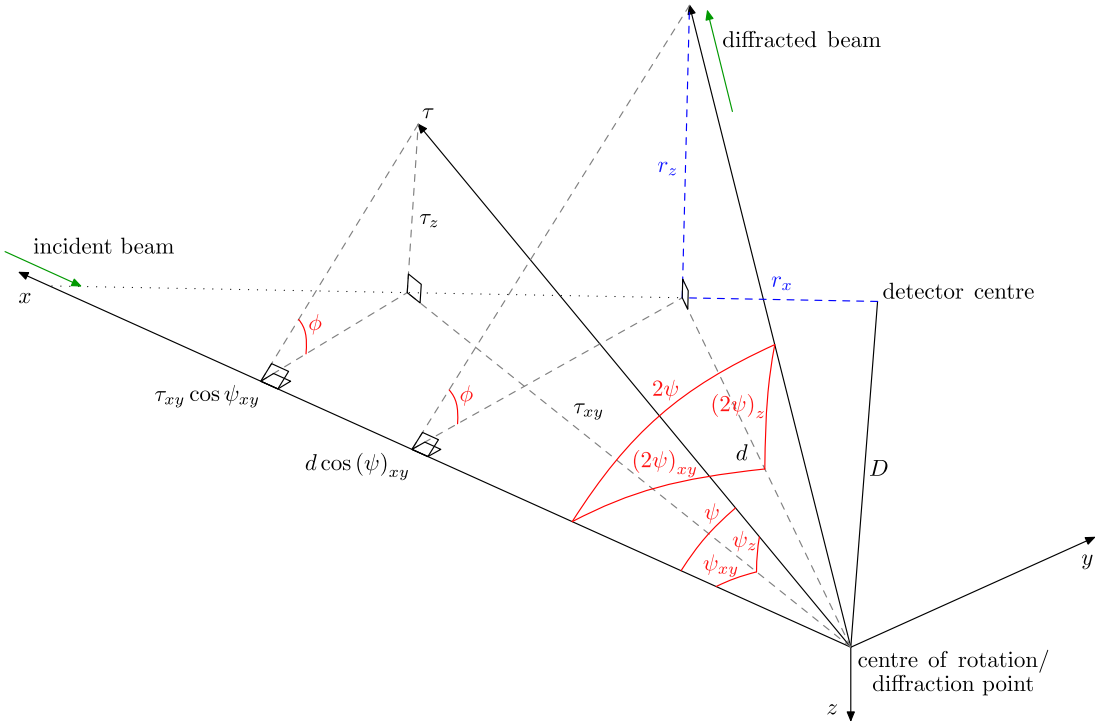

Figure 3.5: Figure showing basic system geometry assuming a central diffraction point.

inspection of Fig. 3.5:

$$\tan\left(2\psi_D - (2\psi)_{xy}\right) = \frac{r_x}{D}$$

$$\therefore (2\psi)_{xy} = 2\psi_D - \arctan\left(\frac{r_x}{D}\right) \tag{3.7}$$

$$\tan\left((2\psi)_z\right) = \frac{r_z}{d}$$

$$\therefore (2\psi)_z = \arctan\left(\frac{r_z}{\sqrt{r_x^2 + D^2}}\right). \tag{3.8}$$

From Fig. 3.5 it can be seen that:

$$\cos\psi_z \cos\psi_{xy} = \cos\psi, \tag{3.9}$$

Eq. 3.9 is also true if all ψs are replaced by 2ψ:

$$\cos(2\psi)_z \cos(2\psi)_{xy} = \cos 2\psi, \tag{3.10}$$

Using Eqs. 3.7, 3.8, and 3.10 allows calculation of 2ψ from the co-ordinates of a pixel. ψ is simply half this angle. The remaining variable required to define the τ-vector direction is ϕ, which by inspection of Fig. 3.5 is given by:

$$\begin{aligned}\phi &= \arctan\left(\frac{r_z}{d\sin(2\psi)_{xy}}\right) \\ &= \arctan\left(\frac{r_z}{\sqrt{r_x^2+D^2}\sin(2\psi)_{xy}}\right).\end{aligned} \tag{3.11}$$

To convert back from angles to pixel co-ordinates, consider that if $\vec{\delta}$ is the vector defining the exiting beam, then the usual spherical polar co-ordinate rules give $\delta_x = \cos 2\psi$, $\delta_y = \sin 2\psi \cos\phi$, and $\delta_z = \sin 2\psi \sin\phi$. Then by definition $(2\psi)_{xy} = \arctan\frac{\delta_y}{\delta_x}$ and $(2\psi)_z = \arctan\frac{\delta_z}{\sqrt{\delta_x^2+\delta_y^2}}$. The positions of spots on the detector then follow from simple re-arrangement of the previous equations.

For the case where diffraction does not occur at the COR, the mapping is more complicated, and requires knowing how far from the COR the diffraction point occurs.

3.4 System Alignment

As long as the incident X-ray beam lies along the lab-frame x-axis, it is relatively simple to use the position of a Bragg peak as found by the Gemstar detector to work out the direction of the corresponding τ-vector, as described in the previous section. The Huber goniometer is not fixed in position with respect to the beam, however, and needs occasional checks to make sure that the alignment has not changed, otherwise these conversions will not work properly. This alignment is carried out in several stages, which are explained in this section.

The first alignment described here ensures that the beam is parallel to the Huber x-axis. A needle supplied by Huber is used to determine the beam path. With the needle in the beam, the integrated counts of the detector are much higher. By performing $\hat{\underline{z}}_l$- or $\hat{\underline{y}}_l$-scans at different positions along the $\hat{\underline{x}}_l$-direction, the integrated counts indicate the path of the beam relative to the Huber axes. Any misalignment of the beam is then corrected for by rotation and redefining the zero point the goniometer ω- or χ-axis, bringing the x-axis into alignment with the beam axis. This alignment method has been automated, so that future

users can quickly and easily determine how good the alignment is before using the apparatus.

The second alignment ensures that the beam travels though the goniometer COR. Once it has been made parallel to the x-axis, the position of the beam with respect to the COR can be determined by tracking the angular dependence of the intensity with the needle or crosshair in the beam. If the beam is through the COR then there should be no angular dependence. The angular movement is done with the ω-axis, or with the χ-axis with $\omega = 90°$. If there is some angular dependence, then the displacement from the COR must be determined as described below.

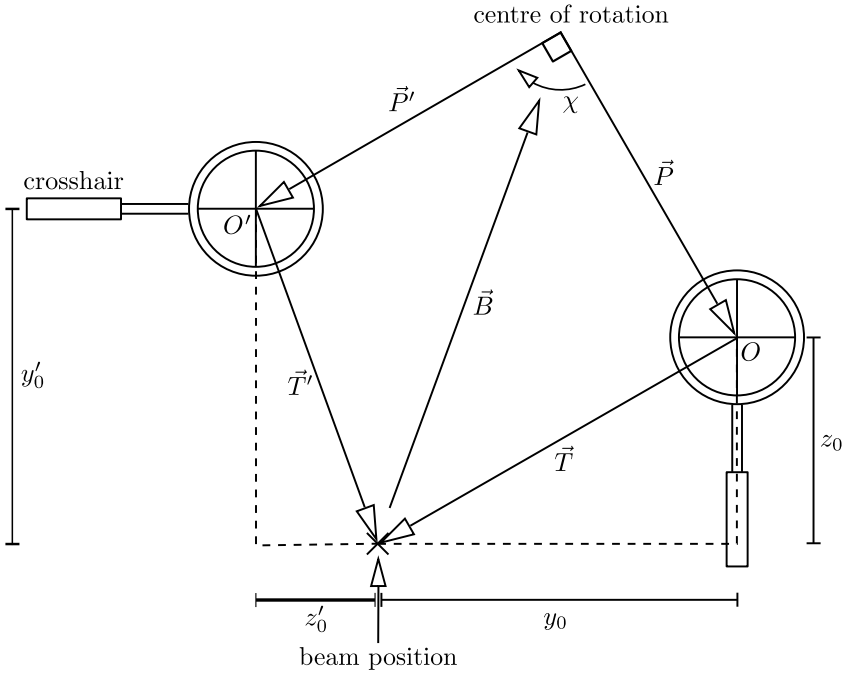

Figure 3.6: Figure showing how to locate the centre of rotation (COR) by rotating the a crosshair with a χ rotation while $\omega = -90°$, $\phi = 90°$. When $\chi = 0$, and $y = z = 0$, then the crosshair centre is at O. Translating by $\vec{T} = (y_0, z_0)$ brings the crosshair centre to sit on the beam. O is offset from the COR in the y-z plane by an unknown vector $\vec{P}$ initially. When the sample stage is rotated by χ then the crosshair centre moves to O'. The crosshair centre is then offset from the beam by $\vec{T} = (y_0, z_0)$. O' will be offset from the COR by a vector $\vec{P}'$ which can be determined from $\vec{P}$ and the size of the χ rotation. The COR must be offset from the beam by a vector $\vec{B} = -\vec{T} - \vec{P} = -\vec{T}' - \vec{P}'$. $\vec{P}$ and $\vec{B}$ can be determined given $\vec{T}$ and $\vec{T}'$.

Fig. 3.6 depicts the geometry which can be used to obtain the information necessary to be able to move the beam to intersect the COR. This method uses a small crosshair to exactly pinpoint where the beam is. This figure is in the y-z plane of the lab-frame. The Huber goniometer will have been moved to $\phi = 90°$, $\omega = -90°$, such that the χ rotation is around the lab-frame x-axis. When the crosshair is mounted on the sample stage, and the Huber co-ordinates are set to $(y, z) = (0, 0)$ then the position of the crosshair centre is at O, which is offset from the COR by vector $\vec{P}$. The Huber must be then set to $(y, z) = (y_0, z_0)$ to bring the crosshair centre into the beam. When the goniometer is rotated by χ then $O \rightarrow O'$ and $\vec{P}$ transforms to $\vec{P}'$. This transformation amounts to $\vec{P} = P_y\hat{y} + P_z\hat{z} \rightarrow \vec{P}' = P_y\hat{y}' + P_z\hat{z}'$, where:

$$\hat{y}' = \hat{y}\cos\chi + \hat{z}\sin\chi \tag{3.12}$$

$$\hat{z}' = -\hat{y}\sin\chi + \hat{z}\cos\chi. \tag{3.13}$$

When y and z are scanned in the non-rotated and rotated position, we find the position of the crosshair centre moves from $\vec{T} = (y_0, z_0) \rightarrow \vec{T}' = (y_0', z_0')$. By inspection of Fig. 3.6:

$$\vec{B} = -\vec{T} - \vec{P} \tag{3.14}$$

$$= -\vec{T}' - \vec{P}' \tag{3.15}$$

$$\therefore \vec{T} - \vec{T}' = \vec{P}' - \vec{P} \tag{3.16}$$

This can be solved for P_y, P_z, giving $\vec{P}$, which in turn gives $\vec{B}$ from $\vec{B} = -\vec{P} - \vec{T}$. Moving the beam by $\vec{B}$, or moving the goniometer by $-\vec{B}$, should move the COR into the beam. In practice, some iteration of this approach is necessary to achieve the best alignment.

3.5 Calibration

3.5.1 Calibration of the optic

Some tuning of the focussing XOS optic was required to ensure that the beam was focussed at the position of the sample. The focus of the optic was tested by moving a 100 micron wire vertically across the beam, along the lab-frame

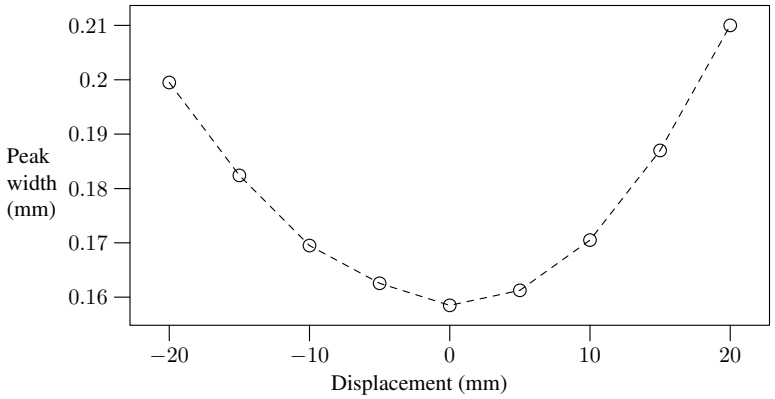

Figure 3.7: Focussing effect of the XOS optic, showing the reduction of spot size at the centre of the goniometer rotation. For this plot, intensity profiles were obtained as a 100 micron wire was translated across the beam, at different positions along the beam length. Gaussians were then fitted to the intensity profiles, and the spot size shown here is the value of the standard deviation obtained from the fits.

z-axis. The width of the intensity maximum was found to depend on where along the beam axis the scan was carried out, as shown in Fig. 3.7. This figure implies that the beam is quite effectively focussed by the optic, with a spot size of approximately 160 μm (standard deviation) or 380 μm (FWHM) diameter. The zero position of Fig. 3.7 corresponds to a focal distance of approximately 140 mm, shorter than the documented focal point by 5 mm.

3.5.2 Determining geometrical constants

As previously mentioned, converting from the position of a Bragg spot in a detected image to the τ-vector that it corresponds to is easier when the beam is well aligned to the goniometer axes. This conversion also requires knowledge of the distance from the COR to the centre of the detector (D). This is difficult to estimate manually, however. Two separate methods have been applied to attempt calculation of this value. These are briefly discussed here, but a more in-depth discussion is presented in Appendix A.

In the first approach, a sample which produced Bragg-spots (*i.e.* a single crystal or polycrystal with sufficiently large grains) was translated along the lab-frame x-axis. Fig. 3.8 shows the geometry appropriate to diffraction not at the COR. We approximate that the diffraction occurs at a point offset from the COR by a distance x. In Fig. 3.8, r_x is the component of the spot position which is in

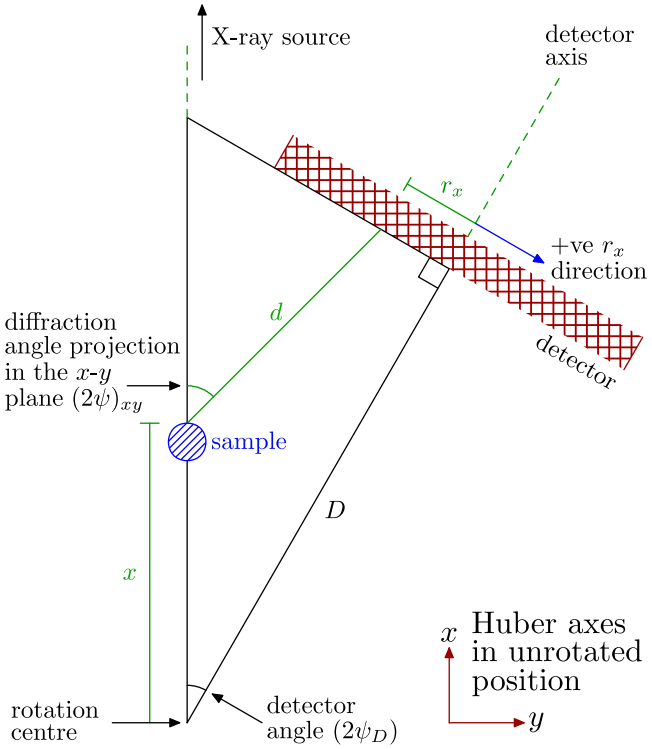

Figure 3.8: Figure showing basic system geometry when diffraction does not occur at the centre of rotation.

the x-y plane. As derived in Appendix A:

$$r_x = -x\left(\sin 2\psi_D + \cos 2\psi_D \tan\left((2\psi)_{xy} - 2\psi_D\right)\right) + D\tan\left((2\psi)_{xy} - 2\psi_D\right) \tag{3.17}$$

$$= mx + c. \tag{3.18}$$

Eq. 3.18 makes clear that the movement of the spots across the detector as the sample is translated along the beam is linearly related to the sample displacement along the beam direction. By tracking the movement of spots as a sample is moved along the beam, 3.17 can be used to determine D and x simultaneously. Fig. 3.9 shows an example of spots that were tracked as part of this approach. The success of this approach is discussed further in Appendix A. One significant advantage of this method is that it has been fully automated, meaning that the values of D and x can be easily determined provided a sample that can produce several Bragg spots is available.

The alternative to the above method is to rotate a sample around the z-axis,

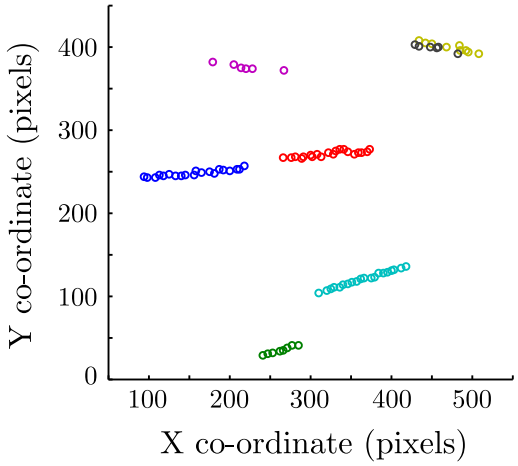

Figure 3.9: Example of the movement of spots seen when translating along the x-axis.

without moving the diffraction point, and again track the movement of spots. Their angular dependence, combined with Eq. 3.17, can then be used to find D. One problem with this method is that if the τ-vetors of the spots used lie outside the x-y lab-frame plane, then the equations used become more complex (as discussed in Appendix A). Another issue is that the point of diffraction will move if the sample is not well-positioned. Therefore, this method requires more care and is not as simple to automate.

3.6 Image Capture and Processing

3.6.1 Basic processing

Fig. 3.2 shows a typical image captured by the detector and a corresponding histogram. Note that the images as received by the computer are as would be seen from behind the scintillator, facing towards the sample stage: this becomes evident when tracking spots as the sample moves.

In most images, there is a sharp peak in the histogram at low counts due to the vignette (the exception being in cases where very few X-rays are reaching the detector). The sharp peak makes it easy to remove the vignette counts by removing all counts below a certain threshold ("thresholding" the image, as seen in Fig. 3.10). It is more reliable, however, to apply a circular mask to images to

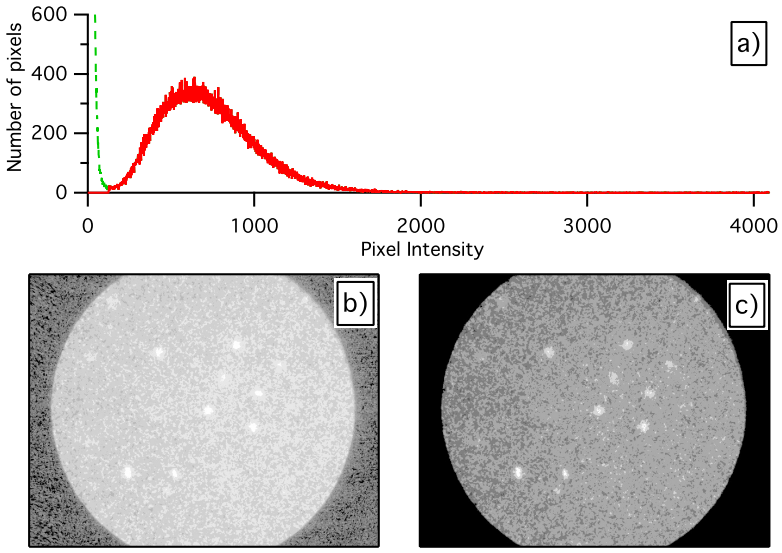

Figure 3.10: Removing the dark vignette counts. a) shows the histogram for an image. The green dashed line shows where the vignette peak would have been, and the red curve marks the remaining histogram. The image that this histogram corresponds to is shown in b) ($\log_{10}$ of intensities is shown to make the vignette clear). c) shows the image with the vignette removed.

do this (the vignette peak in the histogram can be used to calibrate the mask), because the histogram can vary but the vignette is always in the same place in the images. For most purposes, the vignette has little impact, but when overlapping remapped images taken at different goniometer angles the counts in the vignette region make the signal to noise ratio worse, and so should be removed.

3.6.2 Image remapping

Section 3.3.1 described the method for converting between the pixel positions of Bragg peaks and their corresponding τ-vectors. This can be applied to overlay images from different sample rotations, making an enlarged image. To convert an image from one rotation to another, the pixels are converted to τ-vectors, then the matrices described in section 3.3 are applied to convert the τ-vectors to the lab frame. The τ-vectors can then be re-rotated using the same matrices but with different angles, so that they apply for a new sample orientation. The rotated τ-vectors are then converted to pixels in this new frame, so that the counts can then be overlaid with the counts from an image captured in that frame. Fig. 3.11

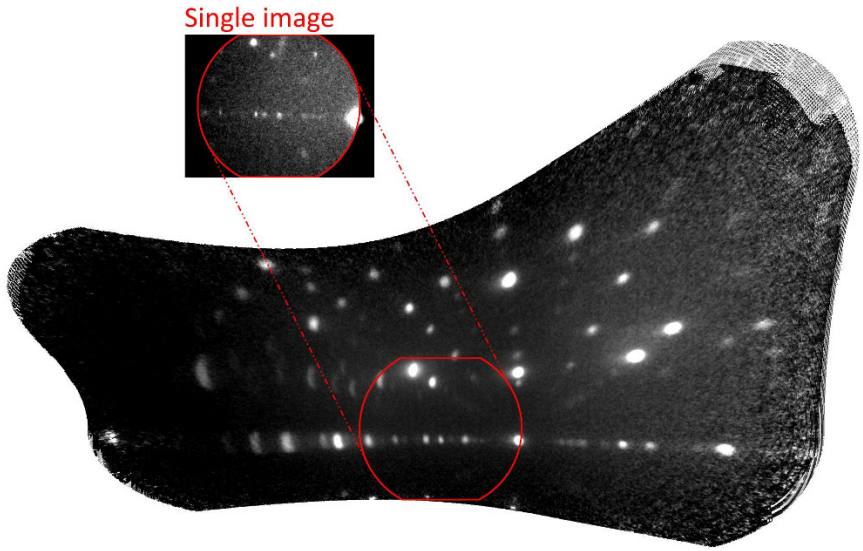

Figure 3.11: Example of an image produced by stitching images together to produce an image that effectively extends the dimensions of the detector.

shows a resulting image that uses this approach to overlay images from a wide angular range.

As is clear from Fig. 3.11, the remapped images produced by this method create images that simulate an enlarged flat detector surface. An alternative method of remapping is to overlay all of the remapped images in τ-vector space, generating an image of intensity as a function of τ-vector angles ϕ and ψ. This has also been attempted but not successfully implemented, as illustrated in Fig. 3.12. The image shown in this figure was generated with the same sample as that used to produce Fig. 3.11. There is a region where the remapping is successful and the Bragg spots are clear, at low ψ. At high ψ, the spots are not well overlaid resulting in blurring to the extreme extent that there is a loss of Bragg peaks. At the highest ψ the sample is not in the beam because of misalignment when the image was captured (the beam was evidently not passing through the COR or it would have been possible to keep the sample in the beam while rotated). For the remapping method of Fig. 3.11, the poorly mapped region is not an issue because the range of the image is restricted to the sharply mapped region. This restriction is imposed by memory constraints: as the angular remapping region is increased, the required planar image will grow to be too large for the processing computer to handle efficiently.

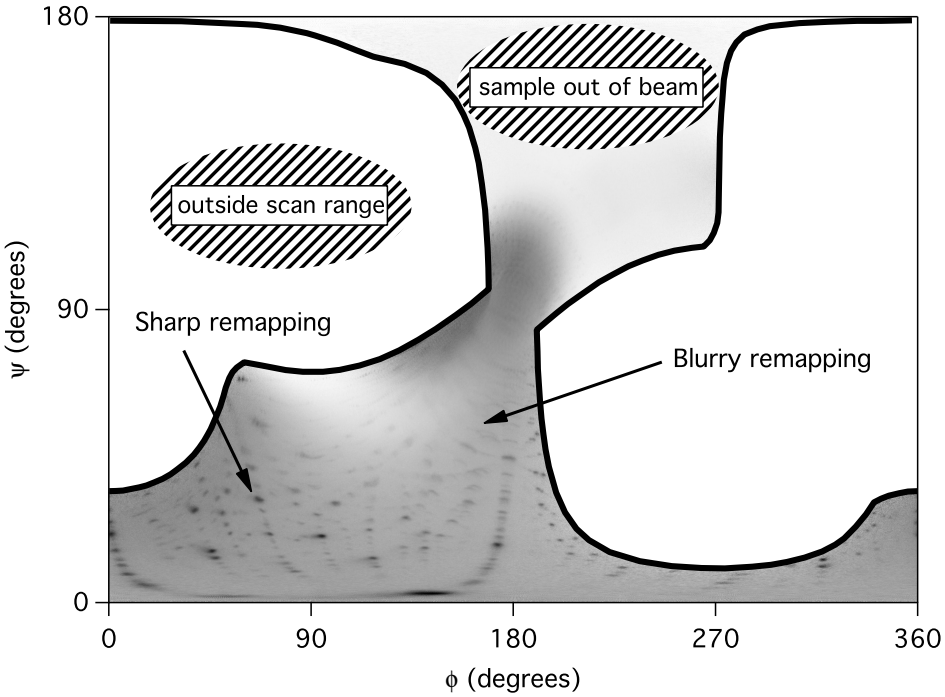

Figure 3.12: Example of an image produced by stitching images together in an angular way. The intensity in this image has been inverted resulting in black spots on a white background. The region swept out during the scan is shown by the thick black outline. There is a sharply remapped region where the Bragg spots are well-defined, and a blurry remapped region where poor remapping results in Bragg spots that appear broadened to the extreme that they cannot be seen. At the top of the image the intensity falls to background levels as the sample was moved out of the beam by the rotation of the goniometer. This is presumably due to misalignment and is evidence for the importance of a well-aligned system.

The blurry remapping probably implies a miscalibration of the system. There is perhaps potential to utilise the remapping of a single crystal as a means of system calibration. The potential for this has not been investigated, however.

3.6.3 Finding Bragg spots

The simplest way to find the location of Bragg spots in an image (which will be clusters of pixels with high intensity) is to threshold away low intensity counts, and then identify the location of any clusters of pixels remaining. The usual question using this approach is of what is the appropriate threshold intensity. Images show a variation in background count levels across the detector, which is reflected in the broad background peak of the histogram. This is most likely because X-rays scattered by the air have less far to go to reach one side of the detector. In areas of the detector where background is lower, some dim peaks may be seen which have an intensity comparable to the background in other areas of the detector. Therefore, it is useful to apply various thresholds over a range of intensities, starting at around the level of the peak in background counts.

A Gaussian was fitted as an approximation to the background peak (using the position of the histogram maximum in that region). The thresholds applied were then those between the peak maximum and 3.5 standard deviations higher in intensity. This was found empirically to usually cover a suitable range for detecting most spots (see Fig. 3.13 for an example). Thresholding images over a large range of intensities is slow, so there is a trade-off between finding the most spots and processing images quickly. At the far end of the histogram are the high-count pixels on the detector surface. Pixels become saturated at an intensity of 4095 counts. In a good-quality (*i.e.* not over- or under-exposed) image the high-count pixels correspond to bright Bragg spots. Therefore rather than threshold at all intensities between 3.5 standard deviations and 4095 counts, it is quicker to just threshold at the maximum intensity to find the brightest spots. These are added to the dimmer spots to make the total set of spots found.

For the spots found at intensity thresholds below the 3.5 standard deviations cutoff, Bragg spots were identified in images by filtering out those features deemed too large or too small. This filtering process works by "erosion" of the image. When an image is eroded, pixels are removed if they have too few neighbours, effectively removing the edge pixels of features. Features deemed too large to be

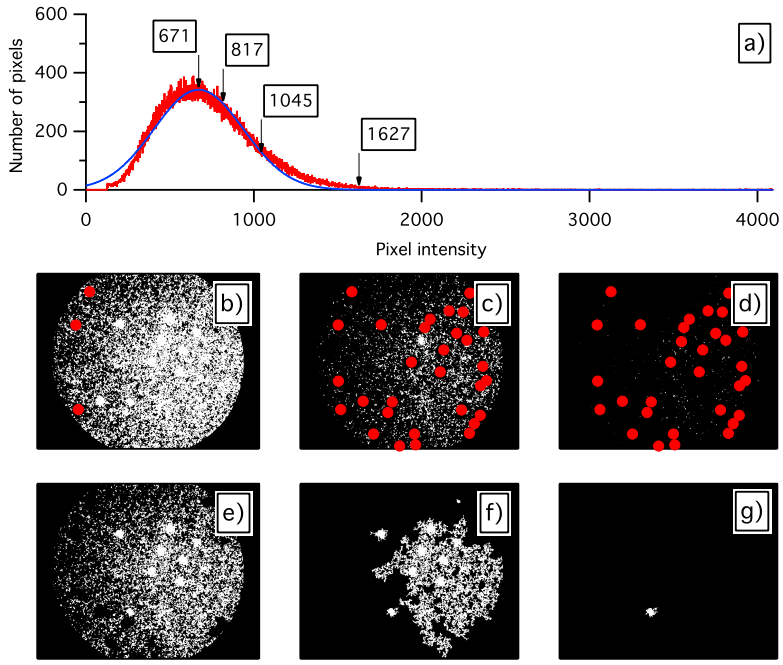

Figure 3.13: Locating Bragg spots. a) shows the histogram for an image. The blue curve is a Gaussian fit to the histogram (red data) with the vignette peak removed. In order to find the Bragg spots in an image, the counts are thresholded using a range of threshold intensities, starting with the Gaussian peak position (671 counts), and increasing up to 3.5 standard deviations away (1627 counts). b), c), and d) show the images obtained when applied thresholds of 671, 1045 and 1627 counts are applied to the corresponding image for a). The white points indicate pixels which have greater or equal magnitude to the applied threshold. The red circles indicate spots that have been found at the applied threshold intensity, or at a lower threshold intensity. e), f), and g) show how spots are filtered out at a given threshold (817 is the example level used). e) is the image initially thresholded, to remove pixels of less than 817 counts. Note there are some conspicuous gaps where spots have been removed at lower thresholds. f) shows the image after small features have been removed from the image in e). g) shows f) after large features have been removed. This leaves a single feature that is deemed not too small and not too large, which will be logged as a Bragg spot. The pixels that make up this feature will be removed from the original image before the next highest threshold is applied. This last step explains in the missing pixels in e).

Bragg spots were those that remained in the image even after a large number of erosions. Features deemed too small were eliminated after a low number of erosions. Bragg spots vary in size in a thresholded image depending on the

intensity level of the applied threshold operation. Using a fixed erosion range filter with a range of threshold intensities ensures that most Bragg spots are found.

3.7 Grain Mapping

The main purpose of this equipment is to enable us to characterise the quality of samples treated by the SSE equipment. The aim is to map grain boundaries (which may be expected to move after the SSE treatment) within a large sample. This grain mapping procedure involves first capturing X-ray images at many points on the sample surface, and then comparing these images to determine which areas of the surface correspond to the same grain. For heavy-element based materials like U_6Fe, it is difficult to probe the quality of the sample below the surface, even using synchrotron-intensity sources.

Software was written using LabVIEW to take snapshots of the diffraction patterns from a sample as it is translated across the beam. After the scan is finished, images are analysed one by one to find the position of Bragg spots within them (using the approach described in 3.6.3). This data is written into the metadata of the saved images so that it cannot be accidentally separated from the image. The surface scans are programmed to auto-detect the edge of the sample and reverse direction when this is reached: the edge is detected by an absence of Bragg spots instead of a dip in integrated intensity. This is because the integrated intensity depends on the power that the source is set to as well as the scattering strength of the sample. This approach is limited, however, because some regions of a sample can be less ordered than others, resulting in fewer or weaker Bragg peaks.

One approach to producing surface grain maps is to automatically index the captured images and then plot the orientation angle *versus* scan position. This is the approach used for μXRD as described in the introduction to this chapter. For the equipment detailed here, it is not feasible to automatically index each image, because the detector size is not large enough to give a sufficient number of spots to conclusively determine orientation from a single image. Moreover, the user will often just be interested in finding the largest single grain and orienting it, rather than orienting all of the grains in a polycrystalline sample.

3.7.1 Refining spots

Once all of the images from a scan have been analysed, to determine the pattern of Bragg peaks within them, these patterns can be compared between images. A grain will be a spatial region over which these patterns are consistent. This is made complicated by inconsistently detected spots, and by slight variation of the position of spots between images. The latter could be caused by the variation of the sample mosaic or by an irregular sample surface. To combat this problem, the spots are matched between images which come from neighbouring points on the surface. This requires a cutoff for the maximum variation of spot position as the sample is translated. After spots have been matched between images, those spots which occur in very few images are classified as noise and removed.

3.7.2 Classifying images by grain

Two images can be classed as belonging to the same grain if they share a sufficient number of the same spots. In theory, this could be applied to every neighbouring pair of points on the sample surface, to build a surface grain map. In practice, however, this approach is limited because as a scan crosses a grain boundary spots from different grains appear together in the same image. This may be because the focussed beam size is not infinitesimal, or because penetrating X-rays scatter from layered grains when a grain boundary is not perpendicular to the surface. The consequence is that it could be possible to traverse a grain boundary, but recognise the neighbouring images crossing it as sufficiently similar such that the boundary is not detected.

Each grain has a defining orientation and diffraction pattern which corresponds to this. The set of grains in a polycrystalline sample could be described then by a set of patterns (the "grain patterns"). Each image taken in a scan set can be compared to each pattern in the grain patterns to find a best fit. The best fit will define to which of the grains the image belongs. This method of sorting images into grains is not as adversely affected by images in which a combination of grains occur, because such images can still be classed as a best fit to one grain or another by a parameter which describes the goodness of fit. The obvious issue with this is that the grain patterns are not known in advance of the analysis. Using this method to produce grain maps relies on being able

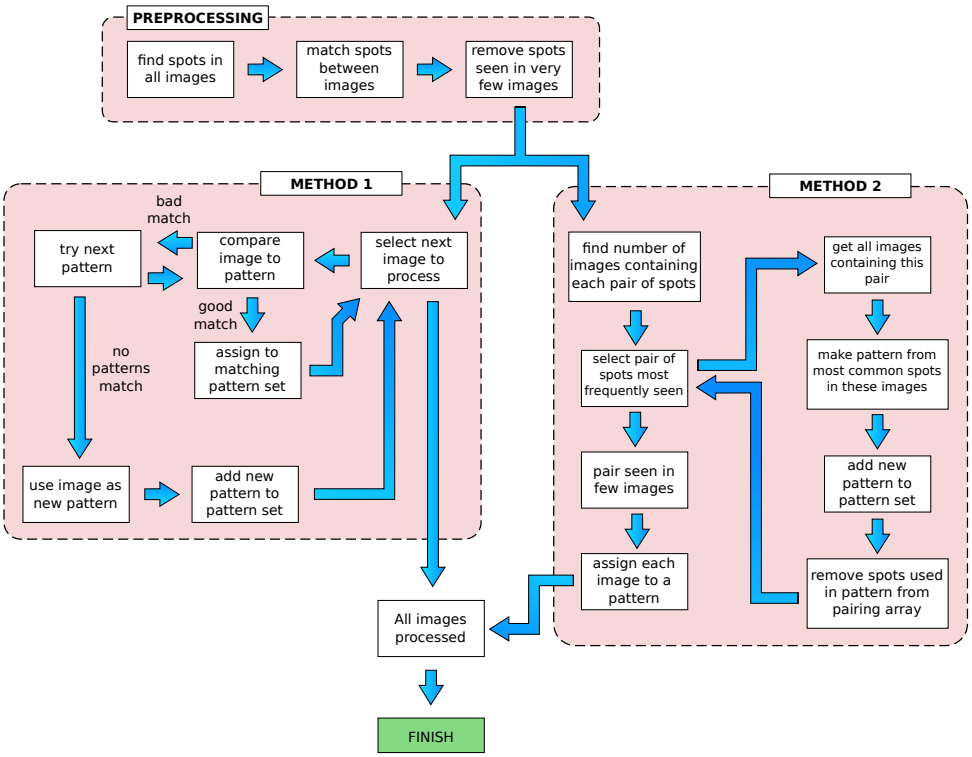

Figure 3.14: Flow diagram of the two grain mapping methods, which are described in more detail in the text.

to determine the grain patterns by some method. One approach might be to determine them by hand. This need not be as labourious as it sounds: after a scan a user could classify several images which they consider representative of the grain patterns, and then these would be used for comparisons to other images. The purpose of this project, however, was to automate the process of grain mapping as much as possible. As such, two approaches to predicting the grain patterns automatically were tested. In the first method, the grain patterns are guessed based on individual images, and then refined using others. In the second method, the patterns are guessed using information from all images at once, without needing to be refined. These methods are illustrated in Fig. 3.14 and are described in more detail below.

3.7.3 Approach 1: Trial and refinement

Some images will be a better representation of their corresponding grain pattern than others, but there is no way to know of which images this is true without knowing this grain pattern in advance. Therefore, the first method takes an arbitrary first image I_1 as its initial prototype ($P_1 = I_1$) for one of the grain patterns. The true grain that I_1 belongs to has a grain pattern G_1. G_1 is representative of I_1, but it is also representative of images captured at other points on the sample surface (assuming the grain is not small). P_1 can therefore be refined towards G_1, using the other images which are represented by G_1. It is unknown, however, which images are represented by G_1, because G_1 is unknown.

Therefore, an image I_2 from a neighbouring region of the sample is chosen and compared to P_1. If it is a good match to P_1 then I_2 joins the set of images that are described by P_1. This set of images is called the "pattern set" of prototype P_1. When this set changes, P_1 should also change, so that it is representative of the images in the pattern set. Subsequently to this update of P_1, the images in the set should be reassessed to see if they still match the new P_1. This is to ensure that images across a grain boundary are not matched to the same prototype. If P_1 was initially guessed using an image at a grain boundary, the reassessment of P_1 based on new images as they are added to the pattern set should prevent the images on both sides of the grain boundary matching to P_1.

If I_2 was not a good match to P_1, then I_2 could be used to form a new grain pattern prototype P_2. Further images I_3, I_4 *etc.* can compared to P_1 and P_2, expanding their pattern sets if good matches are found, or forming new prototypes P_3, P_4 *etc.* in the case of a bad match. Eventually there should be a set of N prototypes $P_i(i = 1 \rightarrow N)$ to which the M images $I_i(i = 1 \rightarrow M)$ are each individually assigned.

3.7.4 Approach 2: Spot coexistence regions and refinement

The second approach attempts to logically construct an initial guess of the grain patterns, and then refine them. As mentioned above, there is some variation in the position of spots between images which is not always due to a change in grain. Before the grain mapping procedure of building grain prototypes is started, spots are matched between images. This means that the i^{th} spot in one image I_1 is

compared to the j^{th} spot in an image from a neighbouring point on the sample surface I_2. If these match then the spots form a set, classified by an average position and the set of images I_1 and I_2. The set of images and average position are changed by looking for the same spot in more neighbouring images. The final result is a reduced array of possible spot positions across the sample, and the region of sample over which an individual spot persists (its "existence region") is known.

Some spots will have larger existence regions than others. A spot with a large existence region is suggestive of a large grain, but by chance two neighbouring grains could share a Bragg spot, which would result in a misleading existence region. Overlapping existence regions ("coexistence regions") of a pair of spots gives a better guess for the spatial extent of a grain. These coexistence regions also define sets of images which can then be used to form a prototype grain pattern. The first prototype P_1 is the set of most frequently occurring spots in the largest coexistence region. The next largest coexistence range is then considered, to form P_2, and so on. Each time a new prototype is formed, the next largest coexistence region cannot correspond to any of the spots used in the last prototype. Therefore after each prototype is formed, the spots used must be removed from consideration.

Eventually, only small regions of coexistence are left for remaining spots which have not been used to form a prototype. At this point, the prototyping process ends. The set of grain pattern prototypes is then used as definition of the grain patterns, so that the grain map of the sample can be determined. This is done by comparing each image in turn to the grain patterns, and therefore finding the grain which is a best match in each case.

3.7.5 Comparison of the approaches

The first approach described here was very problematic to implement because it leaves open the possibility of endless loops. When P_i is re-assessed, after the addition of I_j to its pattern set, it forms P_i'. If another image I_k, previously a match to P_i, is not a match to P_i', then I_k must leave the pattern set. I_k can be then added to the pattern set of P_l, which might reject another image I_m, and so on. This can occasionally form loops. With thousands of images resulting from a small step size scan of a large image, there is a high chance that the first method

will not converge. The second approach does not offer the opportunity to form such loops and so is more reliable.

The grain maps produced using the first approach also depend on the order in which the images are processed. This results from the way that images are processed one at a time. For the second approach all the images are effectively being considered at once, so there is no such dependence. Because the second approach looks for spots which co-exist over a large range, and neglects small coexistence regions, it is biased towards producing maps with larger grains. Most of the time, this is what users will want, because they will not be interested in small grains. With both approaches, it sometimes happens that because the spots were not well matched across the sample, two grains are identified when really there is only one. An example of this is shown in Fig. 2.16. This figure shows four grains but the patterns are very similar, suggesting there is only one grain.

In summary, the second approach is a significant improvement over the first method. Fig. 3.15 shows an example of a grain map produced using the second approach.

3.8 Conclusions

This section describes the successful implementation of apparatus that can be used to produce grain maps of large samples, as shown in Figs. 2.16 and 3.15. In addition, the relatively small detector size has been effectively enhanced by a remapping of images between orientations, as shown in Fig. 3.11.

It should be noted that this equipment is not suitable for all samples. For example, some samples that were studied did not produce enough Bragg spots when scanned using this equipment to characterise images and make a reliable grain map. The same samples, however, could be scanned on another pre-existing Laue setup which has a larger sensitive surface. Ideally, the remapping method described above enhances the detector size, but it is a fairly slow method that should not be used in combination with the grain mapping method. This is because the grain mapping procedure can already be time consuming for large samples, without adding the additional time required for wide-angle images.

There is the possibility that the grain mapping algorithms described here could be done a lot more effectively using modern machine vision and learning

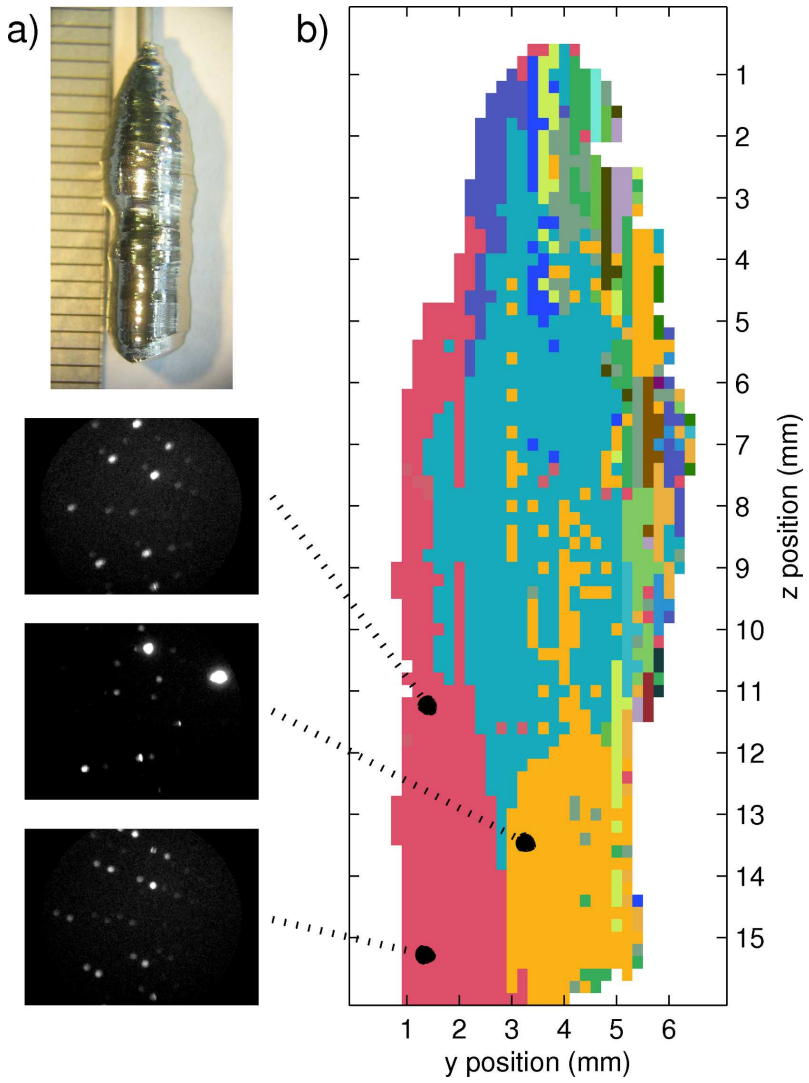

Figure 3.15: Example grain map produced using the co-existence region approach described above. a) A Czochralski-pulled sample of UAu_2 as grown by J. Schmehr [11]. b) The grain map produced. The images show example diffraction patterns from the grains.

techniques. In particular, it is a well established problem to have a computer cluster images based on similar features, or recognise features in an image, as is the basis of facial recognition software. It is unknown, however, what the effectiveness would be of such algorithms applied to the problem at hand. This is possibly an avenue for further research.

Aside from this, there is the usual further work recommended to enhance the efficiency and user-friendliness of the code that was implemented over the course of this project. In particular, the co-existence region grain mapping involves some heavy memory usage for analysis of large samples. This can be easily seen when considering that there may be thousands of images and tens of spots in each. Some care needs to be taken to implement algorithms that more efficiently process the data.

Initially it was intended that the grain mapping procedure would produce maps that are a function of the ϕ angle. This is obviously a more complex problem, because the spots found at different angles need to be mapped onto each other. Fundamentally, angular grain maps like this are only an extension of the methods already described here. They have, however, been left as further work for now.

This project is part of a larger scope which has not yet come into fruition. In the future, the grain maps will be used to program a cutter that will cut along the grain boundaries. Currently this apparatus only classifies images into grains, but this will need to be converted into grain boundary paths for such a cutter. The cutting machine is still in construction at the time of writing, however. It is a significant limitation of this apparatus that there is no implemented way of easily marking the grain boundaries on the surface of a sample. They can be approximately marked with pen with the aid of a built-in laser that is co-incident with the beam, but this makes attempts to improve precision of the grain mapping pointless. In the short term, addressing this issue is of importance.

Chapter 4

X-ray scattering

4.1 Introduction

There have been several previous diffraction studies carried out on the material U_6Fe, including a neutron powder diffraction study in the temperature range $20 - 295$ K [4], a diamond anvil cell X-ray powder diffraction study at ambient temperature [51], and a neutron Laue diffraction study (Huxley *et al.*, unpublished). None of these studies has shown any definitive evidence for Charge Density Wave (CDW) ordering within the material, despite this being postulated in numerous papers.

This chapter discusses the results of the first experimental studies showing conclusively the presence of such a modulated structure in this material. Also discussed is the possible origin of the transition at $\sim$110 K previously observed in transport measurements [3].

4.2 Experimental details

4.2.1 Sample preparation

Six samples were prepared from the highest quality single-crystal samples available, those treated in the small Solid State Electrotransport (SSE) apparatus described in chapter 2, with a Residual Resistivity Ratio (RRR) of approximately 7 measured along the c-axis (chapter 5 also shows that these samples show an

exceptionally sharp transition in specific heat measurements). Two samples were cut with faces perpendicular to the c-axis, and four samples were cut with faces perpendicular to the a-axis (orientation was determined by the white-beam Laue diffraction method before cutting). Based on the unpublished neutron study of Huxley *et al.* (unpublished, see Fig. 1.7), it was decided that the $(10, 0, 0)$ reflection was of significant interest, thus the preference for samples perpendicular to a. The samples were polished using diamond slurry of decreasing grain size, with < 0.25 μm being the smallest grain size used, and then sealed under vacuum for transport to the XMaS beamline at the European Synchrotron Radiation Facility (ESRF). The polishing was deemed necessary to give the best reflection image, and would make it possible to work at lower X-ray energies where the beam is more surface sensitive, since the penetration depth is reduced.

Only two of the six samples were studied, numbers 3 (perpendicular to c) and 6 (perpendicular to a). At the beamline, the samples were mounted on copper pucks using silver paste for best thermal contact when the puck was inserted into a cryostat, as shown in Fig. 4.1 a). During the polishing process, the samples were roughly polished on the reverse side so that the samples contacted the copper over a flat surface.

4.2.2 Beamline equipment

The beamline used was XMaS, or BM28 at the ESRF. As a Bending Magnet (BM) beamline, XMaS provides a lower intensity than an Insertion Device (ID) beamline. This was not a disadvantage for working at low temperatures (such as those used for our study), where beam heating becomes a problem if the source intensity and power density are too high. BM28 offers the potential to study magnetic structure by polarisation analysis of diffracted X-rays, but this capability was not used for most of our study.

For the non-resonant part of this study, the energy of the monochromated beam was chosen as 12 keV, an energy between the upper limits of $14 - 15$ keV where intensity drops off due to the the Rh coated toroidal mirror used in the beamline, and lower energies where $\lambda/3$ harmonics can confuse the data. Higher energies like this are more favourable for penetration through the surface, and therefore less susceptible to a poor quality sample finish.

Additionally, some scattering was also attempted at the Fe K edge (7.112 keV).

It was not possible to work at the U M_{IV} edge (3.726 keV) due to a combination of lower-wavelength contamination, misalignment of the optics, and time constraints. Working at absorption edges allows us to separately analyse, to an extent, the contribution to the scattered signal from the two species of atoms in the system. It also allows for study of local atomic environment *via* methods such as X-ray Absorption Fine Structure (XAFS).

Cryogenics

The work on XMaS was spread over two experiments, which used different Advanced Research Systems (ARS) cryostats. In the first experiment the focus was on looking for changes in structure at ∼100 K, and therefore a cryostat with a relatively high base temperature (≈ 10 K) was used. This cryostat was capable of a fast temperature ramp rate ≈ 10 K/minute. The temperature was monitored using both a Cernox temperature sensor thermometer and a Si diode. The Cernox was mounted closest to the sample, but became unusable at times due to a faulty connection which could not be traced.

In the second experiment the attention shifted to temperatures below ∼20 K, requiring the use of an Institut Laue-Langevin (ILL) built Joule-Thomson cryostat capable of temperatures down to ≈1.6 K, which was slower to cool down. In this cryostat the thermometers used were a calibrated Cernox and a platinum PT-100 sensor.

The modulated structure that will be discussed in the following sections has an onset temperature of around 10−12 K, as measured during the second experiment. During the first experiment this onset was also seen but at a higher temperature (∼20 K). Subsequent recalibration of the thermometers attached to the cryostat of the first experiment showed that the 15 K value taken as base temperature during the first experiment corresponded to 9 K on a calibrated thermometer well thermalised to the cold finger. The remaining apparent difference in onset temperatures could be explained by different degrees of thermalisation between the thermometer and cold finger during the first experiment and the subsequent calibration run. In order to be consistent in this chapter, temperatures quoted from the first experiment will be documented as originally measured. These are within 2 K of the true temperature above 50 K, but are up to 6 K too high at the lowest temperatures.

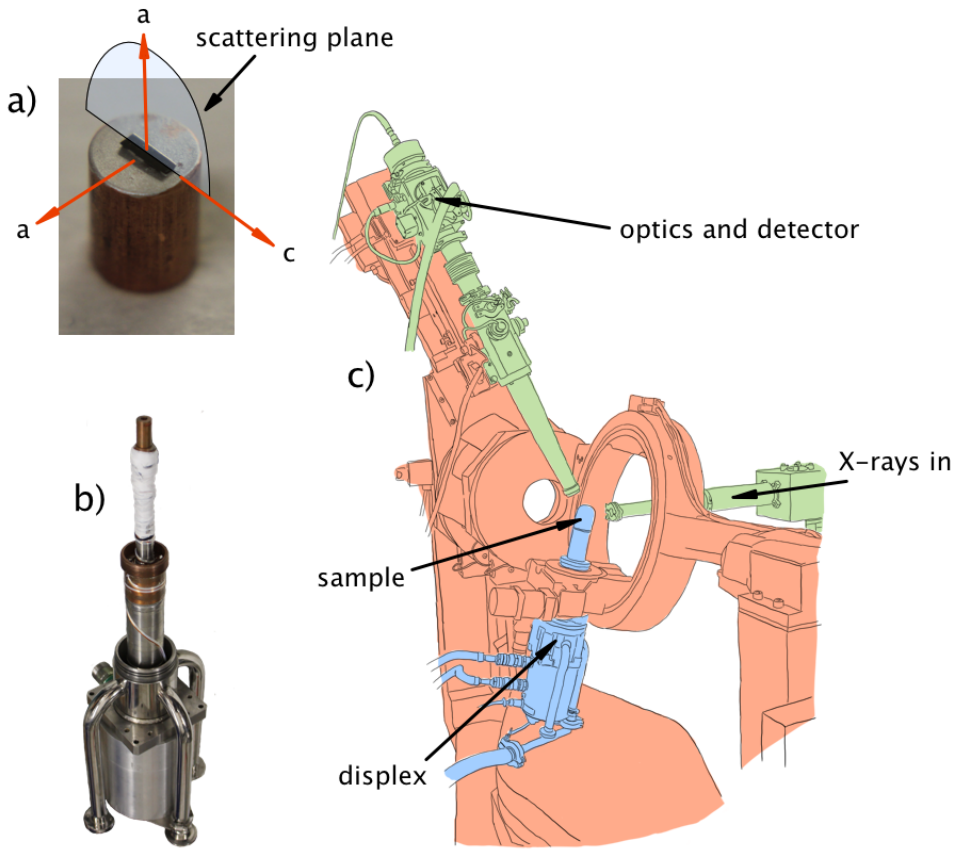

Figure 4.1: Experimental setup at the point of diffraction at BM28. a) U_6Fe sample number 6, shown attached by silver paint to a copper puck for insertion into a cryostat. The a-axis is perpendicular to the polished surface, while the long axis of the sample is parallel to c. The plane of diffraction was closest to the a-c plane. b) The displex cryostat used during the first experiment. The sample puck stage was mounted on top of the cryostat as shown. c) Goniometer (red) with the displex (blue) mounted. The top is shown covered with a Be dome, as described in the text. The optics (green) are setup with the beam incident from the right in this image.

For both cryostats, the sample puck was clamped by grub screws into copper holders that were then screwed into the cold finger. The sample was covered by two Be domes which are fairly transparent to the X-rays at the energies used. Both the sample volume and the space between the inner and outer domes are evacuated, which suppresses thermal conduction to the outside environment. The cryostat from the first setup is illustrated in Fig. 4.1 b).

The Cu puck and the Be domes cause fluorescence, so a Vortex detector was

used which discriminates the energy spectrum of the scattered X-rays. When detecting off-resonance scattering, this detector was used to pick out only those X-rays that are elastically scattered, measuring the intensity at the same energy as the beam coming from the monochromator (12 keV).

Sample alignment

For the sample perpendicular to the a-axis (sample number 6), the sample was aligned such that the c-axis, which was parallel to the long axis of the sample, was approximately parallel to the incident beam. This was to allow us to study reflections with higher H. Reflections of high K or L would be difficult to reach in this orientation, because of limits to the movement of the sample positioning stage. During the first cool down to base temperature, the UB matrix (an orientation matrix which describes the sample orientation with respect to the diffractometer angles) was calculated, using $(10, 0, 0)$ and $(10, 0, 2)$ Bragg peaks as calibration points. For the sample perpendicular to the c-axis (sample number 3), the sample was mounted with the a-axis approximately parallel to the beam. This geometry enabled us to study several Bragg peaks at high L.

4.3 Charge scattering results

4.3.1 Peak searches and artefacts

During the first experiment, scans in K at different H values were carried out using sample 6. By this method, 2D maps of the Brillouin zones around several Bragg peaks, including the $(10, 0, 0)$, $(10, 1, 1)$ and $(8, 3, 1)$ reflections, were generated. This was done to look for possible satellite reflections. Fig. 4.2 shows the maps around the $(10, 0, 0)$ Bragg peak at 15 K and 170 K.

Several satellite peaks can be seen in the $(10, 0, 0)$ map of the Brillouin zone. These are completely masked by an increase in background as temperature increases. This is shown in Fig. 4.3, which shows cross sectional cuts through the Brillouin zone, at 15 K and 170 K. The satellites seen in the 15 K $(10, 0, 0)$ map were additionally studied by looking at H, K and L scans of these locations in other Brillouin zones. The peak seen at $(10.5, 0.22, 0)$ was also tracked as a function of temperature (see Fig. 4.4).

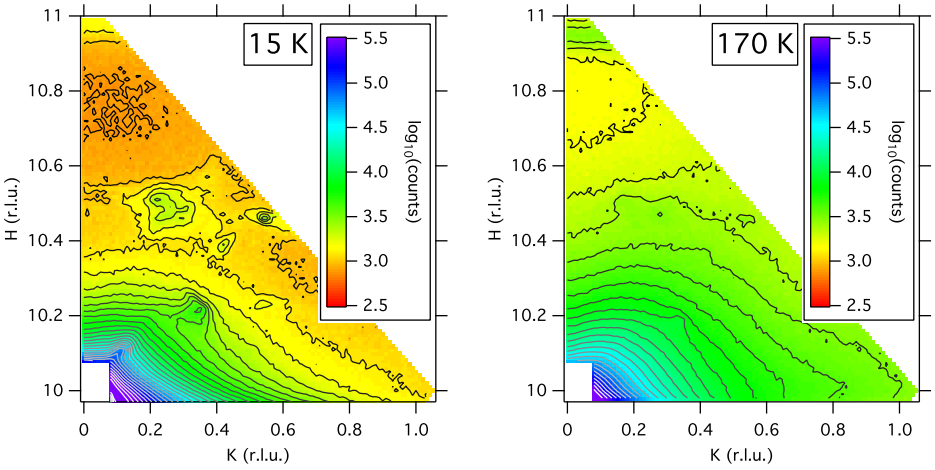

Figure 4.2: Brillouin zone maps around the $(10, 0, 0)$ Bragg position at 15 K and 170 K. Both figures use the same colour scale. The satellites seen at 15 K are completely washed out by an increase in background counts at 170 K.

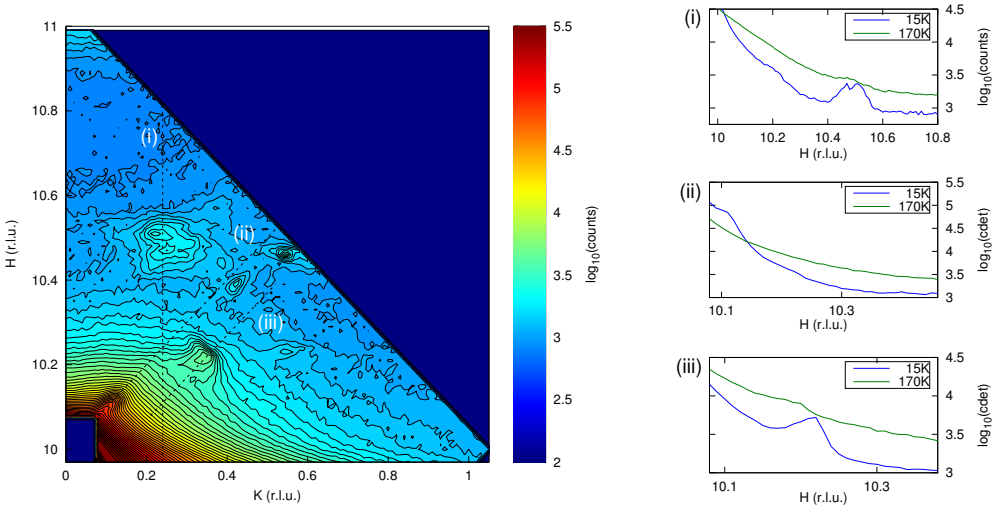

Figure 4.3: Brillouin zone map around the $(10, 0, 0)$ Bragg peak at 15 K. (i)-(iii) show the effect of temperature along various directions in H-K space, using cuts from the 15 K and 170 K maps. The line profiles that correspond to the cuts through the Brillouin zone map illustrate how a rise in background temperature is sufficient to mask low temperature features that were ultimately decided to be artefacts not intrinsic to the sample. The exception is the feature at $(10.11, 0.11, 0)$ seen in (ii). Note the intensities are shown on a logarithmic scale.

Brillouin zone maps around the $(10, 1, 1)$ and $(8, 3, 1)$ Bragg peaks (Fig.

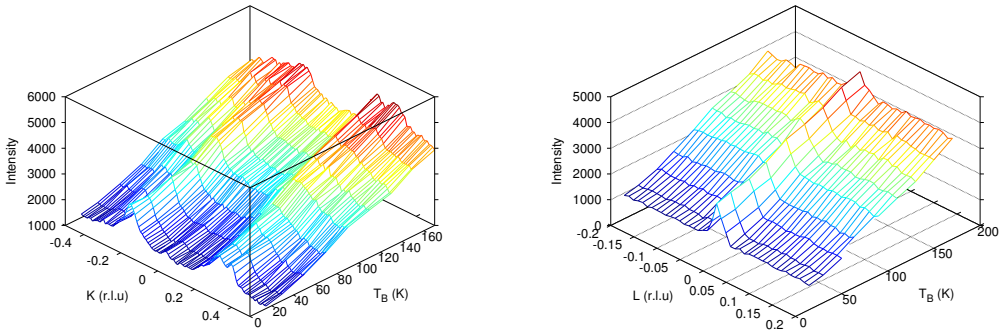

Figure 4.4: Temperature dependence of satellites seen at $(10.5, \pm 0.22, 0)$, determined by scans along K and L. This figure shows clearly that these spurious satellites are temperature independent, although the background intensity is strongly temperature dependent.

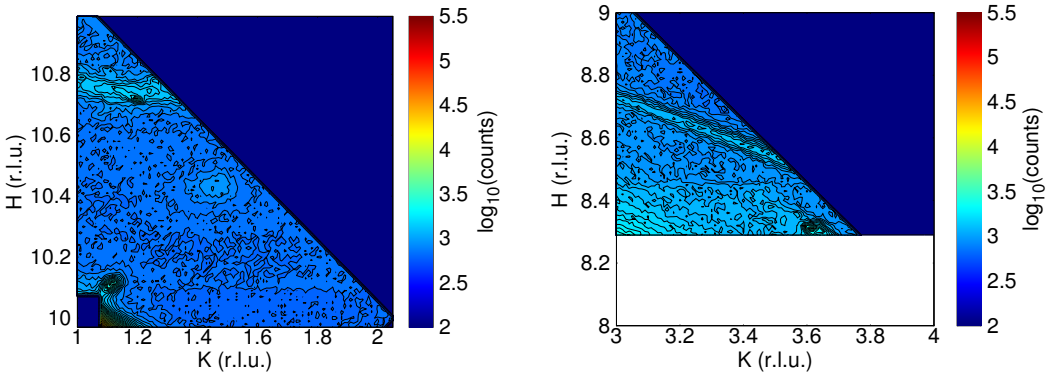

Figure 4.5: Brillouin zone maps around the $(10, 1, 1)$ and $(8, 3, 1)$ Bragg positions respectively at 15 K. Both figures use the same colour scale. Note the absence of peaks seen in the $(10, 0, 0)$ zone (see Fig. 4.3) in the above maps.

4.5) indicate that most of the satellites seen around the $(10, 0, 0)$ Bragg peak were most likely not intrinsic to the sample, because they do not appear systematically around any of the other Bragg peaks. The exception was a satellite at $(\delta H, \delta K, \delta L) = (0.11, 0.11, 0)$ common to both maps of the $(10, 0, 0)$ and $(10, 1, 1)$ zones. A feature close to $(+0.44, +0.44, 0)$ can be seen in Fig. 4.2 and in the $(10, 1, 1)$ map shown in Fig. 4.5. However, aside from the absence of such a feature in the $(8, 3, 1)$ map (Fig. 4.5), these features are also not affected by increasing temperature. This is therefore not a fourth order harmonic of the $(+0.11, +0.11, 0)$ satellite, and is most likely an artefact.

Bragg peak			Satellite observed?				Figure
H	K	L	$(+,+)$	$(-,-)$	$(+,-)$	$(-,+)$	
0	0	4	✗$_3$	✗$_3$	✗$_3$	✗$_3$	4.11
1	0	5	✓$_3$	✓$_3$	✓$_3$	✓$_3$	4.9
1	1	4	✓$_3$	✓$_3$	✓$_3$	✗$_3$	4.9
2	0	0	✗$^a_1$	✗$^a_1$	✗$^a_1$	✗$^a_1$	4.6
2	1	5	✓$_3$	✓$_3$	✓$_3$	✓$_3$	4.9
3	-3	6	✓$_3$	✓$_3$	✗$_3$	✗$_3$	4.9
4	0	0	✓$_1$	✓$_1$	✓$_1$	✓$_1$	4.6
5	5	0	✗$_2$	✗$_2$	✓$_2$	✓$_2$	4.11
6	0	0	✓$_1$	✗$^a_1$	✓$_1$	✗$^a_1$	4.6
6	1	1	✓$_2$	✗$^a_2$	✓$_2$	✗$^a_2$	4.8
6	3	1	✓$_2$	✗$^a_2$	✗$^a_2$	✓$_2$	4.7
7	0	1	✓$_{1,2}$	✓$_{1,2}$	✓$_{1,2}$	✓$_{1,2}$	4.7
7	7	0	✗$_2$	✗$_2$	✓$_2$	✓$_2$	4.11
8	0	0	✓$_1$	✓$_1$	✓$_1$	✓$_1$	4.6
8	1	1	✓$_2$	✓$_2$	✓$_2$	✓$_2$	4.18
9	0	1	✓$_{1,2}$	✓$_{1,2}$	✓$_{1,2}$	✓$_{1,2}$	4.7, 4.18
10	0	0	✓$_{1,2}$	✗$^a_1$	✓$_1$	✗$^a_1$	4.2, 4.6
10	1	1	✓$_1$	-	-	-	4.5
10	0	2	✓$_2$	-	-	-	4.10
11	3	0	✓$_2$	✓$_2$	✓$_2$	✓$_2$	4.7

Table 4.1: Table of CDW peaks observed over the course of the two experiments. Subscripts indicate the experiment during which the study took place (a ^{3} indicates sample 3 studied during the second experiment). ^{a}Could possibly be present as a weak peak on a comparatively strong background. The $(\pm,\pm)$ symobls refer to the satellite positions at $(\pm 0.11, \pm 0.11, 0)$ relative to the Bragg position.

4.3.2 Satellites at $(\delta H, \delta K, \delta L) = (\pm 0.11, \pm 0.11, 0)$

Unlike most of the satellites observed in the maps in the vicinity of the $(10, 0, 0)$ Bragg peak, the $(\delta H, \delta K, \delta L) = (\pm 0.11, \pm 0.11, 0)$ satellites described above were also observed around a host of other peaks. We will henceforth refer to these satellites as the CDW peaks. Table 4.1 lists the CDW peaks that were observed during our studies. The figures that illustrate these observances are listed in table 4.1.

During the second experiment, the temperature dependence of the $(+,+)$ satellite around the $(10, 0, 2)$ Bragg peak of sample 6 was tracked as a func-

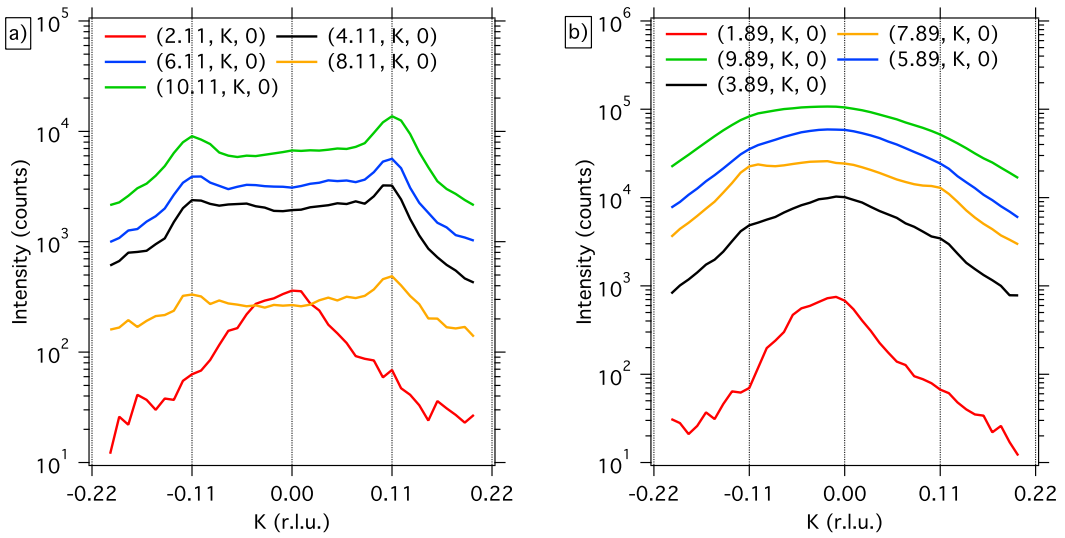

Figure 4.6: Satellites observed around the $(H, 0, 0)$ positions during the first experiment. Apparent absences of some of the satellites could be due to their weak intensity compared to the strong Bragg peak, which masks their signal. The absent satellites around the $(2, 0, 0)$ is perhaps due to the weak nature of this Bragg peak.

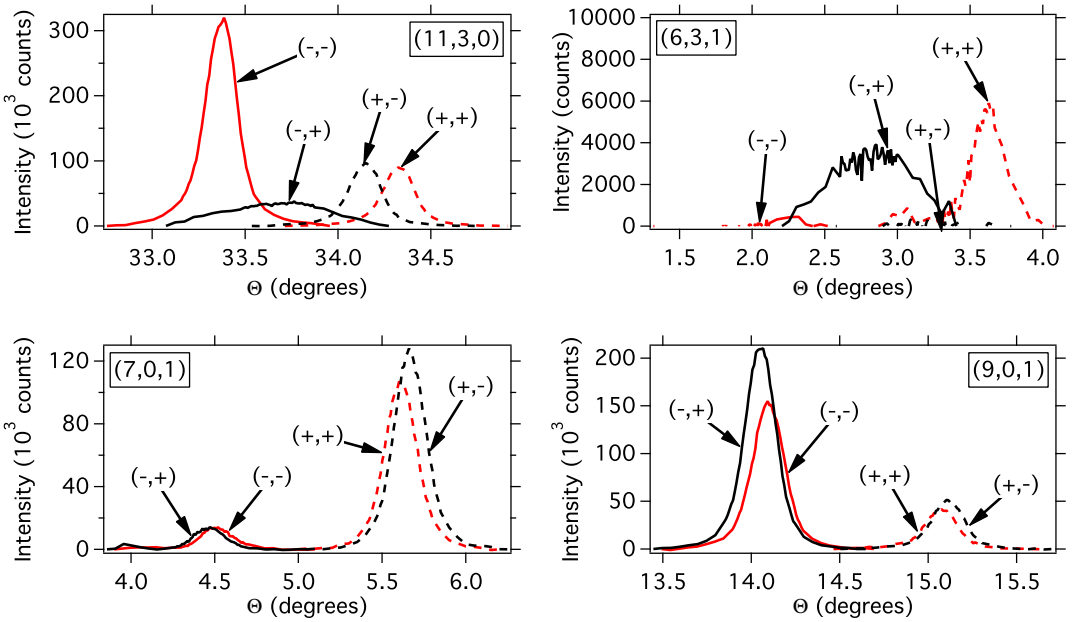

Figure 4.7: Rocking curves of the CDW peaks observed around the $(11, 3, 0)$, $(6, 3, 1)$, $(9, 0, 1)$, and $(7, 0, 1)$ Bragg peaks during the second experiment using sample 6.

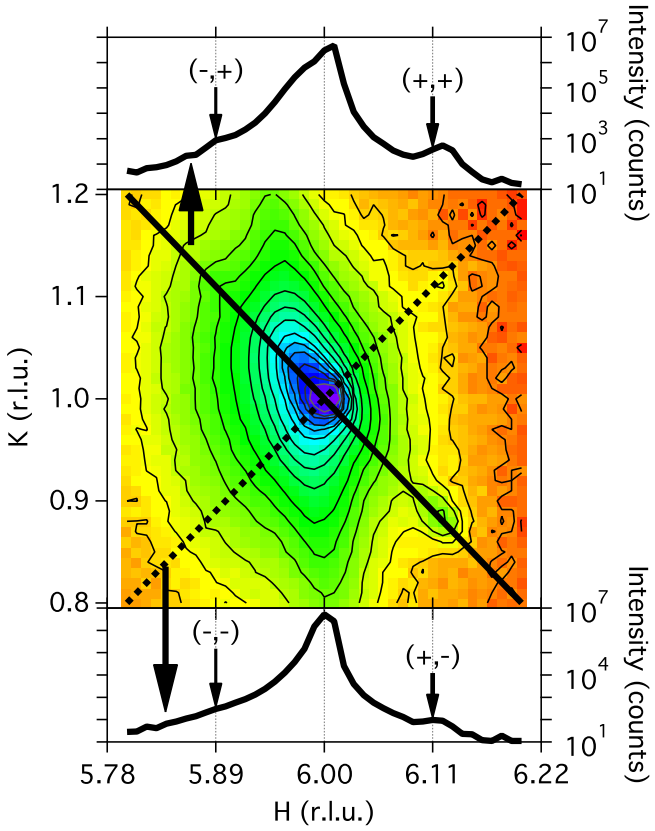

Figure 4.8: Mesh of intensity in H-K space around the $(6, 1, 1)$ Bragg peak. Also shown are line profiles taken along the diagonals of the mesh, illustrating the features at $(\pm 0.11, \pm 0.11, 0)$.

tion of temperature by scanning meshes around the CDW peak at steadily increasing temperatures. These meshes suggest a transition temperature T_{CDW} of approximately 10 K, as shown in Fig 4.10 (from the difference in this transition temperature between the experiments, the poor thermalisation of the thermometers in the first experiment was confirmed). No satellites were observed around any of the Bragg positions above 15 K. The temperature dependence of the satellites around the $(2, 1, 5)$, $(1, 0, 5)$, $(3, -3, 6)$, $(0, 0, 4)$, and $(1, 1, 4)$ Bragg peaks was also investigated, using sample 3. The change of these satellite intensities with temperature suggested a slightly lower T_{CDW}. The temperature dependence shown in Fig. 4.10, however, seems very convincing given the kink in the intensity *versus* temperature plot that coincides with the superconducting transition temperature of 4 K. From the meshes obtained with sample 6, no

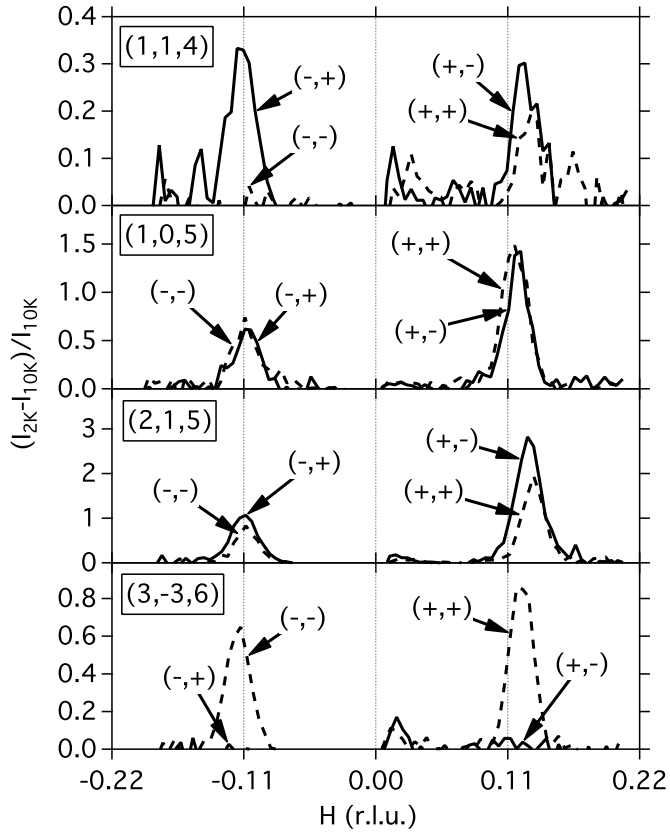

Figure 4.9: Satellites observed from sample 3 during the second experiment. In order to remove the Bragg peak signal (which has a weak temperature dependence compared to the satellites) we have plotted $I_{2\mathrm{K}} - I_{10\mathrm{K}}/I_{10\mathrm{K}}$ where I is scattered intensity. There is a systematic absence of satellites with a $\vec{q}$ as shown by the $(3, -3, 6)$ data.

noticeable change in the position of the satellites was observed with temperature. Scans along L showed the satellites to be especially localised to the H-K plane, even at the lowest temperatures. Comparison of the Full Width at Half Maximum height (FWHM) of the $(11, 3, 0)$ satellite peaks to their corresponding Bragg peak during the second experiment show that the satellites are almost twice as broad as the Bragg peak.

Some noticeable absences of satellites were observed, for example around the $(7, 7, 0)$ and $(5, 5, 0)$ Bragg peaks. Here, only the $(\Delta H, \Delta K) = (+, -)$ and $(-, +)$ satellites were observed. Around the $(0, 0, 4)$ no satellites at all were observed. These absences provide information about the nature of the of charge modulation that is responsible for the satellites, as will be discussed below. The satellite

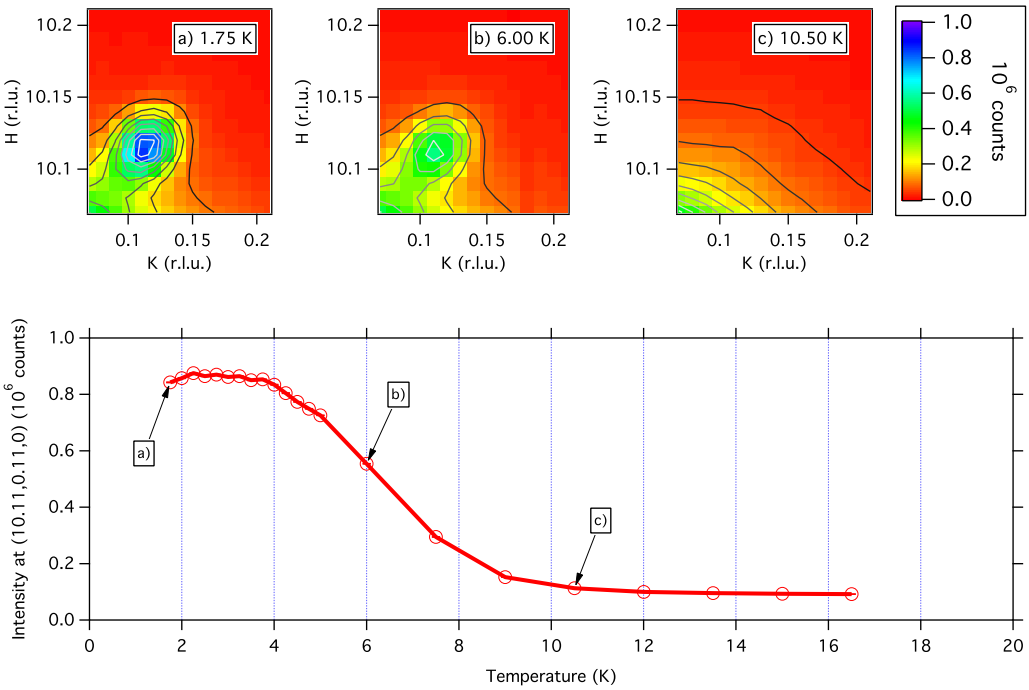

Figure 4.10: Maps in (H, K) space showing the temperature dependence of the $(\delta H, \delta K, \delta L) = (+0.11, +0.11, 0)$ satellite around the $(10, 0, 2)$ peak. The lower plot shows the intensity at the $(0.11, 0.11, 0)$ position as a function of temperature.

peaks have a much stronger temperature dependence than the Bragg peaks, so it is relatively simple to subtract the Bragg tail to obtain a clean satellite signal, as illustrated in Fig. 4.11, which highlights the systematic absences. From diagonal scans in H-K space through the satellite peaks around the $(2, 1, 5)$ Bragg peak, we estimate the $\vec{Q}$-space width of the satellites to be $\Delta Q_{\mathrm{CDW}} \approx 0.02$ r.l.u. ≈ 0.012 Å^{-1}. This implies that the size of the CDW domains will be approximately $(8 \ln 2)/\Delta Q_{\mathrm{CDW}} \sim 462$ Å.

4.3.3 Fe K-edge studies

As previously mentioned, only the Fe K-edge ($E_K = 7.112$ keV) resonance of the satellites could be studied during these experiments. Fig. 4.12 shows the fluorescence spectra in the region near the K edge. In this figure, the fluorescence seen in other Fe containing materials is overlaid for comparison of the structure. Our data have been normalised to the incident beam intensity and the edge

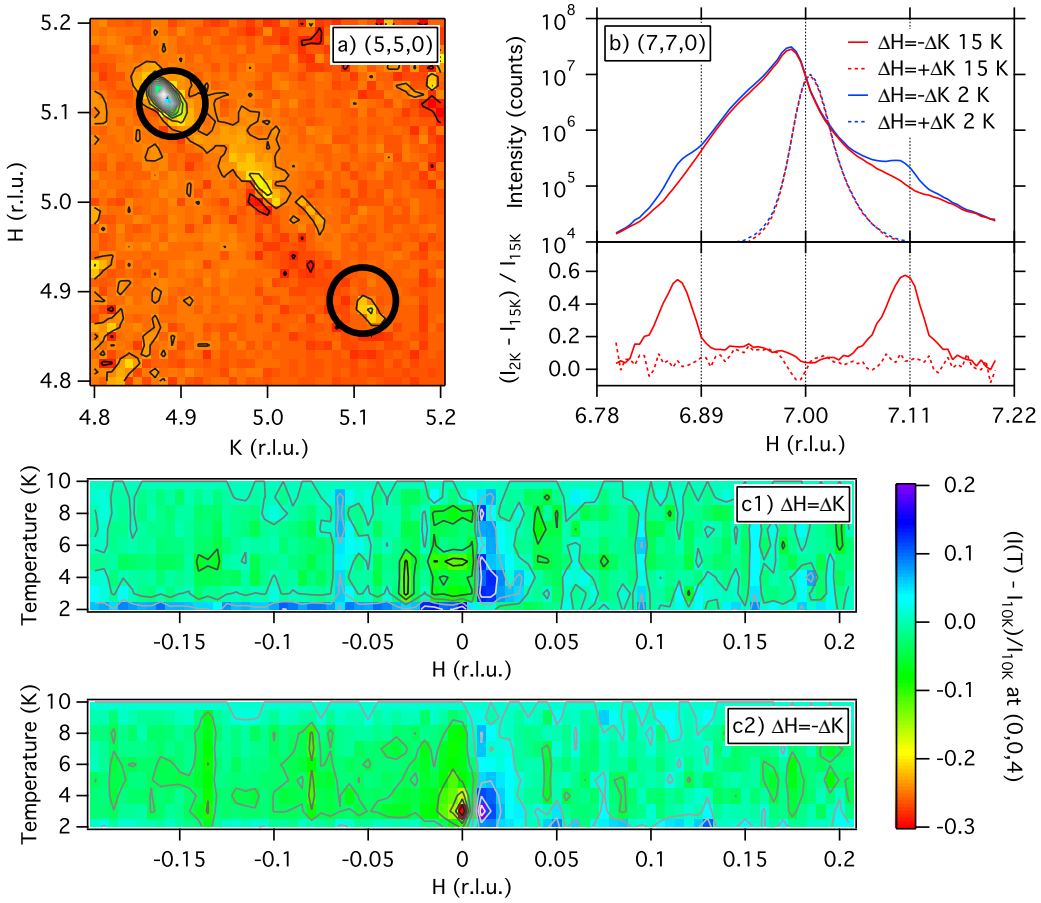

Figure 4.11: Systematic satellite absences. a) Absence of the satellites perpendicular to $\vec{Q}_R$ for $\vec{Q}_R = (5, 5, 0)$. The intensity I shown here as colour is $(I_{2\mathrm{K}} - I_{15\mathrm{K}})/I_{15\mathrm{K}}$. A clear $(+,-)$ and weak $(-,+)$ satellite can be seen, but there is no $(+,+)$ or $(-,-)$ satellite. b) Upper plot: diagonal cuts through the $(7, 7, 0)$ Bragg peak along $\Delta H = \Delta K$ (dashed curves) and $\Delta H = -\Delta K$ (solid curves) at 15 K (red curves) and 1.75 K (blue curves). Lower plot: extracted satellites. As in a), there are no satellites resolvable for the $(+,+)$ or $(-,-)$ direction. The satellites and Bragg peak are slightly offset from the expected positions, indicating a small rotation of the sample. c) $(I(T) - I_{15\mathrm{K}})/I_{15\mathrm{K}}$ as a function of H for the $(0, 0, 4)$ Bragg peak. c1) shows data for $\Delta H = \Delta K$, while c2) shows data for $\Delta H = -\Delta K$. As T decreases, there is no increase in intensity at the satellite positions, which are marked by dashed red lines.

structure of an isolated Fe atom in the usual way for these spectra.

The fluorescence can be broken down into two main energy regions. The region within ±10 eV of the edge is the X-ray Absorption Near Edge Spectra (XANES) region. Features in this region can correspond to excitations of K-edge

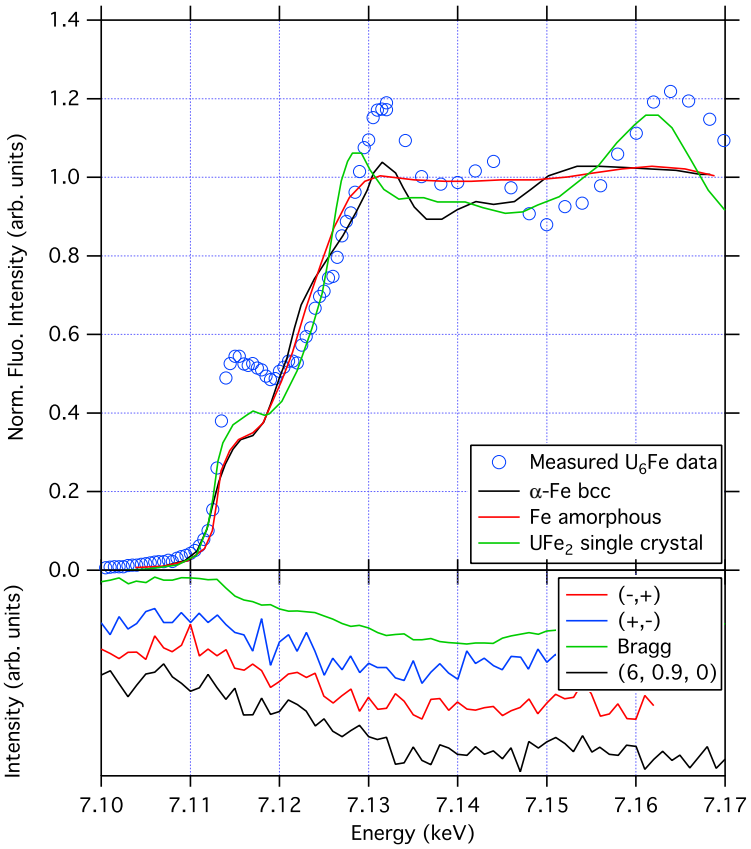

Figure 4.12: Fe edge (7.11 keV) studies of U_6Fe at 1.75 K. Upper plot: X-ray Absorption Near Edge Spectra (XANES) *versus* energy in the region of the Fe K edge. The blue circles show the obtained data. Also shown for comparison are XANES spectra for BCC α-Fe (black curve), amorphous Fe (red curve), and single crystalline UFe_2 (green curve) reproduced from [12]. Lower plot: Elastic scattering intensity as a function of energy in the region of the Fe K edge. The different coloured curves correspond to scans at different positions in (H, K, L) space: $(6, 1, 1)$ (green curve), $(6.11, 0.89, 1)$ (blue curve), $(5.89, 1.11, 1)$ (red curve), $(6, 0.9, 1)$ (black curve). There is a dip in the elastic scattering, presumably due to the increase in the absorption of X-rays by excited Fe atoms. Although this dip is also seen at the satellite position in (H, K, L) space, this could be simply due to the dip in the underlying Bragg tail intensity, rather than a dip in the satellite intensity.

electrons to states just below the unbound energy. The significant intensification of the pre-edge feature at ∼7.115 keV therefore suggests an excess of such states in U_6Fe when compared to UFe_2, for example. Above the XANES in energy is the

XAFS region, which can be used to gain information about the nearest neighbour environment of the Fe atoms. This signal results from the backscattering of the liberated K-edge photoelectron from neighbouring atoms. The XAFS is described by the dimensionless quantity $\chi(q)$, where q is the wavenumber of the photoelectron. This is usually written in terms of the absorption coefficient $\mu(q)$:

$$\chi(q) = \frac{\mu(q) - \mu_0}{\mu_0} \tag{4.1}$$

where μ_0 is the absorption from an isolated atom. Fluoresced intensity is an indirect measure of $\mu(q)$ as the fluorescence results from the absorption of the beam X-rays by the sample. Eq. 4.1 shows that $\chi(q)$ is the variation of $\mu(q)$ on top of the flat value from an isolated atom. The usual way to obtain $\chi(q)$ from the fluorescence intensity I_f is to subtact and normalise to slowly varying curves above and below the fluorescence edge. The standard expression that models the features in XAFS data is [46]:

$$q\chi(q) \propto \sum_j N_j \frac{t_j(q)\sin(2qR_j + \delta_j(q))}{R_j^2} e^{-2(q\sigma_j)^2} e^{-2R_j/\Lambda}, \tag{4.2}$$

Eq. 4.2 expresses the XAFS as a sum of contributions from different photoelectron paths (the index j in Eq. 4.2 refers to the j^{th} path). $t_j(q)$ and $\delta_j(q)$ are the backscattering amplitude and phase shift, which can be calculated using the program FEFF [17] given the position of atoms in the structure as parameters (the values of Kimball *et al.* [4] were used for this). N_j and R_j are the occupation and travelled distance for the path respectively, σ_j handles the thermal vibrations (*i.e.* this term adds Debye-Waller effects), and Λ is a mean-free path that accounts for scattering of the photoelectron by other electrons.

The usual approach to fitting XAFS data is to Fourier transform $\chi(q)$ into the real space function $\chi(R)$, and to fit the data by varying the structural parameters in Eq. 4.2. The number of variables is approximately proportional to the number of paths and is therefore almost unlimited. In order to realistically fit the data the number of free parameters must be limited. The number of independent parameters N_{ind} that can be realistically extracted from the data is estimated by the formula [73]:

$$N_{\text{ind}} = \frac{2\Delta q \Delta R}{\pi} + 2. \tag{4.3}$$

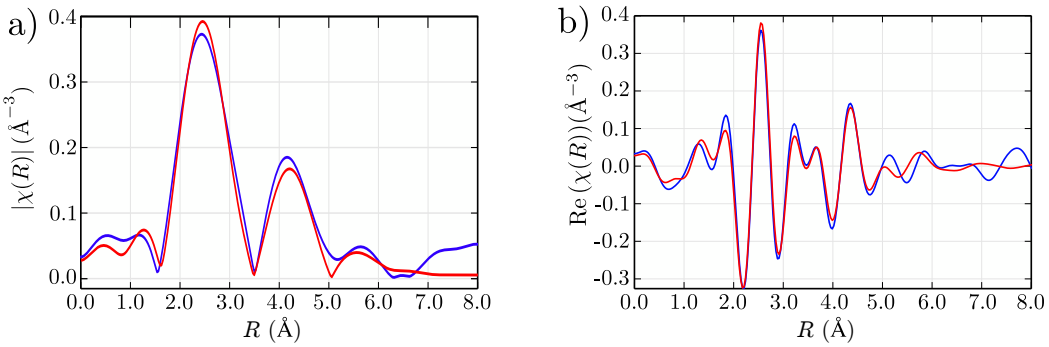

Figure 4.13: Fourier transform of the X-ray Absorption Fine Structure (XAFS) spectrum, with fit obtained from the program Larch overlaid. a) The magnitude of the Fourier transformed signal (blue) and fit (red). b) The real part of the Fourier transformed signal (blue) and fit (red).

In Eq. 4.3, Δq and ΔR are the range of the data fitted to in q and R space respectively. In addition it is normal to apply a window function to $\chi(q)$ to avoid the effects of abruptly truncated spectra causing spurious signals in the Fourier transform. We have fitted our data for 1.4 Å $< R <$ 5 Å, 1 Å^{-1} $< q <$ 5 Å^{-1}, limiting us to about 11 fitting parameters. The fitting procedure was performed using the Larch software (an extension to IFEFFIT [74]). Initially, we fitted our data using the 12 shortest paths and varying σ for each. We found that most paths refined to large σ implying a small contribution to the XAFS signal. The remaining five paths were those that correspond to single backscattering events and the fit obtained by allowing σ to vary for these five paths, discarding the contribution from the others, gives the fit shown in Fig. 4.13. In addition, a slight expansion of the lattice is allowed for using a term α such that $R = (1 + \alpha)R_0$, where R_0 is the documented path length [4]. Table 4.2 shows the fit parameters that correspond to the fitted curve shown in Fig. 4.13.

Further qualitative statements can be made about the general shape of the fluorescence spectra of Fig. 4.12 compared to those of the other compounds shown. For example, it is sometimes possible to linearly combine such spectra if the sample study is a combination of phases with known spectra. Clearly for our sample the spectra features are much more extreme than in the other compounds, indicating that our samples are not heavily contaminated with pure Fe or UFe_2 regions - this corroborates magnetisation studies that found UFe_2 concentrations of 0.05% (as reported in chapter 2). Fig. 4.12 also illustrates that there is a dip

Scatterer	R	degeneracy	σ
Fe	2.61(2)	2	0.000(7)
U	2.75(2)	8	0.015(5)
U	4.44(3)	8	0.01(1)
U	4.61(4)	8	0.01(2)
U	5.17(4)	8	0.00(2)

Table 4.2: Parameters used to obtain the fitted curve shown in Fig. 4.13. This fit is the sum of contributions from various paths as described by the XAFS equation, Eq. 4.2. R is the path length from absorbing atom to backscattering atom, while the degeneracy is how many such paths are available. σ is a term in the XAFS equation (Eq. 4.2) that accounts for thermal vibration of atoms. Paths for which σ is large have a reduced contribution to the XAFS signal. The uncertainty in the last digit is shown in brackets for certain values. Large uncertainties in σ values reflect that the coefficients may be correlated. The backscattering amplitudes and phase shifts for the XAFS equation were calculated using the program FEFF [17] and the atomic positions of Kimball *et al.* [4]. The R values are allowed to vary from the values R_0 set by these atomic positions, by including an expansion parameter α such that $R = (1 + \alpha)R_0$. α, which is the same for all paths, refines to $-0.004(7)$.

in the elastically scattered intensity at the satellite positions crossing the K-edge. However the dip is comparable in shape to the dip away from the satellites and at the Bragg peak. Therefore the dip at the satellite positions does not necessarily imply that the Fe atoms are involved in the CDW.

4.3.4 Forbidden Bragg reflections

During both experiments, various Bragg peaks were observed that are forbidden by the room temperature structure of U_6Fe. In this section we will introduce why these peaks are forbidden, and suggest what information can be extracted based on their observation.

The reflection conditions for the $I4/mcm$ structure are listed in Table 4.3. Among the forbidden reflections are those of the form $(H, 0, L)$, where H and L are odd. This is a special condition for the space group due to the presence of a c-glide plane. It is possible, however, to obtain a Q-vector at such an (H, K, L) position by taking the sum of two allowed (H, K, L) Q-vectors (for example, $(H, 0, L)$ can be written as $(H - 1, 1, L) + (1, -1, 0)$). Therefore intensity at such an $(H, 0, L)$ position can be achieved by multiple scattering, if these two

Bragg peak type	Reflection condition	
	$I4/mcm$	$I4/m$, $I\bar{4}2m$, $I422$
(H, K, L)	$H + K + L$	$H + K + L$
$(H, K, 0)$	$H + K$	$H + K$
$(0, K, L)$	K, L	$K + L$
(H, H, L)	L	L
$(0, 0, L)$	L	L
$(0, K, 0)$	K	K
$(H, H, 0)$	No condition	No condition

Table 4.3: Reflection conditions for the space group $I4/mcm$, the room temperature space group of U_6Fe, and three of the maximal subgroups of $I4/mcm$. These are reproduced from [18]. For each condition, the value noted in the table is required to be even. Note that, because a and b are equivalent in this tetragonal space group, the condition that K and L are even for reflections of the form $(0, K, L)$ is equivalent to the condition that H and L are even for reflections of the form $(H, 0, L)$.

$\vec{Q}$ vectors lie on the Ewald sphere. By comparison, other forbidden reflections for the Body Centred Tetragonal (BCT) lattice cannot be written as the sum of allowed (H, K, L) values, and so multiple scattering cannot cause intensity at their (H, K, L) positions.

In the first experiment, it was found that there was significant intensity at the position of Bragg peaks of the form $(H, 0, L)$ where H and L are odd. The intensity of the $(9, 0, 1)$ peak was found to decrease with increasing temperature and vanish at approximately 100 K (as illustrated in Fig. 4.14). This was considered to be strongly suggestive of a symmetry-breaking phase transition at 110 K. During the second experiment, studies of the energy dependence of the $(7, 0, 1)$ peak at the Fe edge saw large, unexpected peaks in the intensity, suggestive of multiple scattering (see Fig. 4.15). Subsequent azimuthal scans revealed significant structure, confirming that multiple scattering could indeed explain the forbidden peak intensity. Azimuthal scans of intensity at different temperatures and fixed energy were reasonably consistent, apart from shifts of the azimuth at which peaks were seen, which could be explained by thermal expansion of the lattice (see Fig. 4.16 b)). A mesh of $(9, 0, 1)$ intensity as a function of azimuthal angle and energy is shown in Fig. 4.16 a). This figure does not show any clear features that could not be explained by multiple scattering (such a feature should be independent of azimuthal angle).

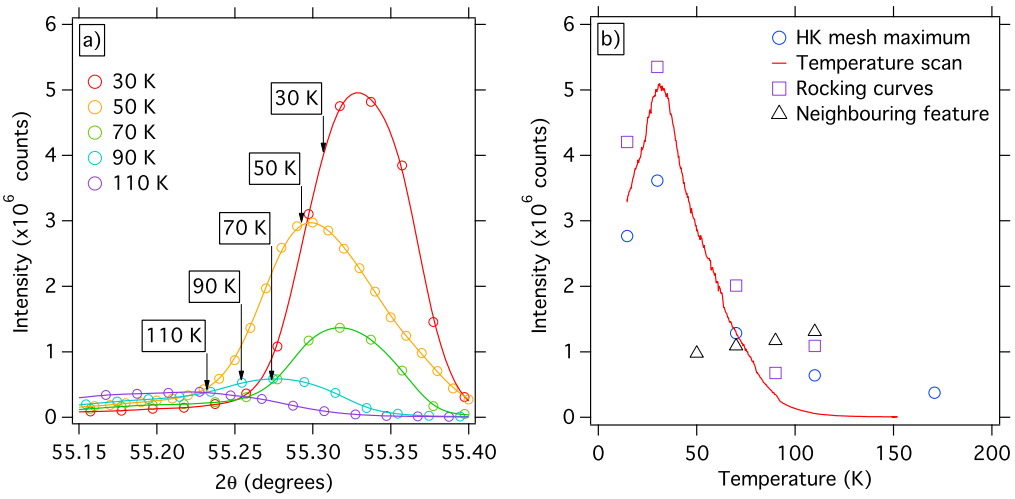

Figure 4.14: Figure illustrating the change of the $(9, 0, 1)$ Bragg peak observed with temperature during the first experiment. a) Change in the $(9, 0, 1)$ 2θ scans with temperature. Arrows mark the expected positions calculated from the thermal expansion data of Kimball *et al.* [4]. At high temperature the $(9, 0, 1)$ position appears to shift more than expected to low angles. This is explained by a background peak that increases in intensity with temperature. b) Intensity of the $(9, 0, 1)$ Bragg peak as a function of temperature measured by various methods. Blue circles show the maximum intensities taken from H-K maps around the Bragg peak. The red curve shows the intensity at the $(9, 0, 1)$ position ramped in temperature from 15 K to 150 K. Magenta squares show the maximum intensities obtained from rocking curves of the $(9, 0, 1)$ at different temperatures. Black triangles show the maximum counts from rocking curves taken through a broad feature that neighbours the $(9, 0, 1)$ and which masks intensity of the $(9, 0, 1)$ at the highest temperatures.

The presence of multiple scattering casts uncertainty on the origin of the $(9, 0, 1)$ and related Bragg peaks. It is not clear based on the above findings as to whether symmetry breaking or multiple scattering causes their intensity. It is noteworthy, however, that the $(\pm 0.11, \pm 0.11, 0)$ satellites also occur around the $(H, 0, L)$ forbidden peaks, while such satellites are not observed around other Bragg peaks that are forbidden by the BCT structure. From Fig. 4.15 it can be seen that the strong energy dependence of the forbidden $(7, 0, 1)$ Bragg peak intensity is not mirrored in that of the satellite at $(6.89, -0.11, 1)$. This is convincing evidence that the satellites around the forbidden peaks are not due to multiple scattering. In order for the satellites to form around the forbidden peak positions, there must be intensity at the forbidden peak positions themselves,

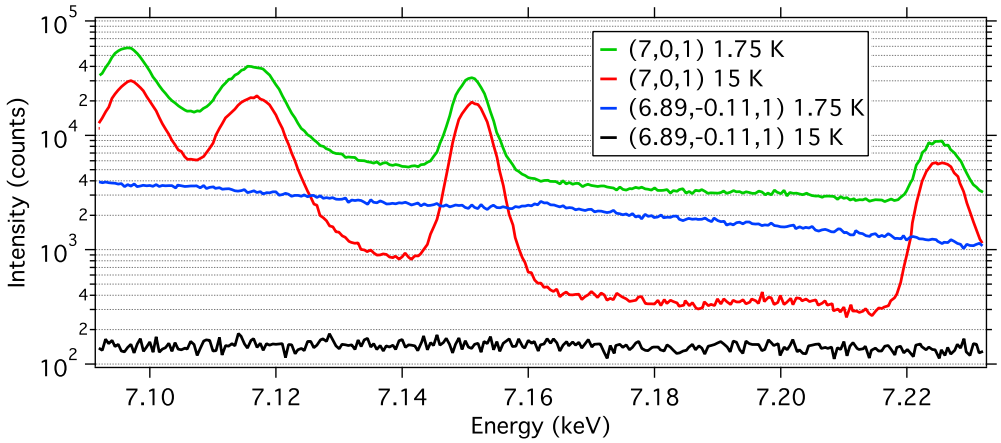

Figure 4.15: Figure illustrating the effects of multiple scattering on the $(7, 0, 1)$ Bragg peak and satellite energy dependence. Strong peaks are evident in the curves of Bragg peak intensity *versus* energy at both 15 K (red curve) and 1.75 K (green curve). The underlying intensity away from these peaks in energy undergoes a large change with temperature. The intensity of the satellite of the $(7, 0, 1)$ at $(6.89, -0.11, 1)$ does not show similar peaks with energy. This implies that, although multiple scattering has a significant effect on the intensity of forbidden peaks, it does not significantly affect the satellites. As found for all observed satellites, there is a significant intensity change of the satellite between 15 K (black curve) and 1.75 K (blue curve).

that is not due to multiple scattering (this will be explained in section 4.4.1 below). Therefore, the *c*-glide symmetry of the $I4/mcm$ space group must be broken. In Fig. 4.15, it can be seen that there is indeed a significant increase, between 1.75 K and 15 K, in the $(7, 0, 1)$ Bragg peak intensity away from the strong multiple scattering peaks. This shows that there is a signal that emerges at these forbidden Bragg peaks at the CDW temperature that can be separated from that due to multiple scattering.

There is therefore clear evidence for symmetry breaking that causes forbidden peak intensity. However, it is not clear from the data what the onset temperature of the symmetry breaking is. It could be that the symmetry breaks as a result of the CDW formation, or it could be that the symmetry is already broken at T_{CDW} as a result of a transition at a higher temperature. This uncertainty is because it is unclear if the intensity of the $(9, 0, 1)$ family above T_{CDW} is entirely due to multiple scattering effects, or is partly due to broken symmetry.

Multiple scattering Bragg peaks are essentially combinations of other Bragg

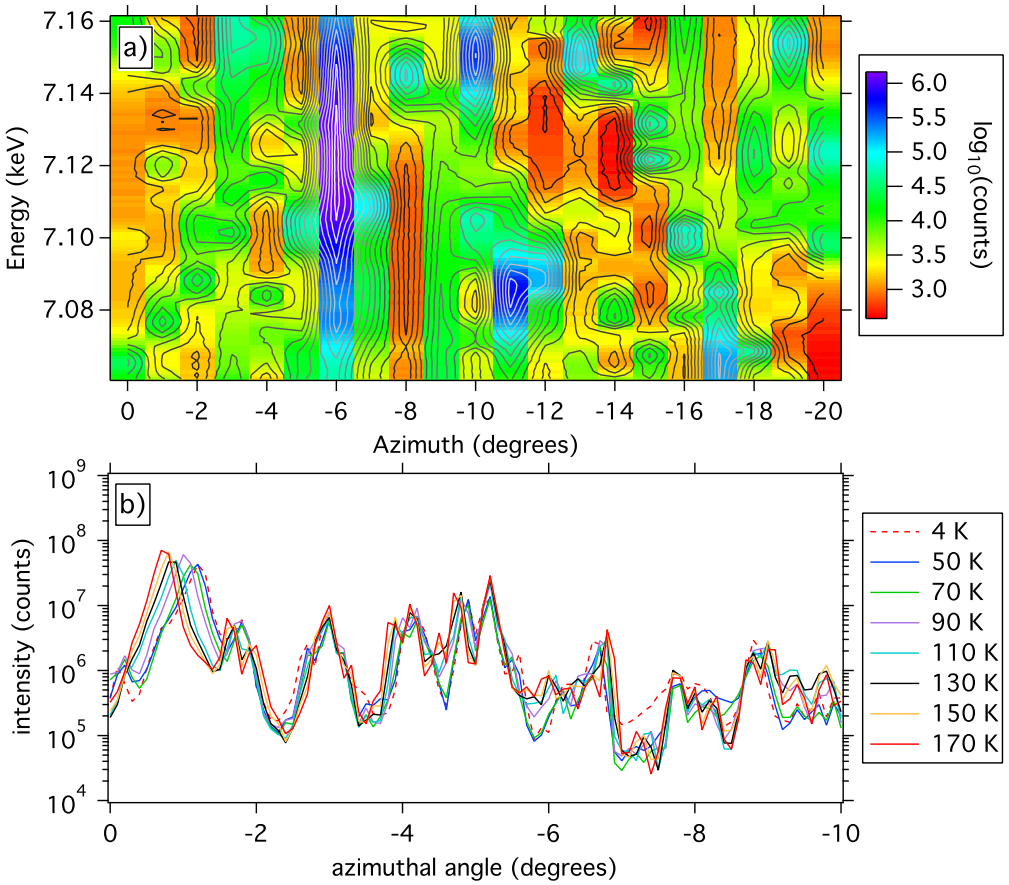

Figure 4.16: Figure illustrating the effects of multiple scattering. a) Mesh showing intensity of the forbidden $(7, 0, 1)$ peak as a function of azimuthal angle and energy at 1.75 K. b) Intensity *versus* azimuthal angle scans at 12 keV for the forbidden $(9, 0, 1)$ peak at various temperatures. The strong dependence of intensity on azimuthal angle shows that there is a great deal of multiple scattering.

peaks. If the forbidden peaks are caused by multiple scattering, then, they are therefore expected to be at least as broad as the allowed Bragg peaks. In an effort to deduce to what extent multiple scattering can explain the forbidden peak intensity seen at high temperature, the width of these Bragg peaks, compared to those that are allowed by the $I4/mcm$ symmetry, have therefore been studied, as discussed below.

During the first experiment, a rocking curve through the $(9, 0, 1)$ peak measured on sample 6 at 15 K showed a peak width of 0.031°, narrower than other Bragg peak widths (0.048° at $(10, 0, 0)$, 0.041° at $(10, 0, 2)$). At this temperature, for the first experiment, the CDW peaks were already apparent (this is explained

by thermometry issues that were discussed earlier). Therefore this narrow Bragg peak could be understood as symmetry breaking related to the CDW. However, this Bragg peak was observed up to high temperatures, as shown in Fig. 4.14. This does not fit with the idea of broken symmetry originating from the CDW, as the CDW is only manifest for $T < T_{\mathrm{CDW}}$. Instead, this sharp, high temperature Bragg peak suggests that the symmetry breaking originates from temperatures $\sim$100 K.

In the second experiment, all of the Bragg peaks (allowed and forbidden) measured on sample 6 were considerably broader than when measured during the first experiment. Additionally, the $(9, 0, 1)$ reflection (width $\sim$0.15° at 15 K) was broader than the $(10, 0, 0)$ reflection (width $\sim$0.12° at 15 K). Sample 3 showed a forbidden $(1, 0, 5)$ reflection with a width of approximately 0.13°, compared to $\sim$0.07° for the $(0, 0, 4)$ and $(2, 0, 4)$ Bragg peaks. The broad forbidden peaks of the second experiment are therefore in line with the concept that multiple scattering explains the forbidden peak intensity above T_{CDW}. This, however, is still inconsistent with the sharp Bragg peak of the first experiment.

The rocking curve widths of the satellites around the $(9, 0, 1)$ peak in the first experiment were found to range from 0.22° to 0.31°, $7 - 10$ times wider than the width of the $(9, 0, 1)$ Bragg peak. The satellites did not change noticeably in width between the experiments, however the Bragg peaks (forbidden and allowed) broadened considerably. This peak broadening between the first and second experiments may be explained by strain on the sample surface, as will be discussed further in the next section.

4.3.5 Further structural studies

A dataset of 64 Bragg peak intensities was collected at 1.75 K and 15 K, in order to investigate the possibility of any structural changes with temperature. We additionally studied the temperature dependence of selected peaks, specifically for any evidence of a transition at around 100 K to match those documented in the literature. A careful study of the $(H, H, 0)$ $(H = 2, 3, 4, 5)$ Bragg peak intensity temperature dependence in the second experiment showed that the integrated intensity of these peaks is increasing significantly below 210 K, and there is perhaps a slight levelling off of intensity below 100 K. The $(10, 0, 0)$ Bragg peak intensity on the other hand, reaches a maximum at $\sim$130 K and falls below this.

Fig. 4.17a) illustrates this behaviour.

For the $(3,3,0)$ reflection, this could perhaps be explained simply by thermal vibrations that reduce as temperature drops. The $(10,0,0)$ Bragg peak behaviour is harder to explain. The structure factor for the $(10,0,0)$ Bragg peak (neglecting the Debye-Waller terms) has the form:

$$4f_{\mathrm{Fe}} + \underbrace{8f_{\mathrm{U}}\cos(20\pi x_1)}_{\mathrm{U}_1\text{ terms}} + \underbrace{8f_{\mathrm{U}}\left(\cos(20\pi x_2)+\cos(20\pi y_2)\right)}_{\mathrm{U}_2\text{ terms}}, \tag{4.4}$$

where f_{Fe} and f_{U} are the Fe and U atomic form factors, x_1, x_2 and y_2 are the fractional co-ordinate positions that describe the U_1 and U_2 atoms at $(x_1, x_1+\frac{1}{2}, 0)$ and $(x_2, y_2, 0)$ respectively. For the x_1, x_2 and y_2 quoted in Kimball *et al.* [4] this reduces to $\sim 4.0f_{\mathrm{Fe}} + 20.2f_{\mathrm{U}}$, showing a significant contribution from the U atoms. The corresponding equation for the $(3,3,0)$ reflection is:

$$4f_{\mathrm{Fe}} - \underbrace{4f_{\mathrm{U}}\left(\cos(12\pi x_1)+1\right)}_{\mathrm{U}_1\text{ terms}} + \underbrace{8f_{\mathrm{U}}\cos(6\pi x_2)\cos(6\pi y_2)}_{\mathrm{U}_2\text{ terms}}. \tag{4.5}$$

Again using the values of [4] gives $\sim 4.0f_{\mathrm{Fe}} + 1.4f_{\mathrm{U}}$, *i.e.* the $(3,3,0)$ reflection is more sensitive to the Fe atoms by comparison to the $(10,0,0)$ reflection (although the atomic form factor of U is approximately four times larger than that of Fe and so the U contribute the most to both expressions). Therefore, the changes in the $(10,0,0)$ Bragg peak intensity could reflect small movements in the U positions as temperature drops. By using the atomic positions as a function of temperature as documented by [4], a minimum in the contribution of the U_1 atoms to the $(10,0,0)$ Bragg peak structure factor is to be expected at 100 K.

There is an abrupt change in integrated peak intensity at 110 K for both the $(10,0,0)$ and $(3,3,0)$ curves. Initially this was presumed to be due to the way the data were obtained: above 100 K an issue with the temperature controller meant that the set point was reset to 0 K. Subsequently the measurements for $T > 100$ K were resumed, and a thermal lag could mean that the 110 K reading is inaccurate. Thermal lag does not explain such a significant drop as shown in Fig. 4.17 a), however (for such reasoning to make sense, the value at 110 K would need to match to a value at low temperature).

Noticeable broadening with reduced temperature was also observed for these Bragg peaks, as shown in Fig. 4.17 b). This figure also shows the broadening of

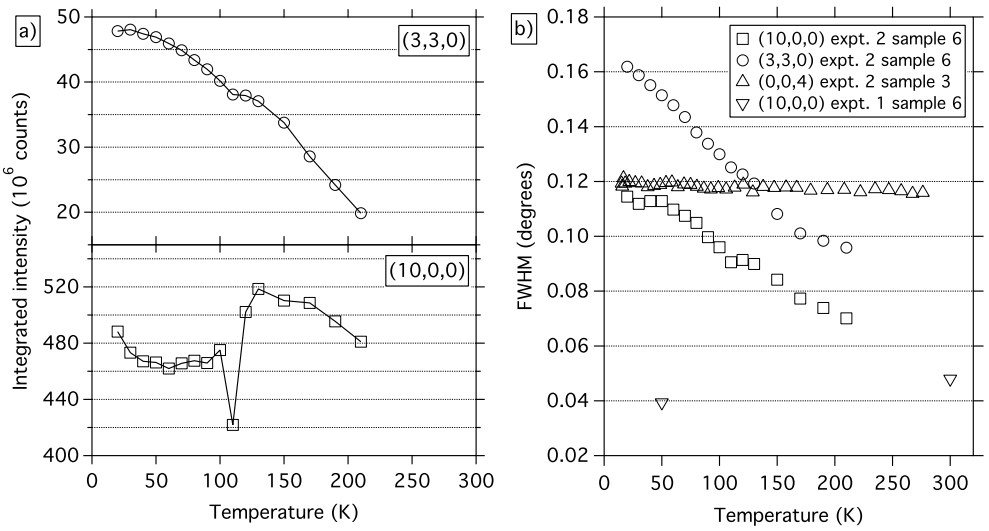

Figure 4.17: Change in the $(3,3,0)$, $(10,0,0)$, and $(0,0,4)$ Bragg peak properties *versus* temperature. a) Change in integrated intensity for the $(3,3,0)$ (circles) and $(10,0,0)$ (squares) Bragg peaks measured on sample 6 during the second experiment. b) Change in peak FWHM *versus* temperature for the $(3,3,0)$ (circles) and $(10,0,0)$ (squares) Bragg peaks for sample 6 during the second experiment, and for the $(0,0,4)$ (upright triangles) Bragg peak measured on a sample 3 during the second experiment. Also shown is the FWHM data from rocking curves of the $(10,0,0)$ Bragg peak for sample 6 during the first experiment. There is a small feature at 110 K in both plots in a), possibly due to a discontinuity in the temperature control between 100 K and 110 K. In b), the sample cut perpendicular to the *c*-axis shows noticeably less broadening at low temperature, possibly due to a less oxidised surface. There is a very significant difference between the broadening observed for the $(10,0,0)$ reflection during the first and second experiments.

the $(0,0,4)$ peak that was measured using sample 3. There is significantly less broadening for this peak, which implies that the effect varies between samples and could be an indicator of the degree of oxidation of the sample used. Sample 3 was freshly polished between the first and second experiments, while sample 6 was untreated. The oxide layer on the surface of a sample will have different thermal expansion properties to the bulk, resulting in strain on the underlying lattice as the sample cools and therefore a broadening of the Bragg peaks. For the first experiment, the $(10,0,0)$ peak for sample 6 (freshly polished at the time) was measured to have a sharper FWHM of $\sim$0.048 degrees at room temperature (compared to $\sim$0.059 degrees) that decreased to $\sim$0.039 degrees at 50 K. These

measured widths are also shown in Fig. 4.17 b). The opposite trend and lower width for the same sample suggest that the surface oxidation may indeed strain the samples.

It was considered that the broadening of Bragg peaks between the first and second experiments could be an explanation for the large amounts of multiple scattering seen during the second experiment. To see this, consider that multiple scattering occurs when the Ewald sphere intersects Bragg peak positions in reciprocal space other than the targeted position. Clearly, multiple peaks will overlap the Ewald sphere more often if Bragg peaks are broad and occupy more reciprocal space. If broadening is the cause of multiple scattering, then there is the possibility that the sharp $(9, 0, 1)$ Bragg peak measured during the first experiment was, in fact, not an artefact of this effect. This is because, as illustrated by Fig. 4.17 b), there was significantly less broadening during the first experiment and therefore there should be much less multiple scattering in this data.

It is additionally notable that, during the first experiment, the broad background peak (on top of which a sharp Bragg peak was observed) remained at temperatures up to 170 K. This was made clear from maps in H-K space (see Fig. 4.18). This broad feature is suggestive of diffuse scattering that could arise from soft phonons, but there could be an element of this background feature that is due to multiple scattering. In the second experiment the Bragg peak was observed only in rocking curves, which do not suggest that there is such a background feature. One interpretation of this is that the sharp Bragg peak has vanished, leaving only the broad feature at the $(9, 0, 1)$ position, which resembles a broad Bragg peak in rocking curves. An H-K mesh around the $(8, 1, 1)$ peak during the second experiment shows a feature quite similar to the broad background peak (as shown in Fig. 4.18). This suggests that the broad background would have still been observed in an H-K mesh, and therefore that the sharp Bragg peak has indeed vanished between experiments. This would explain why the $(9, 0, 1)$ reflection appears to change from being narrower than the $(10, 0, 0)$ reflection in the first experiment, to broader than it in the second experiment.

Vanishing of the sharp peak at the $(9, 0, 1)$ position could possibly be due to the strain from an oxide layer. However, there are flaws in this argument. For example, in this case we should observe a sharp $(1, 0, 5)$ peak for sample 3, but

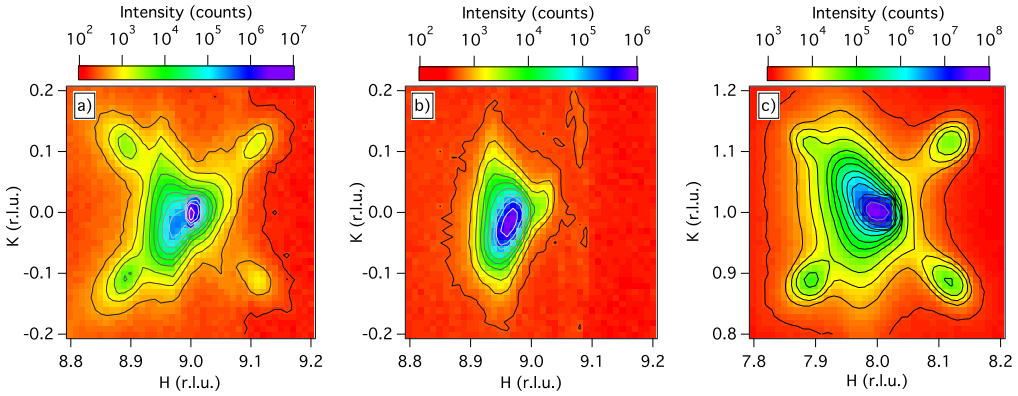

Figure 4.18: Features observed around the $(9, 0, 1)$ and $(8, 1, 1)$ Bragg peaks. a) Mesh of intensity in H-K space around the $(9, 0, 1)$ Bragg peak observed during the first experiment. This mesh was taken at 15 K and the satellites are clearly visible, as is a sharp Bragg peak. b) The same map at 170 K. Only a broad background feature remains. c) H-K map around the $(8, 1, 1)$, taken during the second experiment at 1.75 K. A similar broad background feature is visible.

the $(1, 0, 5)$ peak is broader than the allowed Bragg peaks. Also, the width of the broad feature below the sharp $(9, 0, 1)$ peak in the first experiment ($\sim$0.13°) is similar to that of the $(9, 0, 1)$ Bragg peak in the second experiment ($\sim$0.15°). This is contrary to the observation that the allowed Bragg peaks broadened significantly between experiments. A narrow $(9, 0, 1)$ in the first experiment, that broadened by the second experiment, is more in line with this fact. It is difficult, then, to argue convincingly that the intensity of the $(9, 0, 1)$ family above T_{CDW} could be due to anything other than multiple scattering. The most significant evidence that counters multiple scattering as the origin of these features is the sharp $(9, 0, 1)$ peak width in the first experiment.

Finally, Fig. 4.19 shows the temperature dependence of the a and c lattice parameters, extracted from the temperature dependence of $(10, 0, 0)$ and $(0, 0, 4)$ $\theta - 2\theta$ scans. These compare reasonably well with the data of Kimball *et al.* [4], with no noticeable features within the scatter.

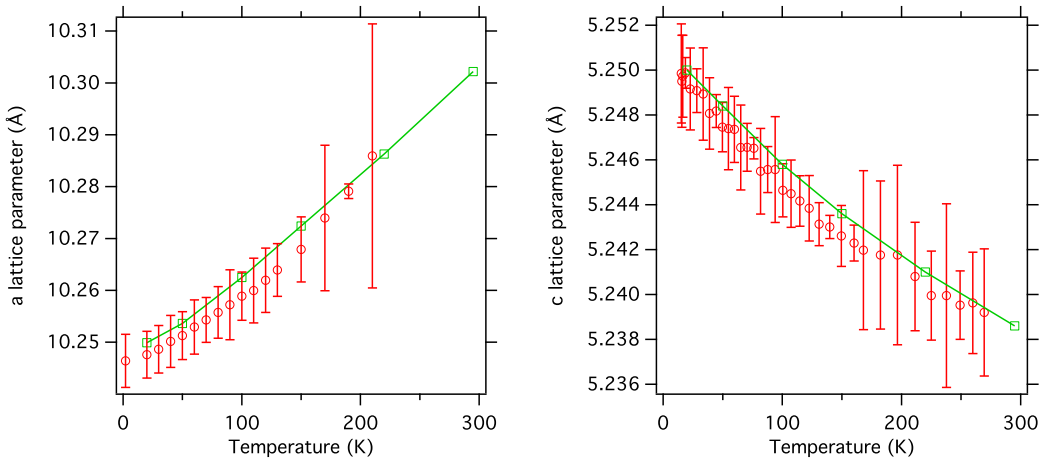

Figure 4.19: Observed trend of the a and c lattice parameters as a function of temperatures (red circles) compared to the data of Kimball *et al.* [4] (green squares and curve). The a parameter was measured on a sample with a faced polished perpendicular to a using the $(10, 0, 0)$ reflection. The c parameter was measured on a sample with a faced polished perpendicular to c using the $(0, 0, 4)$ reflection.

4.4 Analysis and Discussion

4.4.1 Origin of low-temperature satellites

We will briefly discuss here how satellites can be explained by a modulated charge structure. In an X-ray experiment, the intensity I is proportional to the structure factor squared, where the structure factor is given by:

$$S_{\vec{Q}} = \sum_j f_j(\vec{Q}) e^{i\vec{Q}\cdot\vec{R}_j}. \tag{4.6}$$

In this expression (taken from [32]), f_j is the atomic form factor for the j^{th} atom (an approximation for this can be found in the ITC volume C [75]), $\vec{Q} = H\vec{b_1} + K\vec{b_2} + L\vec{b_3}$ is the reciprocal lattice vector for the $(H, K, L)^{\text{th}}$ Bragg peak, and $\vec{R}_j$ is the position vector of the j^{th} atom. For a modulated structure:

$$\vec{R}_j \to \vec{R}_j + \vec{u}\cos\left(\vec{q}\cdot\vec{R}_j\right) \tag{4.7}$$

$$\therefore S_{\vec{Q}} = \sum_j f_j(\vec{Q}) e^{i\vec{Q}\cdot\vec{R}_j} e^{i\vec{Q}\cdot\vec{u}\cos\left(\vec{q}\cdot\vec{R}_j\right)} \tag{4.8}$$

$$\approx \sum_j f_j(\vec{Q}) e^{i\vec{Q}\cdot\vec{R}_j}\left(1 + i\vec{Q}\cdot\vec{u}\cos\left(\vec{q}\cdot\vec{R}_j\right)\right) \tag{4.9}$$

$$= \sum_j f_j(\vec{Q})\left(e^{i\vec{Q}\cdot\vec{R}_j} + \frac{i\vec{Q}\cdot\vec{u}}{2}\left(e^{i\left(\vec{Q}+\vec{q}\right)\cdot\vec{R}_j} + e^{i\left(\vec{Q}-\vec{q}\right)\cdot\vec{R}_j}\right)\right). \tag{4.10}$$

In the above derivation, it is assumed that the size of the modulation is small so that the simple expansion of the exponential can be made. The final result shows that there are extra terms that enhance the structure factor at $\vec{Q}_R \pm \vec{q}$ where $\vec{Q}_R$ is a reciprocal lattice vector. The reason that four satellites were observed in our data is presumably due to domains. The direction of the modulation is along one of the *a*-*b* diagonals of the unit cell, and by symmetry there should be no reason to choose one diagonal over the other.

Importantly, the satellite terms have a prefactor $\vec{Q}\cdot\vec{u}$ that is zero if $\vec{Q} \perp \vec{u}$. As shown by the data around $\vec{Q}_R = (5,5,0), (7,7,0), (3,-3,6)$, we observed the absence of satellites for $\vec{q} \parallel Q_R$ (see Fig. 4.11). If $\vec{u} \perp \vec{q}$ then $\vec{Q}\cdot\vec{u}$ gives zero for $\vec{q} \parallel Q_R$, resulting in the systematic absences observed. This is not the case for $\vec{u} \parallel \vec{q}$, which would result in the satellites that were absent being enhanced instead. Therefore, we can say that the charge is modulated transverse to the modulation wavevector, so that $\vec{u} \perp \vec{q}$ and therefore $\vec{Q}\cdot\vec{u} = (\vec{Q}_R + \vec{q})\cdot\vec{u} = \vec{Q}_R\cdot\vec{u}$.

We also observed an absence of satellites around the $(0,0,4)$ and $(0,0,6)$ Bragg peaks. These absences, if they result from $\vec{Q}_R\cdot\vec{u} = 0$, imply that $\vec{u}$ is confined to the *a*-*b* plane.

The above equations also illustrate how satellite intensity around the forbidden peaks that is not due to multiple scattering implies Bragg peak intensity which must also be free from multiple scattering. Intensity at $\vec{Q}_R \pm \vec{q}$ occurs because at these positions $e^{i\left(\vec{Q}\mp\vec{q}\right)\cdot\vec{R}_j} = e^{i\vec{Q}\cdot\vec{R}_j}$, *i.e.* the structure factor at satellite positions contains terms proportional to Bragg peak intensity. Therefore, assuming the other terms in the expansion above are small (as they are proportional to the structure factor away from the Bragg peak), intensity (proportional to structure factor squared) at the satellite positions implies

intensity at the Bragg peak positions.

4.4.2 Low temperature structural refinement

If not due to multiple scattering, the $(9, 0, 1)$ family reflections imply symmetry breaking. This results in the $I4/mcm$ lattice symmetry reducing to one of $I4/m$, $I\bar{4}2m$ or $I422$ space groups (these are the only maximal subgroups of $I4/mcm$ that allow these forbidden Bragg peaks but still forbid others that were not observed). As detailed above, it has been found that the symmetry is indeed broken below T_{CDW}, and it is clear that multiple scattering is not the cause. The onset of the symmetry breaking may be at T_{CDW} or it may be at higher temperatures, however. In order to test whether symmetry is broken above T_{CDW}, we have carried out structural refinement using the Bragg peak intensities at both 1.75 K ($T < T_{\mathrm{CDW}}$) and 15 K ($T > T_{\mathrm{CDW}}$). During the second experiment, θ and 2θ scans were measured for a set of 64 Bragg peaks at these temperatures. The structural refinement was preformed on this data, with the aid of the JANA software package [13].

Refinement of the structure from the 15 K dataset (using integrated intensities obtained from θ-scans) suggests that there is no significant improvement to the fit to be obtained by assuming $I4/m$, $I\bar{4}2m$ or $I422$ space groups. However, for the 1.75 K dataset, these other space groups do produce slightly better fits to the data (the results of the refinements are presented in appendix B). This evidence is in agreement with what has already been explained: that the c-glide symmetry breaking occurs below T_{CDW}.

To verify the result of the JANA fits, the data were fitted using code to calculate the structure factors and minimise the R-factor by varying the fit parameters of the $I4/mcm$ structure. A plot of the observed *versus* calculated structure factors F obtained by this is shown in Fig. 4.20. Tables 4.5 show the parameters found by this code (which assumes anisotropic atomic displacement factors) using the data from 1.75 K and 15 K. The most significant difference between the parameters fitted to the 1.75 K and 15 K datasets is in the U_1 b_{33} values. This suggests that the thermal motion of the U_1 atoms becomes constricted along the c-axis below the CDW transition. This is reflected in the parameters obtained by fitting the data to the $I4/mcm$, $I422$, and $I4/m$ space groups using JANA. However, the JANA fits indicate that the hardening along

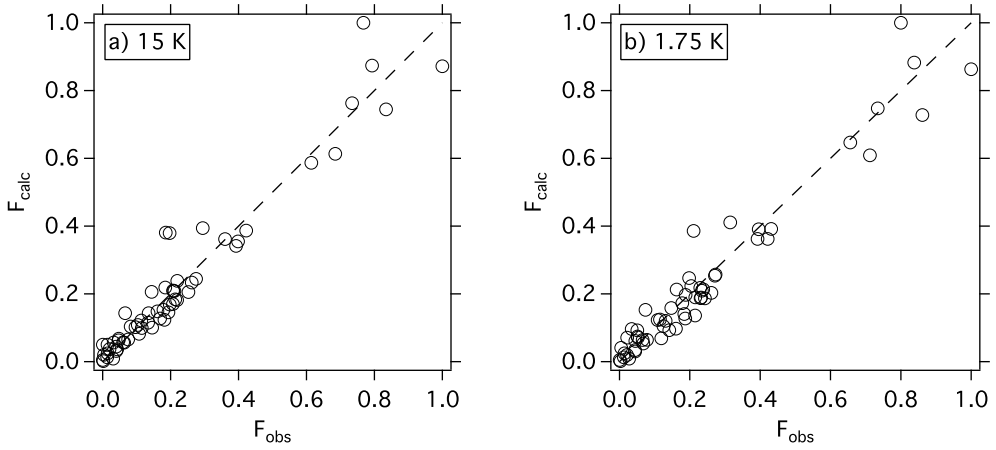

Figure 4.20: Calculated F_{calc} *versus* observed F_{obs} structure factors, found by fitting observed intensities to the $I4/mcm$ space group (the room temperature space group). Other space groups ($I4/m$, $I\bar{4}2m$ and $I422$) were fitted to using JANA [13] but found no significant improvement in the R-factor.

the c-axis occurs for all of the U atoms.

Kimball *et al.* [4] also previously performed refinements at various temperatures that found an increase in atomic displacement of Fe atoms along the c-axis below 100 K. While this trend is at odds with our findings, it should be noted that their powder diffraction study did not venture below 20 K, so there is no overlap in temperature between our data and theirs.

The $I4/m$, $I\bar{4}2m$, and $I422$ subgroups each break the c-glide symmetry in a different way. For $I4/m$, the symmetry is broken by either U_1 atoms moving in the a-b plane from $(x, x + 1/2, 0)$ to $(x, y, 0)$ positions, or by the 16 U_2 atoms in the unit cell moving into two inequivalent sites of multiplicity 8. For $I422$, the symmetry is broken because U_2 is no longer restricted to the $z = 0$ plane. For $I\bar{4}2m$, the restriction that $z = 0$ for both U_1 and U_2 sites is lifted.

We now consider how the symmetry breaking that is observed below T_{CDW} relates to the CDW. The CDW may or may not be the cause of the symmetry breaking. We consider the following two scenarios to illustrate why it is not clear whether the CDW is the direct cause of the symmetry breaking.

In the first scenario, we assume that the reduction of atomic vibration along the c-axis of the U atoms results in the U atoms becoming localised in the a-b plane. Such in-plane localisation forces the U atoms to move closer together because separation along the c-axis is reduced. This may result in U atoms

1.75 K					
Fe		U_1			
b_{11}	b_{33}	x	b_{11}	b_{33}	b_{12}
0.003	0.012	0.40575	0.027	0.006	0
U_2					
x	y	b_{11}	b_{22}	b_{33}	b_{12}
0.10442	0.21613	0.014	0.02	0.102	0.005
15 K					
Fe		U_1			
b_{11}	b_{33}	x	b_{11}	b_{33}	b_{12}
0	0.012	0.40598	0.027	0.078	0
U_2					
x	y	b_{11}	b_{22}	b_{33}	b_{12}
0.10325	0.21613	0.014	0	0.106	0.005

Table 4.4: Fitted structural refinement parameters assuming the space group $I4/mcm$, using Bragg peak intensities collected at 1.75 K and 15 K. The anisotropic temperature factor has the form $\exp(-\frac{1}{2}\vec{Q}(\mathbf{R}_i\mathbf{B}\vec{Q}))$ where $\mathbf{R}_i$ is the rotation matrix that generates the i^{th} atom, $\vec{Q} = \frac{1}{2\pi}(h\hat{\vec{x}}, k\hat{\vec{y}}, l\hat{\vec{z}})$and $\mathbf{B}$ is the 3×3 matrix formed from the elements b_{ij}. The 1.75 K fit refines to an R of 0.168, while the 15 K fit refines to an R of 0.170, based on the formula $R = \sum |F_{obs} - F_{calc}| \,/\, |F_{obs}|$.

Miller indices			Int. intensity (counts)		
H	K	L	15 K	1.75 K	θ (degrees)
9	4	1	9.86×10^5	1.76×10^6	15.0
2	2	0	9.86×10^7	2.94×10^7	4.2
3	3	0	4.75×10^8	3.05×10^8	6.4
11	4	1	3.25×10^8	2.53×10^8	17.9
10	0	0	4.73×10^9	3.73×10^9	15.2
11	1	2	6.66×10^8	5.35×10^8	17.1

Table 4.5: Most significant Bragg peak intensity changes between 15 K and 1.75 K. Also shown is the θ value calculated from the Miller indices. For very low θ, the beam may be cut off by the sample, resulting in a misleading rocking curve.

moving to different equilibrium positions in the a-b plane. The observed $I4/mcm$ symmetry breaking must result from the movement of U atoms in the a-b plane, as we have assumed that the U atoms are localised along the c-axis. Therefore, the new structure must belong to the $I4/m$ space group. This is because only the $I4/m$ space group allows symmetry breaking by the movement of U atoms in the a-b plane. The CDW modulation and displacement are known to be in the a-b plane from systematic satellite absences. Therefore the symmetry breaking distortion and CDW are in the same plane. In this case, then, it then seems quite likely that the CDW is the cause of the symmetry breaking. This scenario is illustrated in Fig. 4.21 a).

In the second scenario, we assume that the reduction of U atomic vibration along the c-axis is due to a the U atoms settling at new equilibrium positions at $z \neq 0$. Such a displacement breaks the symmetry of the $I4/mcm$ space group, before the CDW modulation is even considered. The lattice symmetry in this distorted state is reduced to the symmetry of either the $I422$ or $I\bar{4}2m$ space group, depending on which U atoms are displaced. Clearly, the CDW modulation is not the cause of the symmetry breaking in this case. This is known because systematic satellite absences tell us that the CDW distortion is confined to the a-b plane. The CDW distortion is still possible in this scenario. However, the modulation in the a-b plane cannot break any further symmetry, so the modulation is confined to allowed directions. For example, the U_1 atoms will only be able to be modulated such that they still occupy $(x, x + 1/2, 0)$ positions. This is illustrated in Fig. 4.21 b).

Both of these two scenarios seem plausible based on our data. The JANA fits perhaps indicate a slightly better fit of the low temperature data to the $I4/m$ structure based on the R-factors. However, the difference in the goodness of fit between the subgroups is small. Therefore, a more careful analysis of the data, or further experimental work may be necessary to reduce the possibilities further.

4.5 Conclusions

In this chapter, X-ray scattering data is presented that shows clear evidence for a CDW transition in U_6Fe as temperature is lowered below about 10 K. This is indicated by intensity increases at $(\pm 0.11, \pm 0.11, 0)$ satellite positions

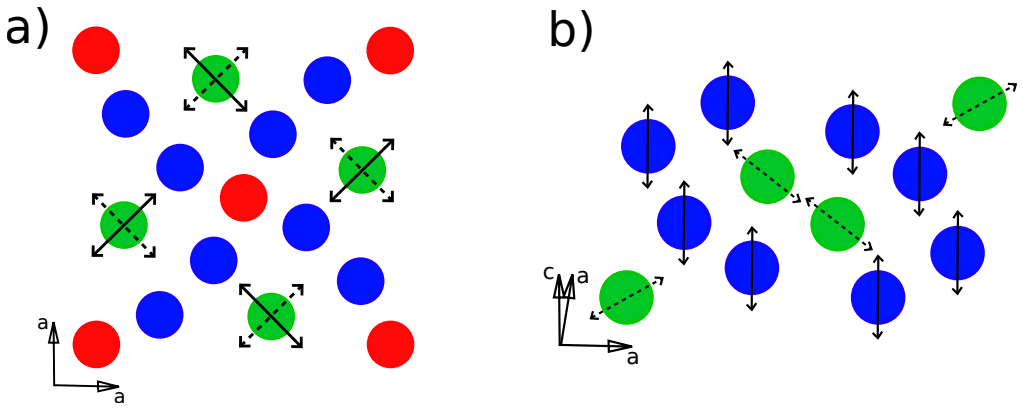

Figure 4.21: Illustration of possible symmetry breaking configurations in the Charge Density Wave (CDW) state. These figures correspond to the two scenarios considered in the text. a) Cross-sectional view along the c-axis, showing the position of the U_1 (green circles) and U_2 (blue circles) atoms in the ($z = 0$) plane. The Fe atoms (red circles) of the $z = 1/4$ (fractional co-ordinates) plane are also shown. Below T_{CDW}, the c-glide symmetry is broken, and the atoms must be at distorted positions. In the first scenario it is considered that this distortion could be in the a-b plane. For example, the U_1 atoms could move as shown by the solid arrows. Then the $I4/mcm$ symmetry would be broken, and the lattice would change to the $I4/m$ subgroup. Movement of the U_1 atoms as shown by the dashed arrows is allowed without breaking the $I4/mcm$ symmetry. In this scenario, the CDW modulation could correspond to modulation of the U_1 atoms in the symmetry-breaking direction. b) The second scenario considered in the text. In this case, instead of a distortion localised to the a-b plane, the U_2 atoms would move be distorted out of the plane as shown by the solid arrows. This would also break the $I4/mcm$ symmetry, moving the lattice to either the $I422$ or $I\bar{4}2m$ space group. In this scenario the CDW would be due to modulation in the a-b plane along directions that do not break the symmetry of the $I4/mcm$ space group (for example, the movement of the U_1 atoms along the direction of the dashed arrows). Such modulation could be encouraged by the displacement of the U_2 atoms along the c-axis, which will quite likely affect the equilibrium positions of the atoms in the a-b plane.

around almost all of the Bragg peaks examined. Systematic exclusions indicate that the modulation amplitude is transverse to the modulation wavevector and confined to the a-b plane. The modulation is presumed to be described by a single modulation vector, with four satellites generated by the effect of domains. There is a kink and flattening off of satellite intensity I_{CDW} *versus* temperature at the superconducting transition temperature T_{SC}, suggesting that the onset of

superconductivity prevents further formation of the CDW state. Unlike in some materials (*e.g.* $YBa_2Cu_3O_{6.67}$ [76]), I_{CDW} does not dip below T_{SC}, implying here a greater level of co-existence between the two states. There is possibly a slight reduction setting in below 2 K, at the lower limit of temperature obtained. There is clear breaking of the lattice symmetry below the CDW transition, as indicated by intensity at forbidden Bragg peaks and at satellites around these positions. It is uncertain whether the symmetry breaking is in the *a*-*b* plane of the CDW modulation or along the *c*-axis.

Significant broadening of Bragg peaks was observed in the second experiment which we have attributed to the increased oxidation of the sample surface. The dependence on the width of the peaks on surface oxidation were not expected, and needs to be more carefully controlled in future work. The width of the CDW peaks (which is larger than the Bragg peaks) is unaffected by the oxidation.

From structural refinement of the intensities of 64 of the Bragg peaks, there is a clear hardening of the U thermal vibration associated with the b_{33} coefficient (*i.e.* the motion along the *c*-axis). This suggests that the U atoms are those primarily involved in the CDW.

While symmetry breaking is clear below the CDW transition, it is unclear whether this originates at a much higher temperature. Data that initially suggested that the symmetry breaking occurs at ∼100 K were not reproduced in a second set of measurements, while strong multiple scattering was found. Anomalies were observed for peak intensities in the strained sample during the second experiment at such temperatures. At the same time, no anomalies were observed in the thermal expansion that can be extracted from the lattice parameters.

While exciting, these results are somewhat difficult to draw together with other experimental studies of U_6Fe into a clear picture. The CDW draws inevitable parallels with α-U, especially considering the enhancement of T_{SC} with applied pressure. In α-U, however, the CDW formation shows clear signals in resistivity and specific heat measurements. For U_6Fe, transport and specific heat signals in the same temperature regions are very subtle compared to those seen in α-U.

At higher temperatures, a transition could not be clearly observed in our X-ray diffraction study, although we have detected a signal in specific heat as is

discussed in chapter 5. It is quite possible that a subtle change in the structure at high temperatures is the driving force for the CDW instability in the low temperature regime. Further studies are necessary to reach a more satisfactory conclusion with regards to this.

Chapter 5

Specific heat measurements of U_6Fe

5.1 Introduction

Chapter 4 describes two X-ray scattering experiments, the most important conclusion of which is the presence in U_6Fe of a Charge Density Wave (CDW) state below ∼10 K. During the first experiment, intensity at forbidden peak locations below 110 K suggested a change in structure at this temperature. This was cast into doubt during the second experiment by azimuthal scans which implied that this intensity was due to multiple scattering. In between the two experiments specific heat measurements, described in this chapter, were carried out that lend credence to the idea of a phase transition at 110 K.

In lay terms, as temperature drops and a low temperature structure starts to become energetically favourable, atoms will begin to vibrate between the low and high temperature positions. At low enough temperature, the vibrations die down and the atoms stabilise in their low temperature positions. More exactly, a phonon (lattice vibration) becomes soft (low in energy) at the transition temperature T_x if the phase transition is continuous. Mean Field Theory (MFT) predicts that for such a transition, there will be a jump in the heat capacity at T_x [77]. Additionally, if a phonon softens with temperature, this also should have consequences for the measured specific heat, which is dependent on the phonon energy levels. It was based on this reasoning that specific heat measurements were carried out on the same samples that were studied by X-ray scattering, to look for further evidence of a ∼110 K transition.

In addition, it was hoped that some evidence of the low temperature structural transition observed in the X-ray diffraction data at T_{CDW} might be seen in the specific heat data. The satellite peaks observed suggest a periodic modulation of the electronic structure, as in a CDW. As described in chapter 1, this results in a gap at the Fermi surface. Such a change in the electronic energy structure will affect the electronic specific heat. Also, it is clear that the lattice symmetry is broken at low temperatures. This is shown by the intensity seen at the $(9, 0, 1)$ family forbidden peak positions and their satellites, which cannot be attributed to multiple scattering in the CDW state (see chapter 4). A CDW is usually accompanied by a Periodic Lattice Distortion (PLD), which this symmetry breaking could be related to. A distortion of the lattice should result in features in the phonon specific heat as described above. For comparison, it is useful to consider what is observed for the case of α-U. This material shows three transitions associated with the CDW state below 43 K. Single crystal studies show different types of features in the specific heat which suggest that some of the transitions are purely electrical while others involve the lattice as well [48]. Only one of the transitions shows an obvious jump in the underlying trend of the specific heat.

The low-temperature ($T < 35$ K) heat capacity of U_6Fe (as well some other U_6X compounds) was previously studied by Yang *et al.* [14]. They fitted the data using a polynomial approach which should be valid in a narrow temperature region above T_{SC}, also employing a phonon moment analysis which fitted a simplified phonon Density of States (DoS) to the data. This DoS predicted a significant weighting for low energy excitations in U_6Fe. There were no clear kinks or other features in the specific heat data, however.

Evidence for change in the energy of phonons with temperature was presented by Renker *et al.* [53], Kimball *et al.* [4] and Lemon *et al.* [52]. Renker *et al.* studied the generalised phonon DoS using inelastic neutron scattering, noting a shift of spectral weight from excitations at $\sim$9 meV at room temperature to low energies at 6 K, implying that some softening of phonons had occurred between the high and low temperature dataset. Kimball *et al.* studied the ^{57}Fe Mössbauer effect in U_6Fe, observing a step in the absorption at $\sim$100 K that suggests hardening of the Fe phonons. They also observed a change in the Mössbauer shift which suggests the opposite, but attributed this instead to a change in valence of the

Fe atoms. Lemon *et al.* also studied the ^{57}Fe Mössbauer effect, but did not see the same evidence for a transition at ∼100 K. Conversely, they noted a change at ∼170 K in the absorption only, corresponding to the softening of Fe phonons at low temperature. Kimball *et al.* also studied the powder neutron diffraction of U_6Fe [4] and observed a minimum in the mean squared displacement of the Fe atoms along the *c*-axis at ∼100 K. Based on this they drew the conclusion that a static distortion of the Fe atoms sets in below ∼100 K.

5.1.1 Theory of specific heat

The constant-volume specific heat c_v of a sample is defined as the rate of change of its internal energy density u with temperature T:

$$c_v = \left.\frac{\partial u}{\partial T}\right|_V , \tag{5.1}$$

where V is the volume of the sample. c_v is made up of contributions from electronic excitations $c_{v,\mathrm{el}}$ and from phonon excitations $c_{v,\mathrm{ph}}$. At low temperatures, the statistics of quantum mechanics define the occupation of excitation energies, and thus define c_v. Fermi-Dirac statistics describe electronic energy level occupation, which results in $c_{v,\mathrm{el}} \propto T$, while phonons obey Bose-Einstein (BE) statistics, leading to $c_{v,\mathrm{ph}} \propto T^3$. Therefore, at high temperatures, the contribution to the specific heat from phonons is dominant. As $T \to \infty$, c_v will approach the value $3k_B$ (where is k_B Boltzmann's constant) per atom. This is the value originally found empirically by Dulong and Petit in 1819, and which can be derived by a classical approach that neglects the quantum mechanical BE statistics. For one mole of U_6Fe, there are seven atoms in the formula, resulting in a Dulong and Petit limit of $7 \times 3k_B \times N_A = 176.4$ J/mol K (specific heat per mole of formula).

The Debye and Einstein approximations

The quantum mechanical derivation of the temperature dependence of $c_{v,\mathrm{ph}}$ proceeds as follows: the internal energy of a sample due to phonons is given by:

$$u = \frac{1}{V}\sum_{s,\vec{k}} \hbar\omega_s(\vec{k}) \left[n_s(\vec{k}) + \frac{1}{2} \right] \tag{5.2}$$

where $\hbar$ is Planck's constant, and $\omega_s(\vec{k})$ is the angular frequency of a phonon with wavevector $\vec{k}$ in the s^{th} band. The function $n_s(\vec{k})$ is the BE distribution:

$$n_s(\vec{k}) = \frac{1}{e^{\beta\hbar\omega_s(\vec{k})} - 1} \tag{5.3}$$

where $\beta = (k_B T)^{-1}$. Further evaluation of c_v requires a sensible approximation for the phonon dispersion $\omega_s(\vec{k})$.

The most frequently used approximation for this is the Debye model. This assumes three identical linear bands. These extend out to k_D in k-space, so as to be equivalent to $3 \times N_D$ bands of extent k_D/N_D (see Fig. 5.1). The slope of the bands is parameterised by the Debye temperature Θ_D. The specific heat in the Debye model is given by:

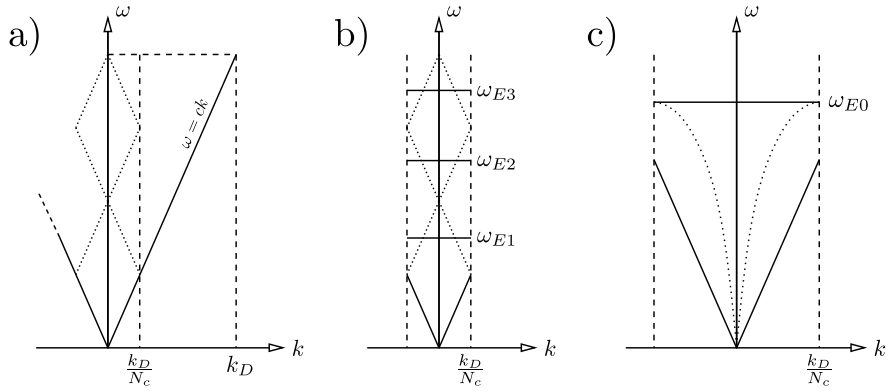

Figure 5.1: Diagram showing the phonon dispersion curves assumed by various different models. a) Dispersion curves under the Debye model. Three equal linear modes extending out to a cutoff k_D are assumed, equivalent to having N_D linear modes out to cutoffs k_D/N_D. b) Modified Debye model replacing the optic modes with flat Einstein modes of varying frequency. c) A phonon softening model where an Einstein mode is allowed to relax in energy at the $k = 0$ point, turning from an optic to an acoustic mode.

$$c_v^D = \frac{9N_D k_B}{V}\left(\frac{T}{\Theta_D}\right)^3 \int_0^{\Theta_D/T} \frac{x^4 e^x}{(e^x - 1)^2}. \tag{5.4}$$

An alternative to having linear modes described by one parameter is to replace the optical bands (those where $\omega \neq 0$ at $k = 0$) by flat bands. This is illustrated in Fig. 5.1b), labelling the frequency of the m^{th} band by ω_{Em}. This is the Einstein model. The specific heat resulting from N_E flat optical mode with frequency ω_E

is given by [32]:

$$c_v^E = \frac{N_E k_B}{V} \frac{(\beta\hbar\omega_E)^2 e^{\beta\hbar\omega_E}}{\left(e^{\beta\hbar\omega_E} - 1\right)^2}. \tag{5.5}$$

There will be three phonon modes for each atom in the cell, corresponding to three directions of motion. Three modes per unit cell will be acoustic modes. Therefore, as there are 28 atoms in the unit cell, there should be 81 optic modes. We will use the Debye model to simulate the acoustic modes and assume that the optic modes can be modelled accurately by the Einstein model.

Mean Field Theory

Landau's theory of second order phase transitions is a general but powerful MFT method to describe the changes to thermodynamic properties due to changes in the ground state energy close to a continuous phase transition. The fundamental principle is that in this scenario the minimum of the Landau free energy density F defines the equilibrium state of a system. This can be modelled by a simple polynomial:

$$F = -ax^2 + bx^4. \tag{5.6}$$

In the above equation, x is the order parameter that defines the state of the system. Above the transition, the order parameter is zero, and the equilibrium energy is zero. Below the phase transition, the free energy decreases due to the squared term outweighing the quartic term, and the position of the new minima correspond to the order parameter becoming nonzero. The simplest way to model this is with a squared term that grows with decreasing temperature in the form $a = a_0(T_x - T)$ below T_x, and is zero above T_x. The specific heat below the transition is then:

$$c_v = -T\frac{\partial^2 F_m in}{\partial T^2} = \frac{T a_0^2}{b}. \tag{5.7}$$

Above T_x the free energy is independent of T, so that $c_v = 0$. Therefore there will be a jump in c_v at the position of a structural transition. Note that Landau theory describes changes to the underlying ground state energy, whereas phonons are excitations above the ground state, so these models contribute to different parts of the specific heat.

5.2 Method and results

A Physical Property Measurement System (PPMS), manufactured by Quantum Design, was used to measure the heat capacity for several single-crystal samples of U_6Fe. The samples chosen were cut from the second Solid State Electrotransport (SSE) treated sample discussed in chapter 2, and were the same samples prepared for X-ray scattering measurements (as detailed in chapter 4) that showed the CDW satellite peaks at low temperature.

Samples prepared for measurement in this PPMS are mounted onto a puck. The puck consists of a small sample platform coupled to the rest of the puck by eight gold wires which establish a calibrated thermal connection. The sample should be well connected to the platform thermally to minimise the uncertainty in the data, and this is ensured by attaching the sample with cryogenic grease. The heat capacity of the puck with grease only on the sample platform is measured prior to the sample measurement (this data is called the "addenda"), and then removed as background to obtain that of the sample only. The specific heat calculated by this equipment is more accurately the specific heat at constant applied pressure c_p, as the sample is free to thermally expand or contract. c_v and c_p are usually very close for metals below room temperature, however, so that $c_v = c_p$ is a reasonable approximation to make [32].

The PPMS calculates the heat capacity of samples attached by applying a pulse of heat to the sample stage and fitting an exponential dependence to the sample stage temperature. This fitting yields characteristic time constants, which can be used to calculate the thermal conductivity of the grease, as well as the sample heat capacity, assuming the sample platform heat capacity is already known [78]. For a sample that is well thermally coupled by the grease to the sample platform, only one time constant is required. This occurs if the thermal conductivity due to the grease is much greater than the thermal conductivity of the gold wires. For some of the measurements of U_6Fe described here, the coupling was not good enough for the data to be described by one time constant, requiring the use of two. The curves obtained during this experiment all fit the expected exponential form. Fitting of the curves by hand yields time constants that, when used to calculate specific heats, give values that fall within 2% of the values found by the PPMS software.

Additionally, for a few measurements in the range $110-130$ K, data was taken in a range where the addenda was not calibrated prior to the measurement. The addenda was estimated by smooth interpolation using the neighbouring points, and the sample c_v was then calculated using the formulae given in [78]. This method is only slightly more involved than simply subtracting the interpolated addenda c_v from the total c_v, but is the method that the PPMS generally employs to calculate the c_v originating from the sample. Therefore, this method was employed for consistency with the sample c_v values otherwise calculated by the PPMS.

Initially, one sample of mass 8.13 mg was used. The heat capacity measured was significantly less than that of the addenda, resulting in a large uncertainty and noise in the signal, as shown in Fig. 5.2. To combat this, two samples were used with a combined weight of 16.72 mg in the following run. Subsequently, the c_v of a third sample of mass 34.58 mg was also measured.

The PPMS can be configured to take several measurements of c_v at each temperature setpoint, in order to reduce the uncertainty by averaging. Most of the datasets collected took two measurements at each temperature setpoint. A systematic error was apparent from the data, because the first value of c_v measured at each temperature setpoint was always lower than the second. One dataset captured using three measurements per setpoint showed that a third measurement finds c_v higher than the second measurement. This systematic error is most apparent in the data around 100 K, as shown in Fig. 5.3. Despite this, there is a clear break in the trend of c_v *versus* T in the data shown in Fig. 5.3, at a temperature of around $108-110$ K. The significance of this will be discussed later in this chapter.

The measured trend of heat capacity with temperature for $0-300$ K (the 16.72 mg data) is shown in Fig. 5.4. This figure also shows the low-temperature data illustrating the jump in c_v at the superconducting transition temperature T_{SC}. Previously published data [3, 14] are also plotted, illustrating that the samples measured here show an exceptionally clean transition of high T_{SC}, as is also the case with the resistive transition seen in these samples (see Fig. 2.14). As noted by Yang *et al.* [14], the specific heat has a T^2 dependence in the temperature range $T_{\mathrm{SC}} < T < 20$ K.

Fig. 5.5 shows the (16.72 mg) data in the temperature range close to

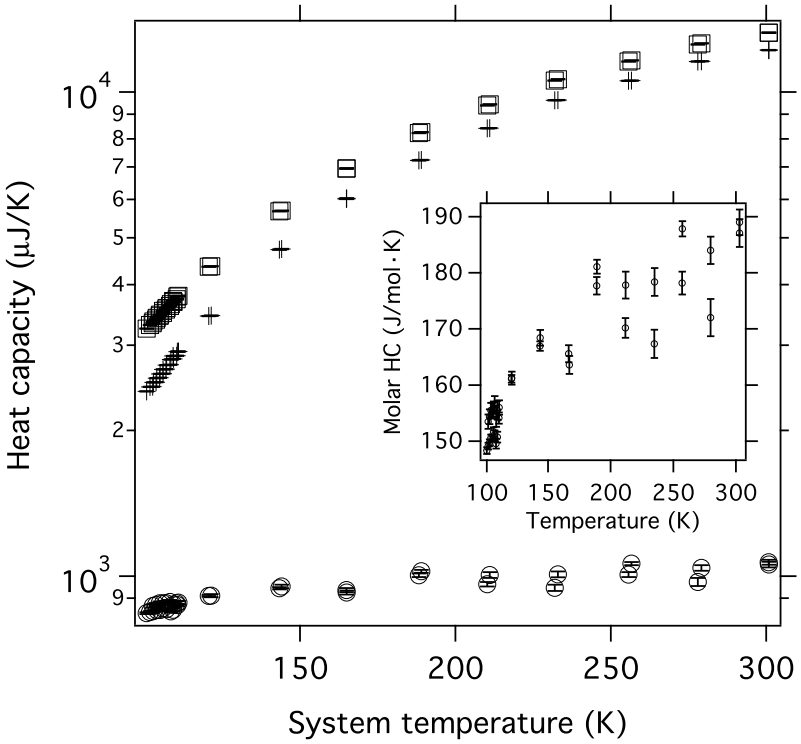

Figure 5.2: Diagram showing the raw heat capacity C_v data using one 8mg sample. Squares show the total C, crosses show the expected background C_v, and circles show the sample C_v. The signal is very small compared to the background at high temperatures and there is a large scatter in the data with the background subtracted.

T_{CDW} plotted as c_v/T *versus* T^2, measured using two samples of combined mass 16.72 mg. The electronic coefficient of specific heat can be estimated by fitting a linear function to the c_v/T *versus* T^2 data in a narrow range above T_{SC} as shown in this figure. The value obtained by this method (0.154 ± 0.025 J/Mol K^2) is within 3 mJ/mol K^2 of the value quoted by [14], therefore we expect that a similar electronic effective mass can be concluded from our measurements.

In the region below T_{CDW}, which is expanded in Fig. 5.6, it can be seen that there is a kink in the data. Taking the derivative of c_v shows the temperature of the change in slope at ∼8.5 K. This kink could perhaps be a broad peak similar to the peaks observed in α-U [48] that are associated with a CDW.

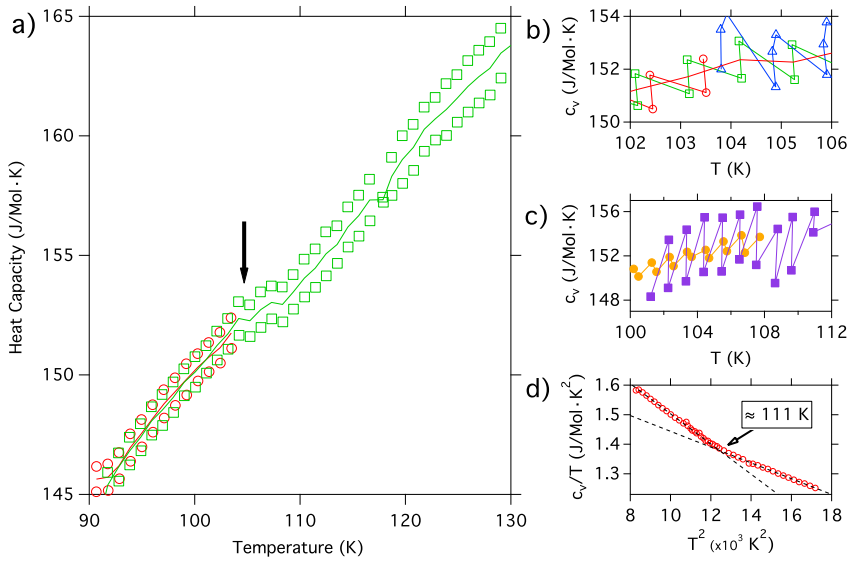

Figure 5.3: Diagram showing the molar heat capacity c_v *versus* temperature T in the region of ∼110 K. a) Several captured datasets using two samples of total mass 16.72 mg. The solid lines show the data after averaging at every temperature setpoint. There is a clear feature in the vicinity of $108 - 110$ K, as indicated by the arrow. b) Datasets in the same region, enlarged. All three datasets shown are taken using sequences in which the temperature setpoint is increasing with time. c) As with b), but with setpoint temperature falling with time. Note that for both cases, the first measured value of c_v is lower than subsequent readings. Also note that for the dataset in b) that used three repetitions per setpoint (blue triangles), the third point is closer to the value of the second point than the second is to the first. The filled purple squares in c) represent a dataset using only one sample of mass 8.13 mg. d) c_v/T *versus* T^2 for the specific heat data over this range, using the averaged datapoints. The curve shows a clear kink in the region of the anomaly seen in a).

5.3 Analysis

We will now discuss how the data can be modelled. The general form of the data can be reasonably well fitted (with some exceptions as will be described below) by a phonon model of 3 acoustic Debye modes and 81 optic Einstein modes. These were initially modelled by 1 Debye temperature and 27 Einstein frequencies, giving 28 modes each weighted 3× to give the same total c_v. The Einstein frequencies were observed to form two broad groups, so a second model was applied which used 3 Einstein modes with $3\times, 39\times, 39\times$ weightings. This

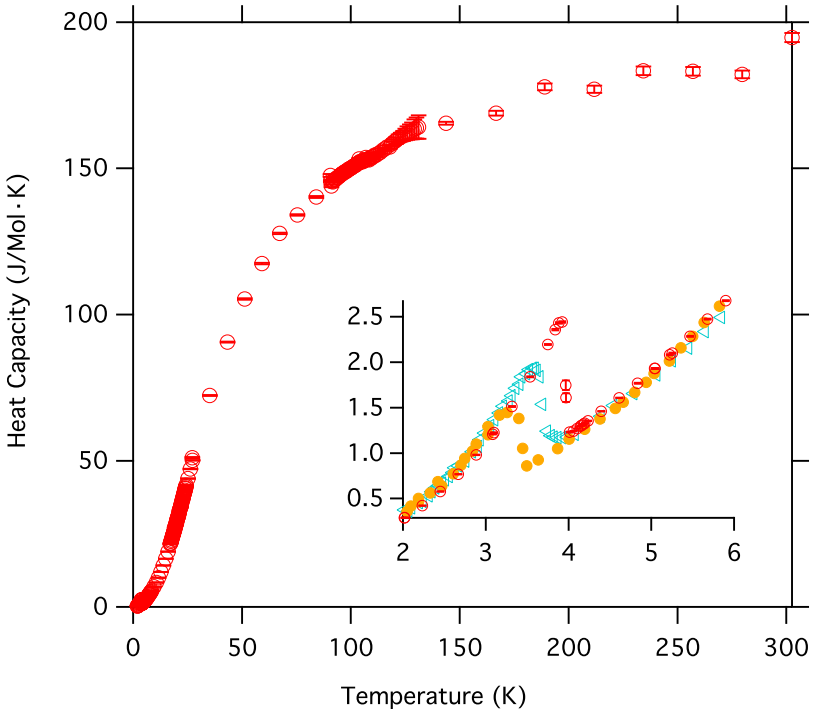

Figure 5.4: Diagram showing the trend of the molar heat capacity c_v *versus* temperature T, measured using two samples of combined mass 16.72 mg. Main figure: c_v *versus* T in the range $T = 0 - 300$ K. Inset: the low temperature behaviour of HC, near to the superconducting transition. The red hollow circles show the measured data. The blue triangles and orange filled circles show the data of Yang *et al.* [14] and DeLong *et al.* [3] respectively.

is in reasonable agreement with the generalised phonon DoS found by Renker *et al.* [53], which is peaked at two energies that closely correspond to the two most heavily weighted Einstein frequencies that our data fits to.

At 300 K, the measured specific heat exceeds the Dulong-Petit limit of 176.4 J/mol K by about 20 J/mol K. This discrepancy can be accounted for by assuming a high-temperature Schottky anomaly, which could be due to crystal field splitting of uranium electron levels. For a singlet splitting, the extra molar specific heat contributed due to an energy gap Δ is [79]:

$$c_v = 6k_B N_A \left(\frac{\Delta}{T}\right)^2 \frac{e^{\Delta/T}}{(1+e^{\Delta/T})^2}. \tag{5.8}$$

In the above equation, the numerical prefactor reflects a contribution from each of the 6 U atoms in the formula unit. The predicted specific heat can match

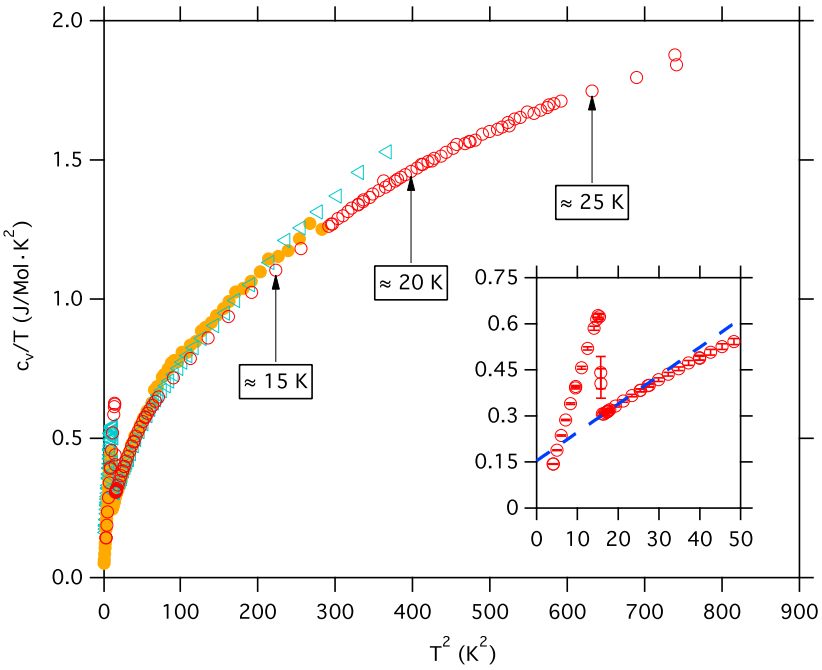

Figure 5.5: Diagram showing c_v/T *versus* T^2 in the range $T = 0 - 30$ K. The red hollow circles show the measured data. The blue triangles and orange filled circles show the data of Yang *et al.* [14] and DeLong *et al.* [3] respectively. Inset: The measured data at low temperature, fitted using a linear curve (blue dashed line). This fit predicts the coefficient of the electronic specific heat γ to be 0.154 ± 0.025 J/Mol K^2

the observed level if Δ is assumed to be of the order of 900 K. For a splitting with higher degeneracy, Δ must be larger in order to obtain a sound fit to the data.

5.3.1 110 K features

As already mentioned briefly, near to 110 K two important features are seen in the specific heat. There is a small dip in c_v above ∼105 K (Fig. 5.3), and a broad peak above ∼113 K (Fig. 5.4). This is corroborating evidence for the structural transition observed in X-ray scattering data at similar temperatures (as reported in chapter 4).

As discussed in the introductory sections of this chapter, MFT predicts that there will be a step in the heat capacity at the transition temperature T_x. The data most likely shows such a feature, but one that is significantly broadened by

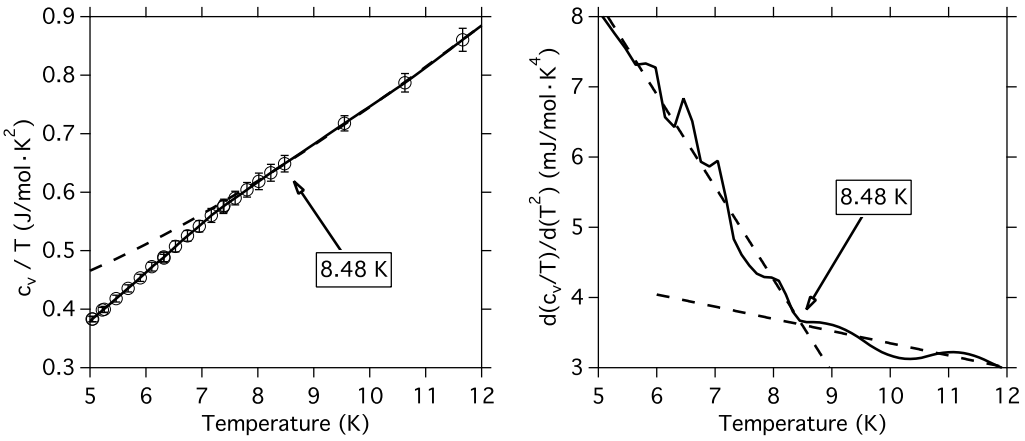

Figure 5.6: Diagram showing the kink in c_v/T *versus* temperature T, and its temperature derivative. The circles show data taken using two samples of total mass 16.72 mg. The dashed lines are linear fits to the data either side of the transition. The position of this kink roughly matches the temperature of the charge density wave transition seen in X-ray scattering measurements.

Θ_D (K)	Θ_{E1} (K)	Θ_{E2} (K)	Θ_{E3} (K)	Δ_S (K)
31.3	34.4	90.6	186.8	861.6

Table 5.1: Parameters obtained by fitting the specific heat data obtained using two samples of total mass 16.72 mg to the model described in the text. The model uses a total of 84 phonon modes: 3 Debye modes of energy $k_B\Theta_D$, 3 Einstein modes of energy $k_B\Theta_{E1}$, 39 Einstein modes of energy $k_B\Theta_{E2}$, and 39 Einstein modes of energy $k_B\Theta_{E3}$.

defects and thermal fluctuations, which can locally change the energy required to excite the system across the transition. The data can be fitted in a limited region close to the transition reasonably well, using the parameters from the Debye-Einstein-Schottky fit discussed so far, plus a linear term as predicted from MFT. However, above 113 K it is difficult to model the data in this way because the gradient is much too steep for any Debye or Einstein fit.

In order to fit the steep data in the region just above T_x, it is necessary to add phonon softening effects. Phonon softening adds a contribution to c_v through a combination of contributions to $\partial\omega/\partial T$ and $\partial n/\partial T$. We have modelled the phonon softening by allowing one of the Einstein modes to drop in energy at the centre, as shown in Fig. 5.1. We have assumed a quadratic dispersion:

$$\omega(k) = \omega_E - \alpha(T)(k - k_{\max})^2 \tag{5.9}$$

where $k_{\max}$ is the band edge and $\alpha(T)$ parameterises the amount of softening at $k = 0$. $\alpha(T)$ was modelled as following a hyperbolic tangent dependence. Using the combination of the Debye-Einstein-Schottky fit with the MFT step and a phonon softening model gives a predicted c_v that agrees well with the data, as shown in Fig. 5.7.

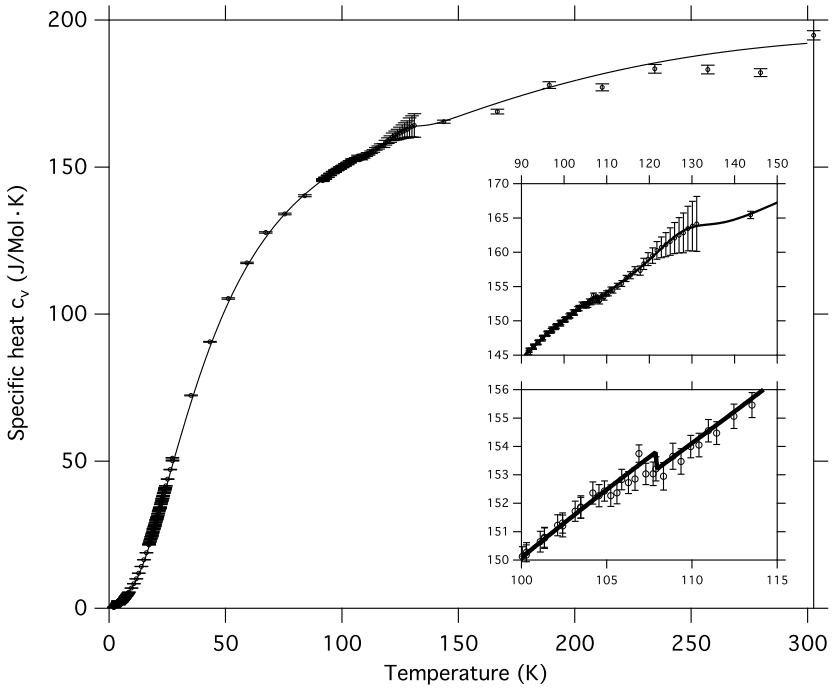

Figure 5.7: Diagram showing the molar heat capacity c_v *versus* temperature T. The circles show data taken using two samples of total mass 16.72 mg. The solid curve shows the fit to the data described in the text. Inset: enlarged plots showing the same data, showing the step predicted by mean field theory and the broad peak (due to phonon softening).

5.3.2 Charge Density Wave

The kink in the data at around 8.5 K is close to the temperature that we expect for the CDW transition. This feature can be taken as further evidence for the occurrence of a CDW in U_6Fe. As mentioned, the kink could also perhaps be a very broad peak on a smooth background. In the case of the CDW transitions observed in α-U, the lowest temperature transition shows a step in the underlying trend that is masked by a peak [48]. For the data presented here, if the kink

corresponds to a broad peak, then it is much too broad to quantify if there is such a step in the underlying trend. A step could be explained by a sudden change in the DoS at the Fermi surface, which is consistent with a CDW state that removes part of the Fermi surface.

A peak with or without the extra step will lead to a slight underestimate of the electronic specific heat coefficient. This will in turn lead to an underestimate of the electronic effective mass. However, based on the data shown in Fig. 5.5, it is difficult to predict the severity of this effect, as the feature at ∼8.5 K is quite broad.

5.3.3 Superconducting transition

The superconducting transition in these samples is exceptionally sharp. According to Bardeen Cooper Schrieffer (BCS) theory, the temperature dependence of the specific heat below T_{SC} should follow the form:

$$c_v = Ae^{-B/T} + \beta T^3 + \alpha T^5. \tag{5.10}$$

In the above equation, the α and β terms come from the contribution of phonons which should be the same above and below the transition. Above T_{SC}, the exponential term is replaced by a linear term $\gamma^* T$ due to the normal state contribution of the electrons to the specific heat. For unconventional superconductors (those with a non s-wave order parameter which therefore have points in k-space where the Fermi surface is not gapped) the exponential dependence is replaced by a power law dependence ($c_v \propto T^n$, where n is a variable of the fit) [80]. Fig. 5.8 show fits to the data from $2-4.4$ K using both functions. The values for α and β were obtained from fits of the specific heat in the range $4-4.4$ K, using the value of $\gamma = 0.154 \pm 0.025$ J/Mol K^2 found as described earlier. The exponential and power law fit give similar quality fits to the data. Lower temperature measurements of the specific heat are necessary in order to eliminate one of these possibilities.

The requirement of entropy balance can be checked by examining the area under curves of c_v/T *versus* T. The entropy excess of the superconducting state over the normal state at high temperatures must balance its deficit at low temperatures. This is illustrated by Fig. 5.8 to be approximately the case for the

exponential superconducting state fit.

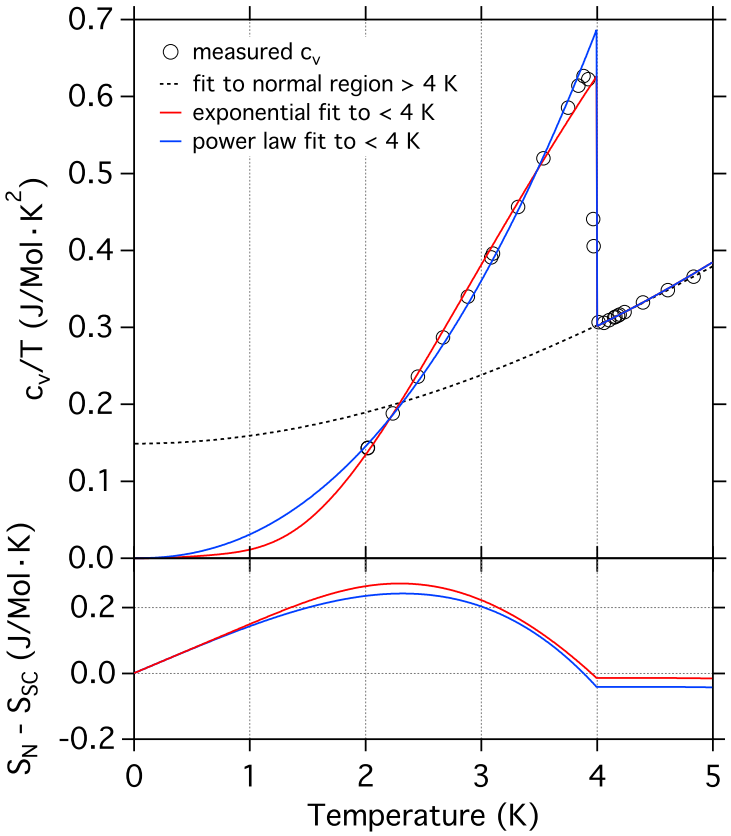

Figure 5.8: Diagram showing the molar heat capacity over temperature c_v/T *versus* temperature T in the superconducting region. The circles show data taken using two samples of total mass 16.72 mg. The blue curve shows a fit to the data in the range $2 - 4.4$ K using a power law fit. The red curve shows a fit to an exponential dependence over the same range. These fits are described in more detail in the text. Lower plot: difference in the normal and superconducting state entropies (S_N and S_{SC} respectively). These were calculated using the correspondingly-coloured curves shown in the upper plot.

5.4 Conclusions

Specific heat measurements of SSE-treated samples of U_6Fe have been carried out. The measurements show exceptionally clean superconducting transitions, although it is not possible to determine if the trend of c_v *versus* T below T_{SC} follows a power law or exponential dependence.

A step in c_v is observed at around 110 K. This feature is a clear indicator of a high temperature transition that is not seen in resistivity studies. Evidence for further low-temperature transitions was also observed in the form of a kink or possibly a broad peak at ∼8.5 K. This feature could be attributed to the transition of the sample to the CDW state, which occurs at similar temperatures as documented in chapter 4.

The general trend of $c_v(T)$ can be well fitted by a Debye-Einstein model with a Schottky anomaly at high temperatures. The transition at 110 K can be incorporated in to this by fitting by a simple phonon softening model with a mean field theory step at ∼108 K. This model implies a large degree of phonon softening occurs below 130 K. From the model used, it seems that the soft phonons do not significantly harden again at low temperature.

Chapter 6

High-Pressure Studies of U_6Fe

6.1 Introduction

It is recorded in the literature that the superconducting transition temperature T_{SC} of U_6Fe is enhanced with applied pressures up to 2 GPa [2]. Pressure enhancement of T_{SC} is also observed in α-U where it is explained by the Charge Density Wave (CDW) state [45]. This state "competes" with the superconducting state but is suppressed by applied pressure (as shown by the reduction of T_{CDW}). Because creation of the CDW state removes or gaps part of the Fermi surface, its suppression makes available extra Fermi surface to the superconducting state (neglecting the effects of any change to the Fermi surface with pressure). From Bardeen Cooper Schrieffer (BCS) theory, T_{SC} is enhanced by a larger density of states at the Fermi surface, therefore T_{SC} rises when the CDW state is suppressed.

We have observed satellite peaks in X-ray scattering measurements that suggest that U_6Fe also exhibits CDW ordering below $T_{CDW} \approx 10$ K (see chapter 4). The transition temperature T_{CDW} roughly corresponds to the temperature at which $d\rho/dT$ goes through a maximum and $\rho(T)$ enters the T^2 regime. This behaviour also bears a resemblance to that seen in $\rho(T)$ of α-U near the CDW onset transition at 43 K. For low quality (Residual Resistivity Ratio (RRR) of 13) samples, 43 K corresponds to a maximum in $d\rho/dT$. For higher quality samples, a bump in $\rho(T)$ becomes apparent [47].

The presence of a CDW in U_6Fe implies that there could be significant Fermi surface nesting or strong electron-phonon coupling, because such properties are

what usually make a system susceptible to formation of CDWs. It is quite likely that the suppression of the CDW with applied pressure (assuming this is the cause of the observed enhancement of T_{SC}) corresponds to a decrease in the severity of these properties, for example there could be a change in the Fermi surface that breaks the nesting condition. Even so, it is uncertain based on the documented evidence exactly how these properties will change. Additionally, it is of significance that some of the properties that favour the formation of the CDW also favour the formation of the Fulde-Ferrell-Larkin-Ovchinnikov (FFLO) state in a system. If the CDW was suppressed, and does leave large nested Fermi surfaces to be gapped by superconductivity, one could easily expect the FFLO state to emerge instead.

It is therefore of interest to us to study the properties of U_6Fe under applied pressure in more detail. We are primarily interested to see if the superconducting state shows any evidence of the FFLO formation when the CDW state is suppressed. We chose to look for evidence of the FFLO formation in the shape of the $H_{c2}(T)$ curves at applied pressures: an FFLO state is predicted to result in unusual, kinked $H_{c2}(T)$ curves. These investigations initially studied the shape of $H_{c2}(T)$ by AC Susceptibility (ACS) measurements, and later by the four-probe resistive method. As part of the latter study we also measured the temperature dependence of the resistivity between room temperature and T_{SC}.

6.2 High-Pressure AC Susceptibility of U_6Fe

A Czochralski-pulled single crystal sample of U_6Fe (RRR approximately 4) was cut for ACS measurements of the superconducting transition under pressure. The sample used was a thin plate perpendicular the to a-axis, of sides 150 μm. Measurements were carried out on the sample inside a plastic Diamond Anvil Cell (DAC), which was inserted into a Magnetic Property Measurement System (MPMS) (supplied by Quantum Design). The measurements were performed by M Misek. The plastic DAC is designed to have a minimised magnetic response, but some is still present and must be compensated for by calibration when the cell is empty. It should be possible to simply subtract the background signal from the data with the sample inside the cell. As shown in Fig. 6.1, the background signal has an unusual field dependence, and the magnetisation from sample and

cell at low applied fields of 1 T is below the level of the background, suggesting a diamagnetic response from the sample. A diamagnetic response from the sample might be expected due to the skin effect if the applied AC field has a high frequency, however the driving frequency was 37 Hz which is reasonably low, and the offset is not observed in zero field. The empty cell measurements as a function of field at 2 K are shown in Fig. 6.1c). An offset of the curve with field is not understood and might be hysteretic. We will therefore not attempt to interpret the normal state signal, but instead focus on the superconducting transition which can still be seen clearly from the data. Fig. 6.2 shows the sample susceptibility that can be estimated after subtraction of the background trend and an assumed flat background, with the sample in the cell at pseudoambient pressures (*i.e.* the cell is closed but not pressurised).

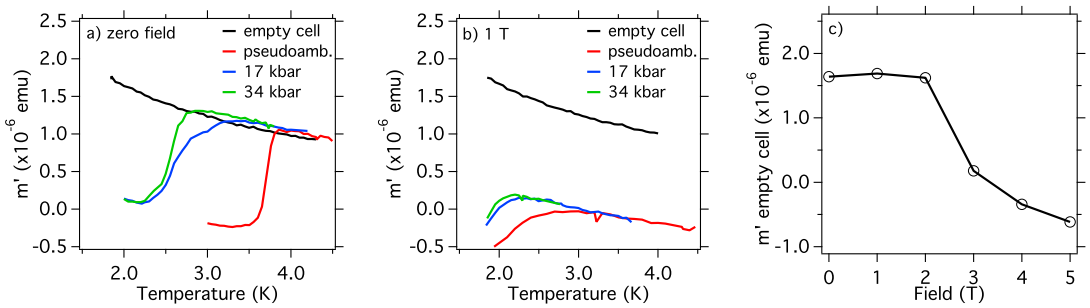

Figure 6.1: Magnetisation response of the cell and sample. a) AC magnetisation of the empty cell, and cell with sample of U_6Fe, at zero field. b) AC magnetisation of the empty cell, and cell with sample of U_6Fe, at 1 T. c) AC magnetisation of the empty cell at various applied fields at 2 K. There is apparently a significant diamagnetic signal from the sample at applied field as shown in b). This could be due to a spurious background signal reading: the response of the cell to applied fields in c) is unexpected.

The expected superconducting transition appears to move in temperature to lower temperatures at the first application of field, and then to increase again slightly. The transition temperature is defined as shown in Figs. 6.2 and 6.3, by linearly extrapolating the steepest gradient to intercept the shallow gradient from the normal temperature region (as shown by the dashed lines). At high fields, the transition is truncated due to the lower limit on the MPMS temperature range. Therefore T_{SC} cannot be accurately determined at high field by this method. Fig. 6.3 shows the signal from 17 kbar and 34 kbar for the same sample in the cell.

Several problems with this method of measuring $H_{c2}(T)$ are apparent from

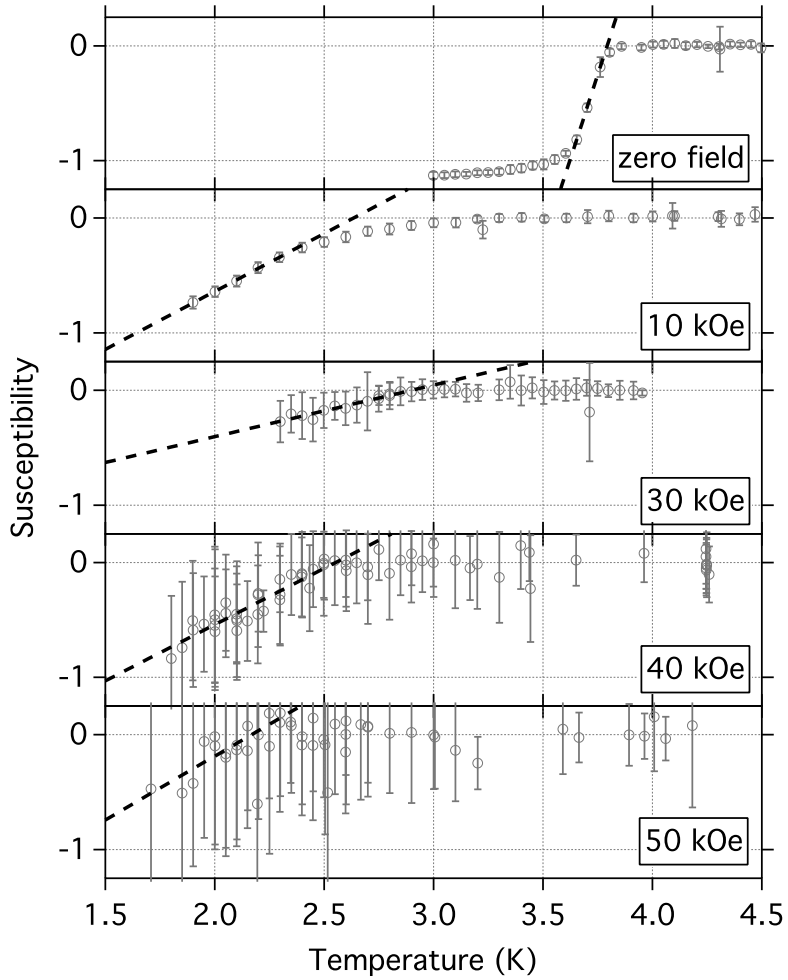

Figure 6.2: The superconducting transition as observed by the AC susceptibility method in a plastic diamond anvil cell, with the cell only just closed, and applied fields as indicated.

the data. One significant issue is the lower limit on the temperature range of approximately 2 K; data for temperatures lower than this can only be predicted by extrapolation. There is also potentially some uncertainty with respect to how well the thermometry performs, because the temperature is measured by the MPMS away from the cell. The sample must thermalise to the surroundings through the cell.

The apparent suppression of T_{SC} at low fields can be explained by weak pinning of the vortex lattice to impurity sites. When the pinning is weak then an applied field results in the movement of the flux lattice lines in and out of the sample,

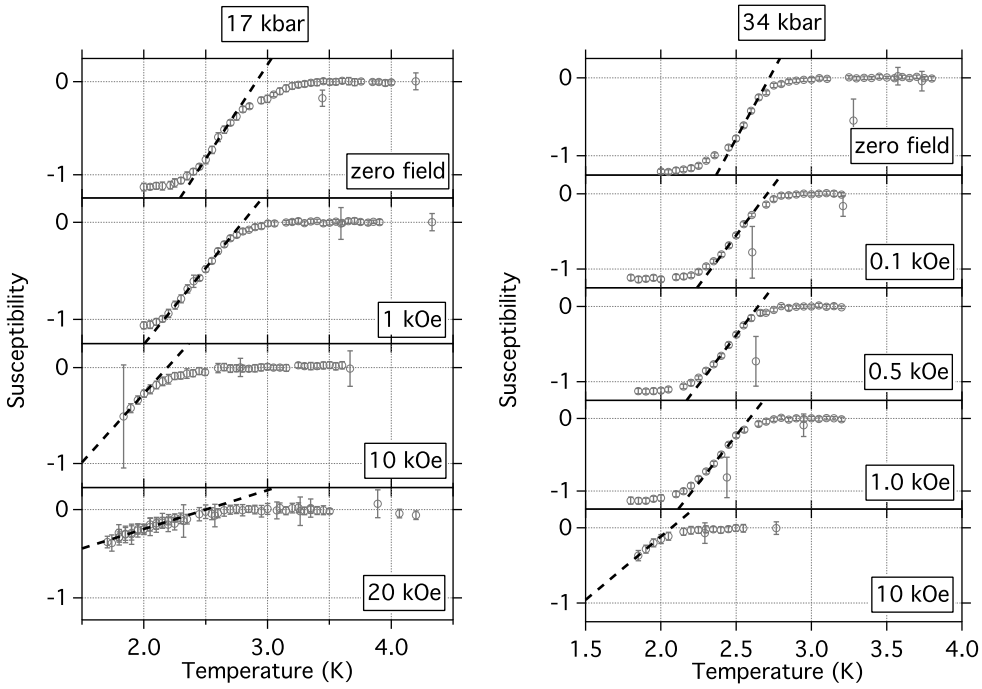

Figure 6.3: The superconducting transition as observed by the AC susceptibility method in a plastic diamond anvil cell, at an applied pressures of 17 kbar and 34 kbar, and applied fields as indicated.

and the response from the sample does not appear diamagnetic. This is what is observed most clearly in our pseudoambient, 10 kOe data. This behaviour is observed in other materials, and it is typical that at higher applied fields the flux lattice is more strongly pinned, so that a diamagnetic response is seen again. This is what is seen in the pseudoambient data at higher fields. As a result of the weak pinning of the vortex lattice, then, it is harder to quantify the shape of the $H_{c2}(T)$ curve by ACS measurements. In an attempt to avoid this issue, subsequent high pressure measurements of $H_{c2}(T)$ were performed by resistive methods.

Fig. 6.4 shows the phase diagram as suggested by Fig. 6.2 and 6.3. Using the data for applied field $H < 2$ T suggests misleadingly that the value of $H_{c2}(T = 0)$ is much lower than measured at ambient pressure by resistive methods ($H_{c2} \sim$ 10 T). This can be understood as due to weak pinning as explained above. Ignoring the 1 T data point for the pseudoambient dataset, $T_{\rm SC}\ dH_{c2}/dT|_{T_{\rm SC}} \sim$ 12.7 T, which is comparable to what is found from resistively determined $H_{c2}(T)$ curves.

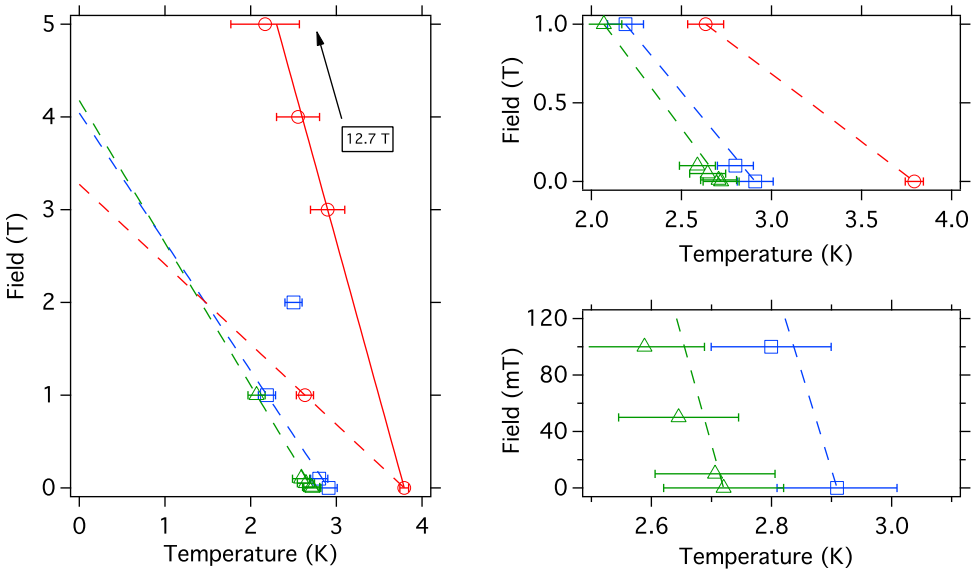

Figure 6.4: The $H_{c2}(T)$ curve as predicted from Figs. 6.2 and 6.3. Red circles, blue squares, and green triangles show the pseudoambient, 17 kbar, and 34 kbar pressure data points respectively, that correspond to the onset of diamagnetic behaviour as shown in Figs. 6.2 and 6.3. The dashed lines show the extrapolated $H_{c2}(T)$ curve based on the datapoints at 0 and 1 T. The red solid line shows the the extrapolated pseudoambient $H_{c2}(T)$ curve based on the datapoints at 0 and 3 T.

It is perhaps interesting to note that the gradient dH_{c2}/dT obtained from the 0 and 1 T datasets, shown by the dashed lines in Fig. 6.4, varies with applied pressure. Under the model explained above, a shallower gradient suggests weaker pinning. Therefore the data suggests that the flux line lattice is better pinned by defects at applied pressures, which suggests that either pressure is putting defects into the sample, or the coupling of the flux line lattice to the defects is strengthening. Since $H_{c2}(T)$ is expected to reduce as T_{SC} reduces, however, datasets taken at the same applied field are measured at different values of $H/H_{c2}(0)$, and this itself could explain the apparent change in the weak pinning behaviour. This will be discussed further later in this chapter.

6.3 High-Pressure Resistivity of U_6Fe

The pinning of the vortex lattice by defects is necessary to give a superconducting response in resistivity measurements, as it is in the ACS measurements described above. The data presented so far illustrates how weak pinning can result in misleading transitions as the flux lattice overcomes the pinning and the sample shows a nearer to normal state response to an applied field. For a resistivity measurement, the applied field equivalent is an applied current, and the corresponding forces on the flux line lattices are orders magnitude smaller. The normal state response is observed in such measurements if the applied current density j exceeds a critical value j_c, one strong enough to cause the vortices to move. j_c usually decays to zero near T_{SC}, but in certain superconductors j_c is peaked close to T_{SC} (a phenomenon known as the peak effect [81]). This peak is more severe at higher applied fields. This effect makes it possible to measure the $H_{c2}(T)$ curve with less uncertainty, because the maximum current that may be applied while superconducting is higher.

6.3.1 Sample and cell preparation

A 800 μm-culet DAC was prepared for four-wire resistivity measurements of a single crystal sample of U_6Fe. The sample (RRR approximately 7.5 along the c-axis) was cut from a rod that had been Czochralksi-grown and SSE-treated, as described in chapter 2. The orientation of the sample was such that current was applied along the a-axis, while applied field is along the a-axis at 90° to the current. The type of cell used is shown in Fig. 6.5. The steel gasket was indented to 100 μm, and insulated with a mixture made from Stycast and alumina powder in a ratio of approximately 1:1 by weight to prevent shorting of the wires across the gasket. The 300 μm hole where the sample was placed was made by spark erosion of the uninsulated gasket. The hole in the insulation was made using a high-powered laser, and filled with Daphne oil as a pressure transmission fluid. Fig. 6.6 shows the sample in the gasket hole with the wires attached. In this figure, there is a small piece of ruby in the hole also, for measuring the cell pressure by standard methods. The 25 μm wires are positioned over small cut pieces of gold foil, which are 10 μm thick.

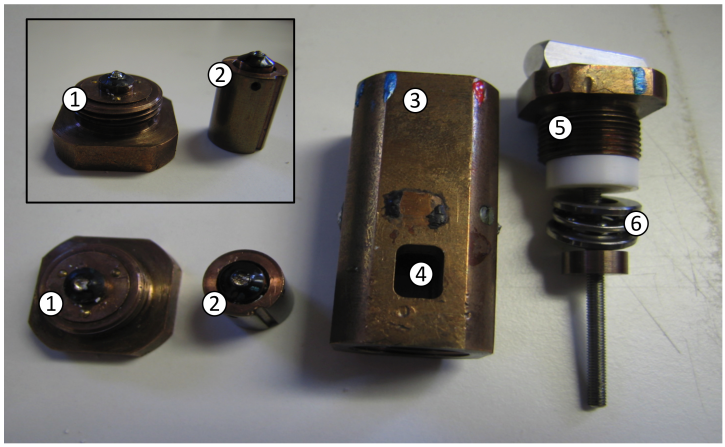

Figure 6.5: Photos showing the style of cell used. Various parts are labelled as follows: 1) bottom diamond seat 2) top diamond seat 3) cel outer housing 4) windows to insert current/voltage wires 5) compression bolt 6) bearings. In assembly, first the bottom seat was prepared with the sample and gasket, then the cell housing was screwed on top and the wires passed through the windows. Finally the top seat was inserted, and moved into place using the compression bolt. The bearings allow the bolt to turn while the top seat does not rotate.

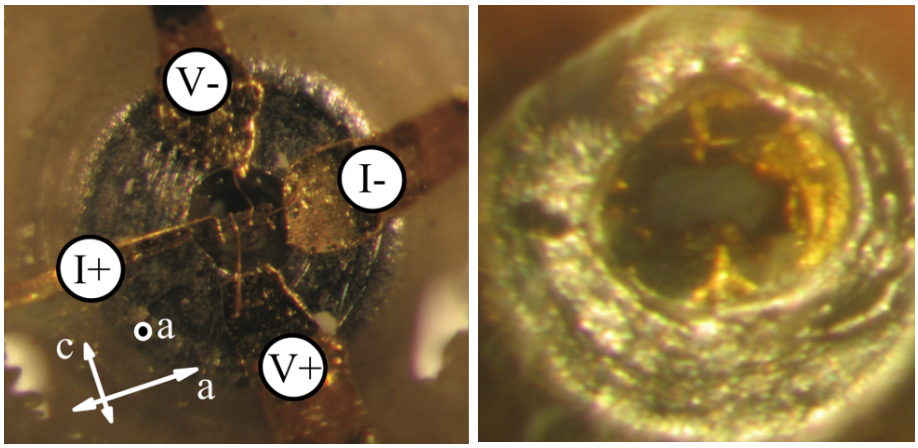

Figure 6.6: Images of the sample inside the cell. a) Image prior to closing the cell. The cut sample can be seen with wires attached and I and V contacts labelled. A small piece of ruby is also present in the cell. The 25μm wires are positioned over gold foil pads of thickness 10μm. The sample orientation is a as indicated in the figure, with the current applied along the sample a-axis. Field was applied perpendicular to this figure, along the a-axis 90° to the current. b) Image taken through the diamonds while the cell pressure was 7.6 GPa. This image is taken from the reverse side of the cell. As such, the contacts are mirrored from a).

6.3.2 Measurement methods

The pressure cell was inserted into different cryostats for the $300 - 2$ K and $4 - 0.05$ K datasets. The low temperature measurements were carried out in a dilution refrigerator in which the $H_{c2}(T)$ curve was mapped out. The high temperature measurements used a 2 K, 9 T Closed Cycle Refrigerator (CCR). As mentioned, the pressure was measured at room temperature using the standard ruby fluorescence technique [82]. The ruby used was chipped from a larger piece, another fragment of which was kept for ambient pressure calibration of the cell ruby fluorescence shift.

We measured the pressure between measurements, *i.e.* before and after each thermal cycle. The change in pressure after a cycle was small ($\sim$ 0.2 GPa) for low pressures, but for the highest pressures was significant. For example an initial pressure of 8.68 GPa dropped to 7.94 GPa after the first two thermal cycles ($300-2$ K, repeated to improve signal to noise) and then dropped to 7.6 GPa after the final cycle ($300-0.05$ K). A ruby reader exists for reading the pressure at low temperature, but cannot be used to measure a clean signal with the type of cell used for these measurements. We therefore have no way to measure the pressure while the cell is cold, but we expect that the pressure will not change dramatically with temperature. For presentation of the following data, the uncertainty in the pressure is taken from the difference in pressure after the thermal cycle. High temperature ($300-2$ K) measurements were done at 1.3 ± 0.1, 2.9 ± 0.1, 4.9 ± 0.1, 6.3 ± 0.2, and 8.3 ± 0.4 GPa, low temperature ($4 - 0.05$ K) measurements were done at 1.2 ± 0.1, 3.0 ± 0.1, 4.8 ± 0.1, 6.0 ± 0.1, and 7.8 ± 0.2 GPa. Measurements were also taken at pseudo-ambient pressures.

At the lowest applied pressures we encountered difficulties because our sample became shorted to ground somewhere inside the cell. When using the usual measurement method we could not then detect the expected shape of the superconducting transition. This was worked around somewhat by a floating current input, however the voltage signal did not drop to zero as expected for the non-shorted geometry. The shape of the transition at different applied pressures and at zero field is plotted in Fig. 6.7. The second and third transitions in the curves as shown were found to match the shape of the $H_{c2}(T)$ curve when mapped out at 1.2 GPa. We suggest that these shapes and the grounding issue can be explained if two of the wires (a current and voltage wire) are shorted

on the sample or *via* the gasket. The measurement then includes some contact resistance which will have an Ohmic response (*i.e.* the extra resistance is not normally superconducting). The unusual features in the curves could be due to induced superconductivity in this contact resistance.

Because the superconducting signal is not accompanied by a drop to zero voltage, it would be misleading to use the midpoint of the transition as a definition of H_{c2} or $T_{\rm SC}$. Therefore we have used the onset of the transition, determined in the same way as with the ACS data, by extrapolating from the position of steepest gradient and from the flat gradient in the normal state. We should note that there is some broadening also of the transition, which is quite sharp for ambient pressure measurements. This could imply non-uniformity in the sample pressure, and could mean that the fall off in $T_{\rm SC}$ and H_{c2} at the highest pressures is steeper than we present here.

6.3.3 Results

Fig. 6.8 show the trend of the resistivity between room temperature and 2 K at different pressures. At ambient pressure the curve is very smooth with a T^2 trend setting in at temperatures below ~ 8 K. At applied pressures of 1.3 GPa a very broad maximum in the resistivity curve becomes apparent. This maximum persists at higher applied pressures up to 6.5 GPa, and we have plotted its temperature dependence with pressure in Fig. 6.9. At 8.3 GPa a feature is still apparent at temperatures roughly corresponding to the maximum in the 6.3 GPa data. There is an extreme pressure dependence of the resistivity, especially at room temperature where the drop in resistivity with pressure is apparently by two orders of magnitude. The ambient temperature resistivity at the highest pressure is 1.4 $\mu\Omega$ cm, less than that of Cu (1.56 $\mu\Omega$ cm) under ambient conditions. This is very surprising if true.

Most of these unexpected trends are most likely not attributable to the same grounding issues that give us features below $T_{\rm SC}$, since the contact resistance is a small fraction of the low T resistance and is assumed not to have a strong T dependence.

At ambient pressures, the the maximum in the derivative $d\rho/dT$ at $T_D \sim 11$ K roughly corresponds to the onset with temperature of the CDW state observed in X-ray scattering experiments (chapter 4). This is close to the temperature at

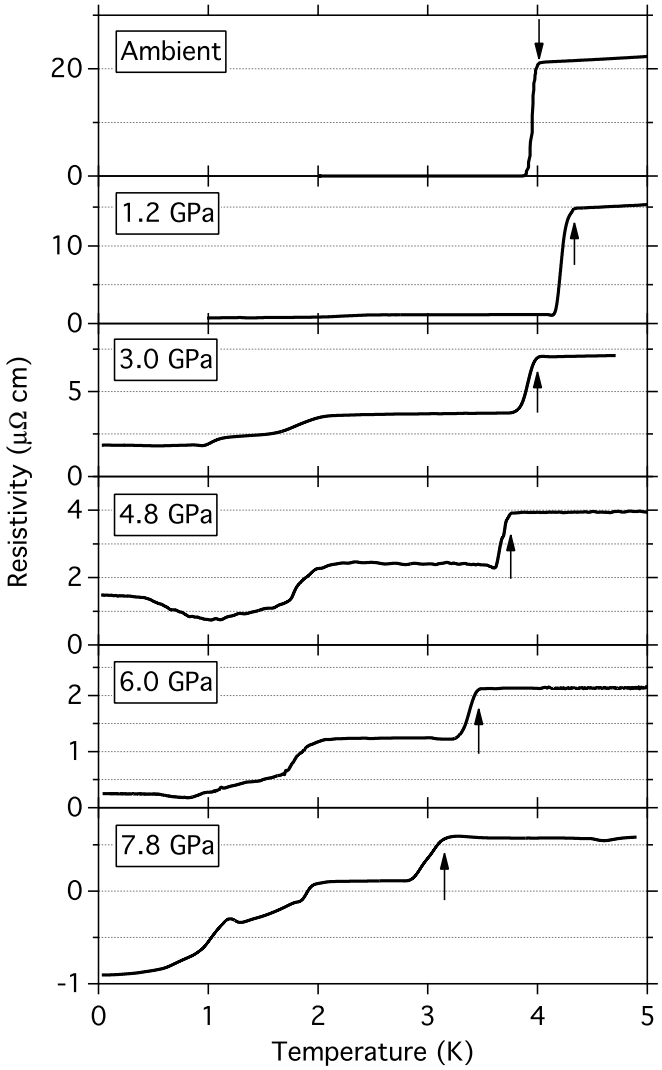

Figure 6.7: Figure showing the effect of pressure on the trend of the resistivity in U_6Fe along the a-axis in the range $0 - 5$ K. These curves are interpolated from the raw datasets. Arrows show the position of T_{SC} interpreted from the data.

which the resistivity begins to show T^2 behaviour, which we label T^*. Fig. 6.9 shows the values of T_D and T^* at different pressures. There is a slight minimum in T_D at 1 GPa, but no such feature is clear for T^* (although this temperature is harder to estimate from the data). At the highest applied pressures, T_D and T^* seem to move to much higher temperatures.

Fig. 6.10 shows the change in the $H_{c2}(T)$ curve with applied pressure. For

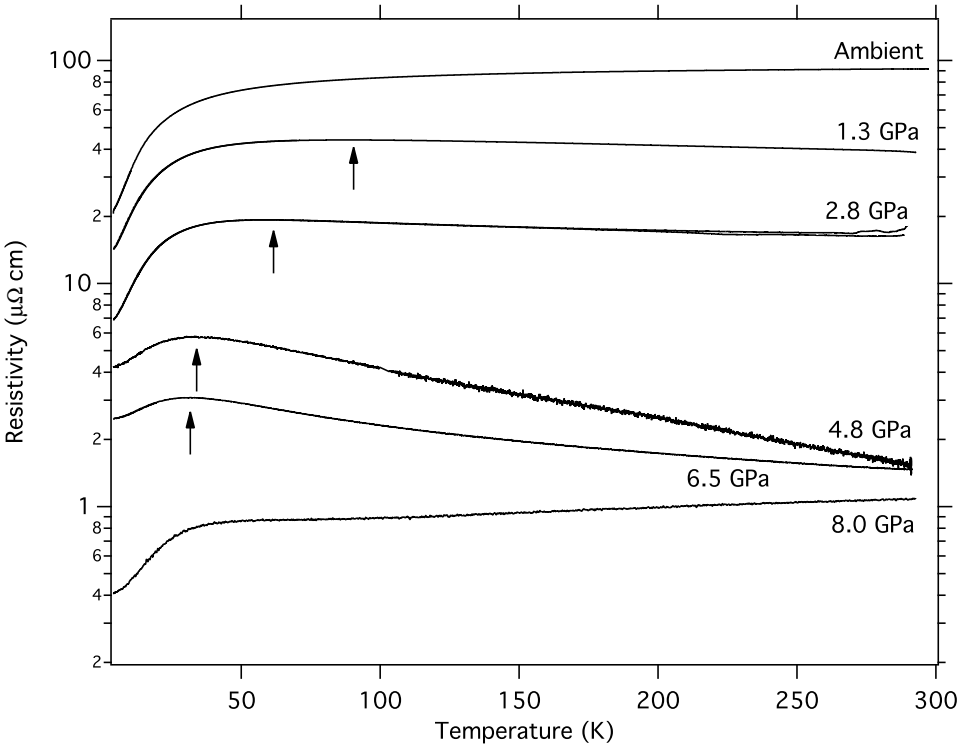

Figure 6.8: Figure showing the effect of pressure on the trend of the resistivity in U_6Fe along the a-axis in the range $300 - 2$ K. The maximum in $\rho(T)$ is marked with an arrow for the curves in which it is seen.

$P \geq 1.3$ GPa, the $H_{c2}(T)$ curve was obtained entirely from measurements taken inside the dilution refrigerator. For the ambient pressure data measurements we encountered problems with the thermal coupling within the dilution fridge for $T < 2$ K that was resolved in subsequent measurements. For the ambient pressure data shown in Fig. 6.10 the data above 2 K was taken with the 2 K, 9 T CCR. This is why there is a break in the data points.

For the ambient pressure data, the thermometer was bolted to the cold finger, to which the cell was connected by a Cu bracket. For subsequent measurements at pressure the thermal coupling was improved by bolting the thermometer (which was changed to one with a larger calibration range) directly onto the base of the cell, close to the sample. At applied field the temperature was read from the mixing chamber thermometer, converted to the cell temperature using a zero-field calibration curve that was obtained as part of each pressure dataset. This was

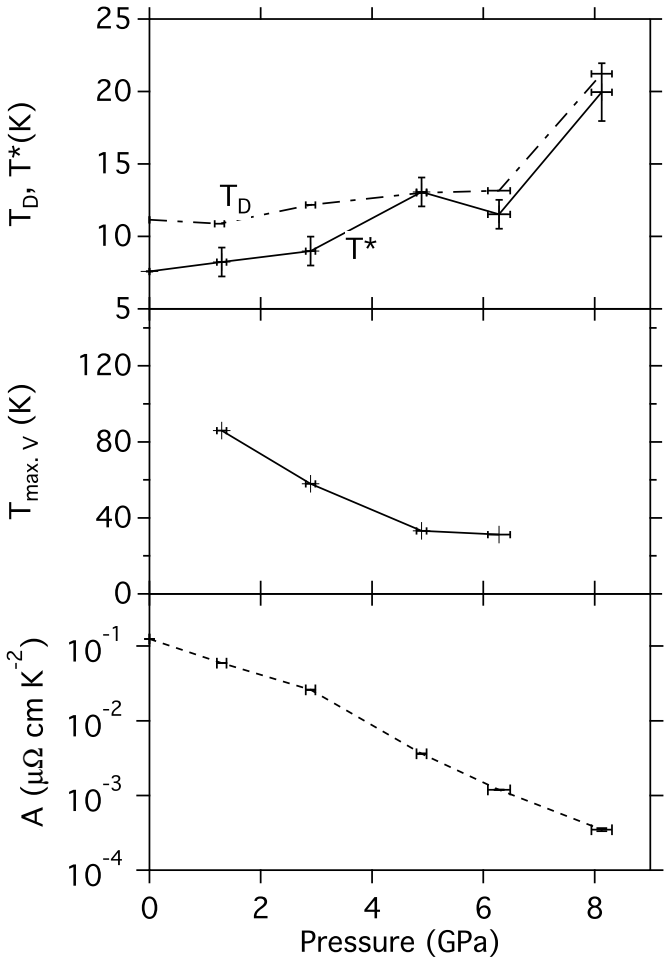

Figure 6.9: Figure showing the effect of pressure on various properties of the resistivity. T^* is the temperature below which the resistance follows a T^2 behaviour (solid curve, top plot), and T_D is the temperature at which the temperature derivative of the resistivity goes through a maximum (dot-dashed curve, top plot). $T_{\mathrm{max.}\ V}$ is the temperature at which the resistance goes through a maximum. A is the coefficient of the T^2 term for the T^2 region of the resistivity curve.

necessary to obtain an accurate temperature reading because the cell thermometer shows a large amount of magnetoresistance that is not calibrated. We used $SrTiO_3$ capacitors to check the amount of field heating and found that this was not a significant issue for our setup, except at the very lowest temperatures ≤ 50 mK.

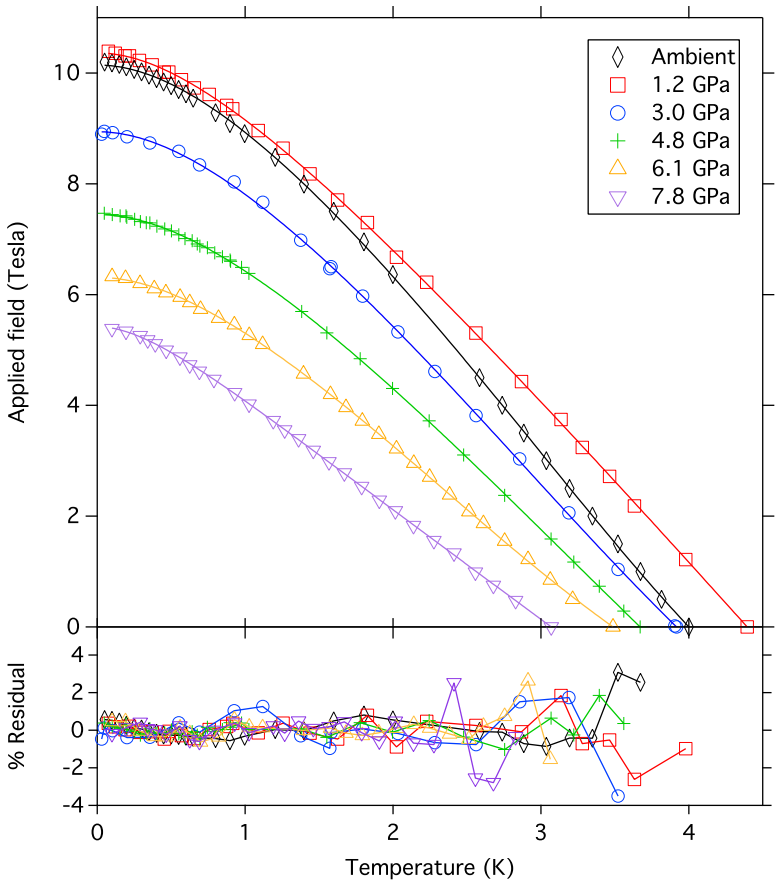

Figure 6.10: Figure showing the effect of pressure on the $H_{c2}(T)$ curve, as measured by resistivity in a diamond anvil cell. For the ambient pressure data, the higher temperature data was obtained in a closed cycle refrigerator, while the low temperature data was obtained using a dilution refrigerator. Upper plot: the measured data points found from the onset point of the superconducting transition. The solid curves show fits found using the dirty limit two band model of [15] described in the text. Lower plot: Percentage residuals found from the fits shown in the upper plot.

6.4 Discussion

6.4.1 High temperature resistivity

The high temperature resistivity curves show a surprising amount of interesting behaviour, especially compared to the extremely smooth nature of the ambient pressure resistivity curves. Of course, it should be taken into consideration that as mentioned, these measurements were carried out in non-ideal conditions where

not all of the signal may originate from the sample. It is certainly tempting to speculate regardless that the maximum of $\rho(T)$ that emerges at 1.2 GPa and moves to lower temperatures could be related to the features seen in heat capacity and X-ray scattering data in the region of 110 K at ambient pressure - extrapolation of the trend of the maximum with pressure to ambient pressure suggests that it will trend towards $\sim 110 - 130$ K. A signal in resistivity at such a temperature and at ambient pressures has been reported in the literature before for polycrystals [3], but we have not observed it in any of our single crystal studies. This is true even in our highest quality single crystal samples which have an RRR almost equivalent to that of the sample in which the feature was measured.

Alternatively, the behaviour of $\rho(T)$ at applied pressures is quite reminiscent of features caused by the Kondo effect. This effect increases the resistance at low temperatures because the magnetic interaction between the conduction electrons and their environment is enhanced. The temperature below which these interactions saturate is the Kondo temperature T_K, above this temperature $d\rho/dT$ is negative. The sites that the conduction electrons magnetically interact with will begin to interact with each other below a coherence temperature $T_{\mathrm{coh,K}}$. A $d\rho/dT \propto T$ dependence occurs below this coherence temperature. If $T_{\mathrm{coh,K}}$ coincide then the crossover from $d\rho/dT \propto T$ to $d\rho/dT < 0$ results in a maximum of $\rho(T)$. The emergence of a maximum in our data suggests that another source of scattering (which presumably masks the Kondo maximum at ambient pressure) is suppressed with pressure. This scattering could potentially be related to electron-phonon scattering and the overall reduction in ρ across the whole temperature range. A reduction in electron-phonon scattering fits with the idea that a CDW is suppressed with pressure as the stability of the CDW state is linked to the electron-phonon coupling strength.

6.4.2 Effect of pressure on vortex pinning

As discussed previously, the ACS data suggests a large suppression of T_{SC} with relatively low applied fields ~ 1 T. This can be explained by the movement of the flux line lattice under applied fields, resulting in a subtler superconducting response from the sample. The movement of the flux line lattice also has an effect on the superconducting transition as detected by resistivity measurements, but

this is reduced as the forces are less. At high fields, the peak effect adds reliability to the measurement of $H_{c2}(T)$. We observed the impact of weak pinning on the $H_{c2}(T)$ curve at ambient pressures (see Fig. 6.11). Weak pinning causes an apparent dip in $H_{c2}(T)$ at low fields, and at high fields the expected shape returns due to the peak effect. Reducing the applied current reduces the range over which the dip is apparent. We have used an applied current of 0.1 mA for our measurements which reduces the weak pinning effects to a reasonable degree while preserving signal amplitude.

We did not observe a noticeable increase in the severity of the dip in $H_{c2}(T)$ close to T_{SC} as pressure was increased. Earlier it was noted that the $H_{c2}(T)$ curves that can be extracted from the ACS data may imply that pinning is enhanced at higher pressures, although the data is rather limited. Stronger pinning implies more defects as these are the pinning centres for the vortex lattice, and an increase in pinning centres leads to an increase in pinning strength. This is at odds with the general decrease in the resistivity, which implies that there is less scattering of electrons from defects. Therefore it is unwise to draw too many conclusions based on the $H_{c2}(T)$ curves that the ACS data suggests.

6.4.3 Pressure dependence of T_{SC} and $H_{c2}(0)$

The ACS and resistivity data are clearly at odds with each other with regards to the change of T_{SC} with applied pressure. The ACS data (which is admittedly quite limited to be extracting a trend) suggests only a suppression of T_{SC} without any apparent increase. On the other hand the resistivity data shows a noticeable increase in T_{SC} at 1.2 GPa. Even neglecting this datapoint, the reduction of T_{SC} above this pressure is significantly more gradual than found in the ACS study. H_{c2} shows a maximum also, but this is not so pronounced as the maximum in T_{SC}. The reduction of H_{c2} with applied pressure is much more severe than the reduction of T_{SC}. These results are summarised in Fig. 6.12. The reason for this could be the improved sample quality between the two measurements.

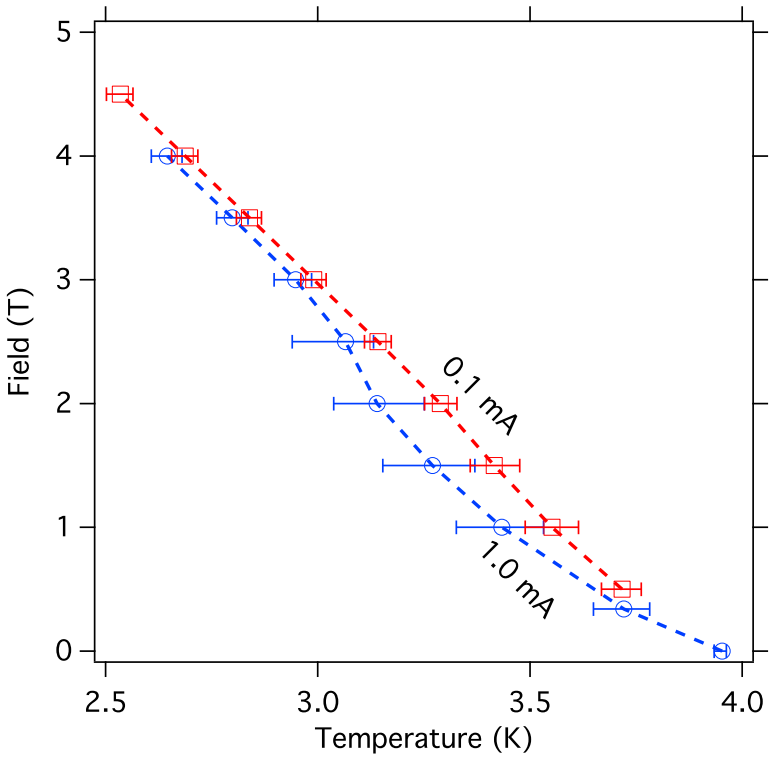

Figure 6.11: Figure showing the pseudoambient results for the $H_{C2}(T)$ curve at 1 mA (blue curve) and 0.1 mA (red curve). The error bars indicate the temperatures at which the resistivity was at 25% and 75% of the normal-state value (*i.e.* they indicate the transition widths). Weak pinning allows flux lines to move, which causes a dip in the $H_{c2}(T)$ curve near to T_{SC}. This effect is reduced by a reduced applied current as shown. At high fields the movement of flux lines is prevented by the peak effect phenomenon.

6.4.4 $H_{c2}(T)$ curve shape and further discussion of the superconducting state in U_6Fe

The general shape of the $H_{c2}(T)$ curves presented in Fig. 6.10 show no unusual kinks or curvature. Such behaviour is observed dramatically in some other materials such as Th-doped UBe_{13}, for example [83]. Even if the shape does not look unusual, however, the value of the zero-temperature reduced field $h(0) = H_{c2}(0)/(dH_{c2}/dT|_{T_{\mathrm{SC}}}T_{\mathrm{SC}})$ clearly exceeds the BCS values for both the clean and dirty limits (0.72 and 0.69 respectively [28]): the values for this are presented in Table 6.1. This means it is impossible for the standard Werthamer, Helfand and Hohenberg (WHH) model [6, 28] (from which these numbers can be

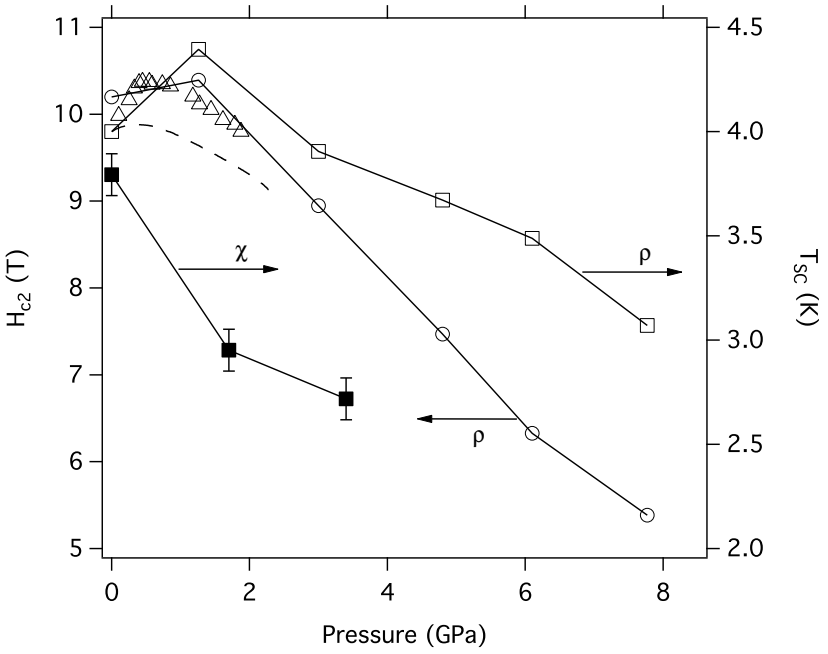

Figure 6.12: Plot of the change in $H_{c2}(T = 0)$ and $T_{\rm SC}$ with applied pressure. The empty circles and squares indicate $H_{c2}(0)$ and $T_{\rm SC}$ as measured by the resistive method. The filled squares represent the $T_{\rm SC}$ measured using ACS in a SQUID magnetometer and a plastic cell. The triangles and dashed line represents the $T_{\rm SC}$ data presented in [2]. For this data, the triangles represent higher quality samples of RRR= 9.

derived) to fit the data very well. This was already true in the ambient pressure case, but we note that there appears to be a minimum in the value of $h(0)$ at around 4.8 GPa. At the highest pressure of 7.9 GPa there is an unusual and almost linear shape to the curve, which exceeds the WHH curve in an even more dramatic fashion than the ambient pressure curve.

Before we discuss the possible models to explain this behaviour, we should consider whether our samples are in the clean or dirty limit. The defining length scales are the mean free path ℓ and the coherence length ξ. For $\xi \gg \ell$ the sample is in the clean limit, for $\xi \ll \ell$ the sample is in the dirty limit. We are able to use the resistivity to estimate the value of ℓ, using the Drude model formula [32] for the resistivity ρ:

$$\rho = \frac{m^*}{ne^2\tau}, \tag{6.1}$$

where n is the number of charge carriers, e is the electron charge, τ is the time

P (GPa)	$T_{\rm SC}$ (K)	$H_{c2}(0)$ (T)	$T_{\rm SC}\left.\frac{dH_{c2}}{dT}\right\|_{T_{\rm SC}}$ (T)	ξ_{GL} (Å)	$h(0)$	$\frac{H_{c2}(0)}{H_P}$
0	4	10.19	12.72	51	0.80	1.39
1.2	4.40	10.39	12.76	51	0.81	1.28
3.0	3.92	8.95	11.28	54	0.79	1.25
4.8	3.67	7.47	9.55	59	0.78	1.11
6.9	3.49	6.33	7.50	66	0.84	0.99
7.9	3.07	5.38	6.06	74	0.89	0.95

Table 6.1: Parameters that define the $H_{c2}(T)$ curve at various pressures for U_6Fe, with field applied along the a-axis. $h(0)$ is the reduced field $\frac{H_{c2}(0)}{T_{\rm SC}\left.\frac{dH_{c2}}{dT}\right|_{T_{\rm SC}}}$. These parameters are derived from H_{c2} alone without reference to the normal state, and as such are safe from some of the uncertainty inherent in our normal state measurements.

between scattering events, and m^* is the effective electron mass. n and m^* must be estimated, which we will come to momentarily. For ρ, we use the value at $T_{\rm SC}$. We then predict ℓ using $\ell = v_F\tau$ where v_F is the Fermi velocity that can be estimated from the slope of the H_{c2} curves (the calculation of v_F is different in the clean and dirty limits). At ambient pressure the value of m^* and n can be estimated using the value of the electronic specific heat coefficient γ in the following formulae (which come from free electron theory [32]):

$$m^* = \sqrt{\frac{3\gamma\hbar^3}{k_B^2 v_F}} \tag{6.2}$$

$$n = \frac{\sqrt{3\gamma\hbar^3 v_F}}{\rho e^2 \ell k_B} \tag{6.3}$$

where k_B and $\hbar$ are the Boltzmann and Planck constants. These predicted values can then be applied to predict ℓ at pressure using Eq. 6.1. We have also investigated the values for ℓ at pressure that are calculated using the formula (which can be obtained by combining the above equations with $n = k_F^3/3\pi^2$ [32]):

$$\ell = \frac{\pi^2 k_B^2}{e^2 \rho v_F \gamma}. \tag{6.4}$$

In order to estimate γ at pressure we have used $\gamma \propto \sqrt{A}$ where A is the T^2 coefficient of ρ at low temperatures. The constant of proportionality is evaluated

P (GPa)	$\sqrt{A}$ ($10^{-3}\sqrt{\mu\Omega\text{cm}}$/K)	$\xi_{GL}T_{\text{SC}}\sqrt{A}$ (10^{-9})	ℓ_1^{clean} (Å)	ℓ_1^{dirty} (Å)	ℓ_2^{clean} (Å)	ℓ_2^{dirty} (Å)
0	352.2	7.15	92.9	29.7	92.9	29.7
1.2	243.5	5.43	152.2	38.0	182.3	74.6
3.0	161.2	3.40	298.7	54.9	605.8	336.9
4.8	60.2	1.30	495.2	73.8	2573.6	1766.6
6.9	34.5	0.79	906.3	105.8	7195.9	6301.1
7.9	18.6	0.42	5045.9	263.7	76847.0	150332.0

Table 6.2: Table showing the pressure dependence of various parameters, as described in the text, obtained from normal state measurements. ℓ_1 are calculated by using Eq. 6.1 and values of n and m^* calculated from ambient pressure data. ℓ_2 are calculated from Eq. 6.4 assuming that $\gamma \propto \sqrt{A}$. The conclusions for the parameters in this table may be affected by contacts touching.

at ambient pressure. Table 6.2 shows the values calculated by both methods.

We have estimated the Ginzburg-Landau coherence length ξ_{GL} using the formula [84]:

$$\xi_{GL} = \sqrt{\frac{\phi_0}{2\pi}\left(T_{\text{SC}}\left.\frac{dH_{c2}}{dT}\right|_{T_{\text{SC}}}\right)^{-1}} \tag{6.5}$$

where ϕ_0 is the flux quantum. The obtained values are presented in Table 6.1. ξ and ℓ are comparable length scales at ambient pressure, and the superconductivity appears to be borderline between clean and dirty limits. Under applied pressure ℓ grows because the normal state resistivity is dropping substantially. All estimates of ℓ suggest that the superconductivity is in the clean limit at high pressure.

The value of A is proportional to $(m^*)^2$ [32]. We should normally expect that the value of $\xi T_{\text{SC}}\sqrt{A}$ is approximately constant with pressure as $\xi T_{\text{SC}} \propto 1/m^*$ (this comes from the BCS expression for the Pippard coherence length $\xi_0 = 0.18\hbar v_F/k_B T_{\text{SC}}$ [84] and $m^* v_F = \hbar k_F$). We do not find this to be true, however, as is shown for the values in Table 6.2. The assumption inherent in this analysis is that the value of k_F, which enters into the expressions for both ξ and A, is constant with applied pressure. The pressure dependence in this supposedly constant value could therefore be explained by a change in the Fermi surface with pressure, which alters k_F.

We now return to considering the enhancement of the reduced field, and possible reasons for this. We will consider briefly two models that can explain

$H_{c2}(T)$ curves that exceed the orbital limit set by the WHH model. The first is the strong-coupling theory. In this model, the band values of properties such as v_F are renormalised depending on the electron-phonon interaction parameter λ_{ep} [85]:

$$\lambda_{ep} = 2\int_0^\infty \alpha^2(\omega)F(\omega)\omega^{-1}d\omega. \tag{6.6}$$

In the above equation we see that λ_{ep} depends on the phonon spectral function and coupling constant $\alpha(\omega)$. A formalism exists for calculating $H_{c2}(T)$ assuming a simple density of states that consists of a delta function at an excitation energy Ω: $\alpha^2(\omega)F(\omega) = (\lambda\Omega/2)\delta(\omega - \Omega)$ [16]. In this model the coupling reduces to a dependence on the parameters λ and Ω rather than the full spectral function shape. Bulaevskii *et al.* [16] present values for the reduced limiting field calculated from this equation in the case where the Pauli limiting field is ignored. Fig. 6.13 shows their calculated values reproduced. For the dirty limit, the reduced field is increased up to the value we obtain at 7.9 GPa for $\lambda \sim 4.5$. The authors note that positive curvature is predicted for $\lambda \sim 4$ in the dirty limit, but if there is positive curvature present in our data it is too subtle to detect within experimental error.

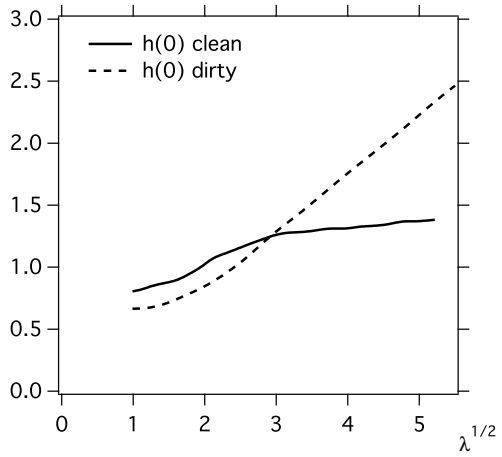

Figure 6.13: Effect of electron-phonon interaction λ on the reduced orbital critical field $h(0) = H_{c2}(T = 0)/(T_{\rm SC}\, dH_{c2}/dT|_{SC})$ (data reproduced from [16]). The curves for the clean and dirty limits are shown.

The second model which could be used to model the excessive $h(0)$ is multiple band superconductivity. As with the strong coupling model, this has been presented as a model to explain positive curvature in some superconductors.

Gurevich developed a remarkably simple model for two band superconductivity in the dirty limit to be applied to MgB_2 [15], which has subsequently been used to model the $H_{c2}(T)$ of many other superconductors (*e.g.* $LaFeAsO_{0.89}F_{0.11}$ [86]). This model gives the following formula that describes $H_{c2}(T)$:

$$a_0 \left[\ln t + U(h)\right]\left[\ln t + U(\eta h)\right] + a_2 \left[\ln t + U(\eta h)\right] + a_1 \left[\ln t + U(h)\right] = 0, \quad (6.7)$$

where a_0, a_1 and a_2 are defined by an electron-phonon coupling matrix L:

$$L = \begin{pmatrix} L_{11} & L_{12} \\ L_{21} & L_{22} \end{pmatrix} \quad (6.8)$$

$$a_1 = 1 + (L_{11} - L_{22})/\sqrt{(L_{11} - L_{22})^2 + 4L_{12}L_{21}} \quad (6.9)$$

$$a_2 = 1 - (L_{11} - L_{22})/\sqrt{(L_{11} - L_{22})^2 + 4L_{12}L_{21}} \quad (6.10)$$

$$a_0 = \frac{2(L_{11}L_{22} - L_{12}L_{21})}{\sqrt{(L_{11} - L_{22})^2 + 4L_{12}L_{21}}}. \quad (6.11)$$

The diagonal terms of L describe the intraband coupling strength and the off-diagonals describe the interband coupling strength. The function $U(x) = \Psi(1/2 + x) + \Psi(x)$ where $\Psi(x)$ is the digamma function. $h = H_{c2}D_1/2\phi_0 T$ where D_1 is the diffusion coefficient of the first band in the model and ϕ_0 is the flux quantum. We have assumed that $D_1 = \ell v_F/3$ where v_F is the Fermi velocity, using values for ℓ estimated from $\rho(T_{SC})$. η is the ratio of the diffusion coefficients of the two bands. An especially large or small η results in a kinked $H_{c2}(T)$ curve, while $\eta = 1$ reduces Eq. 6.7 to the form $\ln t + U(h) = 0$, which is identical to the WHH formula [6] for the case of $\alpha, \lambda \to 0$ (*i.e.* pure orbital limiting in the dirty limit). We have fitted our data to this simple model assuming $L_{12} = L_{21} = 1/2$, the same choice as [86]. We note that the fits are reproducible for different values of $L_{12} = L_{21}$, which changes the fitted values of the other variables. Clearly then this fit is insufficient for determining L and η from the data without further information about the nature of the bands involved, as noted by [86] for their data. Regardless, these two band fits produce a very good match to the $H_{c2}(T)$ trends observed experimentally, as shown in Fig. 6.10. The values of η, L_{11} and L_{22} found at the different pressures are presented in Fig. 6.14.

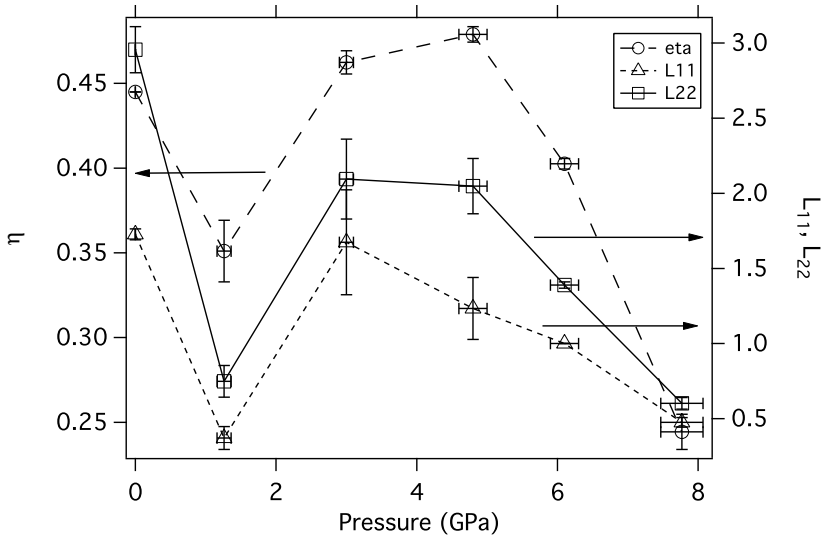

Figure 6.14: Fitting parameters for the two bands fits presented in Fig 6.10. η (circles) is the ratio between the diffusion coefficients for the two bands involved. L_{11} (triangles) and L_{22} (squares) are the intraband electron-phonon coupling strengths.

6.5 Conclusions

The superconducting and normal state properties of U_6Fe have been investigated under applied pressures up to approximately 8 GPa. The superconducting transition temperature T_{SC} goes through a maximum with pressure at around $P = 1$ GPa as measured resistively, and as previously reported [2]. This behaviour was not observed for the ACS measurements, which used a sample of slightly lower RRR. T_D, the temperature at which the trend of resistivity *versus* temperature goes from positive to negative curvature, dips slightly at the same pressure. This temperature roughly corresponds to the onset temperature of the CDW, so this change is in accordance with the idea that the CDW is suppressed at applied pressures. Since an inflection, however, is generic and seen also at higher pressure such a conclusion could be an over interpretation of the data. The suppression of the CDW at 1 GPa is not therefore established.

The behaviour of ρ in the normal state seems to change drastically under applied pressures. The measurements reported here should be repeated, however, owing to the possible touch between an I and V contact. Our measurements indicate a significant room temperature change that should be fairly simple to

verify as no cryogenic equipment is required.

The temperature of the maximum in $\rho(T)$, that is suggestive of the Kondo effect, reduces with pressure, and extrapolation of the curves shown in Fig. 6.9 implies that this temperature will go to zero at $P > 8$ GPa. If this maximum also coincides with a subtle transition at ambient pressure seen in specific heat measurements (see chapter 5) a Quantum Critical Point (QCP) might then be expected. However if we associate the change from $\rho \propto T^2$ behaviour as a coherence temperature we note that this temperature seems to be rising at the highest pressures, and the A coefficient is decreasing, which are the opposite to what is expected on the approach to a QCP.

At the highest pressures the superconductivity is no longer in the dirty limit, and $H_{c2}(0)/H_P < 1$ *i.e.* the superconductivity is within the Pauli limit. The reduced field $h(0)$ is still very large, however, and appears to be growing. It is suggested that the large reduced field value can be explained by multiple bands, and we have managed to obtain satisfactory fits using a two-band model. The fit is fairly insensitive to the parameters, however, and more information about the nature of the electron bands is necessary to further develop this explanation.

We have not successfully fitted our data to a strong-coupling model, but the work of Bulaevskii *et al.* [16] predicts that, if we consider U_6Fe as a dirty superconductor (as is approximately the case for ambient pressure), the superconductivity is approaching an upwardly-curving $H_{c2}(T)$ above the highest pressures measured here. The state of the system at the highest pressures seems to be significantly changed from the ambient pressure state and merits further study to determine the extent to which $h(0)$ continues to increase at higher pressures.

As a concluding remark we note that in this chapter only the case of field applied along a has been studied. It would also be interesting to know if the anisotropy in the critical field is affected by applied pressure. From the literature it does not appear that there is much anisotropy in the compressibility. This suggests that the anisotropy in H_{c2} should not drastically change, but verification of this would provide an interesting extension to our measurements so far.

Chapter 7

Conclusions

7.1 Summary of key findings

Single-crystalline U_6Fe that has been treated by the Solid State Electrotransport (SSE) method has been found to have an Residual Resistivity Ratio (RRR) enhanced by a factor of 2-3 over typical quenched or Czochralski-grown samples. The specific heat and resistivity as a function of pressure for these improved-quality samples have been studied as part of this project. Additionally, the low temperature structure has been investigated by X-ray scattering at the European Synchrotron Radiation Facility (ESRF) in Grenoble, France. In this chapter the results of these studies are considered along side one another to give a broad context to the discussion of the properties of U_6Fe.

7.1.1 Charge density wave

The most significant finding of these studies is that U_6Fe does indeed exhibit a Charge Density Wave (CDW) state. This is evident from the satellite peaks in our X-ray scattering investigation. The ordering vector in reciprocal lattice units is $(\delta H, \delta K, \delta L) = (\pm 0.11, \pm 0.11, 0)$, and systematic absences indicate that the nature of the modulation is transverse and confined to the plane (*i.e.* the charge is modulated in the *a*-*b* plane, perpendicular to the modulation wavevector). The transition to the CDW state occurs below a temperature $T_{\mathrm{CDW}} \approx 10$ K. This is an order of magnitude lower than was previously suggested in published literature.

Also at T_{CDW} intensity is seen at forbidden $(H, 0, L)$ (H, L odd) Bragg peaks

and their satellites that is not attributable to multiple scattering. Therefore the c-glide symmetry operation of the space group $I4/mcm$ is broken in the CDW state. However, it cannot be ruled out that the symmetry is actually broken at a higher temperature and that the CDW only enhances the degree of symmetry breaking.

The increase of I_{CDW} below $\sim$10 K can be tied to features in the specific heat and resistivity, as shown in Fig. 7.1. This reflects the gap that the CDW formation opens at the Fermi surface. A gap removes some of the electronic states of which resistivity and specific heat at low temperatures are sensitive probes. Why the signals are weak (compared to other materials *e.g.* α-U) is still mysterious, but may be linked to sample quality.

The plot of satellite intensity I_{CDW} *versus* T shows a kink at the superconducting transition temperature ($T_{\mathrm{SC}} = 4$ K), which is a clear indicator that the CDW is prevented from further formation by the superconducting state which also gaps the Fermi surface. I_{CDW} does not dip below T_{SC} as in *e.g.* $YBa_2Cu_3O_{6.67}$ [76]. Instead it seems there is coexistence, at least in the temperature range studied. There is perhaps a reduction of I_{CDW} at the lowest temperatures, however our data are too limited to conclude the significance of this.

The investigation of a change in structure below T_{CDW} implies that the U atoms are involved in the transition. This is suggested by anisotropic Debye-Waller factors that reduce below T_{CDW}, implying a hardening of the motion of these atoms along the c-axis. This has given us reason to suggest possible scenarios of the distorted structure in the CDW state. However, the exact repositioning of the atoms (*i.e.* the nature of the Periodic Lattice Distortion (PLD)) that usually accompanies a CDW formation has not been conclusively determined.

The effect of pressure on the CDW state remains unclear. The maximum in T_{SC} with pressure has been put forward as evidence of CDW suppression [2], in analogy with α-U. However the features in the resistivity that are in the region of T_{CDW} are the maximum in $d\rho/dT$ and transition to T^2 behaviour, which are only moderately affected by the same applied pressures that cause a maximum in T_{SC}. At high pressures, the inflection and onset of T^2 has been observed to move to higher temperatures.

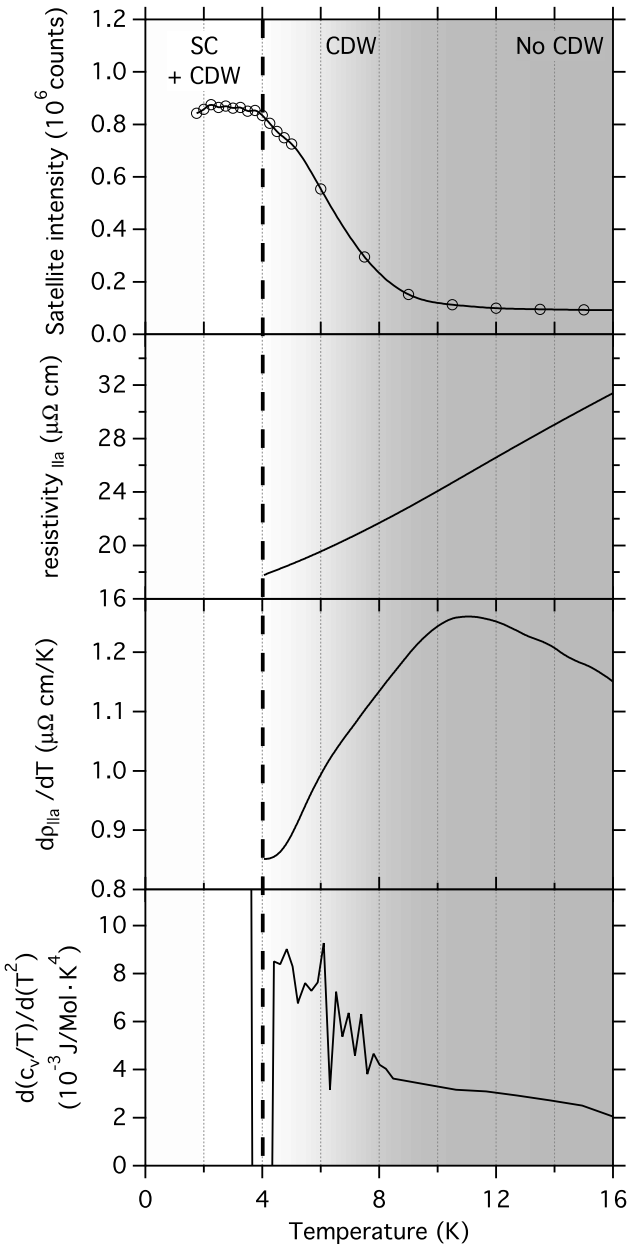

Figure 7.1: Comparison of signals of the charge density wave in various measurements. The satellite intensity temperature dependence, measured around the $(10, 0, 2)$ Bragg peak is reproduced here from Fig. 4.10. Below this are the resistivity along the a-axis $\rho_{||a}$ at ambient pressure, the differential of $\rho_{||a}$, and the differential of the specific heat c_v/T with respect to T. The thick dashed vertical line shows the transition to superconductivity, and the background colour is determined by the satellite intensity.

7.1.2 Transition at 110 K

The clear step seen in specific heat measurements at around 110 K is reflected by only subtle changes of other properties. An example of such a property is the unexpected behaviour of the $(10, 0, 0)$ intensity below this temperature seen in X-ray scattering. From the structure factor it can be seen that Bragg peak's intensity is more sensitive to the position of the U atoms. This suggests that the movement of these atoms are the driving force behind the 110 K transition as well as the CDW transition.

During our first X-ray scattering experiment we observed a vanishing of a sharp, forbidden $(H, 0, L)$ (H, L odd) Bragg peak at around 110 K that fitted very well with the theory of a transition at such temperatures. Our second experiment showed that there is a significant contribution to the intensity at this Bragg peak, and others forbidden by the same rule, due to multiple scattering. Only below T_{CDW} is it clear that there is a signal from these forbidden peaks that cannot be explained by multiple scattering. In retrospect, then, it cannot be ruled out that this apparent high temperature signal of a transition was nothing more than gradual thermal expansion. This is shown in Fig. 4.16 where it can be seen that multiple scattering effects are sufficient to cause a change in intensity at the $(9, 0, 1)$ position of almost two orders of magnitude between 4 K and 170 K.

The transition at $\sim$110 K also has seemingly no signal in our resistivity measurements at ambient pressure, even in samples with RRR = 9, despite the findings of Delong *et al.* [3]. It seems that applied pressures of $\sim 1 - 2$ GPa are enough to reveal this transition in resistivity, if that is what we choose to associate the maximum in $\rho(T)$ with that is seen at such pressures (see Fig. 6.8). However the resistivity curves under pressure also suggest the onset of Kondo effects, which is not normally associated with a thermodynamic transition (an exception is the Kondo volume collapse seen in elemental Cerium [87]). In any case, as mentioned in chapter 6, experimental issues cast some doubt on the findings that must be resolved for us to be able to reliably draw such conclusions from the data.

In conclusion, our specific heat measurements demonstrate that there is a clear continuous (second order) thermodynamic transition at 110 K. The order parameter has not been identified.

7.1.3 Superconductivity

The precise nature of the superconducting state remains uncertain after our studies. Our X-ray scattering results imply that there is a reasonable amount of coexistence between the superconducting and CDW states. There is a maximum in T_{SC} with pressure as previously reported [2], found by our resistivity measurements. This maximum is more extreme for our samples than for those previously measured, which presumably reflects their high quality. By contrast, the maximum in T_{SC} is not observed in Czochralski-grown samples as found by our AC Susceptibility (ACS) measurements. The difference between the ACS and resistivity results indicates the improvement of sample quality achieved by SSE treatment.

The reduced field $h(0) = -\, dH_{c2}/dT|_{T_{\mathrm{SC}}}\, T_{\mathrm{SC}}$ at ambient conditions exceeds the value expected by Bardeen Cooper Schrieffer (BCS) theory when Pauli limiting is neglected. This value dips with applied pressure and subsequently increases. At the highest applied pressures $h(0)$ is even more anomalous than at ambient conditions. This is reflected in the shape of the $H_{c2}(T)$ curve which is almost linear over much of temperature region between T_{SC} and 0 K. After going through a maximum, T_{SC} falls slowly with pressure and may be expected to go to zero at $\sim$25 GPa by linear extrapolation. $H_{c2}(T = 0)$ is falling more rapidly by comparison. At the highest pressures, $H_{c2}(0)$ is below the Pauli limit.

The ambient pressure mean free path suggests that U_6Fe is on the border of the dirty limit. This means that a complete analysis of the superconductivity requires knowledge of normal state properties, as the coherence length is restricted by the mean free path. The precise measurement of the normal state properties at high pressure was not determined reliably owing to contacts touching, and so interpretation of the high pressure superconductivity is limited.

There is some evidence regardless that suggests U_6Fe is potentially approaching a Quantum Critical Point (QCP), caused by the reduction of the temperature of the 110 K transition seen in specific heat to 0 K by applied pressure. The effective mass m^* should be enhanced near to a QCP but the A coefficient, which is proportional to $(m^*)^2$, is falling. This reduction could be related to the general fall of ρ with pressure which seems suspect as at the highest pressures the room temperature resistivity of our sample is comparable to Cu. QCPs are usually masked by a dome of superconductivity, *i.e.* T_{SC} is usually

enhanced in their vicinity, when the fluctuations associated with the QCP drive the superconductivity. This is true for both magnetic transitions approaching a magnetic QCP and phonon mechanisms approaching a lattice instability. Our findings that T_{SC} is continuing to fall even at the highest pressures would then suggest that fluctuations associated with the 110 K transition do not drive the superconductivity.

In summary, while some properties of the low temperature state of U_6Fe have been determined over the course of this project, further work is required to reach a satisfactory conclusion with respect to others. In the remaining section we will discuss some possible projects for future investigation.

7.2 Suggested further work

Clearly there is a need for repeat measurements of the effect of pressure on the resistivity in U_6Fe. The high temperature measurements of the resistivity obtained so far are cast into doubt by the signal grounding, although the step at T_{SC} and hence the $H_{c2}(T)$ curves are reliable. From the measurements so far it seems that even the ambient temperature resistivity should noticeably change with pressure. However, there is plenty of interesting behaviour at low temperatures to investigate, perhaps most significantly the emergence of a maximum in resistivity near 110 K. Given the surprising lack of evidence of a transition at this temperature in ambient pressure resistivity data, confirming that this feature of the resistivity under pressure is intrinsic is important. In addition, it may be of interest to investigate the behaviour of both the resistivity along the c-axis (where the RRR is higher) or the resistivity along the a-axis with field applied along the c-axis (where $H_{c2}(T = 0)$ is higher) under applied pressure, to compare the behaviour.

During this project we have not investigated the magnetic properties of our samples beyond analysing the proportion of UFe_2 contained within them. The possibility of magnetic involvement in the 110 K anomaly is not then precluded. Investigations of the magnetisation at 110 K are therefore of interest. If a signal can be observed at 110 K then it may be of interest to study the effect of pressure on such a signal to tie in with the resistivity studies. Alternatively, it may be of interest to observe any effect of applied field to the jump observed in specific

heat.

It is also worth noting that our studies so far have not precluded the existence of a Spin Density Wave (SDW). This can be thought of as a CDW tied in with a modulation of the electronic spin. In order to determine if the CDW is actually an SDW, it would be necessary to find the transition in studies of the magnetic properties of the system. Given that the transport measurement signals are so weak it might also be difficult to see the signals in magnetisation results and may be necessary to study again with neutron diffraction.

Another interesting study might be an investigation of the ultrasonic response of a sample of U_6Fe. This is sensitive to changes in the elastic moduli, and therefore should at least be able to observe the CDW transition. Similar measurements on α-Uranium show dramatic effects at the onset temperature of the CDW [88]. This is related to the softening of phonons in the vicinity of the phase transition to the CDW state. These measurements could also offer a probe into the high temperature behaviour of U_6Fe in the $\sim$110 K region.

Finally, a related study would be to investigate the phonon dispersion as a function of temperature by inelastic X-ray scattering. This technique enables measurement of the phonon dispersion when combined with band structure calculations. By this method we would be able to see also which phonons soften at the transition and therefore say with more certainty which atoms move and in what way.

There is also still significant room for improvement in the realm of sample synthesis. Although we now have a way to consistently improve the quality of our samples, more should be done to optimise the process. This is limited, perhaps, by the fact that we do not have the ability to measure the temperature of our samples below 600 K in the SSE that was used to treat them. However, even though we have seen that lower annealing temperatures improved the RRR of our polycrystalline samples the most (and high temperatures were detrimental to quality), the SSE approach to treatment may require a new study. Clearly the effect of SSE is not to simply anneal the length of the sample, as there is a gradient in the RRR. Therefore it is worth investigating the effects of this method on U_6Fe purification more thoroughly.

Appendix A

Laue system calibration methods

This appendix discusses in more detail the two methods discussed briefly in chapter 3 for determining the distance between the plane of detection of the Gemstar camera and the Centre of Rotation (COR) of the Huber goniometer.

A.1 Translation method for determining D

In the first method, a sample was translated along the X-ray beam, and the movement of Bragg spots across the detector screen were used to calculate D. This method makes use of Eq. 3.17, which can be derived as follows. It can be seen from Fig. 3.8 that:

$$r_x = -x \sin 2\psi_D + d \sin\Big((2\psi)_{xy} - 2\psi_D\Big) \tag{A.1}$$

keeping in mind the direction of r_x as shown in the figure. In the case of sample movement along the $\underline{\hat{x}}_l$ direction, d, x and r_x vary but $2\psi_{xy}$ is unchanged. The dependence of d on x can be further broken down into:

$$d = \frac{D - x \cos 2\psi_D}{\cos\Big((2\psi)_{xy} - 2\psi_D\Big)}. \tag{A.2}$$

Eq. A.1 and A.2 are combined to give:

$$\begin{aligned} r_x &= -x\sin 2\psi_D + \left(\frac{D - x\cos 2\psi_D}{\cos\left((2\psi)_{xy} - 2\psi_D\right)}\right)\sin\left((2\psi)_{xy} - 2\psi_D\right) \\ &= -x\left(\sin 2\psi_D + \cos 2\psi_D \tan\left((2\psi)_{xy} - 2\psi_D\right)\right) + D\tan\left((2\psi)_{xy} - 2\psi_D\right) \\ &= mx + c. \end{aligned} \tag{A.3}$$

These last two equations are Eqs. 3.17 and 3.18. In the ideal case, when $x = 0$ the diffaction point is at the COR as in Fig. 3.5. In general there will be an offset between these two positions of size x_0, so that $x = x_{\text{Huber}} + x_0$ (where x_{Huber} is the reading of the sample stage position). Regardless of the offset, the change of spot position co-ordinate r_x with movement along x is found by differentiating Eq. 3.17:

$$\frac{\partial r_x}{\partial x} = -\sin 2\psi_D - \cos 2\psi_D \tan\left((2\psi)_{xy} - 2\psi_D\right). \tag{A.4}$$

In the setup as it was used, $2\psi_D = 43°$ and the detector covered a narrow angular range such that $\frac{\partial r_x}{\partial x} < 0$. Using Eq. A.4, $(2\psi)_{xy}$ can be estimated for any spot that can be tracked as a function of x, even if x_0 is not known. From Eq. 3.18, m can be obtained from $(2\psi)_{xy}$. If a pattern containing several spots is tracked as a function of x, then there will be several datapoints for m *versus* r_x available. To be able to use these to obtain a value for D, Eq. 3.17 is rewritten as:

$$\frac{r_x}{\tan\left((2\psi)_{xy} - 2\psi_D\right)} = -x\frac{\left(\sin 2\psi_D + \cos 2\psi_D \tan\left((2\psi)_{xy} - 2\psi_D\right)\right)}{\tan\left((2\psi)_{xy} - 2\psi_D\right)} + D \tag{A.5}$$

$$\frac{r_x}{\sigma} = x\frac{m}{\sigma} - D \tag{A.6}$$

where $\sigma = \tan\left((2\psi)_{xy} - 2\psi_D\right)$ and $m = \frac{\partial r_x}{\partial x}$ as previously defined. We can then plot $\frac{r_x}{\sigma}$ *versus* $\frac{m}{\sigma}$ to get a linear fit with x as a gradient and D as an intercept. $x - x_{\text{Huber}}$ will give the offset x_0.

Implementation of the method

A sequence was programmed which moved a sample along the beam and captured images at different positions along it. These images were analysed to look for

the spots contained within them (as described in section 3.6). Each image was compared with its neighbours, and the equations of the previous section were used to predict where the spots from one would move to in another, so that the spots could be matched up between the images (given an additional radius allowance for noise - see Fig. 3.9). After the spots were tracked they were analysed programatically using the equations above. In practise it was very difficult to fit a line to $\frac{r_x}{\sigma}$ *versus* $\frac{m}{\sigma}$, even though the tracked spots gave reasonable-seeming estimates for the diffraction angles (see Fig. A.1). Instead, by fitting first σ *versus* r_x and m *versus* r_x using linear approximations, we get a much better fit. In theory, from Eq. A.6, we should get the same value of D for each x_{Huber}, but there is a small variation. We also see that the determined value of x is very nearly, but not quite, linear with x_{Huber} (see Fig. A.2). We also see that the plot of $\frac{r_x}{\sigma}$ *versus* $\frac{m}{\sigma}$ becomes easier to fit without intermediate fitting with larger x. In order to make this procedure more accurate, we can fit σ *versus* r_x and m *versus* r_x using non-linear fits, which themselves determine D and x using fitting parameters. Using this method, it will be simple for anybody to calibrate the apparatus (if, for example, the detector is moved to increase or decrease the angular range), because the entire procedure is automated.

Determining geometrical constants: rotation method

Eq. 3.17 shows that r_x is also linearly dependent on $\tan(2\psi_{xy} - 2\psi_D)$ at fixed x. For a sample rotated around the z-axis at constant x, the above relation could also be used to predict D by a different method. This requires knowing the dependence of ψ_{xy} on ϕ or ω at $\chi = 0$. Fig. 3.5 shows the system geometry when the point of diffraction is the COR, which is a simplified case for this kind of calibration.

Note that because the τ-vectors transform in the same way as the sample, a rotation of the ϕ angle results in an equal change in ψ_{xy} (provided $\chi = 0$, as we assume here). However, the change of ψ with ϕ is more complicated. This is because $(2\psi)_{xy}$, the projection of 2ψ in the x-y plane, is not always equal to $2 \times \psi_{xy}$, as is clear from simple consideration of Eqs. 3.9 and 3.10. $(2\psi)_{xy}$ has a more complicated dependence on ϕ, but tends towards $2 \times \psi_{xy}$ for all ϕ in the

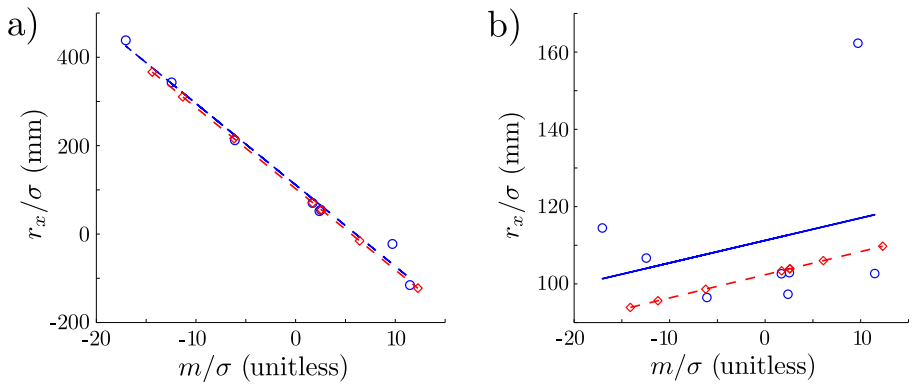

Figure A.1: Fitting $\frac{r_x}{\sigma}$ *versus* $\frac{m}{\sigma}$. These values are calculated using the equations in the text, and the variation of the position of Bragg peaks with x. Each datapoint corresponds to one tracked spot (this data corresponds to the tracked spots shown in Fig. 3.9). a) shows fitted data using large x_{Huber}, and therefore the lowest r_x values, whereas b) uses the opposite. The blue circles are data calculated directly from the tracked spots, and fitted to by the solid blue line. The red diamonds are determined by first linearly fitting σ *versus* r_x and m *versus* r_x. In the left plot, the gradient is positive, reflecting that the predicted x is positive, whereas in the right hand plot it is negative. The intercept is approximately the same in both plots, reflecting consistency in the estimated value of D.

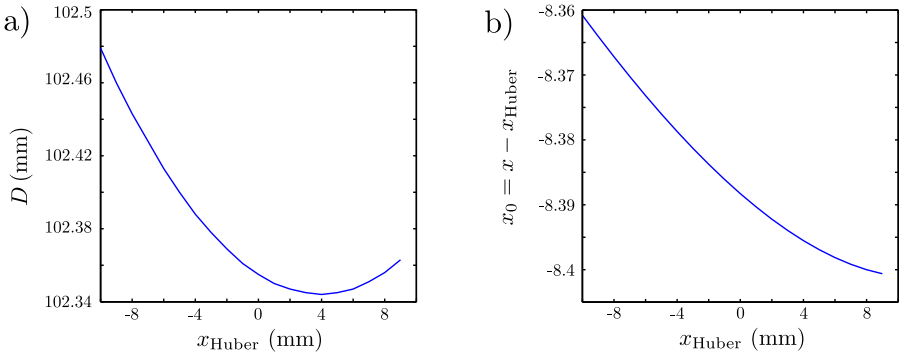

Figure A.2: Plots showing a) predicted D and b) predicted $x - x_{\text{Huber}}$. a) shows there is a small amount of variation in D as x_{Huber} varies. b) shows that the predicted x is very nearly proportional to x_{Huber}.

limit of small ψ_z. This can be seen as follows. From Fig. 3.5 it can be seen that:

$$\tan\phi = \frac{\tau_z}{\tau_{xy}\sin\psi_{xy}} = \frac{\tan\psi_z}{\sin\psi_{xy}}. \tag{A.7}$$

Similarly from Fig. 3.5 it can be seen that:

$$\tan\phi = \frac{r_z}{d\sin\left(2\psi\right)_{xy}} = \frac{\tan\left(2\psi\right)_z}{\sin\left(2\psi\right)_{xy}}. \tag{A.8}$$

Eqs. 3.10, A.7 and A.8 combine to give:

$$\sin\left(2\psi\right)_{xy} = \frac{\tan\left(\arccos\left(\frac{\cos 2\psi}{\cos(2\psi)_{xy}}\right)\right)\sin\psi_{xy}}{\tan\psi_z}. \tag{A.9}$$

This can be solved for $(2\psi)_{xy}$. Fig. A.3 shows the difference $(2\psi)_{xy} - 2(\psi_{xy})$ as a function of ψ_{xy} and ψ_z. The calibration methods mentioned here give an estimate for the maximum ψ_z that would still be seen at the detector as about 12 degrees. This corresponds to about 2 degrees difference between $(2\psi)_{xy}$ and $2(\psi_{xy})$. Because the detector is a circle, most spots tracked under rotation would have a lower ψ_z. The consequence of this is that it is not very unreasonable to model $(2\psi)_{xy} \approx 2(\psi_{xy})$. In this approximation, and with the diffraction at the COR, the equation:

$$r_x = D\tan\left(2\psi_D - 2\psi_{xy}\right) \tag{A.10}$$

is true and D can be obtained from a simple fit with a tan function, rather than the much more complicated fitting method described in section 3.5.1. This method has not been automated however.

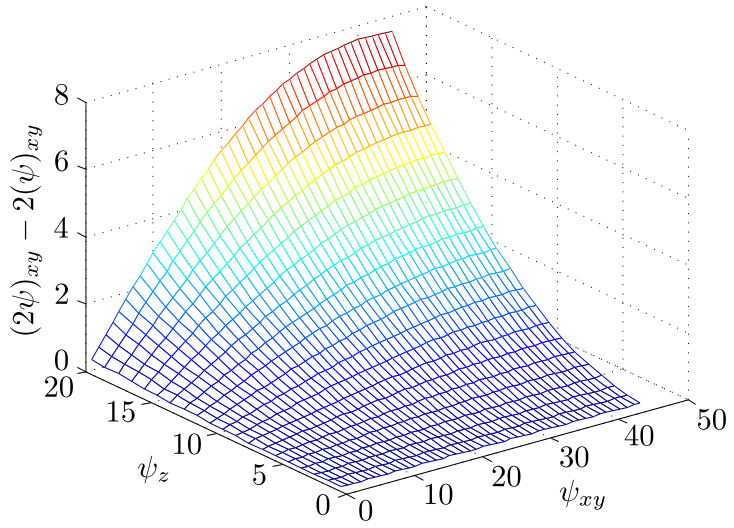

Figure A.3: Figure showing the difference $(2\psi)_{xy} - 2(\psi_{xy})$ as a function of ψ_{xy} and ψ_z.

Appendix B

Refinement of Bragg peak intensities using JANA

In this appendix, the results of attempted refinement using the JANA software package [13] are documented. Four space groups were tried: the room temperature structure space group $I4/mcm$, and three maximal subgroups $I422$, $I\bar{4}2m$, and $I4/m$. These are the only three subgroups which would allow extra Bragg peaks of the form $(H, 0, L)$ with H, L odd and $H + L$ even, while forbidding the peaks that were not observed as part of the X-ray diffraction study documented in chapter 4. In the following tables, the number in brackets is the error in the final digit. Asterisks note parameters which had to be fixed in order to get a convergent fit. Note that, while JANA returns Debye-Waller parameters as U_{ij} values, the other calculations performed (as described in Chapter 4) calculated b_{ij} values, as defined in the caption of Table 4.5. The U_{ij} and b_{ij} are defined differently, but large b's in a set imply corresponding large U's.

B.1 Fits to data at 15 K

B.1.1 $I4/mcm$

R(obs) = 19.74, wR(obs) = 24.32, R(all) = 19.74, wR(all) = 24.32.

Fe		U_1			
U_{11}	U_{33}	x	U_{11}	U_{33}	U_{12}
-0.02(1)	0.1(2)	0.4062(7)	-0.018(7)	0.30(9)	-0.002(4)
U_2					
x	y	U_{11}	U_{22}	U_{33}	U_{12}
0.2157(8)	0.1025(7)	-0.019(6)	-0.018(7)	0.29(6)	-0.001(2)

B.1.2 $I422$

R(obs) = 20.32, wR(obs) = 24.70, R(all) = 20.92, wR(all) = 27.25.

Fe_1		Fe_2		
U_{11}	U_{33}	U_{11}	U_{33}	
0.0(1)	-0.1(4)	-0.05(2)	1(1)	
U_1				
x	U_{11}	U_{33}	U_{12}	U_{13}
0.4058(9)	-0.019(7)	0.3(1)	-0.003(5)	-0.00(2)
U_2				
x	y	z	U_{11}	
0.215(1)	0.102(1)	0.245(7)	-0.021(7)	
U_2				
U_{22}	U_{33}	U_{12}	U_{13}	U_{23}
-0.021(8)	0.30(7)	-0.001(4)	0.00(1)	0.01(2)

B.1.3 $I\bar{4}2m$

R(obs) = 39.91, wR(obs) = 45.61, R(all) = 39.9, wR(all) = 45.61.

Fe					
U_{11}	U_{22}	U_{33}			
0.01(9)	0.02(9)	0(1)			
U_1					
x	z	U_{11}	U_{33}	U_{12}	U_{13}
0.906(4)	0.24(2)	0.02(3)	0.0(3)	0.00(1)	0.04(4)
U_2					
x	y	z	U_{11}	U_{22}	
0.716(4)	0.102(3)	0.25(3)	0.02(3)	0.02(3)	
U_2					
U_{33}	U_{12}	U_{13}	U_{23}		
0.1(2)	0.00(2)	0.00(3)	0.00(3)		

B.1.4 $I4/m$

R(obs) = 18.83, wR(obs) = 24.32, R(all) = 19.26, wR(all) = 25.69.

Fe					
z*	U_{11}	U_{33}*			
0.25	-0.00(4)	1			
U_1					
x	y	U_{11}	U_{22}	U_{33}	U_{12}
0.406(1)	0.905(1)	-0.014(9)	-0.019(8)	0.3(1)	-0.003(6)
$U_{2,1}$					
x	y	U_{11}	U_{22}	U_{33}	U_{12}
0.215(1)	0.103(1)	-0.020(8)	-0.021(9)	0.26(7)	-0.003(6)
$U_{2,2}$					
x	y	U_{11}	U_{22}	U_{33}	U_{12}
0.215(1)	-0.102(1)	-0.025(7)	-0.024(9)	0.38(8)	-0.001(5)

B.2 Fits to data at 1.75 K

B.2.1 $I4/mcm$

R(obs) = 16.16, wR(obs) = 20.73, R(all) = 16.16, wR(all)= 20.73.

Fe		U_1			
U_{11}	U_{33}	x	U_{11}	U_{33}	U_{12}
-0.03(1)	0.1(2)	0.4059(6)	-0.018(5)	0.11(6)	-0.001(3)
U_2					
x	y	U_{11}	U_{22}	U_{33}	U_{12}
0.2155(7)	0.1025(5)	-0.019(5)	-0.018(6)	0.10(3)	-0.002(2)

B.2.2 $I422$

R(obs) = 15.80, wR(obs) = 20.32, R(all) = 15.89, wR(all)= 20.39.

Fe_1		Fe_2		
U_{11}	U_{33}	U_{11}	U_{33}	
-0.01(3)	0.1(7)	-0.04(2)	0.1(2)	
U_1				
x	U_{11}	U_{33}	U_{12}	U_{13}
0.4059(7)	-0.018(5)	0.10(6)	-0.001(4)	-0.010(8)
U_2				
x	y	z	U_{11}	
0.2152(8)	0.1027(6)	0.243(3)	-0.018(5)	
U_2				
U_{22}	U_{33}	U_{12}	U_{13}	U_{23}
-0.019(6)	0.11(4)	0.000(3)	0.01(1)	-0.014(8)

B.2.3 $I\bar{4}2m$

R(obs) = 15.64, wR(obs) = 20.26, R(all) = 15.64, wR(all) = 20.26.

Fe		
U_{11}	U_{22}	U_{33}
-0.04(2)	-0.01(3)	0.1(3)

U_1					
x	z	U_{11}	U_{33}	U_{12}	U_{13}
0.906(8)	0.238(8)	-0.015(7)	0.07(7)	0.001(4)	-0.004(8)

U_2				
x	y	z	U_{11}	U_{22}
0.7158(8)	0.1026(6)	0.26(2)	-0.018(6)	-0.019(6)

U_2			
U_{33}	U_{12}	U_{13}	U_{23}
0.13(5)	0.001(3)	-0.006(9)	-0.01(1)

B.2.4 $I4/m$

R(obs) = 16.17, wR(obs) = 20.13, R(all) = 16.21, wR(all) = 20.16.

Fe		
z*	U_{11}	U_{33}*
0.25	-0.01(2)	1

U_1					
x	y	U_{11}	U_{22}	U_{33}	U_{12}
0.4052(8)	0.9056(9)	-0.009(7)	-0.019(6)	0.08(6)	-0.004(5)

$U_{2,1}$					
x	y	U_{11}	U_{22}	U_{33}	U_{12}
0.215(1)	0.103(1)	-0.020(8)	-0.021(9)	-0.003(6)	-0.003(6)

$U_{2,2}$					
x	y	U_{11}	U_{22}	U_{33}	U_{12}
0.215(1)	-0.1020(7)	-0.020(6)	-0.016(7)	0.11(4)	-0.002(4)

Bibliography

[1] E. Yamamoto, M. Hedo, Y. Inada, T. Ishida, Y. Haga, and Y. Onuki. "Single crystal growth and the upper critical field of the superconductor U_6Fe." *Journal of the Physical Society of Japan*, volume 65, no. 4, pages 1034–1037, 1996.

[2] L. E. De Long and K. Gschneidner, Jr. "High pressure phase stability of U_6X(X = Mn, Fe, Co, Ni) compounds." *Physica B: Condensed Matter*, volume 163, no. 1-3, pages 158–162, 1990.

[3] L. E. De Long, G. W. Crabtree, L. Hall, and H. Kierstead. "Normal and superconducting state properties of U_6Fe at low temperatures and high magnetic fields." *Physica B & C*, volume 135, no. 1-3, pages 81–85, 1985.

[4] C. W. Kimball, P. P. Vaishnava, A. E. Dwight, J. D. Jorgensen, and F. Y. Fradin. "Phonon Anomalies and Local Atomic Displacements in the Exchange-Enhanced Superconductor U_6Fe." *Physical Review B*, volume 32, no. 7, pages 4419–4425, 1985.

[5] H. Shimahara. "Fulde-Ferrell state in quasi-two-dimensional superconductors." *Physical Review B*, volume 50, no. 17, pages 12760–12765, 1994.

[6] N. H. Werthamer, E. Helfand, and P. C. Hohenberg. "Temperature and Purity Dependence of Superconducting Critical Field H_{c2}. III. Electron Spin and Spin-Orbit Effects." *Physical Review*, volume 147, no. 1, pages 295–302, 1966.

[7] Y. Matsuda and H. Shimahara. "Fulde-Ferrell-Larkin-Ovchinnikov state in heavy fermion superconductors." *Journal of the Physical Society of Japan*, volume 76, no. 5, 2007.

[8] G. Grüner. "The Dynamics Of Charge-Density Waves." *Reviews of Modern Physics*, volume 60, no. 4, pages 1129–1182, 1988.

[9] S. Chatain, C. Gueneau, D. Labroche, J. Rogez, and O. Dugne. "Thermodynamic assessment of the Fe-U binary system." *Journal of Phase Equilibria*, volume 24, no. 2, pages 122–131, 2003.

[10] D. R. Lide. *CRC Handbook of Chemistry and Physics, 84th Edition* (CRC Press, Boca Raton, Florida), 2003.

[11] J. Schmehr. *Incommensurate Magnetism in UAu_2*. Ph.D. thesis, University of Edinburgh, 2015.

[12] F. Wilhelm, N. Jaouen, A. Rogalev, W. G. Stirling, R. Springell, S. W. Zochowski, A. M. Beesley, S. D. Brown, M. F. Thomas, G. H. Lander, S. Langridge, R. C. C. Ward, and M. R. Wells. "X-ray magnetic circular dichroism study of uranium/iron multilayers." *Physical Review B*, volume 76, no. 2, 2007.

[13] V. Petricek, M. Dusek, and L. Palatinus. "Crystallographic Computing System JANA2006: General features." *Zeitschrift Fur Kristallographie*, volume 229, no. 5, pages 345–352, 2014.

[14] K. N. Yang, M. B. Maple, L. E. De Long, J. G. Huber, and A. Junod. "Low-temperature heat-capacity study of the U_6X (X≡Mn, Fe, Co, Ni) compounds." *Physical Review B*, volume 39, no. 1, pages 151–166, 1989.

[15] A. Gurevich. "Enhancement of the upper critical field by nonmagnetic impurities in dirty two-gap superconductors." *Physical Review B*, volume 67, no. 18, 2003.

[16] L. N. Bulaevskii, O. V. Dolgov, and M. O. Ptitsyn. "Properties of Strong-Coupled Superconductors." *Physical Review B*, volume 38, no. 16, pages 11290–11295, 1988.

[17] J. J. Rehr, J. J. Kas, F. D. Vila, M. P. Prange, and K. Jorissen. "Parameter-free calculations of X-ray spectra with FEFF9." *Physical Chemistry Chemical Physics*, volume 12, no. 21, pages 5503–5513, 2010.

[18] T. Hahn. *International Tables for Crystallography, Space-Group Symmetry* (Springer), 5 edition, 2005.

[19] M. Tinkham. *Introduction to Superconductivity.* Second Edition (Courier Corporation), 2004.

[20] J. F. Annett. *Superconductivity, Superfluids and Condensates* (Oxford University Press), 2004.

[21] H. K. Onnes. "Further experiments with liquid helium D - On the change of the electrical resistance of pure metals at very low temperatures, etc V The disappearance of the resistance of mercury." *Proceedings of the Koninklijke Akademie Van Wetenschappen Te Amsterdam*, volume 14, pages 113–115, 1911.

[22] C. Pfleiderer. "Superconducting phases of f-electron compounds." *Reviews of Modern Physics*, volume 81, no. 4, pages 1551–1624, 2009.

[23] N. C. Baenziger, R. E. Rundle, A. I. Snow, and A. S. Wilson. "1950 Baenziger (first structure characterised)." *Acta Crystallographica*, pages 1–7, 1950.

[24] M. K. Hou, C. Y. Huang, and C. E. Olsen. "Penetration Depths of Superconducting U_6Fe, U_6Co, U_6Mn." *Solid State Communications*, volume 61, no. 2, pages 101–103, 1987.

[25] R. W. White, J. Lindsay, and R. D. Fowler. "Effects of Stoichiometry on Superconducting Transition Temperature of U_6Fe and Uranium Isotope-Effects." *Solid State Communications*, volume 13, no. 5, pages 531–532, 1973.

[26] J. Bardeen, L. N. Cooper, and J. R. Schrieffer. "Theory of Superconductivity." *Physical Review*, volume 108, no. 5, pages 1175–1204, 1957.

[27] A. A. Abrikosov. *Doklady Akademii Nauk SSSR*, volume 86, page 489, 1952.

[28] E. Helfand and N. H. Werthamer. "Temperature and Purity Dependence of Superconducting Critical Field, H_{c2}. II." *Physical Review*, volume 147, no. 1, pages 288–294, 1966.

[29] A. M. Clogston. "Upper Limit for Critical Field in Hard Superconductors." *Physical Review Letters*, volume 9, no. 6, pages 266–267, 1962.

[30] K. Maki. "The magnetic properties of superconducting alloys. II." *Physics*, volume 1, no. 2, pages 127–143, 1964.

[31] P. Fulde and R. A. Ferrell. "Superconductivity in a Strong Spin-Exchange Field." *Physical Review*, volume 135, no. 3A, pages A550–A563, 1964.

[32] N. W. Ashcroft and N. D. Mermin. *Solid State Physics* (Brooks/Cole), 2011.

[33] A. I. Larkin and Y. N. Ovchinnikov. "Inhomogeneous State of Superconductors." *Soviet Physics JETP-USSR*, volume 20, no. 3, page 762, 1965.

[34] V. P. Mineev and K. V. Samokhin. *Introduction to Unconventional Superconductivity* (Gordon and Breach), 2009.

[35] L. Gruenberg and L. Gunther. "Fulde-Ferrell Effect in Type-II Superconductors." *Physical Review Letters*, volume 16, no. 22, pages 996–998, 1966.

[36] S. Takada. "Superconductivity in a Molecular Field II: Stability of Fulde-Ferrel Phase." *Progress of Theoretical Physics*, volume 43, no. 1, pages 27–38, 1970.

[37] S. E. Brown. "Organic superconductors: The Bechgaard salts and relatives." *Physica C*, volume 514, pages 279–289, 2015.

[38] H. Mayaffre, S. Kraemer, M. Horvatic, C. Berthier, K. Miyagawa, K. Kanoda, and V. F. Mitrovic. "Evidence of Andreev bound states as a hallmark of the FFLO phase in κ-(BEDT-TTF)$_2$Cu(NCS)$_2$." *Nature Physics*, volume 10, no. 12, pages 928–932, 2014.

[39] B. Bergk, A. Demuer, I. Sheikin, Y. Wang, J. Wosnitza, Y. Nakazawa, and R. Lortz. "Magnetic torque evidence for the Fulde-Ferrell-Larkin-Ovchinnikov state in the layered organic superconductor κ-(BEDT-TTF)$_2$Cu(NCS)$_2$." *Physical Review B*, volume 83, no. 6, 2011.

[40] H. A. Radovan, N. A. Fortune, T. P. Murphy, S. T. Hannahs, E. C. Palm, S. W. Tozer, and D. Hall. "Magnetic enhancement of superconductivity from electron spin domains." *Nature*, volume 425, no. 6953, pages 51–55, 2003.

[41] A. Bianchi, R. Movshovich, I. Vekhter, P. G. Pagliuso, and J. L. Sarrao. "Avoided antiferromagnetic order and quantum critical point in CeCoIn5." *Physical Review Letters*, volume 91, no. 25, 2003.

[42] Y. Kato, C. D. Batista, and I. Vekhter. "Antiferromagnetic Order in Pauli-Limited Unconventional Superconductors." *Physical Review Letters*, volume 107, no. 9, 2011.

[43] R. E. Peierls. *Quantum Theory of Solids* (Oxford University Press), 1955.

[44] R. H. Friend and D. Jerome. "Periodic lattice distortions and charge density waves in one- and two-dimensional metals." *Journal of Physics C*, volume 12, no. 8, pages 1441–1477, 1979.

[45] G. H. Lander, E. S. Fisher, and S. D. Bader. "The solid-state properties of uranium: A historical perspective and review." *Advances in Physics*, volume 43, pages 1–111, 1994.

[46] J. Als-Nielsen and D. McMorrow. *Elements of Modern X-ray Physics* (John Wiley & Sons), 2011.

[47] G. M. Schmiedeshoff, D. Dulguerova, J. Quan, S. Touton, C. H. Mielke, A. D. Christianson, A. H. Lacerda, E. Palm, S. T. Hannahs, T. Murphy, E. C. Gay, C. C. McPheeters, D. J. Thoma, W. L. Hults, J. C. Cooley, A. M. Kelly, R. J. Hanrahan, and J. L. Smith. "Magnetotransport and superconductivity of alpha-uranium." *Philosophical Magazine*, volume 84, no. 19, pages 2001–2022, 2004.

[48] J. C. Lashley, B. E. Lang, J. Boerio-Goates, V. G. Woodfield, G. M. Schmiedeshoff, E. C. Gay, C. C. McPheeters, D. J. Thoma, W. L. Hults, J. C. Cooley, R. J. Hanrahan, and J. L. Smith. "Low-temperature specific heat and critical magnetic field of alpha-uranium single crystals." *Physical Review B*, volume 63, no. 22, 2001.

[49] A. M. Gabovich, A. I. Voitenko, and M. Ausloos. "Charge- and spin-density waves in existing superconductors: competition between Cooper pairing and Peierls or excitonic instabilities." *Physics Reports*, volume 367, no. 6, pages 583–709, 2002.

[50] J. J. Engelhardt. "Lattice-Parameters and Superconductivity of Compounds U_6Mn, U_6Fe, U_6Co and U_6Ni and Alloys Between Them." *Journal of Physics and Chemistry of Solids*, volume 36, no. 3, pages 123–126, 1975.

[51] J. S. Olsen, L. Gerward, J. P. Dancausse, and E. Gering. "Developments and New Possibilities in High-Pressure Powder Diffraction with Synchrotron-Radiation - Results for Cerium Metal and U_6Fe." *Physica B: Condensed Matter*, volume 190, no. 1, pages 92–97, 1993.

[52] G. Lemon, P. Boolchand, M. Stevens, M. Marcuso, L. E. De Long, and J. G. Huber. "^{57}Fe Mössbauer spectroscopy of U_6Fe." *Journal of the Less Common Metals*, volume 127, pages 329–334, 1987.

[53] B. Renker, F. Gompf, E. Gering, and H. Rietschel. "Observation of Pronounced Phonon Softening in the Strongly Interacting Fermi-Liquid U_6Fe." *Physica B & C*, volume 148, no. 1-3, pages 70–72, 1987.

[54] Y. F. Popov, R. Z. Levitin, M. Zeleny, A. V. Deryagin, and A. V. Andreev. "Giant magnetoelastic distortions of the crystal structure of the low anisotropic material UFe_2." *Soviet Physics JETP-USSR*, volume 51, pages 1223–1226, 1980.

[55] L. Paolasini, F. Formisano, R. Caciuffo, G. H. Lander, and G. Lapertot. "Giant magnetoelastic interaction in UFe_2." *Journal of Physics: Conference Series*, volume 340, 2012.

[56] D. A. Hukin. "Crucibles." US Patent, 1972.

[57] D. A. Sokolov, R. Ritz, C. Pfleiderer, T. Keller, and A. D. Huxley. "Neutron scattering studies of the lattice expansion in a ferromagnetic superconductor UGe_2 under pressure." *Journal of Physics: Conference Series*, volume 273, no. 1, page 012085, 2011.

[58] D. Fort, V. K. Pecharsky, and K. Gschneidner, Jr. "Solid-State Electrotransport Purification of Dysprosium." *Journal of Alloys and Compounds*, volume 226, no. 1-2, pages 190–196, 1995.

[59] C. K. Lee, J. S. Park, S. H. Yeon, and K. I. Rhee. "Modeling of solid-state electrotransport for purification of gadolinium." *Metals and Materials International*, volume 7, no. 4, pages 343–348, 2001.

[60] J. D. Marchant, E. S. Shedd, T. A. Henrie, and M. M. Wang. *Electrotransport of impurities in rare-earth metals, using a pulsed current.* Report of investigations (U.S. Dept. of Interior, Bureau of Mines), 1971.

[61] A. Iserles. *A First Course in the Numerical Analysis of Differential Equations* (Cambridge University Press), 2009.

[62] C. Bosvieux and J. Friedel. "Sur Leelectrolyse Des Alliages Metalliques." *Journal of Physics and Chemistry of Solids*, volume 23, page 123, 1962.

[63] D. N. Bly and P. J. Rous. "Theoretical study of the electromigration wind force for adatom migration at metal surfaces." *Physical Review B*, volume 53, no. 20, pages 13909–13920, 1996.

[64] Y. Haga, E. Yamamoto, N. Kimura, M. Hedo, H. Ohkuni, and Y. Onuki. "High-quality single crystal growth of uranium-based intermetallics." *Journal of Magnetism and Magnetic Materials*, volume 177, pages 437–438, 1998.

[65] H. Over. "Surface chemistry of ruthenium dioxide in heterogeneous catalysis and electrocatalysis: from fundamental to applied research." *Chemical Reviews*, volume 112, no. 6, pages 3356–3426, 2012.

[66] G. J. Abdul-Jabbar. *The Emergence of Magnetic Order in the Rare Earth Intermetallic PrPtAl.* Ph.D. thesis, University of Edinburgh, 2014.

[67] Y. Haga, T. Honma, E. Yamamoto, H. Ohkuni, Y. Onuki, M. Ito, and N. Kimura. "Purification of uranium metal using the solid state electrotransport method under

ultrahigh vacuum." *Japanese Journal of Applied Physics*, volume 37, no. 6A, pages 3604–3609, 1998.

[68] G. E. Ice and J. W. L. Pang. "Tutorial on x-ray microLaue diffraction." *Materials Characterization*, volume 60, no. 11, pages 1191–1201, 2009.

[69] X. Guangyong, X. Su, C. B. Stagarescu, D. E. Eastman, B. Lai, Z. Cai, I. C. Noyan, and C. K. Hu. "Quantitative metrology study of Cu/SiO_2 interconnect structures using fluorescence x-ray microscopy ." *Applied Physics Letters*, volume 78, no. 6, pages 820–822, 2001.

[70] W. Ludwig, P. Reischig, A. King, and M. Herbig. "Three-dimensional grain mapping by x-ray diffraction contrast tomography and the use of Friedel pairs in diffraction data analysis." *Review of Scientific Instruments*, volume 80, page 033905, 2009.

[71] W. Whitley, C. Stock, and A. D. Huxley. "A laboratory-based Laue X-ray diffraction system for enhanced imaging range and surface grain mapping." *Journal of Applied Crystallography*, volume 48, pages 1342–1345, 2015.

[72] W. R. Busing and H. A. Levy. "Angle Calculations for 3- and 4- Circle X-Ray and Neutron Diffractometers." *Acta Crystallographica Section A*, volume 22, pages 457–464, 1967.

[73] E. A. Stern. "Number of Relevant Independent Points in X-Ray-Absorption Fine-Structure Spectra." *Physical Review B*, volume 48, no. 13, pages 9825–9827, 1993.

[74] M. Newville. "IFEFFIT: interactive XAFS analysis and FEFF fitting." *Journal of Synchrotron Radiation*, volume 8, pages 322–324, 2001.

[75] A. J. C. Wilson and E. Prince. *International Tables for Crystallography, Mathematical, Physical and Chemical Tables* (Kluwer Academic Pub), 2 edition, 1999.

[76] J. Chang, E. Blackburn, A. T. Holmes, N. B. Christensen, J. Larsen, J. Mesot, R. Liang, D. A. Bonn, W. N. Hardy, A. Watenphul, M. von Zimmermann, E. M. Forgan, and S. M. Hayden. "Direct observation of competition between superconductivity and charge density wave order in $YBa_2Cu_3O_{6.67}$." *Nature Physics*, volume 8, no. 12, pages 871–876, 2012.

[77] P. M. Chaikin and T. C. Lubensky. *Principles of Condensed Matter Physics* (Cambridge University Press), 2000.

[78] J. S. Hwang, K. J. Lin, and C. Tien. "Measurement of heat capacity by fitting the whole temperature response of a heat-pulse calorimeter." *Review of Scientific Instruments*, volume 68, no. 1, pages 94–101, 1997.

[79] S. J. Blundell and K. M. Blundell. *Concepts in Thermal Physics* (Oxford University Press, Oxford), 2 edition, 2010.

[80] M. Sigrist and K. Ueda. "Phenomenological Theory of Unconventional Superconductivity." *Reviews of Modern Physics*, volume 63, no. 2, pages 239–311, 1991.

[81] W. DESORBO. "Peak Effect in Substitutional + Interstitial Solid Solutions of High-Field Superconductors." *Reviews of Modern Physics*, volume 36, no. 1, pages 90–94, 1964.

[82] A. Dewaele, M. Torrent, P. Loubeyre, and M. Mezouar. "Compression curves of transition metals in the Mbar range: Experiments and projector augmented-wave calculations." *Physical Review B*, volume 78, no. 10, 2008.

[83] G. M. Schmiedeshoff, Z. Fisk, and J. L. Smith. "Upper Critical Fields of the Heavy-Fermion Superconductor UBe_{13}." *Physical Review B*, volume 45, no. 18, pages 10544–10548, 1992.

[84] P.-G. de Gennes. *Superconductivity of Metals and Alloys* (Westview Press), 1999.

[85] T. P. Orlando, E. J. McNiff, Jr, S. Foner, and M. R. Beasley. "Critical Fields, Pauli Paramagnetic Limiting, and Material Parameters of Nb_3Sn and V_3Si." *Physical Review B*, volume 19, no. 9, pages 4545–4561, 1979.

[86] F. Hunte, J. Jaroszynski, A. Gurevich, D. C. Larbalestier, R. Jin, A. S. Sefat, M. A. McGuire, B. C. Sales, D. K. Christen, and D. Mandrus. "Two-band superconductivity in $LaFeAsO_{0.89}F_{0.11}$ at very high magnetic fields." *Nature*, volume 453, no. 7197, pages 903–905, 2008.

[87] P. W. Bridgman. "The compressibility and pressure coefficent of resistance of ten elements." *Proceedings of the American Academy of Arts and Sciences*, volume 62, no. 1/8, pages 207–226, 1927.

[88] E. S. Fisher and H. J. McSkimin. "Low-Temperature Phase Transition in Alpha Uranium." *Physical Review*, volume 124, no. 1, pages 67–70, 1961.

JOURNAL OF APPLIED CRYSTALLOGRAPHY
ISSN 1600-5767

A laboratory-based Laue X-ray diffraction system for enhanced imaging range and surface grain mapping

William Whitley,* Chris Stock and Andrew D. Huxley

Centre for Science at Extreme Conditions, Erskinne Williamson Building, Mayfield Road, Edinburgh EH9 3JZ, Scotland. *Correspondence e-mail: w.whitley@sms.ed.ac.uk

Received 22 September 2014
Accepted 11 May 2015

Edited by D. Pandey, Indian Institute of Technology (Banaras Hindu University), Varanasi, India

Keywords: laboratory-based Laue X-ray diffraction; grain mapping.

Although CCD X-ray detectors can be faster to use, their large-area versions can be much more expensive than similarly sized photographic plate detectors. When indexing X-ray diffraction patterns, large-area detectors can prove very advantageous as they provide more spots, which makes fitting an orientation easier. On the other hand, when looking for single crystals in a polycrystalline sample, the speed of CCD detectors is more useful. A new setup is described here which overcomes some of the limitations of limited-range CCD detectors to make them more useful for indexing, whilst at the same time making it much quicker to find single crystals within a larger polycrystalline structure. This was done by combining a CCD detector with a six-axis goniometer, allowing the compilation of images from different angles into a wide-angled image. Automated scans along the sample were coupled with image processing techniques to produce grain maps, which can then be used to provide a strategy to extract single crystals from a polycrystal.

1. Introduction

White-beam (Laue) X-ray backscatter diffraction is a standard laboratory technique for determining the orientation of single crystals, but it also finds use when extracting a single-crystal from a larger polycrystalline structure. This would be done by taking images with the beam intercepting the sample at various different points and then comparing the patterns seen to determine if a grain is continuous between these points. Although this is a simple laboratory technique, more sophisticated implementation of this method has been used with synchrotron radiation to produce three-dimensional maps of the structure of polycrystals (Chung & Ice, 1999; Ice & Pang, 2009). This involves automated capture and indexing of Laue patterns across a sample, which requires a large CCD detector that can obtain a sufficient number of spots for indexing. With modern optics, it is possible to focus the incident beam and extract information on sub-micrometre-sized structures using this approach (Eastman *et al.*, 2002; Xu *et al.*, 2001).

In the laboratory environment, for indexing and aligning single crystals, it is usually cheaper to use a plate detector than such a large CCD detector. Furthermore, when separating a large single-crystal from a polycrystalline structure, usually all that is important is knowing where the boundary is of the largest grain, and it is unnecessary to index the whole structure. However, scanning a large sample grown by, for example, Czochralski pulling would be much faster done point-by-point using a CCD detector than with a plate detector. In addition, when scanning such samples (which can often have uneven surfaces and contain heavy atoms) it is much harder to get

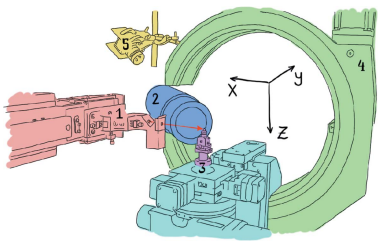

information on the depth of grains, even with high-energy radiation sources.

The University of Edinburgh employs both plate and CCD detectors for different applications. One of the Laue backscatter setups makes use of photostimulable plates and a scanner, both of which have been recently updated to use a new Fujifilm FCR Capsula XL II system. The Fujifilm system is aimed at medical applications, but was adapted to Laue backscatter imaging by drilling a hole in the centre of the image plates, to allow the beam collimator to pass through. Although this adds the risk of contamination from outside light sources leaking in, this was not found to have any significant impact on the obtained images.

CCD detectors are not produced with holes, meaning that it is not simple to replace such a plate detector with a CCD detector. Photonic Science Laboratories produce detectors in which the backscattered rays either side of the source beam are reflected onto two separate detectors, and the resulting images are stitched together to produce an image with larger area. However, with the extra processing required for each image, the capture cannot be continuous. These considerations led us to decide to use a CCD detector positioned at an angle in a different setup.

A large six-axis automated goniometer has been combined with a CCD camera X-ray detector, which allows users to scan the surface of samples and find the large single grains within a sample using a quick and fully automated procedure. It is also possible to use the goniometer to automatically enlarge the effective area of the detector by rotating and stitching together images that cover different ranges in k space.

The equipment used a 2 kW tungsten X-ray tube. The beam produced by this was focused using an optic from XOS, with a focal distance of 140 mm. This had a focal spot size of <0.34 mm, and an intensity gain of >10, when tested at 17.4 keV. This was partly done to increase the beam intensity but also to reduce the size and therefore maximize the resolution of surface scans. The effects of this optic were studied as part of the system calibration.

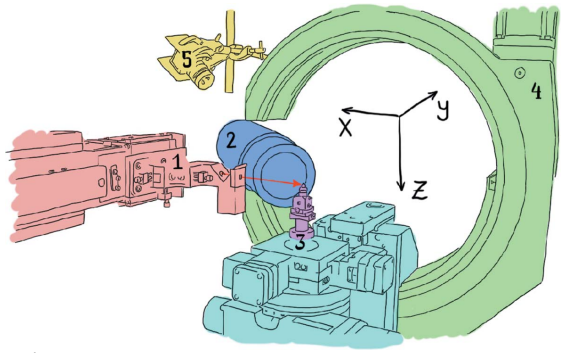

Figure 1
Labelled sketch of the setup. Shown items: (1) X-ray source and focusing optic; (2) detector; (3) sample mounting stage of six-axis goniometer (shown fitted with a smaller goniometer used for system alignment); (4) six-axis goniometer; (5) over-beam webcam. The red arrow shows the path of the incident beam, parallel to the x axis.

The CCD detector was supplied by Photonic Science Laboratories and has a sensitive surface area of diameter 66 mm. The detector uses a 'circle in a square' configuration, resulting in a dark area (a 'vignette') encircling the illuminated region. The goniometer was supplied by Huber (who also made the controller with which the main software controlling the setup interfaces). The goniometer has three rotational axes, as well as three large perpendicular ranges (25, 25, 100 mm) of translational motion.

2. Experimental setup

2.1. System calibration

At zero rotation, the x axis was calibrated to be co-aligned with the X-ray beam (Fig. 1). The goniometer sits on air pads which allow us to move it along the x- and y-axis directions in a controlled manner to achieve this. The alignment was done by traversing a fine needle in the path of the beam and marking the peak in intensity at various positions. By traversing a 100 µm wire across the beam at various distances along it, we were able to examine the focusing behaviour of the optic. Fig. 2 shows the effects of the beam focusing along the length of the x axis.

The detector axis was fixed to intercept the beamline at the centre of rotation, as seen in Fig. 1. The distance between the centre of the detector and the centre of rotation (D) needed to be determined as it is an important variable in most geometry calculations. This was done in two ways. In the first method, the Bragg spot positions were tracked as a sample at the centre of rotation was rotated by an angle φ. In the second method, the spot positions were tracked as the sample was translated along the x axis. The dependence of the spot positions on these variables was fitted with D as a fitting parameter. The first method requires the diffraction point to be at the centre of rotation and is more difficult to fit when the diffraction is not in the plane, but was included for comparison. Both methods gave consistent results and found that the point of detection was at the very front of the detector.

2.2. Image capture

The X-ray detector allows capture on microsecond timescales, but in reality captures become acceptable after

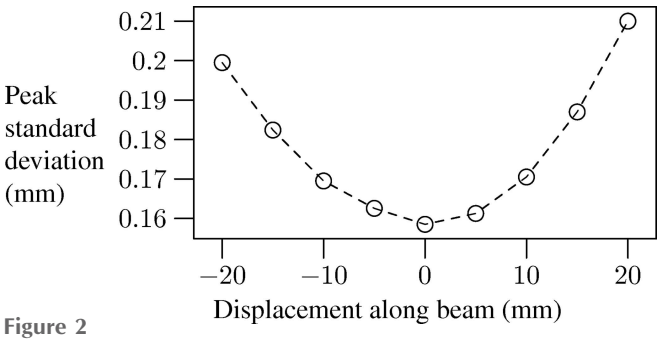

Figure 2
Focusing effect of the XOS optic, showing the reduction of spot size at the centre of the goniometer rotation.

approximately 1 s. It is possible to average many images in order to significantly reduce the signal-to-noise ratio. This system used the *IMAQ Vision* package from National Instruments (Relf, 2004) for such image processing. Fig. 3 shows an example averaged image from the detector.

A wide-angle capture technique was implemented, in which images taken at different sample rotations were remapped and stitched onto each other in a fully automatic fashion. The remapping process involved calculating the corresponding **k**-vector direction of each pixel in each image, then calculating the rotation necessary to bring this into a reference frame common to all of the images, and finally calculating the diffraction angles for those pixels in this frame. The sharp spike in the image histogram (an example of which is shown in Fig. 3) at low intensity makes it easy to apply a threshold to remove the counts detected in the image vignette, which would cause distortion to the overlaid images otherwise. Fig. 4 shows an example of such wide-angle imaging applied to a single-crystal sample of URhGe.

2.3. Surface scans

Surface scans detect that the sample is in the beam by comparing the peak counts with the intensity of the background peak in image histograms. This was more reliable than using the integrated intensity, which can vary significantly across the sample and also depends on the power of the X-rays used. The path finding algorithm looks only for two sample edges or one edge and one limit of motion reached to determine if the sample exists in the current plane of motion. The algorithm works for two-dimensional surface scans at different rotational angles.

2.4. Grain mapping

Determination of grain maps from surface scans first required image processing of all acquired images to automatically find the spot positions within them. This was done by thresholding images at different intensities within a range to the right of the background peak in the image histogram (see Fig. 3), and also at the saturation value. *IMAQ* particle finding programs (Relf, 2004) were then used to identify and filter by size the spots seen at each threshold.

After the spots had been found for all images within a sample surface scan, the set of all spots seen could be reduced so that the same spot appearing in multiple images was only included once. To do this, neighbouring images were compared and a limit on spot drift was then necessary as a parameter of the program.

Finally, the characteristic patterns which identified individual grains were determined. Two different approaches were used for this. In the first method, a database of characteristic patterns was built up by a trial and refinement process, using the spot patterns seen in captured images. The database was added to whenever an image displayed a pattern that could not be matched to any already listed. This method was found to be unreliable when automated for several reasons and so an alternative was developed.

The second method looked for Bragg spots which were found to exist within a large region of the sample being studied. Then, the algorithm looked for any significant overlap of such regions. Where these co-existence regions were large, the images within them were assessed to find the most frequently occurring spots, and these were used to form the characteristic patterns. This method has proved more reliable for automatically finding large grains within a polycrystal.

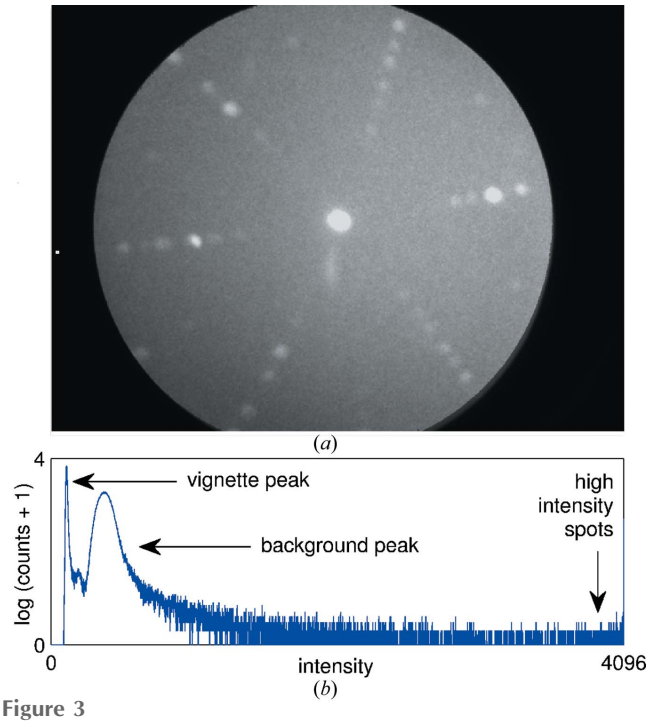

Figure 3
(*a*) An example image produced by the Gemstar detector (this image is an averaged image composed from 3 s-long exposures taken on a sample of MgV_2O_4); (*b*) a histogram that shows the different features seen in a typical image.

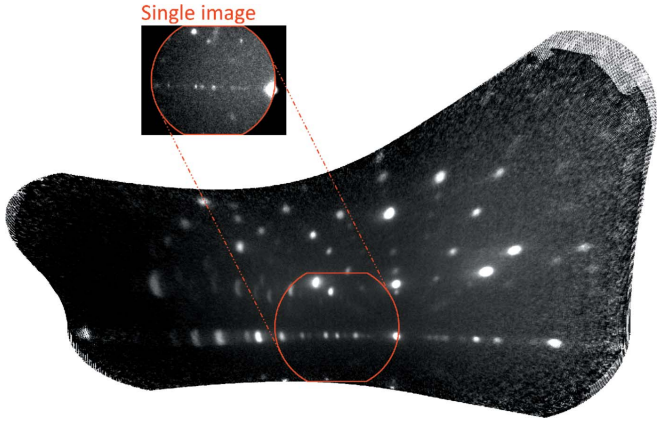

Figure 4
An example image produced by combining images taken at different rotational positions. For this image, the angular range was +20 to −20° around the *z* axis and 0 to 20° perpendicular to this. The red border shows the size of a single unmapped image for comparison. The individual image captured at this rotation is also shown.

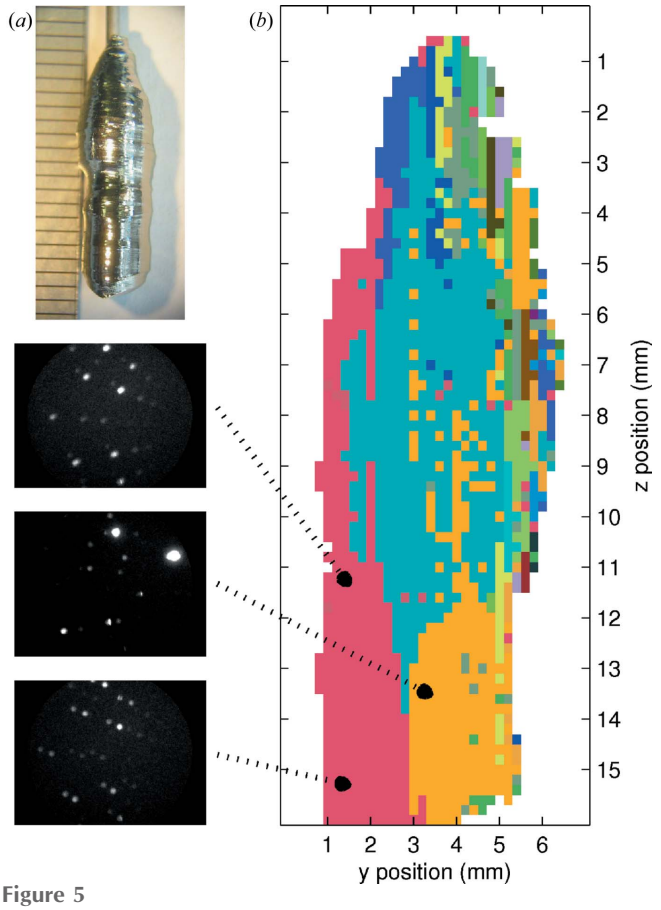

Figure 5
Grain mapping, using the co-existence approach described in the text, applied to a Czochralski-grown sample of UAu_2. (*a*) Photograph of the sample used. (*b*) Colour-coded grain map. Different colours correspond to different detected patterns within the sample and hence different grains. The images on the left show example patterns which were used for the grain-mapping method.

Once patterns were formed, all images in the scan set were compared with the set of patterns to determine which they fitted the best. An example map produced using this method can be seen in Fig. 5(*b*), which shows examples of the images that were compared. For this map, a single crystal of UAu_2 was used, grown by the Czochralski method by J. Schmehr and shown in Fig. 5(*a*).

3. Conclusions

An X-ray setup has been designed which combines a fast CCD detector with a computer-controlled goniometer to overcome some of the detector limits and also enable automated surface grain mapping. Wide-angled images have been produced, using a pixel-remapping approach. Two approaches to producing automated surface grain maps have been studied, and an approach in which large regions of co-existence between Bragg spots are identified has been found to be the more effective.

Acknowledgements

This work was funded by the EPSRC. The authors would like to thank R. Perry for the sample of MgV_2O_4 used, and J. Schmehr for providing the shown sample of UAu_2.

References

Chung, J.-S. & Ice, G. E. (1999). *J. Appl. Phys.* **86**, 5249–5255.
Eastman, D. E., Stagarescu, C. B., Xu, G., Mooney, P. M., Jordan-Sweet, J. L., Lai, B. & Cai, Z. (2002). *Phys. Rev. Lett.* **88**, 156101.
Ice, G. E. & Pang, J. W. L. (2009). *Mater. Charact.* **60**, 1191–1201.
Relf, C. (2004). *Image Acquisition and Processing with LabVIEW*. Boca Ranton: CRC Press LLC.
Xu, G., Su, X., Stagarescu, C., Eastman, D. E., Lai, B., Cai, Z., Noyan, I. C. & Hu, C.-K. (2001). *Appl. Phys. Lett.* **78**, 820.